National Technical University of Athens

School of Electrical and Computer Engineering

Division of Information Transmission Systems and Material Technology

Photonic integrated circuits for optical phased array beam steering and remote sensing based on heterodyne detection

A dissertation

by

Adam Raptakis

submitted to the School of Electrical and Computer Engineering,

in partial fulfillment of the requirements for the degree of

Doctor of Philosophy

Athens, November 2025

Page intentionally left blank.

ΕΘΝΙΚΟ ΜΕΤΣΟΒΙΟ ΠΟΛΥΤΕΧΝΕΙΟ
ΣΧΟΛΗ ΗΛΕΚΤΡΟΛΟΓΩΝ ΜΗΧΑΝΙΚΩΝ ΚΑΙ ΜΗΧΑΝΙΚΩΝ ΥΠΟΛΟΓΙΣΤΩΝ
ΤΟΜΕΑΣ ΣΥΣΤΗΜΑΤΩΝ ΜΕΤΑΔΟΣΗΣ ΠΛΗΡΟΦΟΡΙΑΣ ΚΑΙ ΤΕΧΝΟΛΟΓΙΑΣ ΥΛΙΚΩΝ

Photonic integrated circuits for optical phased array beam steering and remote sensing based on heterodyne detection

Διδακτορική διατριβή

του

Αδάμ Ν. Ραπτάκη

Συμβουλευτική Επιτροπή: Ηρακλής Αβραμόπουλος, Καθηγητής Ε.Μ.Π.
Εμμανουήλ Βαρβαρίγος, Καθηγητής Ε.Μ.Π.
Αθανάσιος Παναγόπουλος, Καθηγητής Ε.Μ.Π.

Εγκρίθηκε από την επταμελή εξεταστική επιτροπή την 24η Νοεμβρίου 2025.

…….……..	…….……..	…….……..
Ηρακλής Αβραμόπουλος Καθηγητής Ε.Μ.Π.	Εμμανουήλ Βαρβαρίγος Καθηγητής Ε.Μ.Π.	Αθανάσιος Παναγόπουλος Καθηγητής Ε.Μ.Π.
…….……..	…….……..	…….……..
Ηλίας Γλύτσης Ομότιμος Καθηγητής Ε.Μ.Π.	Παναγιώτης Κωττής Ομότιμος Καθηγητής Ε.Μ.Π.	Νικόλαος Πλέρος Καθηγητής Α.Π.Θ.

…….……..
Δημήτριος Αποστολόπουλος
Επίκουρος Καθηγητής
Ε.Μ.Π.

Αθήνα, Νοέμβριος 2025

…….……..

Αδάμ Ν. Ραπτάκης

Διδάκτωρ Ηλεκτρολόγος Μηχανικός και Μηχανικός Υπολογιστών Ε.Μ.Π.

“Χαράξου κάπου με οποιονδήποτε τρόπο

και μετά πάλι σβήσου με γενναιοδωρία.”

Οδυσσέας Ελύτης

Page intentionally left blank.

Περίληψη

Η φωτονική ολοκλήρωση βρίσκεται στο επίκεντρο της ερευνητικής δραστηριότητας για περισσότερο από δύο δεκαετίες, έχοντας σημειώσει αξιοσημείωτη πρόοδο στην κατασκευή ολοκληρωμένων οπτικών συσκευών και κυκλωμάτων, κυρίως λόγω της ανάγκης για οπτικές διασυνδέσεις υψηλού εύρους ζώνης στα δίκτυα επικοινωνιών. Ωστόσο, η ωρίμανση της τεχνολογίας έχει ανοίξει τον δρόμο σε νέες εφαρμογές τα τελευταία χρόνια. Οι εφαρμογές τηλεπισκόπησης έχουν αποκτήσει σημαντική δυναμική ως η επόμενη μεγάλη εμπορική ευκαιρία για τα φωτονικά ολοκληρωμένα κυκλώματα (PICs), κυρίως λόγω του ενδιαφέροντος της αυτοκινητοβιομηχανίας για συστήματα LiDAR. Προς αυτή την κατεύθυνση έχουν αναπτυχθεί πολλές τεχνολογίες, με στόχο την αντιμετώπιση προκλήσεων που σχετίζονται με την υψηλή ακρίβεια μέτρησης, τη γρήγορη σάρωση, καθώς και την ανάπτυξη οικονομικά αποδοτικών λύσεων κλίμακας.

Μεταξύ των διάφορων τεχνολογιών ολοκλήρωσης, η πλατφόρμα ολοκλήρωσης του silicon nitride (SiN) και η ολοκλήρωση που βασίζεται σε πολυμερή, παρουσιάζουν ιδιαίτερο ενδιαφέρον για εφαρμογές τηλεπισκόπησης λόγω των χαμηλών οπτικών απωλειών, την ικανότητα διαχείρισης υψηλής οπτικής ισχύος, καθώς και του φασματικού εύρους λειτουργίας που υποστηρίζουν. Η παρούσα εργασία αξιοποιεί τις δύο παραπάνω πλατφόρμες για την ανάπτυξη δύο νέων λειτουργιών: την μετατόπιση οπτικής συχνότητας (Optical Frequency Shifting - OFS) για ετερόδυνη συμβολομετρία και τη σάρωση μίας οπτικής δέσμης laser στο χώρο με χρήση οπτικών στοιχειοκεραιών (Optical Phased Arrays - OPAs). Για την υλοποίηση κυκλωμάτων μετατόπισης της οπτικής συχνότητας χρησιμοποιούνται λεπτές στρώσεις PZT επάνω από τους κυματοδηγούς SiN για τη διαμόρφωση του δείκτη διάθλασης μέσω του πιεζο-οπτικού φαινομένου, το οποίο προσφέρει μεγαλύτερο εύρος ζώνης σε σχέση με τους συμβατικούς θερμο-οπτικούς διαμορφωτές φάσης. Τα OFS PICs ενσωματώνονται σε ένα σύστημα απομακρυσμένης μέτρησης δονήσεων Laser Doppler Vibrometer (LDV). Επιπλέον, προτείνεται μια διαδικασία υβριδικής ολοκλήρωσης πολυμερικών κυματοδηγών επάνω στην πλατφόρμα SiN για το συνδυασμό των λειτουργιών που υποστηρίζει η κάθε πλατφόρμα σε ένα τσιπ. Οι διατάξεις οπτικών στοιχειοκεραιών υλοποιούνται στην πολυμερική πλατφόρμα, στην οποία χρησιμοποιείται μία προσέγγιση κάθετης ολοκλήρωση για το σχηματισμό πολλαπλών επιπέδων κυματοδήγησης και συνεπώς δισδιάστατων OPAs στην άκρη του τσιπ. Για τη ρύθμιση της φάσης του οπτικού πεδίου σε κάθε κυματοδηγό χρησιμοποιούνται θερμο-οπτικοί διαμορφωτές φάσης χαμηλής κατανάλωσης ισχύος. Επιπλέον, μελετώνται

γραμμικές διατάξεις στοιχειοκεραιών με ανομοιόμορφη κατανομή των στοιχείων, για τη βελτίωση του οπτικού πεδίου (FOV) και τη μείωση της πολυπλοκότητας ελέγχου. Συζητούνται θέματα χαρακτηρισμού και βαθμονόμησης των OPAs, καθώς και παράμετροι κατασκευής των πολύ-επίπεδων πολυμερικών PICs. Η παρούσα εργασία αποτελεί την πρώτη πειραματική υλοποίηση στροφής δέσμης στις δύο διαστάσεις με χρήση PIC πολλαπλών επιπέδων κυματοδήγησης.

Λέξεις κλειδιά: Φωτονική ολοκλήρωση, οπτική διαμόρφωση συχνότητας, πιεζο-οπτικό φαινόμενο, ετερόδυνη ανίχνευση, laser Doppler δονητόμετρο, υβριδική ολοκλήρωση, πλατφόρμα νιτριδίου του πυριτίου, πολυμερική πλατφόρμα ολοκλήρωσης, τρισδιάστατη ολοκλήρωση, οπτικές στοιχειοκεραίες, σάρωση οπτικής δέσμης, τηλεπισκόπιση

Abstract

Photonic integration is a powerful technology for miniaturizing optical devices and systems. Being in the center of research interest for over two decades, photonic integration has made tremendous progress, driven primarily by the information industry's demand for high-bandwidth optical interconnects. However, its maturation has opened the door to new applications in recent years. Remote sensing and ranging applications have gained significant momentum as the next potential mass-market opportunity for photonic integrated circuits (PICs), particularly due to the automotive industry's growing interest in LiDAR. Many different technologies have spawn to address challenges related to high accuracy sensing and fast scanning and develop scalable and cost-effective solutions.

Among the various existing integration platforms, silicon nitride (SiN) and polymer-based photonic integration are particularly interesting for remote sensing applications, primarily due to their low loss waveguides and passive components, their wide spectral range of operation, and the high-optical-power handling capabilities. This work leverages these platforms to develop two novel functionalities: optical frequency shifting (OFS) for heterodyne interferometry and two-dimensional laser-beam steering based on optical phased arrays (OPAs). OFS is based on stress-optic index modulation, that offers larger bandwidth than conventional thermo-optic phase shifters, by using lead zirconate titanate (PZT) thin films deposited on top of the SiN waveguides with a wafer-scale process. The OFS PICs are integrated into a NIR laser Doppler vibrometer (LDV) system for non-contact measurements of a vibrating surface. Furthermore, a process for hybrid integration of polymer waveguides on top of the SiN platform is introduced, to combine functionalities from both platforms in a fully compact manner. Optical phased arrays (OPAs) are implemented in the polymer-based technology platform, where multiple waveguiding layers are used to form rectangular apertures at the edge facet of the PICs. Two-dimensional (2D) steering of a NIR laser beam is demonstrated by individual phase control of each OPA channel using thermo-optic phase shifters. Linear aperiodic OPAs with non-uniform emitter spacing are explored to enhance the field of view and reduce control complexity. OPA characterization and calibration aspects are discussed, as well as fabrication considerations for multi-layer polymer PICs. Although the multi-waveguide-layer approach for 2D edge-emitting OPAs has been previously suggested, this work presents the first experimental demonstration of 2D beam steering based on this concept.

Keywords: Photonic integration, optical frequency shift, stress-optic modulation, thin-film PZT, silicon nitride platform, Heterodyne detection, laser Doppler vibrometer, hybrid integration, optical phased arrays, laser beam steering, optical polymers, 3D integration, optical communications, remote sensing, LiDAR

Acknowledgments

The journey of attaining a Ph.D. in engineering is a unique experience filled with challenges and excitement, frustration and success. Ph.D is not only a degree but also a kind of life in which we fall, we learn, and we grow. It is a worthful journey with hard work that ultimately paid off. My journey at PCRL would not be so wonderful without any of the following people I would like to give my heartful thanks to.

First and foremost, I would like to thank Prof. Hercules Avramopoulos, the founder of PCRL, for cultivating an exceptional environment where brilliant people, technological excellence, and creative thinking thrive. His vision and unwavering commitment have been a constant source of inspiration for me.

I would like to give my heartful thanks to my advisor Prof. Christos Kouloumentas. His passion, dedication, and constant encouragement to strive for excellence have profoundly inspired me and shaped my approach to research. His mentorship and continuous support helped me achieve my best and overcome the challenges I faced throughout my doctoral journey, and for this I am deeply grateful.

I would like to thank both Prof. Hercules Avramopoulos and Prof. Christos Kouloumentas for supporting my visit to LIP6 in Paris, to the research group of Eleni Diamanti, where I had the opportunity to collaborate with leading researchers in the exciting field of Quantum Information.

Next, I would like to thank my lab mates and closest partners throughout my PhD years Dr. Lefteris Gounaridis, Dr. Panos Groumas, Dr. Christos Tsokos and Efstathios Andrianopoulos for their professionalism, their camaraderie, and for making every working day so joyful. I would like to give special thanks to Dr. Lefteris Gounaridis for guiding me through the testing methodologies of bare dies in my early stages, and for encouraging me to publish my work and actively participate in conferences and workshops. My trip to San Francisco wouldn’t have been possible without his support. I would also like to thank Dr. Panos Groumas, Dr. Christos Tsokos, and Stathis Andrianopoulos for our fruitful discussions, for always being available and willing to share their experience, and for their continuous support during my test campaigns. Moreover, I would like to thank my colleague George Lymperakis for his inspiring commitment and motivation. The outcomes of his thesis were a decisive contribution to this work. In addition, I would like to thank my former colleagues Hlias Mylonas and Michalis Gergopoulos, who preceded me and laid the

foundation for the theoretical modelling of optical antennas. Additionally, I would like to thank my friend and colleague Nikos Baxevanakis. Without his design skills in electronics, some of the experimental demonstrations of this work would not have been so successful.

Furthermore, I would like to thank the researchers Adamantia Grammatikaki, Dimitrios Gounaridis, and Georgios Megas for their valuable contributions to the team. I would also like to thank Nikolaos Lyras, Giannis Giannoulis, and Dimitris Zavitsanos for our research discussions and exciting collaboration in the early years of my PhD. For our seamless collaboration, I would like to thank every member of PCRL, senior and junior researchers, as well as the administrative staff. Above all, I am grateful to them for creating such an enjoyable and inspiring working environment. It has been an absolute pleasure to be part of such an exciting team.

Subsequently, I would like to thank the external partners that contributed to this work. I would like to thank Madeleine Weigel, Moritz Kleinert and Norbert Keil from the Fraunhofer Institute for Telecommunications, HHI, for our research discussions, their guidance, and their commitment to the vision of this work. Similarly, I would like to thank Marco Wolfer, Alexander Draebenstedt, and Volker Seyfried from Polytec GmbH for their valuable insights on LDVs, as well as for their contribution to the experimental part of this work. I would also like to thank Jörn Epping, Erik Schreuder, Philip P. J. Schrinner and Ronald Dekker from LioniX for our discussions and their commitment to advancing silicon nitride technology.

I would also like to thank Prof. Elias Glytsis for serving my thesis committee and for teaching me the fundamentals of integrated optics and electro-optic devices during my master's studies, as well as laying the foundations of electromagnetic theory during my undergraduate years. In addition, I would like to express my heartfelt gratitude to the late Prof. Aristidis Arageorgis for inspiring my scientific curiosity and cultivating my intellectual growth through his introduction to philosophy during my undergraduate years.

I would like to thank my close friends for their support throughout my PhD years. Special thanks go to my friend and colleague Stelios Stavroulakis for providing valuable insights into optimization algorithms, and to my friend and colleague George Chalkiopoulos for keeping me company during the countless hours spent in cafeterias while writing this thesis.

Finally, I would like to thank my parents for helping me develop the determination and patience that made this journey possible.

Εκτεταμένη Περίληψη

Ο τομέας των οπτικών αισθητήρων απομακρυσμένης ανίχνευσης ή τηλεπισκόπισης (remote optical sensors) έχει γνωρίσει ιδιαίτερη άνθιση τα τελευταία χρόνια, κυρίως λόγω του αυξανόμενου ενδιαφέροντος της αυτοκινητοβιομηχανίας, αλλά και της βιομηχανίας γενικότερα, για συστήματα LiDAR. Η παρούσα διατριβή εστιάζει σε δύο βασικές προκλήσεις στο πεδίο των οπτικών αισθητήρων τηλεπισκόπισης: τη μετατόπιση της οπτικής συχνότητας για εφαρμογές συμβολομετρίας ετερόδυνης ανίχνευσης και τη σάρωση μίας οπτικής δέσμης στο χώρο. Οι προκλήσεις αυτές αφορούν την υλοποίηση των παραπάνω λειτουργιών σε ολοκληρωμένη μορφή αξιοποιώντας τη φωτονική ολοκλήρωση, καθώς οι συμβατικές υλοποιήσεις βασίζονται σε ογκώδη οπτικά εξαρτήματα και, στην περίπτωση της σάρωσης οπτικής δέσμης, σε μηχανικά μέρη. Η εργασία αξιοποιεί δύο διαφορετικές πλατφόρμες φωτονικής ολοκλήρωσης: την πλατφόρμα silicon nitride της εταιρείας LioniX, με την εμπορική ονομασία ‘‘TriPleX’’ (silicion nitride) και την πολυμερική πλατφόρμα ολοκλήρωσης του ερευνητικού ινστιτούτου Fraunhofer Heinrich-Hertz Institute (HHI), με την εμπορική ονομασία ‘‘PolyBoard’’.

Το πρώτο μέρος της εργασίας αφορά την ανάπτυξη ενός συστήματος Laser Doppler Vibrometer (LDV) βασισμένο σε φωτονικά ολοκληρωμένα κυκλώματα (PICs), εστιάζοντας στη μελέτη κυκλωμάτων που επιτελούν μετατόπιση της οπτικής συχνότητας (optical frequency shifter – OFS). Η τεχνική του LDV χρησιμοποιεί μία οπτική δέσμη laser για να μετρήσει μακρόθεν τα χαρακτηριστικά της μηχανικής ταλάντωσης μίας δονούμενης επιφάνειας. Βασίζεται στη συμβολομετρία για να αποδιαμορφώσει τη φάση του λαμβανόμενου οπτικού σήματος, το οποίο κατόπιν της ανάκλασής του στην παρατηρούμενη επιφάνεια διαμορφώνεται λόγω του φαινομένου Doppler. Υπάρχουν δύο τεχνικές συμβολομετρίας που χρησιμοποιούνται στο LDV, η ομόδυνη και η ετερόδυνη ανίχνευση, όπου η δεύτερη είναι περισσότερο διαδεδομένη λόγω της υψηλότερης αξιοπιστίας και ευαισθησίας που προσφέρει. Η μετατόπιση της οπτικής συχνότητας αποτελεί μία βασική λειτουργία στην ετερόδυνη ανίχνευση καθώς επιτρέπει τη διάκριση της κατεύθυνσης της κίνησης ή της ταλάντωσης του παρατηρούμενου σώματος, ενώ παράλληλα βελτιώνει το σηματοθορυβικό λόγο (SNR), μετατοπίζοντας το φάσμα συχνοτήτων μακριά από τον θόρυβο βασικής ζώνης. Τα συστήματα μετατόπισης συχνότητας που είναι εμπορικά διαθέσιμα σήμερα βασίζονται κατά κύριο λόγο σε ακουστο-οπτικούς διαμορφωτές, οι οποίοι προσφέρουν υψηλή απόδοση μετατροπής και χαμηλό θόρυβο, όμως βασίζονται σε κρυστάλλους, οι οποίοι είναι ογκώδεις, απαιτούν την

ακριβή ευθυγράμμιση της εισερχόμενης δέσμης, ενώ παρουσιάζουν μικρή ευελιξία στην επιλογή της συχνότητας.

Αρχικά, η εργασία εστιάζει στη θεωρητική ανάλυση και την πειραματική αξιολόγηση ολοκληρωμένων κυκλωμάτων οπτικών διαμορφωτών που επιτελούν μετατόπιση της οπτικής συχνότητας, στην πλατφόρμα του silicon nitride. Συγκεκριμένα μελετώνται δύο οπτικά κυκλώματα διαμόρφωσης, τα οποία αξιοποιούν διαφορετικές τεχνικές για την μετατόπιση της συχνότητας του οπτικού φέροντος. Το πρώτο κύκλωμα βασίζεται στη τεχνική serrodyne κατά την οποία η μετατόπιση της συχνότητας προκύπτει από τη γραμμική αύξηση της οπτικής φάσης. Το δεύτερο κύκλωμα επιτυγχάνει μετατόπιση της συχνότητας μέσω διαμόρφωσης μονής πλευρικής ζώνης με χρήση ενός IQ διαμορφωτή. Στα πλαίσια της θεωρητικής ανάλυσης αναπτύσσονται μοντέλα προσομοίωσης των κυκλωμάτων και μελετάται η επίδοσή τους συναρτήσει της ποιότητας των σημάτων οδήγησης και των πιθανών κατασκευαστικών ατελειών. Επιπλέον, αναδεικνύονται οι πρακτικοί περιορισμοί τους ως προς την απόδοση μετατροπής και την καταπίεση ανεπιθύμητων αρμονικών. Χρησιμοποιώντας την τεχνική serrodyne επιβεβαιώνεται πειραματικά μετατόπιση συχνότητας κατά 100 kHz και καταπίεση αρμονικών κατά 22.1 dB, ενώ με τη διαμόρφωση πλευρικής ζώνης επιτυγχάνεται μετατόπιση 2.5 MHz και καταπίεση της πλευρικής ζώνης κατά 39 dB. Η τεχνική serrodyne βασίζεται σε ηλεκτρικά σήματα οδήγησης πριονωτής μορφής, τα οποία απαιτούν ηλεκτρονικά με εύρος ζώνης σημαντικά μεγαλύτερο της συχνότητας μετατόπισης, γεγονός που περιορίζει τη μέγιστη συχνότητα μετατόπισης. Η υλοποίησή των παραπάνω κυκλωμάτων πραγματοποιείται στην πλατφόρμα φωτονικής ολοκλήρωσης TriPleX, στην οποία μελετάται ένα πρωτότυπο είδος διαμορφωτή, ο οποίος βασίζεται στο πιεζο-οπτικό (stress-optic) φαινόμενο για τη διαμόρφωση της φάσης του οπτικού σήματος. Αυτό επιτυγχάνεται με την εναπόθεση ενός λεπτού στρώματος πιεζοηλεκτρικού υλικού, συγκεκριμένα του lead zirconate titanate (PZT), πάνω από τους κυματοδηγούς του TriPleX, το οποίο, με την εφαρμογή ηλεκτρικής τάσης, ασκεί μηχανική πίεση στο υλικό του κυματοδηγού μεταβάλλοντας το δείκτη διάθλασης. Το πιεζο-οπτικό φαινόμενο χαρακτηρίζεται από μικρότερη σταθερά χρόνου σε σχέση με το θερμο-οπτικό φαινόμενο επιτρέποντας υψηλότερες ταχύτητες απόκρισης. Σε χαμηλές συχνότητες, ο πιεζο-οπτικός διαμορφωτής παρουσιάζει εξαιρετικά χαμηλή κατανάλωση λόγω της χωρητικής του συμπεριφοράς και για το λόγο αυτό, σε προηγούμενες υλοποιήσεις στο TriPleX, είχε περιοριστεί σε dc λειτουργία, ως εναλλακτική των θερμο-οπτικών διαμορφωτών για τη στροφή της οπτικής φάσης. Για πρώτη φορά στην

παρούσα εργασία μελετάται πειραματικά στην περιοχή των MHz, αξιοποιώντας μία ενναλακτική τοποθέτηση των ηλεκτροδίων οδήγησης προκειμένου να μειωθεί η χωρητικότητα και συνεπώς να αυξηθεί το εύρος ζώνης του διαμορφωτή. Πειραματικά, στην περίπτωση της μετατόπισης συχνότητας μέσω του IQ διαμορφωτή, επιτυγχάνεται ημιτονοειδής μετατόπιση φάσης π/4 στα 2.5 MHz, με κατανάλωση ισχύος 156 mW, με τον καλύτερο διαμορφωτή, ενώ η μέση κατανάλωση ισχύος για όλους τους διαμορφωτές που υλοποιήθηκαν ήταν περίπου 660 mW για την ίδια μετατόπιση φάσης. Για τον πειραματικό χαρακτηρισμό χρησιμοποιούνται κατάλληλα ηλεκτρονικά οδήγησης καθώς απαιτείται τάση οδήγησης της τάξης των 100 Vpeak-to-peak, ή και περισσότερο, για μήκη διαμόρφωσης της τάξης των 15 mm.

Κατόπιν της πειραματικής αξιολόγησης των επιμέρους ολοκληρωμένων κυκλωμάτων μετατόπισης συχνότητας, τα κυκλώματα ενσωματώνονται σε ένα ευρύτερο σύστημα LDV ετερόδυνης ανίχνευσης, με μήκος κύματος λειτουργίας στο εγγύς υπέρυθρο, συγκεκριμένα γύρω από τα 1550 nm. Για την ανίχνευση αναπτύσσεται και αξιολογείται πειραματικά δέκτης στην πολυμερική πλατφόρμα ολοκλήρωσης PolyBoard. Η πλατφόρμα αυτή επιτρέπει την τοποθέτηση thin-film πολωτικών στοιχείων σε μικρές σχισμές επάνω στο τσιπ για τον έλεγχο της πόλωσης του σήματος, καθώς επίσης και την υβριδική ολοκλήρωση με InP φωτοδιόδους για την ανίχνευση του σήματος. Χρησιμοποιώντας τις παραπάνω δυνατότητες ο δέκτης σχεδιάστηκε κατάλληλα προκειμένου να υποστηρίζει τη σύμφωνη ανίχνευση των δύο ορθογωνικών πολώσεων του λαμβανόμενου σήματος. Για την υλοποίηση του συστήματος LDV χρησιμοποιήθηκαν επιπλέον εμπορικά διαθέσιμα οπτικά στοιχεία, μεταξύ των οποίων μια οπτική πηγή laser χαμηλού θορύβου φάσης και ένα σύστημα φακών της εταιρείας Polytec, το οποίο απαιτείται για την εστίαση και τη συλλογή της οπτικής δέσμης προς και από την μετρούμενη επιφάνεια. Σε συνεργασία με την γερμανική εταιρεία Polytec, στα πλαίσια του ευρωπαϊκού έργου ICT-3PEAT, πραγματοποιήθηκαν μετρήσεις ταλαντώσεων έως 15 kHz με ανάλυση μετατόπισης 10 pm, χρησιμοποιώντας το κύκλωμα μετατόπισης συχνότητας του IQ διαμορφωτή. Παρόλο που τα πειράματα περιορίστηκαν στην ακουστική περιοχή, λόγω του ηχείου που χρησιμοποιήθηκε για την παραγωγή των δονήσεων, επιβεβαιώθηκε πειραματικά η δυνατότητα του συστήματος να ανιχνεύει συχνότητες έως 1 MHz με ανάλυση 10 pm. Το συγκεκριμένο σύστημα βασίστηκε σε επιμέρους φωτονικά ολοκληρωμένα κυκλώματα (PICs) τα οποία συσκευάστηκαν ξεχωριστά και συνδέθηκαν με οπτικές ίνες. Ως επόμενο βήμα, προς την επίτευξη υψηλού βαθμού ολοκλήρωσης, υιοθετήθηκε μια καινοτόμος

προσέγγιση υβριδικής ολοκλήρωσης, με σκοπό τον συνδυασμό των πλατφορμών TriPleX και PolyBoard σε ένα τσιπ. Χάρη στην ευελιξία κατασκευής που προσφέρουν οι πολυμερικές πλατφόρμες μέσω της τεχνικής spin-coating, το οπτικό κύκλωμα του δέκτη στο PolyBoard κατασκευάστηκε επάνω από το κύκλωμα μετατόπισης συχνότητας στο TriPleX, δημιουργώντας ένα τρισδιάστατο υβριδικό φωτονικό ολοκληρωμένο κύκλωμα (3D PIC). Παρότι ο πειραματικός χαρακτηρισμός κατέδειξε απώλειες σύζευξης μεταξύ των δύο πλατφορμών της τάξης των 15 dB, τα αποτελέσματα προσομοιώσεων υποδεικνύουν ότι οι απώλειες μπορούν να μειωθούν σημαντικά, έως και κάτω από 1 dB, με τις αντίστοιχες βελτιώσεις στη διαδικασία κατασκευής. Οι αυξημένες απώλειες στο σύστημα που υλοποιήθηκε οφείλονται σε κατασκευαστική αστοχία κατά τη διαδικασία ευθυγράμμιση μεταξύ των κυκλωμάτων του TriPleX και του PolyBoard. Χρησιμοποιώντας το ενσωματωμένο κύκλωμα του serrodyne διαμορφωτή και το δέκτη σύμφωνης ανίχνευσης στο PolyBoard ολοκληρώθηκαν μετρήσεις μετατόπισης συχνότητας, επαληθεύοντας τη λειτουργικότητα του τσιπ. Καταλήγουμε στο συμπέρασμα πως τα ολοκληρωμένα κυκλώματα μετατόπισης συχνότητας που αναπτύχθηκαν μπορούν να ενσωματωθούν με επιτυχία σε ένα πλήρως λειτουργικό LDV σύστημα, το οποίο επιτρέπει τη μέτρηση συχνοτήτων δόνησης τουλάχιστον τρεις τάξεις μεγέθους υψηλότερα από ό,τι είναι εφικτό με τους συμβατικούς θερμο-οπτικούς διαμορφωτές της silicon nitride πλατφόρμας. Η ενσωμάτωση της λειτουργίας μετατόπισης συχνότητας στην πλατφόρμα του TiPleX αποτελεί σημαντικό επίτευγμα καθώς ανοίγει το δρόμο για το συνδυασμό με άλλες λειτουργίες, όπως ανίχνευση μέσω συμβολομετρικών διατάξεων ή κυκλωμάτων οπτικών στοιχειοκεραιών, μέσω μονολιθικής ή υβριδικής ολοκλήρωσης, επιτρέποντας την ανάπτυξη συστημάτων αισθητήρων μικρού μεγέθους και χαμηλού κόστους.

Το δεύτερο μέρος της εργασίας επικεντρώνεται στην ανάπτυξη οπτικών στοιχειοκεραιών (Optical Phased Arrays - OPAs) στην πολυμερική πλατφόρμα ολοκλήρωσης PolyBoard, με σκοπό τη στροφή μία οπτικής δέσμης laser στο χώρο με ηλεκτρονικό τρόπο. Καινοτόμες εφαρμογές, όπως τα συστήματα LiDAR, οι πλατφόρμες επαυξημένης και εικονικής πραγματικότητας (AR/VR), καθώς και οι οπτικές ασύρματες επικοινωνίες (OWC), έχουν εντείνει την ανάγκη για συστήματα σάρωσης μικρού μεγέθους και μειωμένου κόστους. Η πρόοδος που έχει σημειωθεί τα τελευταία χρόνια στον τομέα της φωτονικής ολοκλήρωσης καθιστά τις οπτικές στοιχειοκεραίες μια ιδιαιτέρως ελκυστική τεχνολογική λύση για τις εφαρμογές αυτές, γεγονός που έχει δώσει σημαντική ώθηση στην ερευνητική δραστηριότητα γύρω από το συγκεκριμένο αντικείμενο. Οι

εμπορικά διαθέσιμες συσκευές σάρωσης βασίζονται κατά κύριο λόγο σε οπτομηχανικά εξαρτήματα για την εκτροπή της οπτικής δέσμης. Η χρήση μηχανικών στοιχείων, όπως κινούμενων κατόπτρων και σερβοκινητήρων, αυξάνει σημαντικά τον όγκο και το βάρος των συστημάτων, δυσχεραίνοντας την ενσωμάτωσή τους σε πλατφόρμες περιορισμένου χώρου, όπως αυτοκίνητα ή μη επανδρωμένα αεροσκάφη (drones). Παράλληλα αυξάνουν το κόστος και την πολυπλοκότητα συναρμολόγησης, ενώ καθιστούν τις συσκευές περισσότερο ευάλωτες σε φθορά και μηχανικές αστοχίες. Επιπλέον, η ταχύτητα και η ακρίβεια σάρωσης περιορίζονται εγγενώς από τη μάζα και την αδράνεια των κινούμενων εξαρτημάτων. Αντιθέτως, οι οπτικές στοιχειοκεραίες επιτρέπουν την επίτευξη σάρωσης της οπτικής δέσμης χωρίς την ανάγκη κινούμενων μηχανικών μερών, αξιοποιώντας την αρχή λειτουργίας των συμβατικών στοιχειοκεραιών. Συγκεκριμένα, μια συστοιχία επιμέρους εκπομπών μπορεί να κατευθύνει την εκπεμπόμενη ηλεκτρομαγνητική ισχύ σε επιθυμητή κατεύθυνση μέσω κατάλληλης ρύθμισης της φάσης διέγερσης των στοιχείων της. Η προσέγγιση αυτή προσφέρει τη δυνατότητα δραστικής μείωσης του μεγέθους, βάρους, κατανάλωσης ισχύος και κόστους (SWaP-C).

Οπτικές στοιχειοκεραίες έχουν υλοποιηθεί σχεδόν σε κάθε πλατφόρμα φωτονικής ολοκλήρωσης: silicon on insulator (SOI), silicon nitride (SiN), III-V (InP, GaAs), lithium niobate on insulator (LNOI), silica, πολυμερική ολοκλήρωση, κάθε μία από τις οποίες χαρακτηρίζεται από τα δικά της πλεονεκτήματα και προκλήσεις. Τα πολυμερικά οπτικά υλικά αποτελούν ιδιαίτερα ελκυστική επιλογή για την ανάπτυξη οπτικών στοιχειοκεραιών (OPAs), καθώς χαρακτηρίζονται από χαμηλή πολυπλοκότητα κατασκευής, θερμο-οπτικά στοιχεία χαμηλής κατανάλωσης, ανοχή σε υψηλά επίπεδα οπτικής ισχύος, καθώς και από ευρεία φασματική περιοχή λειτουργίας. Η κατασκευή πολυμερικών φωτονικών διατάξεων βασίζεται σε τεχνικές όπως το spin-coating για τη δημιουργία των στρωμάτων του πυρήνα και του μανδύα, καθώς και σε λιθογραφία υπεριώδους ακτινοβολίας (UV lithography) χαμηλής ανάλυσης για τον σχηματισμό των οπτικών δομών στο υπόστρωμα. Η διαδικασία αυτή προσφέρει σημαντική ευελιξία και οικονομική αποδοτικότητα σε σύγκριση με πιο απαιτητικές πλατφόρμες, όπως η silicon-on-insulator (SOI) ή οι πλατφόρμες III–V υλικών, οι οποίες απαιτούν τεχνολογίες patterning υψηλής ανάλυσης, επιταξιακές διεργασίες, υψηλές θερμοκρασίες επεξεργασίας και ακριβότερα υποστρώματα. Επιπλέον, οι πλατφόρμες που βασίζονται σε πολυμερή υποστηρίζουν θερμο-οπτικούς διαμορφωτές φάσης χαμηλής κατανάλωσης ισχύος, λόγω του εγγενώς υψηλού θερμο-οπτικού συντελεστή τους ($-1 \cdot 10^{-4}\, K^{-1}$ έως $-3 \cdot 10^{-4}\, K^{-1}$), καθώς και της χαμηλής θερμικής

αγωγιμότητας των πολυμερικών υλικών (περίπου 0.3 W/m/K). Ο περιορισμός της κατανάλωσης ισχύος αποτελεί κρίσιμο παράγοντα στον σχεδιασμό οπτικών στοιχειοκεραιών, όπου δεκάδες έως και χιλιάδες θερμο-οπτικά στοιχεία μπορούν να ολοκληρωθούν στο ίδιο τσιπ. Η χαμηλή θερμική αγωγιμότητα των πολυμερών συμβάλλει σημαντικά στη μείωση της απαιτούμενης ισχύος σε σχέση με αντίστοιχες διατάξεις στην πλατφόρμα silicon-on-insulator (SOI), ωστόσο συνοδεύεται από αυξημένους χρόνους απόκρισης (της τάξης των millisecond). Παρόλο που δεν αποτελεί αντικείμενο της παρούσας εργασίας, αξίζει να αναφερθεί η δυνατότητα των πολυμερών να υποστηρίξουν διαμορφωτές υψηλών ταχυτήτων μέσω του ηλεκτρο-οπτικού φαινομένου, προσφέροντας περαιτέρω ευελιξία στον σχεδιασμό ολοκληρωμένων φωτονικών κυκλωμάτων. Ένα ακόμη σημαντικό πλεονέκτημα των πολυμερικών κυματοδηγών είναι η ικανότητά τους να διαχειρίζονται υψηλές οπτικές ισχείς. Σε αντίθεση με το πυρίτιο, το οποίο παρουσιάζει απορρόφηση δύο φωτονίων (two-photon absorption) για μήκη κύματος μικρότερα των 2 μm, τα πολυμερικά υλικά δεν επηρεάζονται από το συγκεκριμένο φαινόμενο. Πειραματικές μελέτες στην πλατφόρμα PolyBoard έχουν αποδείξει ότι οι πολυμερικοί κυματοδηγοί μπορούν να μεταφέρουν οπτική ισχύ έως και 23 dBm (~200 mW) για παρατεταμένα χρονικά διαστήματα και σε ευρύ εύρος θερμοκρασιών, χωρίς να εμφανίζουν πρόσθετες απώλειες διάδοσης ή μεταβολές του δείκτη διάθλασης. Το γεγονός αυτό καθιστά τις πολυμερικές πλατφόρμες κατάλληλες για την ανάπτυξη διατάξεων εκπομπής σχετικά υψηλής οπτικής ισχύος.

Η πολυμερική πλατφόρμα φωτονικής ολοκλήρωσης PolyBoard, η οποία αξιοποιείται στην παρούσα εργασία, βασίζεται σε εμπορικά διαθέσιμα πολυμερικά υλικά της ChemOptics Inc. (σειρά ZPU-12). Λόγω της χαμηλής πολυπλοκότητας, τα βήματα κατασκευής μπορούν να επαναληφθούν διαδοχικά για τη δημιουργία πολλαπλών επιπέδων κυματοδήγησης και τρισδιάστατων δομών κάθετης ολοκλήρωσης (3D integration) για τη μεταφορά του φωτός μεταξύ των διαφορετικών επιπέδων. Η διαδικασία κατασκευής βασίζεται στη χρήση δύο πολυμερικών ρητινών, της ρητίνης πυρήνα (core) και της ρητίνης του μανδύα (cladding) και περιλαμβάνει τα εξής στάδια: (α) spin-coating της ρητίνης του μανδύα επάνω σε υπόστρωμα πυριτίου (Si), (β) spin-coating της ρητίνης κυματοδηγού, (γ) σχηματισμό των κυματοδηγών με λιθογραφία υπεριώδους ακτινοβολίας (UV lithography) και εγχάραξη μέσω της μεθόδου Reactive Ion Etching (RIE), και (δ) spin-coating της ρητίνης περίβλημα για τη δημιουργία του άνω στρώματος μανδύα (top cladding layer). Η διαδικασία επαναλαμβάνεται διαδοχικά, χρησιμοποιώντας διαφορετικές μάσκες για κάθε

επίπεδο κυματοδήγησης, με αποτέλεσμα το σχηματισμό κάθετα ολοκληρωμένων και πλήρως ανεξάρτητων επιπέδων κυματοδήγησης. Η μεταφορά του φωτός μεταξύ των διαφορετικών επιπέδων επιτυγχάνεται μέσω κατακόρυφων δομών MMI ενώ η κατανομή ισχύος στο ίδιο επίπεδο πραγματοποιείται μέσω συμβατικών δομών MMI. Τρισδιάστατα ολοκληρωμένα κυκλώματα στην πλατφόρμα PolyBoard έχουν αναπτυχθεί στο παρελθόν κυρίως για εφαρμογές σύζευξης με οπτικές ίνες πολλαπλών πυρήνων (multi-core fibers) ή για την κατασκευή μεγάλων κυκλωμάτων μεταγωγής χωρίς διασταυρώσεις κυματοδηγών. Ωστόσο, η ανάπτυξη τρισδιάστατων φωτονικών κυκλωμάτων ειδικά προσανατολισμένων στην υλοποίηση οπτικών στοιχειοκεραιών αξιολογείται πειραματικά για πρώτη φορά στο πλαίσιο της παρούσας εργασίας.

Το κύκλωμα μιας οπτικής στοιχειοκεραίας αποτελείται από τρία βασικά τμήματα: (α) το δίκτυο κατανομής της οπτικής ισχύος μεταξύ των εκπομπών (power distribution network), (β) το τμήμα ελέγχου της οπτικής φάσης (phase tuning section) και (γ) το τμήμα εκπομπής (aperture). Στην προσέγγιση που προτείνεται στην παρούσα εργασία, η κατανομή της οπτικής ισχύος προς τους επιμέρους εκπομπούς πραγματοποιείται μέσω ενός συνδυασμού κατακόρυφων και συμβατικών δομών MMI, οι οποίες επιτρέπουν την κατανομή της ισχύος εντός της τρισδιάστατης φωτονικής αρχιτεκτονικής. Ο έλεγχος της φάσης υλοποιείται με τη χρήση θερμο-οπτικών διαμορφωτών, τοποθετημένων επάνω από το ανώτερο επίπεδο κυματοδήγησης. Ωστόσο, καθώς ο αριθμός των επιπέδων αυξάνεται, η απαιτούμενη ισχύς για τη ρύθμιση της φάσης των κυματοδηγών που βρίσκονται βαθύτερα στη δομή αυξάνεται σημαντικά, λόγω της ανάγκης μεταφοράς επαρκούς ποσότητας θερμότητας σε μεγαλύτερο βάθος. Η προσέγγιση αυτή καθίσταται, επομένως, περιοριστική και εφαρμόζεται μόνο σε διατάξεις με δύο επίπεδα κυματοδήγησης. Για την επέκταση της αρχιτεκτονικής σε περισσότερα επίπεδα, η μεταφορά των λειτουργιών κατανομής ισχύος και ελέγχου φάσης στο ανώτερο επίπεδο αποτελεί πιο αποδοτική στρατηγική. Με αυτόν τον τρόπο, η φάση όλων των καναλιών μπορεί να ρυθμιστεί με υψηλή αποδοτικότητα, προτού η οπτική ισχύς κατανεμηθεί στα κατώτερα επίπεδα μέσω των κατακόρυφων MMI. Εναλλακτικά, οι θερμο-οπτικοί διαμορφωτές θα μπορούσαν να ενσωματωθούν ενδιάμεσα στα διαφορετικά κυματοδηγικά επίπεδα· ωστόσο, η λύση αυτή συνεπάγεται σημαντικά αυξημένη τεχνολογική πολυπλοκότητα, καθώς απαιτεί την εισαγωγή πρόσθετων μεταλλικών στρωμάτων για τη δημιουργία των ηλεκτροδίων, και δεν διερευνάται στο πλαίσιο της παρούσας εργασίας. Στο τελικό τμήμα του κυκλώματος, οι κυματοδηγοί συγκλίνουν σταδιακά ώστε να σχηματίσουν το άνοιγμα εκπομπής (emitting

aperture) απ' όπου το φως εξέρχεται στον ελεύθερο χώρο από την άκρη του τσιπ. Η συγκεκριμένη κατηγορία στοιχειοκεραιών αναφέρεται ως edge-emitting ή end-fire OPAs, όπου η διατομή του κυματοδηγού λειτουργεί ως το μοναδιαίο στοιχείο εκπομπής της συστοιχίας.

Παρά τα πλεονεκτήματά της, η υλοποίηση οπτικών στοιχειοκεραιών στην πολυμερική πλατφόρμα συνοδεύεται από ορισμένες προκλήσεις, οι οποίες πηγάζουν κυρίως από τη χαμηλή αντίθεση δείκτη διάθλασης μεταξύ του πυρήνα και του μανδύα των πολυμερικών κυματοδηγών. Η χαμηλή αντίθεση έχει ως αποτέλεσμα ο κυματοδηγούμενος ρυθμός να μην περιορίζεται έντονα μέσα στο υλικό του πυρήνα, γεγονός που εμποδίζει την τοποθέτηση παράλληλων κυματοδηγών σε πολύ μικρές αποστάσεις, καθώς εντείνεται το φαινόμενο σύζευξης (cross-coupling). Από την άλλη, η τοποθέτηση των κυματοδηγών σε αποστάσεις μεγαλύτερες του μισού του μήκος κύματος λειτουργίας (εν προκειμένω μεγαλύτερες των 775 nm) οδηγεί στη δημιουργία ανεπιθύμητων αντιγράφων του κύριου λοβού στο διάγραμμα ακτινοβολίας, περιορίζοντας το εύρος σάρωσης, το οποίο αναφέρεται ως οπτικό πεδίο (field of view). Η τοποθέτηση των εκπομπών σε επαρκώς μικρή απόσταση μεταξύ τους (1-2 μm), ώστε να μην περιορίζεται σημαντικά το οπτικό πεδίο της σάρωσης, αποτελεί πρόκληση γενικά στις στοιχειοκεραίες που λειτουργούν στα οπτικά μήκη κύματος (ορατό και εγγύς υπέρυθρο) ανεξαρτήτως της πλατφόρμας ολοκλήρωσης. Ωστόσο, αυτός ο περιορισμός μπορεί να μετριαστεί μέσω διάφορων στρατηγικών, όπως ο σχεδιασμός κυματοδηγών ώστε να μειώνεται η διασταυρούμενη σύζευξη μέσω αναντιστοιχίας φάσης (phase mismatch), ή η τοποθέτηση των εκπομπών με μη περιοδικό τρόπο (sparse aperiodic OPAs), η οποία μελετάται στην παρούσα εργασία. Ένα ακόμα αποτέλεσμα της χαμηλής αντίθεσης του δείκτη διάθλασης, είναι η περιορισμένη απόκλιση της οπτικής δέσμης όταν αυτή εξέρχεται από το υλικό του τσιπ στον ελεύθερο χώρο. Δεδομένου ότι το διάγραμμα ακτινοβολίας του μοναδιαίου εκπομπού καθορίζει το οπτικό πεδίο της στοιχειοκεραίας, η υψηλή κατευθυντικότητα του μοναδιαίου στοιχείου συνεπάγεται περιορισμένο εύρος σάρωσης. Σε επίπεδο κατασκευής, η κατευθυντικότητα αυτή μπορεί να τροποποιηθεί μόνο σε περιορισμένο βαθμό μέσω μικρών μεταβολών στους δείκτες διάθλασης της πλατφόρμας, καθώς σημαντικότερες αλλαγές θα επηρέαζαν δυσμενώς τα κυματοδηγικά χαρακτηριστικά των ολοκληρωμένων διατάξεων. Σε επίπεδο συστήματος, το οπτικό πεδίο μπορεί να επεκταθεί με τη χρήση κατάλληλων εξωτερικών οπτικών στοιχείων. Μια ακόμη πρόκληση αφορά τη δυνατότητα επέκτασης της τρισδιάστατης ολοκλήρωσης. Ο μέγιστος αριθμός επιπέδων

κυματοδήγησης που μπορούν να υλοποιηθούν εξαρτάται από την ακρίβεια ευθυγράμμισης των μασκών μεταξύ διαδοχικών σταδίων λιθογραφίας. Η δυνατότητα κατασκευής έως και πέντε διακριτών επιπέδων κυματοδηγών έχει αποδειχθεί πειραματικά, ενώ τα τελευταία χρόνια, οι ερευνητικές προσπάθειες εστιάζουν κυρίως στη βελτιστοποίηση των κατακόρυφων δομών MMI για την αποδοτική διασύνδεση των επιπέδων. Λαμβάνοντας υπόψη τις τρέχουσες τεχνολογικές δυνατότητες και τη συνεχή πρόοδο στον τομέα, εκτιμάται ότι ο διπλασιασμός του αριθμού των επιπέδων αποτελεί ρεαλιστικό μεσοπρόθεσμο στόχο. Ωστόσο, η υπέρβαση των δέκα επιπέδων αποτελεί σημαντική πρόκληση με βάση τις τρέχουσες τεχνολογικές δυνατότητες κατασκευής.

Το δεύτερο μέρος της εργασίας οργανώνεται ως εξής. Στο πρώτο κεφάλαιο παρουσιάζονται αναλυτικά τα πλεονεκτήματα και οι προκλήσεις της προτεινόμενης πολυμερικής πλατφόρμας ολοκλήρωσης, καθώς και οι κυριότερες υλοποιήσεις οπτικών στοιχειοκεραιών που έχουν προταθεί στη διεθνή βιβλιογραφία. Στο δεύτερο κεφάλαιο αναπτύσσονται τα θεμελιώδη στοιχεία της θεωρίας των στοιχειοκεραιών και συζητούνται οι βασικές αρχές σχεδιασμού τους. Στο τρίτο κεφάλαιο μελετώνται διατάξεις στοιχειοκεραιών με ομοιόμορφη κατανομή των στοιχείων. Αρχικά, αναπτύσσεται μια μέθοδος υπολογισμού του διαγράμματος ακτινοβολίας του μοναδιαίου εκπομπού με βάση την αρχή της ισοδυναμίας πεδίου (field equivalence principle) και τη θεωρία κεραιών ανοίγματος (aperture antennas). Η μέθοδος αυτή αποδεικνύεται ότι παρέχει υψηλότερη ακρίβεια σε σχέση με συμβατικές FDTD προσομοιώσεις σε εμπορικά λογισμικά. Το εύρος ημίσειας ισχύος (FWHM) του μοναδιαίου εκπομπού, ο οποίος είναι ο τυπικός κυματοδηγός του PolyBoard στα 1550 nm με διαστάσεις 3.2 μm × 3.2 μm, υπολογίζεται στις 12.7°. Στη συνέχεια, εξετάζεται το φαινόμενο ανεπιθύμητης οπτικής σύζευξης (optical crosstalk) μεταξύ παράλληλων κυματοδηγών. Διαπιστώνεται ότι η απόσταση των 6 μm μεταξύ των κέντρων κυματοδηγών (pitch) με παράλληλη διάδοση 100 μm, μπορεί να θεωρηθεί ασφαλές όριο για την αποφυγή σημαντικής σύζευξης. Για την πειραματική επαλήθευση των θεωρητικών αποτελεσμάτων κατασκευάζονται δοκιμαστικές διατάξεις γραμμικών (ενός επιπέδου) και ορθογώνιων (δύο επιπέδων) ομοιόμορφων OPA με αποστάσεις 6 μm, 8 μm και 10 μm (lateral pitch), και τέσσερις κυματοδηγούς ανά επίπεδο. Στις διατάξεις δύο επιπέδων, η κατακόρυφη απόσταση μεταξύ των κυματοδηγών καθορίζεται από το ύψος των κατακόρυφων MMI για τη μεταφορά της οπτικής ισχύος και ισούται με 7.2 μm. Παρουσιάζονται αναλυτικά τα αποτελέσματα των μετρήσεων των διαγραμμάτων ακτινοβολίας των 1×4 και 2×4 OPA και επιδεικνύεται στροφή της οπτικής δέσμης στις δύο

διαστάσεις με τις αντίστοιχες δισδιάστατες δομές. Επιτυγχάνεται οπτικό πεδίο (FOV) 12°×8° (azimuth × elevation) με τη διάταξη με 6 μm απόσταση μεταξύ των στοιχείων και με εύρος δέσμης 3.3°×5.9°. Το μικρότερο εύρος δέσμης, 2.1°×5.8°, επιτυγχάνεται με τη διάταξη με απόσταση 10 μm μεταξύ των στοιχείων, λόγω του μεγαλύτερου μεγέθους του ανοίγματος εκπομπής. Για το χαρακτηρισμό των δομών αναπτύχθηκε πειραματική διάταξη μέτρησης του διαγράμματος ακτινοβολίας. Η μέτρηση του μακρινού πεδίου πραγματοποιείται μέσω ενός συστήματος απεικόνισης αποτελούμενο από έναν αντικειμενικό φακό υψηλού NA σε συνδυασμό με ένα 4-f σύστημα και ένα CCD αισθητήρα στο εγγύς υπέρυθρο. Η κατασκευή και η διαδικασία βαθμονόμησης του συστήματος περιγράφεται αναλυτικά στο αντίστοιχο κεφάλαιο.

Στη συνέχεια, η μελέτη επεκτείνεται σε στοιχειοκεραίες με ανομοιόμορφη (μη περιοδική) κατανομή των στοιχείων. Οι μη περιοδικές συστοιχίες επιτρέπουν την τοποθέτηση των εκπομπών σε αποστάσεις μεγαλύτερες του μήκους κύματος λειτουργίας, προσφέροντας παράλληλα τη δυνατότητα σημαντικής καταπίεσης των ανεπιθύμητων λοβών (grating lobes). Επιπλέον, η αραιή τοποθέτηση των στοιχείων απλοποιεί τον σχεδιασμό και επιτρέπει τη δημιουργία μεγαλύτερων ανοιγμάτων εκπομπής, οδηγώντας σε μικρότερο εύρος δέσμης (narrow beamwidth), με λιγότερα στοιχεία σε σχέση με τις ομοιόμορφες στοιχειοκεραίες. Στο πλαίσιο της παρούσας εργασίας σχεδιάζονται, κατασκευάζονται και αξιολογούνται πειραματικά γραμμικές στοιχειοκεραίες με δεκαέξι στοιχεία. Τα στοιχεία τοποθετούνται είτε σύμφωνα με μια συγκεκριμένη, προκαθορισμένη ανομοιόμορφη κατανομή, είτε με τυχαία χωρική κατανομή. Στη δεύτερη περίπτωση απαιτείται διαδικασία βελτιστοποίησης με κατάλληλους αλγορίθμους, προκειμένου να επιτευχθεί ικανοποιητική καταστολή των ανεπιθύμητων λοβών. Για τον σκοπό αυτό αναπτύχθηκε γενετικός αλγόριθμος για την εξερεύνηση του χώρου σχεδίασης, ενώ η τελική βελτίωση των επιλεγμένων διατάξεων πραγματοποιείται μέσω αλγορίθμου gradient descent. Το τέταρτο κεφάλαιο παρουσιάζει τη διαδικασία μελέτης και επιλογής των διατάξεων προς υλοποίηση, η οποία βασίστηκε σε εκτενείς προσομοιώσεις του πεδίου ακτινοβολίας. Ακολούθως, παρατίθενται τα αποτελέσματα του πειραματικού χαρακτηρισμού των υλοποιημένων στοιχειοκεραιών. Επιτυγχάνεται στροφή της οπτικής δέσμης στη μία διάσταση με καταστολή των ανεπιθύμητων λοβών άνω των 11 dB εντός εύρους γωνίας σάρωσης ±5° και 6 dB εντός ±8°. Παρ' ότι η ανομοιόμορφη κατανομή των στοιχείων μελετάται μόνο σε διατάξεις με ένα επίπεδο κυματοδήγησης, η προσέγγιση αυτή μπορεί να επεκταθεί στις τρισδιάστατες διατάξεις πολλών επιπέδων διατηρώντας τα

πλεονεκτήματά της. Ο έλεγχος της φάσης των καναλιών πραγματοποιείται, όπως και στις ομοιόμορφες στοιχειοκεραίες, μέσω θερμο-οπτικών διαμορφωτών. Σημειώνεται μάλιστα ότι ο καλύτερος διαμορφωτής που μετρήθηκε επιδεικνύει κατανάλωση ισχύος ίση με 1.28 mW/π, επιβεβαιώνοντας τη δυνατότητα υλοποίησης αποδοτικών θερμο-οπτικών διατάξεων στην πολυμερική πλατφόρμα.

Για τον πειραματικό χαρακτηρισμό των στοιχειοκεραιών, τόσο των ομοιόμορφων όσο και των μη περιοδικών, είναι απαραίτητη η αντιστάθμιση των αρχικών σφαλμάτων φάσης. Όταν δεν εφαρμόζεται τάση για τη ρύθμιση της φάσης των καναλιών, μια οπτική στοιχειοκεραία εμφανίζει τυχαίο διάγραμμα εκπομπής. Αυτό οφείλεται κυρίως σε τυχαίες μεταβολές των πλευρικών διαστάσεων των κυματοδηγών (side wall roughness), οι οποίες προκύπτουν από ατέλειες στη διαδικασία κατασκευής. Επιπλέον ανομοιομορφία στην αρχική φάση μπορεί να εισαχθεί από διαφορές στα μήκη των οπτικών διαδρομών από το δίκτυο κατανομής ισχύος προς τους εκπομπούς. Για τον λόγο αυτό απαιτείται μια διαδικασία αρχικοποίησης της φάσης (phase calibration), η οποία να αντισταθμίζει το αρχικό σφάλμα εφαρμόζοντας κατάλληλη μετατόπιση φάσης σε κάθε στοιχείο. Λαμβάνοντας υπόψη ότι κάθε στοιχείο ελέγχεται μέσω ενός καναλιού DAC, το οποίο μπορεί να διαθέτει έως και 16-bit ανάλυση (2^{16} διακριτά επίπεδα), και δεδομένου ότι μια στοιχειοκεραία μπορεί να περιλαμβάνει δεκάδες ή και εκατοντάδες στοιχεία, καθίσταται σαφές ότι ο αντίστοιχος χώρος αναζήτησης παραμέτρων είναι εξαιρετικά μεγάλος. Στη βιβλιογραφία έχουν χρησιμοποιηθεί διάφοροι αλγόριθμοι για την αρχικοποίηση της φάσης, όπως ο hill-climbing, ο particle swarm optimization (PSO), ο γενετικός αλγόριθμος και παραλλαγές του gradient descent. Στο πέμπτο κεφάλαιο εξετάζονται οι αλγόριθμοι hill-climbing και gradient descent, σε διάφορες εκδοχές τους, τόσο θεωρητικά όσο και μέσω πειραματικού χαρακτηρισμού. Από την ανάλυση προκύπτει ότι ο αποδοτικότερος αλγόριθμος σε διατάξεις με περισσότερα από δεκαέξι στοιχεία, τόσο από πλευράς απαιτούμενων υπολογιστικών πόρων όσο και ως προς την ταχύτητα σύγκλισης, είναι ο stochastic parallel gradient descent (SPGD). Επιπλέον, παρουσιάζεται η διαδικασία πειραματικής αντιστάθμισης των σφαλμάτων που εισάγονται από τους ίδιους τους θερμο-οπτικούς διαμορφωτές, όπως η μη γραμμική αύξηση της αντίστασης λόγω θέρμανσης (self-heating) και η θερμική αλληλεπίδραση (thermal crosstalk) μεταξύ γειτονικών στοιχείων. Η αρχικοποίηση της φάσης καθώς και η διαδικασία της βαθμονόμησης, πραγματοποιούνται μέσω του διαγράμματος ακτινοβολίας, το οποίο καταγράφεται από το οπτικό σύστημα της πειραματικής διάταξης. Μέσω ενός συστήματος ανάδρασης εφαρμόζεται κατάλληλη τάση

στους θερμο-οπτικούς διαμορφωτές για τη ρύθμιση της φάσης έως ότου επιτευχθεί το επιθυμητό διάγραμμα ακτινοβολίας. Τα αποτελέσματα της βαθμονόμησης για τις διάφορες γωνίες στροφής της οπτικής δέσμης αποθηκεύονται σε πίνακα αναζήτησης (look-up table), ο οποίος χρησιμοποιείται κατά τη λειτουργία της στοιχειοκεραίας.

Στο έκτο κεφάλαιο παρουσιάζεται η υλοποίηση μιας ομοιόμορφης στοιχειοκεραίας 4×8, με στόχο την επέκταση της προτεινόμενης αρχιτεκτονικής σε διατάξεις μεγαλύτερης κλίμακας. Στο πλαίσιο αυτό, κατασκευάστηκε μία παθητική δομή με τέσσερα επίπεδα κυματοδήγησης και οχτώ κυματοδηγούς ανά επίπεδο. Επιπλέον υλοποιήθηκε ένα ξεχωριστό PIC με 32 θερμο-οπτικούς διαμορφωτές για την ρύθμιση της φάσης των καναλιών. Η πλήρης συναρμολόγηση και συσκευασία των δύο PICs δεν ολοκληρώθηκε, με αποτέλεσμα να μην υπάρχουν διαθέσιμα πειραματικά αποτελέσματα. Παρότι δεν πραγματοποιήθηκε πειραματική επιβεβαίωση, η επιτυχής κατασκευή ενός ολοκληρωμένου κυκλώματος τεσσάρων επιπέδων κυματοδήγησης αποτελεί ένα σημαντικό βήμα προς την υλοποίηση στοιχειοκεραιών πολλαπλών επιπέδων στο PolyBoard.

Η παρούσα εργασία αξιοποιεί τις πλατφόρμες silicon nitride (TriPleX) και πολυμερικής ολοκλήρωσης (PolyBoard) για την ανάπτυξη οπτικών συστημάτων σε εφαρμογές τηλεπισκόπισης. Τα πειραματικά ευρήματα συνέβαλαν καθοριστικά στην απόκτηση τεχνογνωσίας γύρω από τους τομείς: (α) της υβριδικής ολοκλήρωσης TriPleX και PolyBoard, (β) της οπτικής διαμόρφωσης μέσω του πιεζο-οπτικού φαινομένου στο TriPleX, (γ) της ανάπτυξης φωτονικών ολοκληρωμένων κυκλωμάτων για μετρήσεις LDV, (δ) της τρισδιάστατης ολοκλήρωσης πολλαπλών επιπέδων κυματοδήγησης στο PolyBoard, (ε) του σχεδιασμού, χαρακτηρισμού και βαθμονόμησης οπτικών στοιχειοκεραιών. Η εργασία πραγματοποιήθηκε στα πλαίσια του ευρωπαϊκού προγράμματος ICT-3PEAT, το οποίο αποτέλεσε το εφαλτήριο για το ευρωπαϊκό έργο LOLIPOP, το οποίο, μεταξύ άλλων, στοχεύει στην ανάπτυξη συστημάτων τηλεπισκόπησης LDV και FMCW LiDAR.

Table of Contents

Introduction

Photonics emerged as a field with the invention of the laser in 1960, and gained significant traction in the 1980s and 1990s, with the development of optical amplifiers and fiber optics technology that revolutionized communications. The term *photonics*, in analogy to *electronics*, was introduced to emphasize the particle nature of light, and the technologies that emerged from this perspective, as opposed to the classical optics, that treat light primarily as a wave or ray. In that regard, photonics can be understood as the technological manifestation of the quantum revolution in the field of optics, encompassing a broad range of technologies based on light-matter interaction, that enable key optical functions including light generation, amplification, modulation, and detection [1].

The invention of the semiconductor laser in the spring of 1970, independently demonstrated at the Ioffe Physico-Technical Institute in St. Petersburg and, just days later, at Bell Labs in New York, stands as one of the most significant milestones in the evolution of photonics. These first continuous-wave (CW) semiconductor lasers operating at room temperature paved the way for replacing the bulky solid-state and gas lasers with compact integrated devices. This achievement marked the onset of integrated photonics, in the same way that the invention of the transistor in 1947 initiated the field of microelectronics by replacing the bulky vacuum tubes. This emerging field, originally referred to as “integrated optics”, was destined to follow the path of microelectronic integration, miniaturizing not just lasers, but every optical functionality, including light manipulation, filtering, modulation and detection. Today, integrated photonics is recognized as a foundational technology, where its combination with integrated electronics, referred to as co-packaged optics, will enable compact, scalable, and high-performance platforms to support applications spanning high-bandwidth data transfer, computation, and sensing [2].

So far, the primary driver behind the development of photonic integrated circuits (PICs) has been the communications market, and particularly fiber-optic communication systems. With a clear roadmap for increasing channel capacity and density with more compact and power-efficient optical transceivers, this market has propelled the advancement of photonic integration platforms. A pivotal point was the introduction of generic integration processes and standardized building blocks in the early 2000s, enabling designers to incorporate their designs into multi-project wafers (MPWs), similar to the microelectronics industry. This approach significantly reduced prototyping costs and allowed technology to evolve

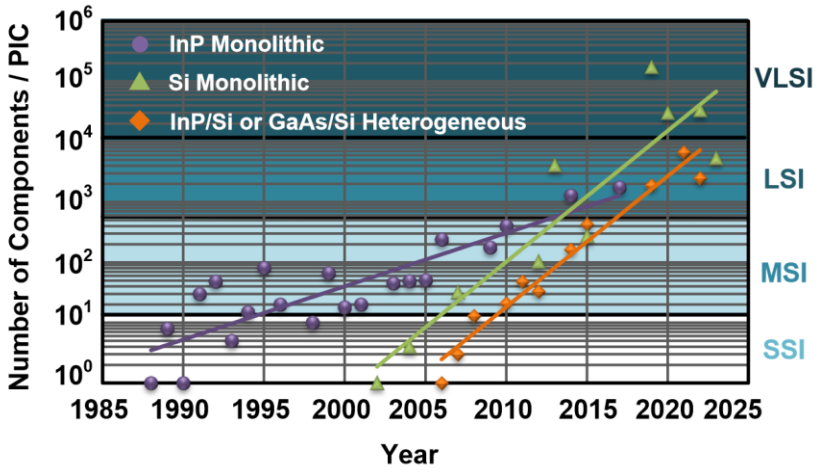

Figure 1: Evolution of integration density in silicon and InP-based integrated photonics from small-scale integration (SSI) towards medium-scale (MSI), large-scale (LSI), and very-large-scale integration (VLSI) [6].

independently of individual designs. Today, silicon photonics, along with their silicon nitride variant [3], and group III–V indium phosphide (InP) platform are the more mature photonic integration technologies. Silicon photonics offers a key advantage in scalability and rapid fabrication, leveraging compatibility with CMOS integration tools and processes, and access to the mature CMOS ecosystem [4][5]. This platform has enabled large-scale integration (LSI), with demonstrated circuits containing 500 to 10,000 components on a single chip [6]. Significant research efforts have focused on developing highly efficient silicon photonic devices, including low-loss waveguides, wavelength multiplexing-demultiplexing filters, large-bandwidth modulators and Germanium-based photodetectors. However, due to silicon's indirect bandgap, monolithic integration of light sources and amplifiers in silicon remains a challenge. In contrast, III-V materials such as Indium Phosphide (InP) and Gallium Arsenide (GaAs) enable the integration of optical gain elements. InP-based integration provides the broadest range of photonic functionality, supporting efficient lasers, modulators, optical amplifiers, detectors, and various passive components [7]. However, its low index contrast leads to larger passive device footprints, limiting integration density. To address this, methods to combine III-V active functionality with silicon photonics are being explored, such as heterogeneous integration or III-V epitaxial growth on silicon substrate [8]. In Europe, SMART Photonics in the Netherlands and Fraunhofer Heinrich Hertz Institute (HHI) in Germany are the main foundries that provide services in an InP-based platform, while silicon photonics platforms are offered by GlobalFoundries, STMicroelectronics, IMEC, Cornerstone, VTT, and CEA-LETI. A well-established photonic ecosystem in Europe, North America and south-east Asia, has enabled

several companies, such as Intel, Infinera, Finisar, Lumentum, Acacia, Luxtera, OpenLight, Juniper, and Cisco, to name a few, to develop and commercialize PIC-based products, primarily datacom transceivers for intra- and inter-datacenter interconnects [2]. This market has already reached multi-million units per year and is expected to grow, as optical interconnects are a critical technology for data centers and high-performance computing (HPC) systems, which demand fast and efficient data transfer [9].

Despite their widespread deployment and commercial adoption, silicon photonics and InP-based platforms present certain limitations. These are related to optical losses, handling of high optical power, modulation bandwidth, and most importantly supporting wavelengths below 1 μm. To address these challenges, additional material platforms have been employed to support photonic integration. Among the most prominent are: i) silicon nitride (SiN), a variant of silicon photonics that utilizes Si3N4 waveguides to minimize optical losses and enable low-loss passive devices, ii) thin-film lithium niobate (TFLN), known also as lithium niobate on insulator (LNOI), which offers high-bandwidth electro-optic (EO) modulators, and iii) polymer-based photonic integration which offers low-cost passive devices and can potentially support high-bandwidth EO modulation. In Europe, several MPW service providers support these technologies: SiN is offered by LioniX in the Netherlands and Ligentec in Switzerland, lithium niobate platform is provided by CSEM, Lightium, and Luxtelligence, in Switzerland, and a polymer-based technology platform is offered by the Fraunhofer Heinrich Hertz Institute in Germany.

Photonic integrated circuits are a well-established technology today, with the potential to expand beyond communications. By leveraging economies of scale to drive down unit costs, they are seeking the next high-volume application to justify large-scale investments. There are numerous potential applications: biomedical sensing based on evanescent-field biosensors, microwave photonics for wideband RF signal processing in next-generation wireless networks, augmented/mixed/virtual reality (AR/MR/VR) systems, optical processors, quantum computing, quantum key distribution, optical circuit switching, remote sensing and ranging [10]. One of the most promising mass-market opportunities for PICs is LiDAR for autonomous vehicles (AVs). Advanced driver-assistance systems (ADAS), the next step in automotive safety, rely on multiple sensors like microwave radar, ultrasound sensors, and optical cameras [11]. LiDAR is emerging as a key solution for delivering high spatial resolution imaging in long-range. Startups like Luminar, Scantinel, and Aurora have secured multi-million-dollar funding to develop PIC-based LiDARs for

the automotive industry, with Luminar's LiDAR technology already integrated in Volvo's EX90 and ES90 models. MIT spin-off Analog Photonics has also played a key role in advancing PIC-based LiDAR technology. Similar solutions are being pursued by major industry players including Toyota and Mitsubishi, while Apple and Huawei are advancing LiDAR technology for various spatial awareness applications in their mobile devices. For sensing applications, PICs provide advantages in size, weight, and power (SWaP) efficiency, along with cost reduction, scalability, reliability, and interferometric stability. Therefore, for over the past decade, LiDAR has been the primary driving force behind the advancement of PIC technology for remote sensing applications, sparking research interest in vaious photonic technologies including low-linewidth lasers, high-efficiency photodetectors, integrated interferometers, and optical phased arrays (OPAs).

This work builds upon this line of research. It leverages TriPleX, the SiN platform of LioniX, and PolyBoard, the polymer-based platform of Fraunhofer HHI, to develop novel functionalities and demonstrate their potential in enabling compact systems for remote sensing. It targets the development of a PIC-based laser Doppler vibrometer (LDV) as an example sensor and OPAs for two-dimensional beam steering, operating in the NIR (1550 nm). The thesis is organized into two parts. The first part describes the work towards the miniaturization of the heterodyne LDV sensor, focusing on the development of an integrated optical frequency shifter (OFS), which is an essential part of heterodyne interferometry, typically implemented with bulk optics. The OFS is based on a novel PZT-based phase shifter in the TriPleX platform, that utilizes the piezoelectric effect to realize stress-optic index modulation. Signal reception is implemented on PolyBoard, which offers a mature platform for dual-polarization coherent detection in telecom wavelengths, based on thin-film elements (TFE) for polarization handling. The second part of the thesis focuses on the development of OPAs in PolyBoard to facilitate solid-state beam-steering, which is the ability to scan a laser beam without relying on moving parts, a feature that is expected to play a key role in the next-generation of remote optical sensors. The two technologies developed within this work, the stress-optic OFS in TriPleX and the 2D scanning OPAs in PolyBoard, are envisioned to be combined in a remote optical sensing system as presented in Figure 2. By combining the complementary features and advantages of TriPleX and PolyBoard through hybrid integration, we establish a powerful technological platform that unlocks new opportunities for compact, high-performance photonic systems in advanced sensing applications.

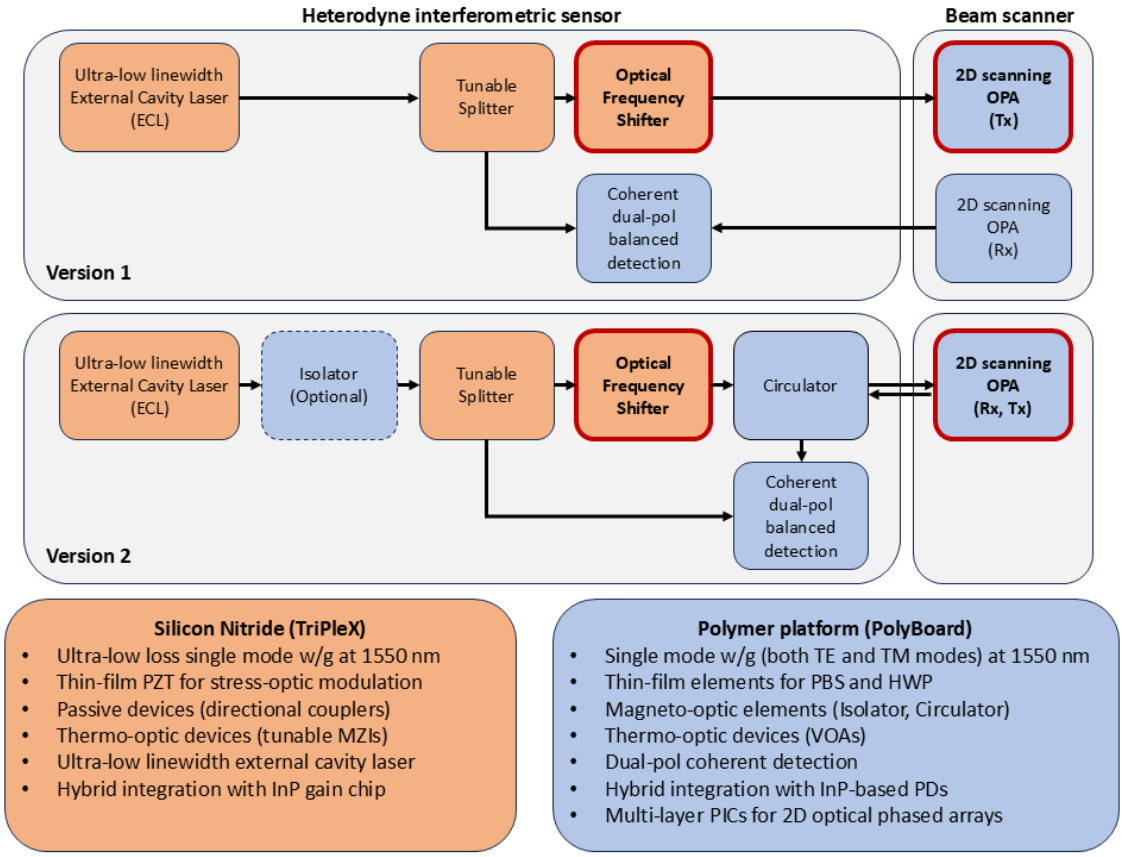

Figure 2: Envisioned PIC-based system for remote optical sensing. The first implementation comprises two OPAs, a Tx and a Rx OPA, while the second version utilizes a circulator to separate the transmitted and the received signal. PolyBoard enables the integration of thin-film magneto-optic elements, although this feature is not used in the current work.

Key objectives

1. Employ stress-optic index modulation technology on the TriPleX (SiN) platform to realize an optical frequency shifter (OFS).
2. Demonstrate a miniaturized PIC-based Laser Doppler Vibrometer (LDV).
3. Implement multi-waveguide-layer (3D) integration technology on the PolyBoard platform to enable planar (2D) optical phased arrays (OPAs).
4. Demonstrate one-dimensional (1D) and two-dimensional (2D) optical beam steering using PolyBoard-based OPAs.

References

[1] C. E. S. Castellani, L. C. B. Silva, and M. E. V. Segatto, “The Rise of Photonics Engineering”.

[2] N. Margalit, C. Xiang, S. M. Bowers, A. Bjorlin, R. Blum, and J. E. Bowers, “Perspective on the future of silicon photonics and electronics,” *Applied Physics Letters*, vol. 118, no. 22, p. 220501, May 2021, doi: 10.1063/5.0050117.

[3] D. J. Blumenthal, R. Heideman, D. Geuzebroek, A. Leinse, and C. Roeloffzen, “Silicon Nitride in Silicon Photonics,” *Proc. IEEE*, vol. 106, no. 12, pp. 2209–2231, Dec. 2018, doi: 10.1109/JPROC.2018.2861576.

[4] W. Bogaerts and L. Chrostowski, “Silicon Photonics Circuit Design: Methods, Tools and Challenges,” *Laser & Photonics Reviews*, vol. 12, no. 4, p. 1700237, Apr. 2018, doi: 10.1002/lpor.201700237.

[5] S. Y. Siew *et al.*, “Review of Silicon Photonics Technology and Platform Development,” *J. Lightwave Technol.*, vol. 39, no. 13, pp. 4374–4389, Jul. 2021, doi: 10.1109/JLT.2021.3066203.

[6] S. Shekhar *et al.*, “Silicon Photonics - Roadmapping the Next Generation,” 2023.

[7] M. Smit, K. Williams, and J. Van Der Tol, “Past, present, and future of InP-based photonic integration,” *APL Photonics*, vol. 4, no. 5, p. 050901, May 2019, doi: 10.1063/1.5087862.

[8] J. E. Bowers and A. Y. Liu, “A Comparison of Four Approaches to Photonic Integration,” in *Optical Fiber Communication Conference*, Los Angeles, California: OSA, 2017, p. M2B.4. doi: 10.1364/OFC.2017.M2B.4.

[9] C. Minkenberg, R. Krishnaswamy, A. Zilkie, and D. Nelson, “Co-packaged datacenter optics: Opportunities and challenges,” *IET Optoelectronics*, vol. 15, no. 2, pp. 77–91, 2021, doi: 10.1049/ote2.12020.

[10] C. Zhang *et al.*, “Integrated photonics beyond communications,” *Applied Physics Letters*, vol. 123, no. 23, p. 230501, Dec. 2023, doi: 10.1063/5.0184677.

[11] J. Hecht, “Lidar for Self-Driving Cars,” *Optics & Photonics News, OPN*, vol. 29, no. 1, pp. 26–33, Jan. 2018, doi: 10.1364/OPN.29.1.000026.

Part 1

Integrated Heterodyne Laser Doppler Vibrometer

In this section, we present our work on miniaturizing a laser Doppler vibrometer (LDV) using silicon nitride and polymer-based photonic integration platforms. We theoretically analyze and experimentally evaluate two integrated optical frequency shifters (OFSs), based on serrodyne and single sideband (SSB) modulation, which are key components in heterodyne detection schemes. Both OFSs employ stress-optic modulators (SOMs) based on the non-resonant piezoelectrical actuation of lead zirconate titanate (PZT) thin-films deposited on top of the silicon nitride waveguides with a wafer-scale process. For the detection part, a dual-polarization coherent receiver with balanced photodetection was realized in the polymer-based photonic integration platform of the Heinrich Hertz Institute (HHI). By combining the functionalities from silicon nitride and polymer photonic circuits we demonstrate accurate LDV measurements. To the best of our knowledge, this is the first demonstration of a PIC-based heterodyne LDV with a bandwidth in the MHz range and a resolution below 10 pm. Finally, we present an approach for combining the two platforms into a single PIC through 3D hybrid photonic integration.

1.1Introduction

Optical frequency shift (OFS) is a key function for the operation of sensing systems based on heterodyne interferometry, including distance metrology, laser Doppler velocimetry and vibrometry [1][2], or light detection and ranging (LIDAR) [3][4]. Today these systems are mostly large, since they still rely on free-space optical components. Their OFS unit in particular is typically based on bulky acousto-optic modulators that offer high conversion efficiency and low-noise operation, but they exhibit low flexibility in the selection of the frequency shift and require precise beam alignment at their input optical port [5][6]. Efforts over the past years to miniaturize those sensing systems by means of photonic integration have resulted in waveguide-integrated implementations of their OFS unit based either on serrodyne modulation in a single-phase shifter [7]-[9] or on single-sideband (SSB) modulation in a quad array of phase shifters inside an in-phase/quadrature

modulator (IQM) [10]. In [8][9] the corresponding implementations were based on serrodyne modulation using thermal phase shifters in a silicon-on-insulator (SOI) platform, enabling the miniaturization of an LDV, which is a prominent example of heterodyne sensors [11]. Despite their importance from the miniaturization point of view, the low bandwidth of the thermal phase shifters in those works (which is by nature in the kHz regime) limits their applicability to only a short range of LDV applications.

At the higher end of the efforts for photonic integration of OFS units, the main work so far has involved the use of electro-optic phase shifters inside IQMs to perform SSB modulation. Many implementations have been originally concentrated in LiNbO3 [12]-[14] due to its good electro-optical properties, but the emergence of silicon photonics in the more recent years, with the potential for large-scale integration, has motivated realizations also in silicon photonics [10][15]-[17], including the silicon organic hybrid (SOH) platform [18]. Although broadband enough to enable spectral shifts in the GHz regime, those phase shifters can have a complex fabrication process and can exhibit unwanted amplitude modulation in parallel with the target phase modulation. Via this mechanism, they can reduce in turn the side-mode suppression ratio (SMSR) of the original carrier and the spurious side modes with respect to the shifted spectral line, resulting in substantial degradation of the overall heterodyne detection [19]. In order to remove this amplitude modulation, SOH phase shifters can replace the pure silicon ones at the expense of additional complexity and cost in the fabrication process [18]. Alternatively, a pair of modulators inside an MZI switch has been proposed in [20] for improving the SMSR performance with conventional silicon modulators, but fast switching and precise synchronization between the modulators is required. A more direct approach to improve the SMSR in SSB modulation is to use driving signals with higher harmonics that can suppress the nonlinearity of the MZM inside the IQM [18][21], but these techniques require driving electronics with significant larger bandwidth.

In the case of heterodyne sensors [7]-[10][22], wherein the target OFS remains in the MHz regime, the development of a photonic integrated phase shifter technology that can fill the gap between the thermal phase shifters (operating in the kHz regime) and the electro-optic phase shifters (operating in the GHz regime) is a milestone, as it can offer beneficial tradeoffs in terms of bandwidth, cost and integration scale. Relevant efforts have primarily involved the development of phase shifters based on strain-induced geometrical deformations of the modal cross-sections of waveguides in SOI or in silicon nitride. In [23]

a comb-drive actuator in the form of a complex micro-electro-mechanical system (MEMS) was integrated in SOI to induce the deformation of a suspended silicon waveguide with operation bandwidth close to 1 MHz. Similar tuning speeds, but with piezoelectrical actuation of lead zirconate titanate (PZT) films, have been reported with a suspended ring resonator in silicon nitride [24]. A slightly different approach is the use of mechanical strain to change the refractive index of the waveguides [25]. Initial demonstrations of the stress-optic effect included dynamic control of the refractive index or the birefringence of silica [26] or silicon waveguides [27]-[29]. To our specific interest in the present work, PZT films were used to apply stress-optic index modulation in the silicon nitride platform of LioniX, with the commercial name "TriPleX" [30]-[33]. Each PZT film was integrated on the surface of the TriPleX platform and in very close proximity to the corresponding waveguide, allowing for a non-resonant piezo-actuation of the mechanical strain. Non-resonant stress-optic modulation in the silicon nitride platform has also been demonstrated by LETI in [34]. Despite the theoretical potential of the PZTs for operation at 10 s or even 100 s of MHz, the demonstrated modulation speed of the PZT-based phase shifters in those works was kept in the kHz regime since the focus of the investigations was on the basic characterization of the phase shifters and the minimization of their power consumption in quasi-static operation. Modulation in the MHz regime based on the stress-optic effect has been recently demonstrated in silicon nitride using piezo-electric actuation of a micro-ring modulator [35]. A theoretical analysis for silicon nitride platforms and an early experimental work in a SOI platform were presented in [36] and [37] respectively, highlighting the potential for resonant creation of strain and deformation of the modal cross-section of waveguides via Rayleigh surface acoustic waves (SAWs). Excitation of SAWs has been previously relied in the good acousto-optical properties of $LiNbO_3$ to realize a heterodyne interferometer [22]. In [36] and [37] the SAW excitation was based on the use of PZT films on the surface of the platform and the use of inter-digital transducers (IDTs) instead of simple electrodes for the resonant actuation of those films. The phase shifters had operating speeds well into the MHz regime, but only at the frequencies matching the periodicity of the IDT structures.

Typically, light modulation in TriPleX relies on thermo-optic phase shifters, that are limited to modulation speeds of a few kHz. In cases where larger modulation bandwidth is needed, high-speed electro-optic modulators in Indium Phosphide (InP) are used [38][39]. Although these modulators can offer bandwidth of several GHz, hybrid integration is used

to combine them with the TriPleX platform, which increases the cost and complexity of the assembly, as the PICs must be diced and coupled together optically, rendering the process unsuitable for high-volume manufacturing (HVM). Deposition of PZT on the other hand, as well as the structuring of the stress-optic modulators (SOMs), is a wafer-level process that can be scaled for HVM [40][41] and has the potential for significant cost-reduction in applications where modulation in the MHz regime is sufficient. Eliminating the need for hybrid integration in such applications has the obvious benefit of reducing the overall size of the PIC assembly, as well as the number of coupling interfaces, and thus, minimizing the optical loss. On top of that, SOMs introduce minimal loss, since the PZT thin films are placed a few microns above the TriPleX waveguiding structures, leaving the propagating mode undisturbed. In this work, we demonstrate, for the first time to the best of our knowledge, the operational potential of non-resonant PZT-based SOMs in the MHz range. This demonstration is not merely an early characterization but part of a full system demonstration of a compact LDV based on photonic integrated OFS units.

LDVs are non-contact optical sensors that can extract velocity and displacement information from a vibrating surface by focusing a laser beam onto the surface and collecting the backscattered light. The returning light undergoes a Doppler-induced frequency shift, which is proportional to the instantaneous velocity of the out-of-plane vibrations. By using an interferometer to detect the phase of the incoming light, the vibration characteristics, i.e., the vibration amplitude and frequency, can be retrieved. The same principle is used for velocity measurements in frequency modulated continuous wave (FMCW) LiDAR. There are two primary LDV configurations: homodyne and heterodyne. The latter is more widely used due to its superior reliability and sensitivity. In a heterodyne LDV, the laser source is split into the measurement beam, which is emitted towards the object under measurement, and the reference beam, which is kept localy in the device, and a frequency shift is introduced to either of the two beams. This enables the differentiation of the vibration direction while also improves the signal-to-noise ratio (SNR) by moving the frequency band away from low-frequency noise. Thus, OFS is a crucial part of heterodyne LDVs.

In our system, we explore two integrated OFS configurations. The first utilizes four SOMs in a cascaded configuration, driven by a sawtooth function, enabling serrodyne modulation up to 100 kHz. The second configuration employs a quad array of SOMs within an IQM, enabling SSB modulation up to 2.5 MHz. In both versions, the OFS PIC is

combined with an external beam scanning unit for the emission and collection of the measurement beam, and with a second part developed in the optical polymer platform of HHI, with the commercial name “PolyBoard” [42]. PolyBoard is employed in our LDV system to realize a dual-polarization balanced photodetector, due to its capability to accommodate polarization handling elements and enable low-loss integration with indium-phosphide (InP)-based photodiodes [43]-[45],

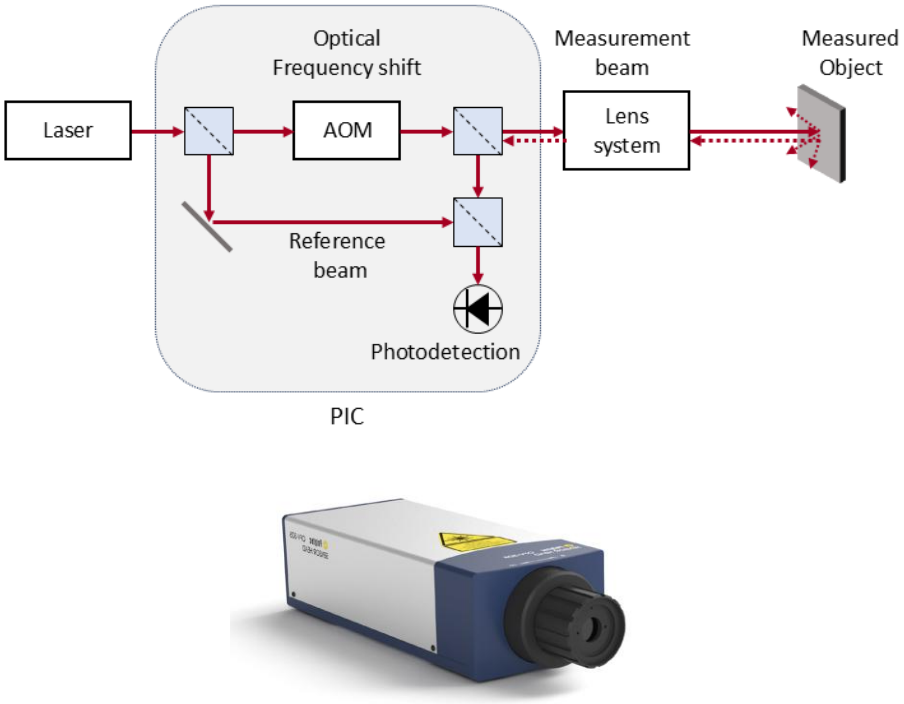

Figure 1.1: (Top) Schematic of a heterodyne laser Doppler vibrometer (LDV) with bulk optics and acousto-optic modulation. The gray area indicates the optical circuit that this work aims to miniaturize. (Bottom) Example of an LDV device based on free-space optics by the Germany-based company Polytec.

1.2Working principle of heterodyne LDV

In an LDV the velocity information $v(t)$ of a vibrating surface is transformed to a Doppler frequency shift $f_D(t)$ in the optical signal, that corresponds to an instantaneous phase shift $\varphi_D(t)$, described by

$$f_D(t) = \frac{d\varphi_D(t)}{dt} = \frac{2n}{\lambda} v(t) \tag{1.1}$$

where λ is the wavelength of the laser source and n the refractive index. The information in the phase of the optical signal is extracted with the help of an interferometer. The latter is formed by splitting the light from a laser source into two parts: the measurement and the reference signal. The measurement signal is sent to the vibrating surface, where it is reflected and scattered. A small portion of the light is collected and coupled back into the interferometer to be recombined with the reference signal. In a heterodyne LDV, a frequency shift f_0 is introduced to the optical frequency f_{opt} of either the measurement or the reference signal, to introduce directional sensitivity to the measurement. The reference signal is expressed as

$$E_r(t) = E_r \exp\left(j2\pi f_{opt} t\right) \tag{1.2}$$

and the collected measurement signal can be written as

$$E_m(t) = \sqrt{a} E_m \exp\left\{j\left[2\pi\left(f_{opt} + f_0\right)t + \varphi_D(t)\right]\right\} \tag{1.3}$$

where a the attenuation factor due to the scattering, reflection, and propagation loss of the signal. The combined signal is sent to a photodetector that produces a photo-current according to the beating signal, given by

$$\begin{aligned} I &\propto |E_m(t) + E_r(t)|^2 \\ &= I_r + I_m + I_{het}(t) \end{aligned} \tag{1.4}$$

where $I_r = (E_r)^2$, $I_m = a(E_m)^2$, and

$$I_{het}(t) = 2\sqrt{a} E_r E_m \cos[2\pi f_0 t + \varphi_D(t)] \tag{1.5}$$

The dc terms I_r and I_m are filtered out, while the I_{het} is sent to the demodulator. Demodulation can be performed either in the analog domain, using a frequency-to-voltage converter or in the digital domain, by sampling the signal $I_{het}(t)$ and using digital signal processing (DSP) techniques[46][47]. Although good performance can be achieved with analog demodulation, digital approaches provide better performance in terms of stability

and linearity, with the arctangent phase IQ demodulation being the most popular method for decoding the LDV signal [48]. In the case of IQ demodulation, the phase $\varphi(t)$, which is calculated using the orthogonal components u_q and u_i of the analytic signal, and the corresponding displacement are given by

$$\varphi(t) = \tan^{-1}\frac{u_q(t)}{u_i(t)} \tag{1.6}$$

$$s(t) = \frac{\lambda}{4\pi}\varphi(t)\,. \tag{1.7}$$

1.3 Optical Frequency Shift

1.3.1 Modelling

1.3.1.1 Serrodyne Frequency Shifter (SFS)

Serrodyne frequency shift is based on the modulation of the phase of an optical carrier with a linear phase ramp. The linear increase of the optical phase in the time domain, i.e. $\varphi(t) = 2\pi f_0 t$, shifts the frequency of the output optical signal by f_0:

$$\begin{aligned} E_{out} &= E_{in}e^{j\varphi(t)} \\ &= E_0 e^{j\left(2\pi f_{opt}t+\varphi(t)\right)} \\ &= E_0 e^{j2\pi(f_{opt}+f_0)t} \end{aligned} \tag{1.8}$$

where E_0 is the amplitude and f_{opt} is frequency of the input signal's electric field. A linearly increasing phase profile can be realized by driving the phase modulator with a sawtooth signal of period $T_0 = 1/f_0$ and with an amplitude such that a total of 2π shift is inserted, as shown in Figure 1.2(b). In the ideal case, the falling time τ_f of the sawtooth is infinitely small relative to the period T_0, and the optical phase increases in a continuous manner. The input optical power is shifted entirely to the desired frequency $f_{opt} + f_0$. In a practical implementation though, where the ratio τ_f/T_0 cannot be infinitely small due to bandwidth limitations, the phase ramp of the optical field will be disrupted for an amount of time equal to τ_f in every period. Thus, a portion of the input optical power will appear in harmonic sidemodes in the optical spectrum around the frequency shifted carrier and the modulated optical signal is described by

$$E_{out} = E_{in}\sum_k a_k e^{j2\pi(f_{opt}+kf_0)t}\,, \qquad k \in \mathbb{Z} \tag{1.9}$$

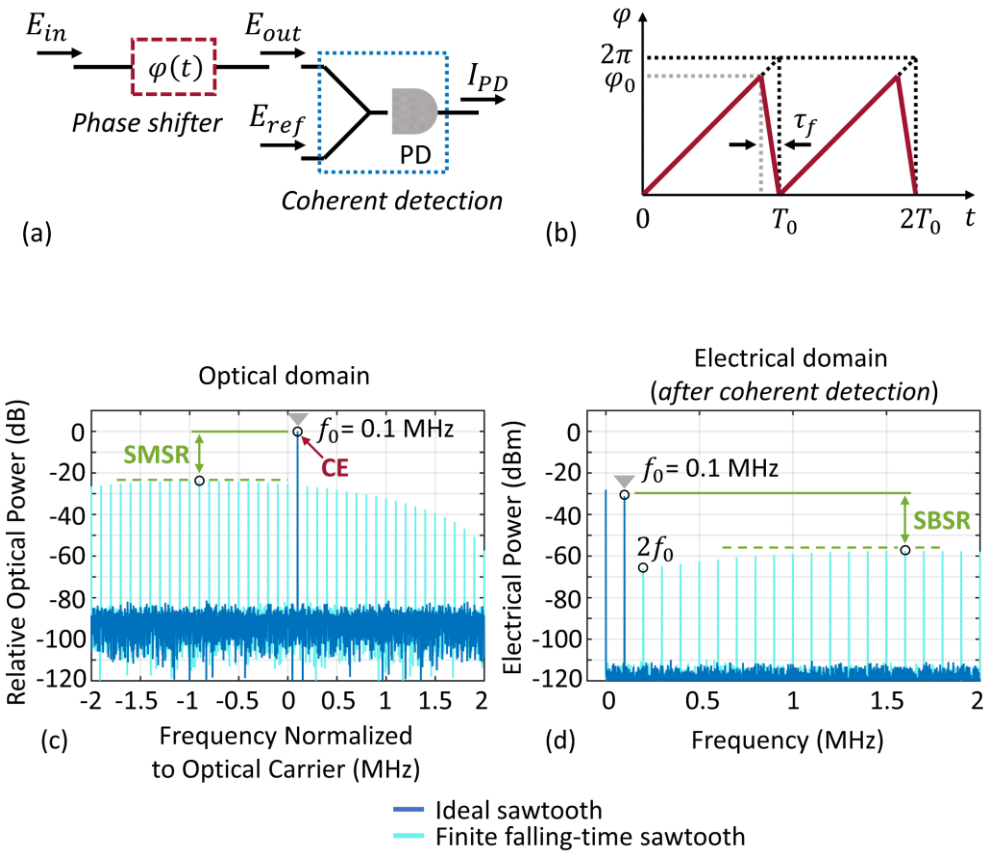

Figure 1.2: (a) Illustration of the simulation setup for the serrodyne OFS and (b) the sawtooth phase modulation with period $T_0 = 1/f_0$. (c) Output optical spectrum for modulation frequency f_0 = 0.1 MHz. The dark blue spectrum corresponds to an ideal sawtooth with infinitely small falling time. The light blue lines appear in the case of sawtooth with finite falling time ($0.05T_0$). (d) The electrical spectrum after the coherent detection. The sidebands in the electrical spectrum are created from the down-converted side-modes present in the optical spectrum around the frequency shifted carrier at $f_{opt} + f_0$.

where k is the order of the harmonic sidemode and a_k the corresponding amplitude [49].

Figure 1.2(c) shows the simulated output optical spectrum produced with a modulating sawtooth of frequency f_0= 0.1 MHz for the cases of infinitely small and finite falling time. We define the falling time as the interval between the end of the rising slope and the beginning of the next one, from maximum to minimum point, as it is depicted in Figure 1.2(b). In the case of a perfect sawtooth the sidemode suppression ratio (SMSR), i.e., the ratio between the fundamental frequency and the highest sidemode, is only limited by the noise foor, while in the sub-optimal case the presence of harmonic sidemodes deteriorates the SMSR (see Figure 1.2(c)). The amount of the input optical power that is shifted to the desired frequency $f_{opt} + f_0$ is not significantly deteriorated, preserving the high conversion efficiency (CE) of the serrodyne frequency shifter. Figure 1.3(a) shows in more detail the impact of the sawtooth falling-time on the SMSR and the CE performance. A falling-time

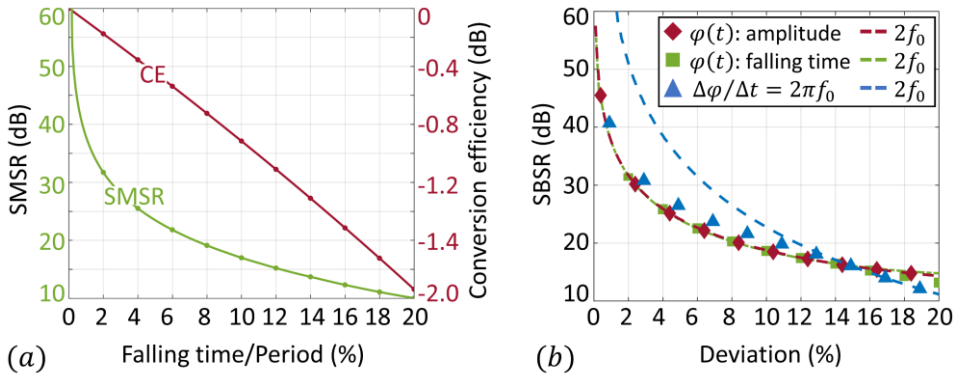

Figure 1.3: (a) Impact of the falling time of the sawtooth waveform on SMSR and CE. (b) Effect of imperfect amplitude and falling time of the modulating sawtooth on SBSR.

of less than 1% of the sawtooth period is required to keep the SMSR above 40 dB, while the deterioration of CE is limited to less than 2 dB, even if the falling-time reaches 20% of the period. The high conversion efficiency is one of the main advantages of the serrodyne technique, which makes it a considerable candidate for sensing applications with strict requirements in optical power budget. The limiting factor is the large bandwidth required to accommodate the sawtooth modulation. To achieve good SMSR performance, both the optical modulator, as well as the driving circuit must exhibit analog bandwidth significantly larger than the fundamental frequency of the desired shift f_0 e.g., a 3dB bandwidth of more than $35f_0$ is needed to keep the τ_f/T_0 ratio below 1%, assuming a 1st order linear system [49]. Since heterodyne LDV systems rely on the coherent detection of the measurement signal using a local reference, it is meaningful to study the impact of an imperfect modulation directly on the electrical domain after the coherent detection. Figure 1.2(d) presents the corresponding simulated electrical power spectrum. The modulated optical field E_{out} is combined with an optical reference E_{ref} i.e., a copy of the input field E_{in}, and the beating signal is detected on a photodiode, as depicted in Figure 1.2 (a). As a result of the optical beating, the frequency shifted tone at $f_{opt} + f_0$ is down converted to f_0 along with the sidemodes, and harmonic sidebands appear in the electrical spectrum after photodetection. To refer to the ratio between the highest sideband and the fundamental at f_0 in the electrical spectrum we use the term sideband suppression ratio (SBSR), to distinguish it from the SMSR used for the optical domain.

Figure 1.3(b) shows the impact of the amplitude and falling time of the phase modulation on the SBSR performance. For the first two cases (red and green colored marks), each parameter is sweeping independently from 0% to 20% deviation from the

ideal value, while the non-sweeping parameter is kept constant to its ideal value i.e., 2π for the amplitude and 0 for the falling time. In the last case (blue marks), both phase amplitude and falling time are sweeping such that the slope $d\varphi(t)/dt$ is constant and equal to $2\pi/T_0$. The markers indicate the overall SBSR performance i.e., the suppression ratio between the fundamental harmonic and the highest sideband in the output spectrum, where the dotted lines show the suppression ratio between the fundamental and the $2f_0$ component. When the amplitude or the falling time are changing independently the dotted lines coincide with the markers, suggesting that the $2f_0$ component is the highest sideband which determines the overall SBSR. In the case of constant slope $2\pi/T_0$ the SBSR performance for deviations below 15% is determined from sidebands at positions further away from the fundamental frequency, as the suppression ratio of the $2f_0$ component is significantly higher. Since most of the sidebands can be later suppressed through appropriate filtering, it is important to keep the highest sidemodes away from the f_0 component [48]. Moreover, it can be derived that in cases in which achieving a full 2π shift is not possible due to driving limitations, the falling time should be adjusted accordingly such that it holds $\Delta\varphi/\Delta t = 2\pi/T_0$.

1.3.1.2 Single Sideband Frequency Shifter (SSB-FS)

The dual-parallel (DP) MZM configuration, originally introduced four decades ago, has been used to demonstrate single sideband (SSB) modulation and frequency shifting [12]. The circuit layout is shown in Figure 1.4(a). Two MZMs are combined in parallel with a relative optical phase shift of π/2 to form an IQ configuration. Each MZM operates in push-pull mode and is biased at its minimum transmission point, thus an optical phase difference of is introduced between the two arms. The driving signal is a sinewave of frequency f_0 which is applied to the upper and lower MZMs with a relative phase shift of π/2. The frequency shift achieved by the IQ configuration can be understood as a two-step process. First, multiple spectral lines are generated in the optical domain through the phase modulation of the input light. In the second step, unwanted spectral components are precisely canceled through destructive interference. A detailed illustration of this process is provided in Figure 1.4(b). The optical input is divided into four paths and modulated by four individual phase modulators, each driven by a sinewave with carefully adjusted amplitude and phase. The optical spectrum at the output of each modulator consists of spectral lines located at multiples of the modulation frequency f_0 with their magnitude and phase determined by Bessel functions [18]. When the light recombines at the output of each

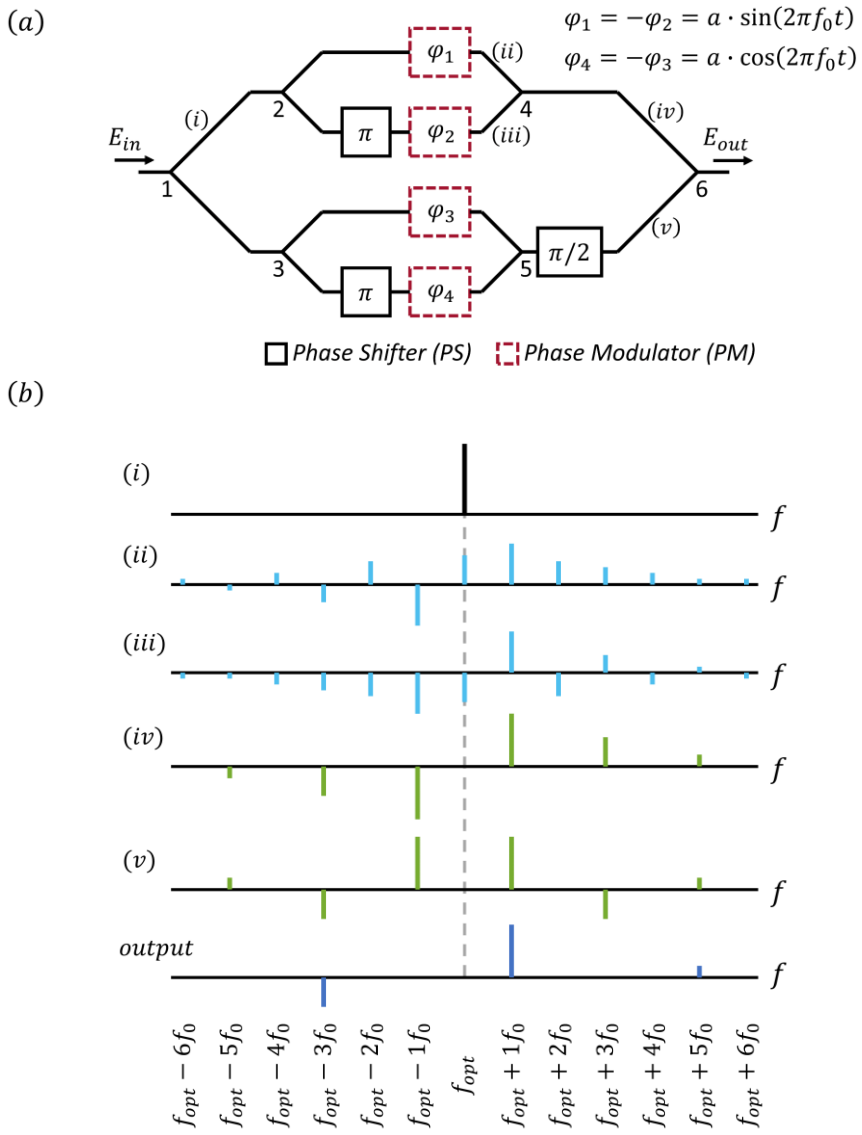

Figure 1.4: (a) Schematic of the SSB-OFS and (b) the field amplitude spectrum at different points of the circuit.

MZM, only the odd-order spectral lines remain, as the even-order lines have opposite phases and are eliminated through destructive interference. By combining the outputs of the two MZMs with a relative phase shift of π/2, additional spectral lines are eliminated, leaving only specific components in the output spectrum of the SSB-FS. These remaining spectral components are located at frequencies…, $f_{opt} - 3f_0$, $f_{opt} + 1f_0$, $f_{opt} + 5f_0$ etc., described by the expression

$$E_{out} = E_{in} \sum_{k=4n+1} J_k(a) exp\left[j2\pi\left(f_{opt} + kf_0\right)t\right] \tag{1.10}$$

where $J_k(a)$ is the k-th order Bessel function of the first kind, a the amplitude of the phase modulation with frequency f_0, assuming uniform excitation, and f_{opt} the frequency of the

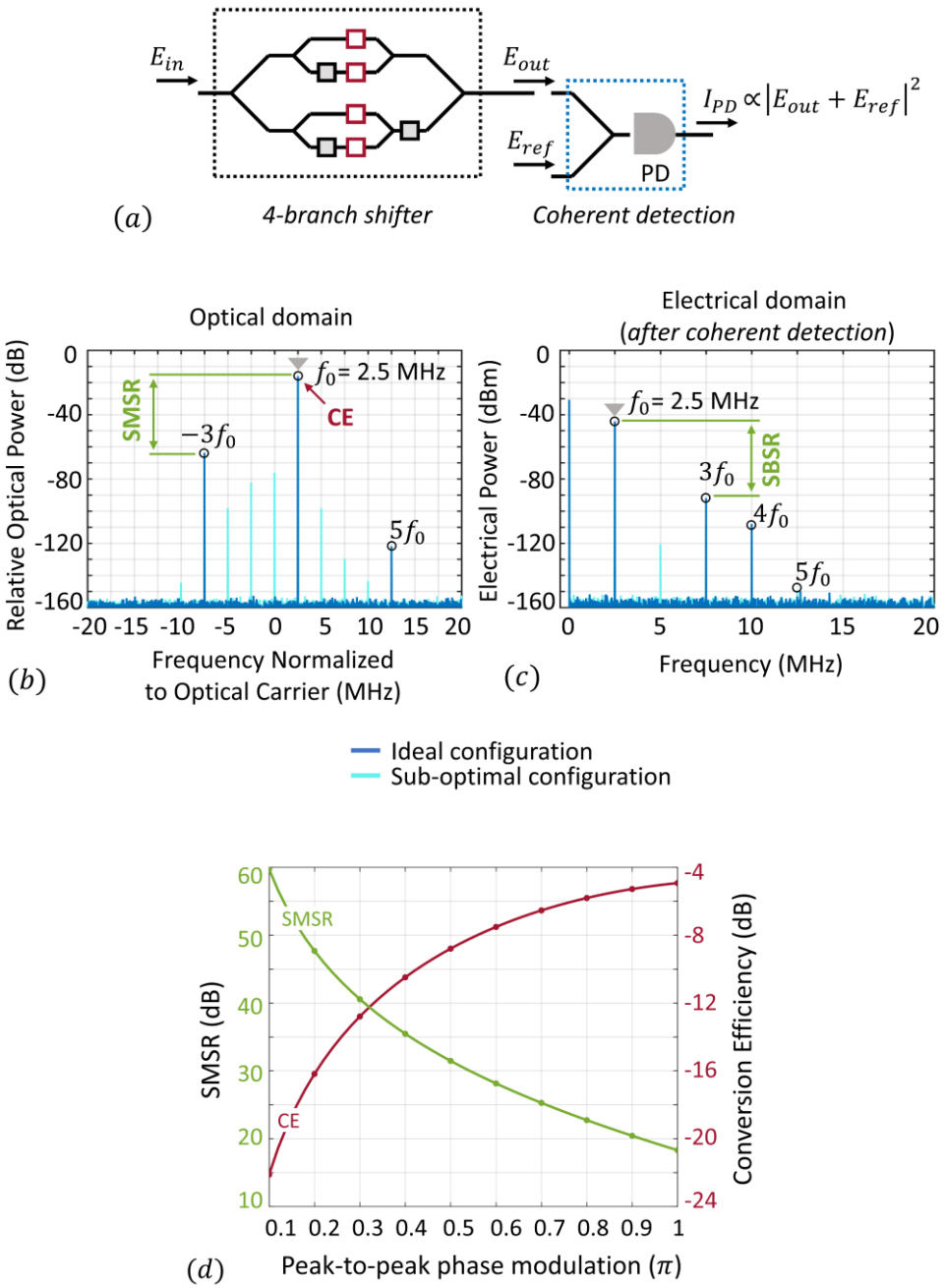

Figure 1.5: (a) Block-diagram of the simulation of the coherent detection. Simulated spectrum in the (b) optical domain and in the (c) electrical domain after coherent detection of the output of the SSB-OFS. (d) CE and SMSR determined/imposed by the driving amplitude.

input optical signal. From equation (1.10), it becomes evident that even in the ideal case, where all spurious side-modes undergoing destructive interference within the circuit are completely suppressed, unwanted side-modes still appear in the output spectrum around the fundamental component $f_{opt} + f_0$ of the desired frequency shift. If the π/2 phase shift is applied to the opposite arm of the circuit, the optical spectrum is mirrored around f_0, resulting in a fundamental frequency of $f_{opt} - f_0$. Both up-shifted and down-shifted

carriers can be generated simultaneously by utilizing the complementary outputs of a 3 dB directional coupler to combine the I and Q arms [14][16].

Stronger modulation induces higher-order side-modes in the optical spectrum due to the nonlinear transfer function of the MZM. Consequently, achieving high SMSR necessitates operating in the small-signal regime, albeit at the expense of reduced CE. This inherent trade-off of the IQ topology is illustrated in Figure 1.5(d). The maximum CE of -4.7 dB occurs at a phase modulation peak-to-peak amplitude of 1.176π, where the SMSR is limited to 14.8 dB, assuming optimal configuration. For the remainder of our analysis, we consider a peak-to-peak amplitude of 0.2π, which corresponds to a CE of -16.2 dB and an SMSR of 47.7 dB under ideal conditions. To address the limitations imposed by this trade-off, a solution involving pre-distorted driving signals has been demonstrated, effectively compensating for the MZM's nonlinear transfer function [18]. Figure 1.5(b) illustrates the simulated optical output of the SSB-OFS shifter for both an optimal configuration and a random sub-optimal configuration of the device, with a modulation frequency f_0 at 2.5 MHz. In the sub-optimal case, spectral lines appear at multiples of the modulation frequency. Following coherent detection, the spurious side-modes in the optical domain are down-converted, manifesting as sidebands in the electrical spectrum, as shown in Figure 1.5(c), which degrades the SBSR. In the ideal case in which only the terms of equation (1.10) are present, the SMSR and SBSR are identical, as both are determined by the height of the $3f_0$ component. However, in a sub-optimal configuration, the beating of the reference carrier signal with the SSB-OFS output produces a spectral line at $2f_0$, which can exceed the $3f_0$ component and further restrict the SBSR.

Three key factors are crucial for maintaining the desired symmetry between the canceling spectral components:

- Phase modulation depth: The same phase modulation must be applied uniformly across all branches. This may require calibration of the driving amplitudes if the modulators exhibit non-uniform modulation efficiencies.
- Power splitting ratio in the splitting and combining components: It determines the effectiveness of spectral line suppression through destructive interference. These components can be implemented as Y-branches, directional couplers, or tunable MZIs, with their extinction ratio playing a critical role.
- Modulator biasing: The two MZMs must be biased at the zero-transmission point and have a π/2 phase shift between them.

A fourth consideration is the relative phase shift between the driving signals. However, in most cases, a common oscillator is used to generate these signals, resulting in shared phase noise. As a result, the impact of this factor on the SBSR is negligible. We investigate the impact of the aforementioned factors on the performance of the SSB-OFS. To assess its performance, we analyze the spectrum of the electrical signal generated at the photodiode, which results from the beating of the frequency-shifted signal with the optical carrier. This process is illustrated in Figure 1.5(a). The phase modulation depth is set to 0.2π peak-to-peak for the analysis. To evaluate the impact of deviations, we introduce up to a 20% variation in each parameter from its ideal value and calculate the resulting SBSR in the spectrum. For each case, all other circuit parameters are assumed to remain at their ideal values, except for the one being varied.

Figure 1.6(a) shows the impact of unbalanced phase modulation across the four branches. The dotted lines represent the suppression ratio of the component at $2f_0$, while the solid line shows the overall SBSR performance. The phase modulation depth is varied from 0% to 20% deviation from the set value (0.2π) for each of the four modulators. For small deviations, the configuration remains close to the ideal, and the SBSR is primarily limited by the spectral line at $3f_0$. In this scenario, the SBSR is 47.7 dB (see Figure 1.5(c-d)). For larger deviations, the spectral line at $2f_0$ surpasses the one at $3f_0$, and the SBSR becomes determined by the $2f_0$ component. Each of the four modulators has a different effect on the overall SBSR. A small deviation of only 4% in the phase modulation φ_4 significantly deteriorates the SBSR, while a deviation of more than 15% in φ_3 is required to cause the same effect. This asymmetry is attributed to the way in which the different spectral lines, generated by phase modulation, are combined within the optical circuit. A more in-depth explanation can be obtained using Bessel functions [18], but such an analysis

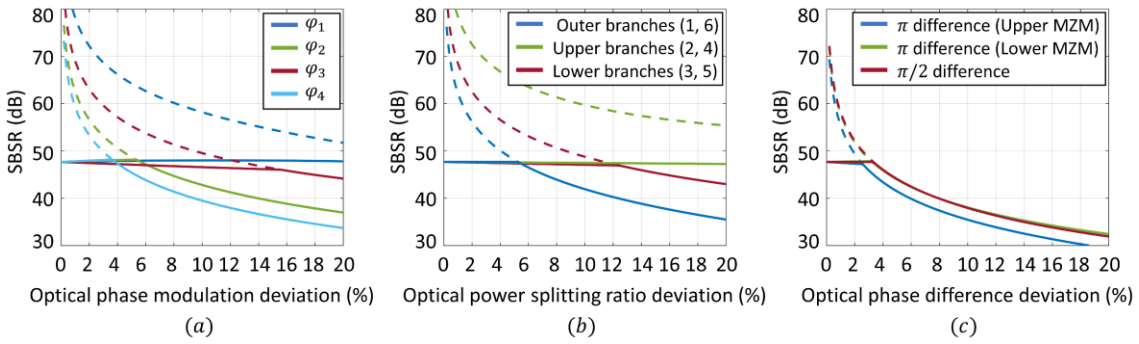

Figure 1.6: Effect of (a) Power splitting ratio deviation (b) Optical phase difference (c) Amplitude deviation independently. Driving amplitude is set to 0.2Vπ peak-to-peak.

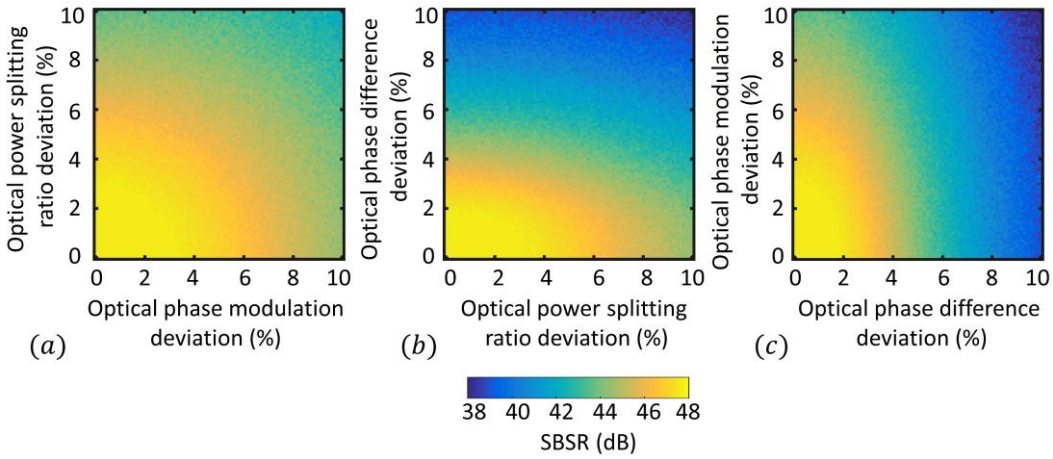

Figure 1.7: Effect of (a) Power splitting ratio deviation (b) Optical phase difference (c) Amplitude deviation in combination per two. Driving amplitude is set to 0.2Vπ peak-to-peak.

is beyond the scope of this work. Figure 1.6(b) presents the SBSR performance in relation to deviations from the ideal 50:50 optical power splitting ratio of the circuit's splitting and combining elements. The symmetrical power splitting in the outer MZI, formed by branches 1 and 6 (see Figure 1.4(a)), is the most critical. A deviation of more than 5% from the exact 50:50 ratio can significantly degrade the SBSR. A deviation of over 12% in the lower MZM branches also negatively impacts the SBSR, while deviations in the upper MZM branches have little to no effect on the SBSR, even for values up to 20%. This unequal impact of the upper and lower MZMs on the SBSR is again linked to how the spectral lines interfere throughout the circuit. Additionally, the precise configuration of the phase difference between the optical paths of the MZMs is crucial. As shown in Figure 1.6(c), an inaccuracy of less than 4% from the ideal phase difference can degrade the SBSR.

The analysis presented in Figure 1.6 assumes that, aside from the sweeping parameter, the rest of the circuit operates ideally. Each parameter is considered to act independently on the performance, while all other parameters are fixed at their ideal values. While this modeling approach highlights the significance of each individual parameter, it fails to capture the true performance of the SSB-OFS in real-world scenarios, where all factors interact simultaneously. To address this, we conducted Monte Carlo simulations where the phase modulation, optical power splitting ratio, and optical phase difference were considered in pairs. The deviations were randomly selected from a uniform distribution in the interval [0, 0.2], over 200 trials. The results are summarized in Figure 1.7. Regarding the SBSR, the simulations reveal that the most critical parameter is the optical phase

difference between the paths of the MZIs. We note that, within the study, CE experienced a degradation of less than 1.2 dB.

1.3.2 Stress-optic index modulation

TriPleX is a photonic integration platform based on silicon nitride (Si_3N_4) and silicon dioxide (SiO_2), offering single mode operation, low propagation losses (0.1 dB/cm at 1.55 μm) and high integration density over a wide wavelength range (0.4 μm – 2.35 μm) [50]. The high contrast between the refractive index of the silicon nitride core material (~1.98) with respect to the silicon oxide cladding material (1.45) supports the realization of waveguiding structures with strong confinement profile that enable the actualization of compact photonic circuits. A wide variety of waveguide geometries that support the propagation of TE polarized light is provided, such as box, single stripe, symmetric or asymmetric double stripe. Based on these geometries, a palette of standardized building blocks is provided that are manufactured in a single monolithic process flow with CMOS-compatible tools. In our designs, the asymmetric double stripe (ADS) geometry was used, optimized for low-loss propagation of the fundamental TE-mode at 1.55 μm. This consists of two Si3N4 stripes with unequal heights (core material) in a top-bottom configuration, surrounded by SiO2 (cladding material). The height of the top and bottom Si3N4 stripes are 180 and 80 nm respectively, with 100 nm SiO2 layer in between. Wet thermal oxidation is used to create the bottom cladding SiO2 layer on top of a single-crystal silicon substrate, typically at temperatures equal to or above 1000 °C. Low pressure chemical vapor deposition (LPCVD) is used to form the Si3N4 layers. The SiO2 top cladding layer is formed with the combination of TEOS (using the gas tetraethylorthosilicate) LPCVD deposition and plasma-enhanced chemical vapor deposition (PECVD), to create cladding thicknesses of at least 8 μm. Typical deposition temperatures are between 300 °C and 400 °C. The waveguide structures are specified with E-beam lithography (EBL), while deep reactive ion etching (DRIE) is used to embed the pattern after resistive development.

By depositing a thin layer of piezoelectric material on top of the waveguiding structures, the stress-optic effect can be employed to realize phase index modulators. The piezoelectric material of lead zirconate titanate (PZT) is used, due to its relatively large effective piezoelectric coefficients ($d_{33f} > 200$ pm/V and $e_{31f} > 18$ C/m^2) [40]. In the conventional approach, the PZT layer is deposited between a top and a bottom Platinum (Pt) electrode, forming a top-bottom configuration. By applying a voltage between the two electrodes, the

PZT layer expands and contracts due to the piezoelectric effect, causing stress to the waveguiding structure underneath. The relationship between the electric field and mechanical deformation in a piezoelectric material is described by

$$S = s^E \cdot T + d_t \cdot E \tag{1.11}$$

$$D = d \cdot T + \varepsilon^T \cdot E \tag{1.12}$$

, where D is the electrical displacement vector, S is the strain tensor, T the stress tensor, E the electrical field vector, s^E the elastic compliance under constant or zero electric field, ε^T the dielectric permittivity tensor under constant or zero stress, and d the piezoelectric constants tensor and d_t its transpose.

The stress induced to the waveguide results in phase modulation of the propagating TE-mode, due to the change of the refractive indices of the SiO2 and Si3N4 layers, and, consequently, of the effective refractive index of the mode. With this configuration, stress-based phase shifters can support tuning frequencies at least one order of magnitude higher than conventional phase heaters (PHs), while they offer significant reduction in the steady state power consumption (by a factor of 10^6) relative to their thermo-optic counterparts [30]-[33]. As an electrical load, the PZT-based SOM is characterized by the typical crystal model, which exhibits capacitive behavior when the excitation frequency is not close to its resonance. The capacitance is primarily formed by the upper and bottom electrodes that are separated by the non-conductive PZT layer. While ultra-low power consumption can be achieved in steady state operation due to the capacitive nature of the structure, the power increases linearly with the modulation frequency f, limiting the bandwidth of the device. Power dissipation is proportional to the capacitance C, the modulation frequency f and the square of the applied voltage V ($P = CV^2f$). In this work, an alternative structure was developed to increase the bandwidth of the device by lowering the capacitance between the two electrodes, to make it more suitable for modulation. In the top-bottom configuration the distance of the electrodes is defined by the thickness of the PZT layer, which is fixed to 2 μm for optimum stress-optic modulation of the effective refractive index. By placing both electrodes on top of the PZT layer, their position can be selected freely and thus optimized. With the top-top configuration shown in Figure 1.8, a capacitance of 100 pF is achieved, an order of magnitude lower from what is possible with the top-bottom configuration. The length of the SOM was set to 15 mm. When growing the PZT layer on top of SiO2, usually an intermediate seeding layer is used to enhance the growth of the piezoelectric layer. In the case of the conventional top-bottom electrode configuration the

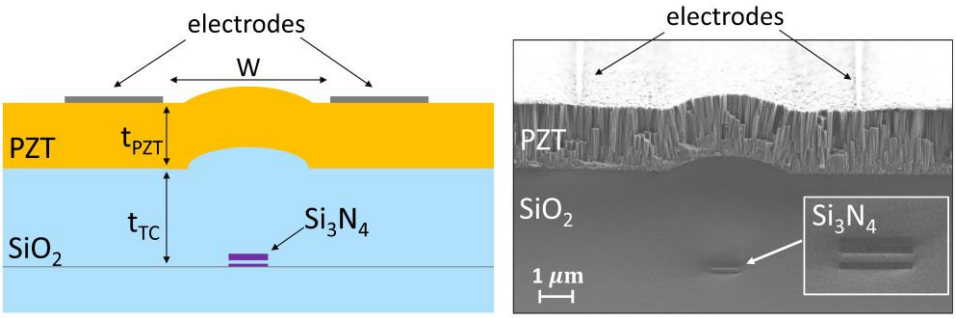

Figure 1.8: Illustration of the PZT thin film on top of the TriPleX structure. Both electrodes are placed on top of the PZT layer with a gap (W) of 5 µm. The thickness of the PZT layer (t_{PZT}) is 2 µm. The ADS waveguide is buried under 3 µm of SiO2 top cladding (t_{TC}).

seeding layer material that is widely used is Lanthanum Nickel Oxide (LNO). However, the conducting nature of the latter makes it unsuitable for the top-top configuration, as a non-conducting layer is required below the PZT structure. The proposed non-conducting material for the seeding layer is BTO (Barium Titanate), which demonstrates good material growth directly on SiO2. A Pulsed Laser Deposition (PLD) growth method built by Solmates is used to deposit the BTO/PZT bilayer on a wafer-level [41][51][52]. The processing steps for forming the PZT-based SOMs are detailed in paragraph 1.6.1, where we discuss the hybrid integration with the polymer platform.

1.3.3 Experimental results

The experimental setup that was used to evaluate the performance of the implemented OFS circuits is shown in Figure 1.9. A continuous wave (CW) ultra-low linewidth (< 2 kHz) laser source provided TE light at 1550.12 nm wavelength. Optical power of 6.3 dBm was coupled into the PIC via a single mode fiber (SMF), after passing through an optical isolator to prevent undesired back-reflections and a polarization controller to ensure TE polarization. The optical power was split into a modulated path and a reference path inside the PICs, and the two signals were recombined externally via a fused fiber coupler. The optical beating between these signals was detected on an external photodiode. An electrical spectrum analyzer is then used to capture the power spectrum of the photodiode's signal, i.e., the voltage measured across a 50 Ω load. Dedicated electronics were used for the control of the low-speed thermo-optic phase shifters and for driving the SOMs in the MHz regime. A commercial high-voltage amplifier was also used for driving the SOMs with a sawtooth signal up to 100 Vp-p at 100 kHz frequency.

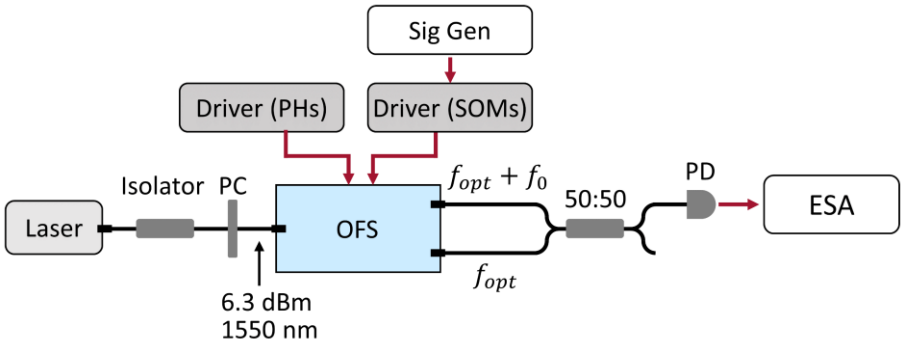

Figure 1.9: Setup for the characterization of the OFS PICs. PC: Polarization controller, PHs: Phase heaters, ESA: Electrical spectrum Analyzer

1.3.3.1 Serrodyne Frequency Shifter (SFS)

Figure 1.10 presents the schematic layout of the serrodyne frequency shifter. At the input, a tunable MZI based on thermo-optic tuning, is responsible for splitting the inserted light into the measurement and the reference path. A small portion of the light in the measurement path is tapped for monitoring, using a 95:5 coupler. The largest portion of the light in the measurement path is guided towards the OFS section, where it is modulated by the stress-optic PZT modulators. Four stress-optic modulators in series are used to distribute the total 2π phase among multiple elements, lowering the required driving amplitude. The dimensions of the PIC are 11.25 mm × 6.9 mm.

Figure 1.11 presents the experimental results from the characterization of the stress-optic serrodyne frequency shifter at a modulation frequency of 100 kHz. Figure 1.11(a) shows the spectrum of the beating signal on the photodiode, while Figure 1.11(b) shows the beating signal in the time domain, along with the driving signal of the modulator. The SBSR is 22.1 dB, limited by the $2f_0$ spectral components. As we discussed in paragraph 1.3.1.1, a significant factor for the SBSR performance is the quality of the sawtooth phase profile, in terms of bandwidth and amplitude. From the signals in the time-domain we can see that the discontinuity in the phase modulation due to the sawtooth falling time is approximately 6% of the total period. The manifestation of this discontinuity in the beating signal is practically an inverse modulation caused by the falling slope of the sawtooth. The result is the same sinusoidal waveform as the one produced from the rising slope of the sawtooth, but significantly faster. Two out of the four SOMs were functional, and they were used for modulating the optical signal. A 90% of 2π was accomplished with 100 V peak-to-peak driving amplitude. According to the simulation results presented in paragraph 1.3.1.1 the quality of the experimentally realized sawtooth is expected to limit the SBSR at

23.8 dB. The 1.7 dB difference between the theoretical and the experimentally measured SBSR may arise from small non-linearities in the response of the stress-optic PZT modulators that become apparent when the amplitude of the driving signal exceeds their polling voltage [33]. The measured CE was approximately -1 dB, assuming total optical losses (coupling and propagation loss) of 5.2 dB.

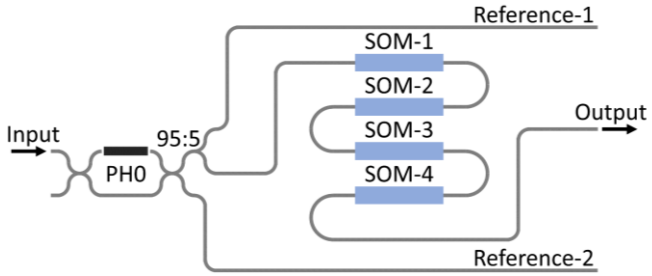

Figure 1.10: Schematic of the serrodyne frequency shifter (SFS) circuit in TriPleX. A phase heater (PH) is used to control the MZI that splits the input into the modulation path, where the stress-optic modulators (SOMs) are placed, and the reference path.

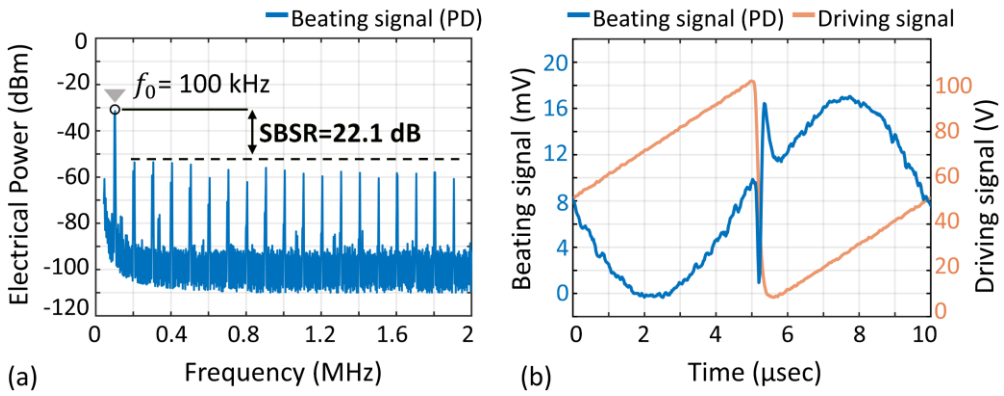

Figure 1.11: Experimental results for the serrodyne frequency shifter at 100 kHz in (a) the frequency and (b) the time domain.

1.3.3.2 Single Sideband Frequency Shifter (SSB-FS)

Higher modulation frequencies are possible with the IQ topology of the SSB-OFS, since the sinewave driving signals that are used are much less bandwidth-demanding. Figure 1.13 presents the power spectrum with a modulation frequency of 2.5 MHz. The $2f_0$ component at 5 MHz imposes a 39 dB SBSR, while the suppression ratio of the $3f_0$ is equal to 43.8 dB. The phase shift inserted by the stress-optic phase modulators was configured to be equal to 0.25π peak-to-peak, which corresponds to a suppression ratio of exactly 43.8 dB for the $3f_0$ sideband, according to our modelling presented in paragraph 1.3.1.2 (Figure 1.5). With an input optical power of 7 dBm, the optical power of the frequency shifted

component at $f_{opt} + f_0$ was measured -14.0 dBm. Optical coupling and propagation losses of 6.3 dB were determined, suggesting a CE of -14.7 dB, only 0.4 dB less than our simulation (Figure 1.5).

Unequal driving amplitudes were applied to each SOM, since they exhibited different phase shift efficiency. Amplitudes from 25 Vp-p to 70 Vp-p were applied to achieve the desired 0.25π phase shift at 2.5 MHz. The results of our characterization are shown in Figure 1.14. The difference in the performance originates from variations in the piezoelectric coefficient among the different structures, which are known to depend on the structural properties of the deposited PZT films [33][56]. Since the driving amplitudes differ, the power dissipation is also different for each modulator. At the operation frequency of 2.5 MHz, the average power consumption was equal to 660 mW, while the best performing structure dissipated 156 mW (SOM-2). The fabrication process for the specific PZT structures with the top-top electrode configuration was developed for the first time within the present work, and thus, lacks the maturity of the conventional PZT technology based on the top-bottom electrode configuration, which demonstrates higher homogeneity across the wafer [41]. To characterize the phase-shift efficiency of each SOM we used the on-chip MZIs to translate the inserted phase-shift to intensity modulation. For example, to characterize the SOM-1 we used the MZI controlled by PH2 to split the light between the upper and the lower path, where the SOM-1 and SOM-2 are located, respectively (see Figure 1.12). The SOM-1 was driven with a ramp voltage from 0 to 100 Vp-p at 2.5 MHz frequency, while no signal was applied to SOM-2. The MZI controlled by PH4 was used to combine the modulated with the unmodulated light and the optical beating was observed on a PD directly connected to the monitor port-1. The same procedure was followed for the characterization of all the SOMs, accordingly, and the results are presented in Figure 1.14. Before performing any modulation with the stress-optic shifters, the device was carefully characterized to identify the correct biasing currents for the integrated PHs of the circuit, to introduce the appropriate phase-shifts and splitting ratios with the MZIs. Despite the optimization, it is evident from the spectrum in Figure 1.13 that imperfections in the configuration of the device were present. The fact that the $2f_0$ component is higher than any other sideband indicates that the optical circuit is not perfectly configured. According to our analysis in paragraph 1.3.1.2 there are deviations within 10% in either the inserted phase shift by the stress-optic shifters, the splitting ratio of the MZIs or the optical phase shift bias (see Figure 1.7).

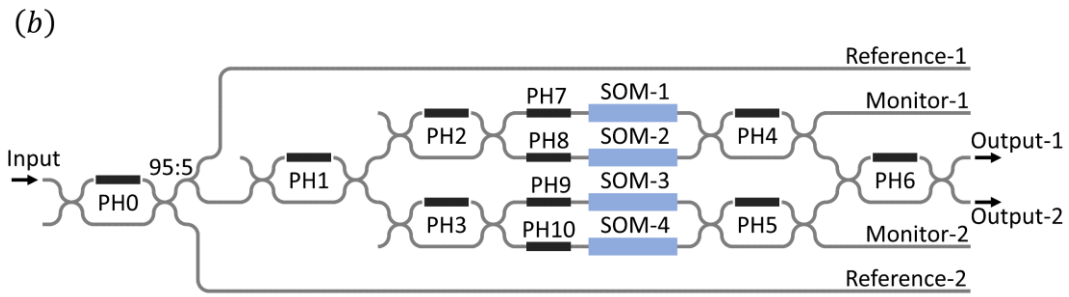

Figure 1.12: Schematic of the circuit of the SSB optical frequency shifter (OFS) in TriPleX. Phase heaters (PH) are used for the control of the MZIs and stress-optic modulators (SOMs) for the optical modulation.

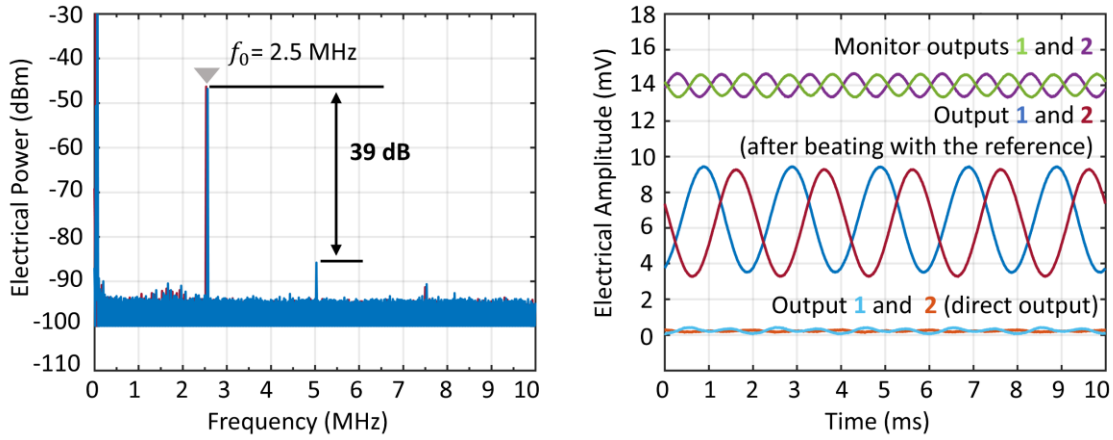

Figure 1.13: Experimental results from the testing of the SSB-OFS frequency shifter. (Left) Electrical spectrum of the beating signal on the PD. The fundamental frequency is at 2.5 MHz and the SBSR is 39 dB due to the 2nd order harmonic sideband at 5 MHz. (Right) Time-domain signals at the output ports of the circuit with and without mixing with the reference signal.

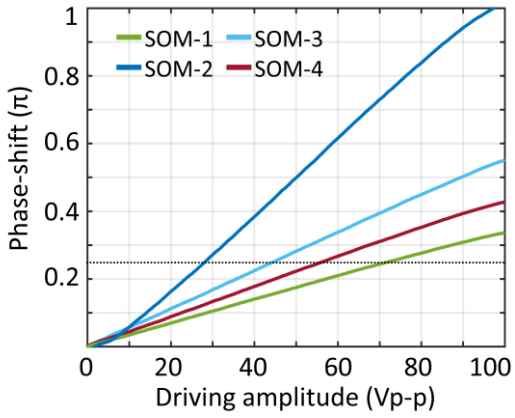

Figure 1.14: Phase-shift relative to the applied driving voltage for the four SOMs in the SSB OFS. The stress-optic response is linear in the interval 10–90 V. The characterization was performed with a rising slope of 100 V peak-to-peak amplitude and 10 μs duration.

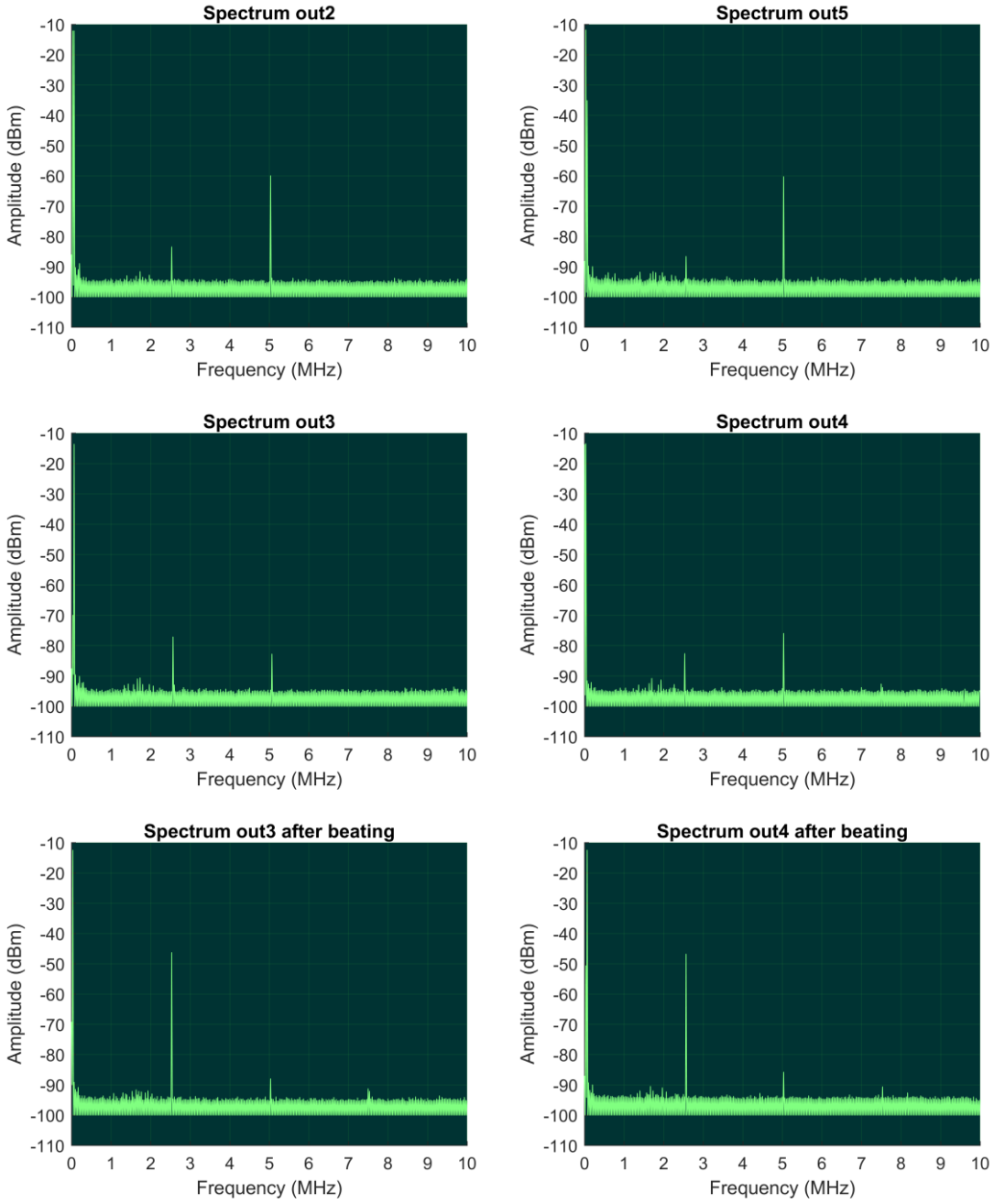

Figure 1.15: Power spectrum of the signal of an external photodetector connected to the optical output ports of the SSB OFS, captured with an ESA. The photodetector is connected at the monitor ports out2 (monitor-1) and out5 (monitor-2), and the modulation output ports out3 (output-1) and out4 (output-2). Spectrum in the case of mixing with the optical reference is also shown.

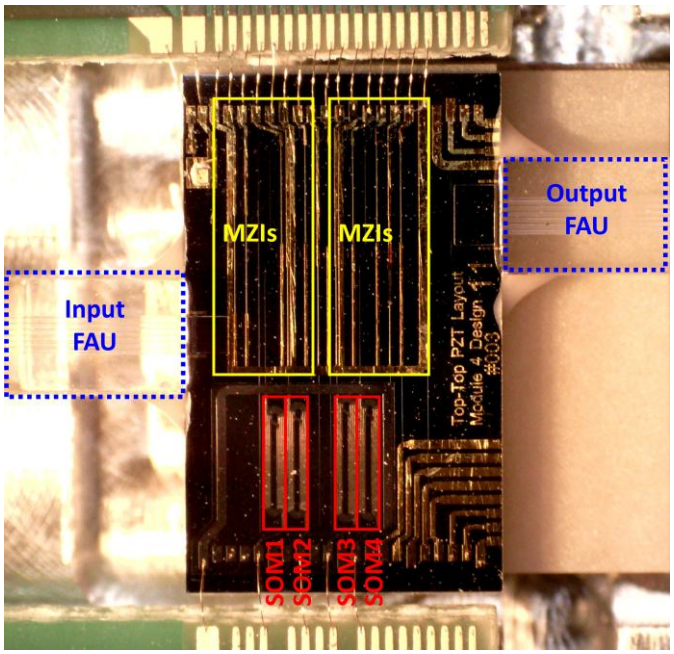

Figure 1.16: Top view photograph of the TriPleX PIC with the SSB-OFS. The circuit comprises 7 MZIs controlled by phase heaters and 4 PZT-based stress-optic modulators (SOMs). The PIC of the serrodyne OFS is similar, without including the MZIs.

1.3.3.3 Stress-optic modulator bandwidth

The stress-optic modulator (SOM) presented in this work is based on the mechanical strain applied on the SiN waveguide of the TriPleX platform by the piezoelectric actuation of a thin-film PZT layer deposited on top of the waveguide structure. Stress-optic effect can support modulation frequencies in the order of hundreds of MHz [37]. The limitation in bandwidth comes from the power required for driving the SOM at high frequencies.

As an electrical load, the PZT-based SOM is characterized by the typical crystal model, which is a dominant capacitance in parallel with an (R-L-C) branch that models the resonance region. Therefore, when the excitation frequency is not close to the resonance region, the SOM exhibits capacitive behavior. This means that there is a high driving current demand, that increases proportionally with the excitation frequency ($P = CV^2 f$), which poses a great challenge to the driving circuit. In addition to this, the electrodes that are used for the excitation of the PZT are also increasing the capacitance of the structure. The bandwidth of the custom driving electronics can support modulation up to 20 MHz, which means that, in principle, a frequency shift of 20 MHz is possible with the SSB modulator, without significant reduction of the SBSR performance. The reason for focusing our measurements around 2.5 MHz was that a complete LDV system provided by Polytec was designed to operate with this IF. The dedicated read-out electronics (TIAs, OP-AMPs,

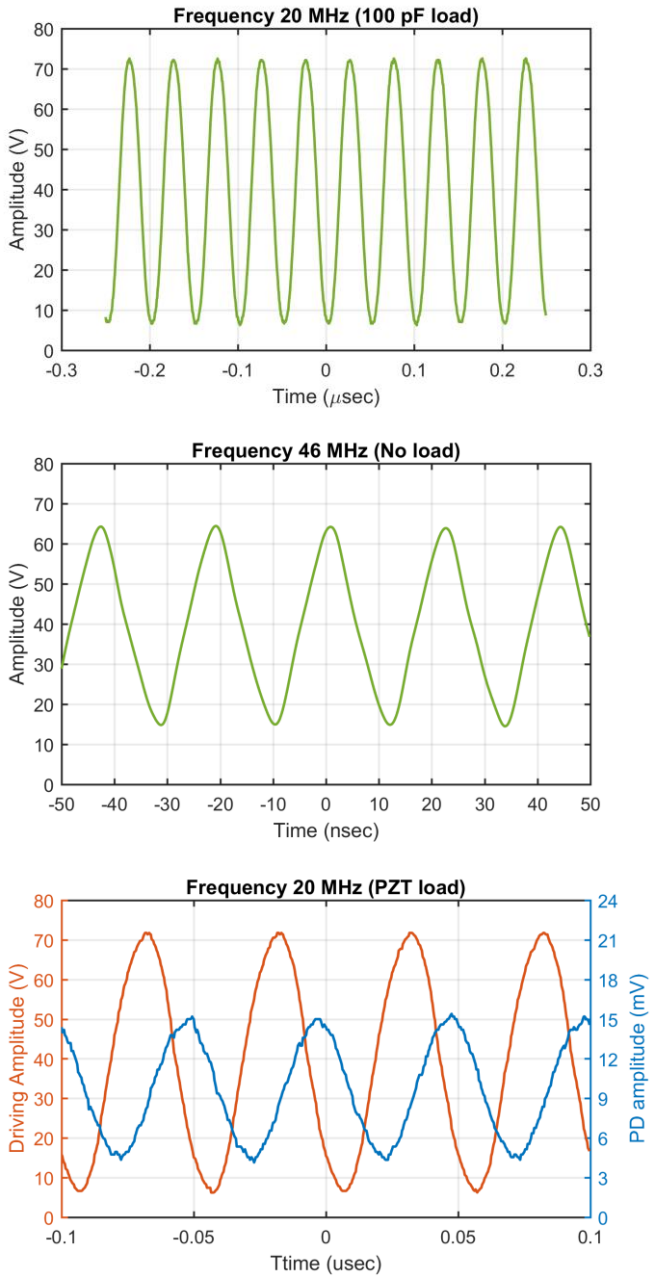

Figure 1.17: Performance of the custom electronics designed for the driving of the PZT-based stress-optic modulators (SOMs). (Top) Measured amplitude on a 100-pF test load at 20 MHz. (Middle) Measured 3dB frequency of the power bandwidth at 46 MHz. Distortion at the output waveform is clearly visible. (Bottom) Stress-optic modulation at 20 MHz (SOM No2 of the SSB-OFS). The driving signal is measured at the output of the driving amplifier.

analog filters, etc.), as well as the packaging PCBs, have been designed accordingly. The LDV system demonstration is presented in paragraph 1.5.

In Figure 1.17 we present the measurements that we have implemented to determine the maximum achievable frequency with our custom driving electronics. In Figure 1.17(a) we present the measured amplitude (70 Vp-p) on a 100-pF test load, which models the dominant capacitance of the PZT-based SOM at 20 MHz. The power consumption at 20

MHz was five times greater than at 2.5 MHz which caused heat removal issues. The heat sink capacity of our design was not sufficient to support operation at 20 MHz for a long period of time, but with an appropriate heat sink, operation at this frequency is feasible, since there is no limitation from the power bandwidth of the amplifier. To roughly measure the latter, we removed the test load and increased the frequency of the input signal until we reached the 3dB frequency (output amplitude equal to $70/\sqrt{2}$ Vp-p). This occured at 46 MHz and as shown in Figure 1.17(b), at that frequency the output signal is clearly distorted. Finally, we used our custom electronics to drive a stress-optic modulator (SOM-2 of the SSB-OFS) at 20 MHz and measure the result of the modulation on a photodetector. We used an on-chip MZI to achieve intensity modulation, that can be observed with an external photodetector, as we described in the previous paragraph. Figure 1.17(c) presents the driving amplitude along with the intensity modulation measured on the photodetector. Some signal deterioration is expected at the modulator's end since the PCBs were designed for a lower modulation frequency (2.5 MHz). We concluded that the maximum achievable frequency for SSB modulation would be approximately 20 MHz. The power bandwidth of the amplifier is causing significant signal distortion at higher frequencies, as well as excessive heat dissipation.

1.4Polymer-based receiver

A second PIC realized in PolyBoard was used for the detection part. PolyBoard is a polymer-based multifunction photonic platform, offering a single-mode operation, low propagation losses (0.7 dB/cm at 1.55 μm), and the possibility for integration of polarization handling elements [42] and indium-phosphide (InP) components [43]-[45] [53]. The core and the cladding have refractive indexes of n_{core}= 1.48 and n_{clad}= 1.45 respectively, supporting both the transverse electric (TE) and magnetic (TM) components, because of the waveguide symmetry which is rectangular with thickness in both axes of 3.2 μm. The single-waveguide PolyBoard stack consists of a waveguide and a cladding resin and is realized by using procedures of consecutive layer deposition. The fabrication of the PolyBoard chip, comprises the spin-coating of the cladding resin on the silicon (Si) substrate, the spin-coating of the waveguide resin, the structuring of the waveguiding layer with reactive ion etching (RIE) and ultraviolet (UV) lithography, and the spin-coating of the second layer of cladding resin to create the top cladding layer.

Figure 1.18 shows a photograph of the coherent receiver PIC. The schematic of the photonic circuit is presented in Figure 1.19. From the left side of the circuit (fiber-6) unmodulated TE polarized light is inserted, to act as the local oscillator for the coherent detection. The reference light is divided into two paths by a 50:50 coupler, and in one of the two paths a half-wave plate (HWP) is used to rotate the polarization by 90 degrees and thus create a TM optical LO. The light from the measurement beam is coupled into the PIC from the right side of the circuit. The polarization state of measurement beam is arbitrary. The random polarization state of the measurement beam is split into two orthogonal components by means of an integrated polarization beam splitter (PBS) [53]. The two components are mixed with the corresponding LO using 2×2 multimode interference couplers (MMIs). The balancing of the optical power between the reference and the measurement signal prior to the mixing for the two polarization components, is achieved with thermo-optic-based variable optical attenuators (VOAs) [54]. Finally, the TE and TM mixed signals are guided to four InP-based photodiodes (PDs), realizing a dual-pol coherent detection scheme. Additional photodiodes are placed on the top side of the circuit for monitor and testing purposes. The optical losses for each path were calculated by measuring the photodiodes' current while assuming a responsivity of approximately 1 A/W [43], and the results are presented in Table 1. The size of the PolyBoard PIC is 11.25 mm × 9.6 mm.

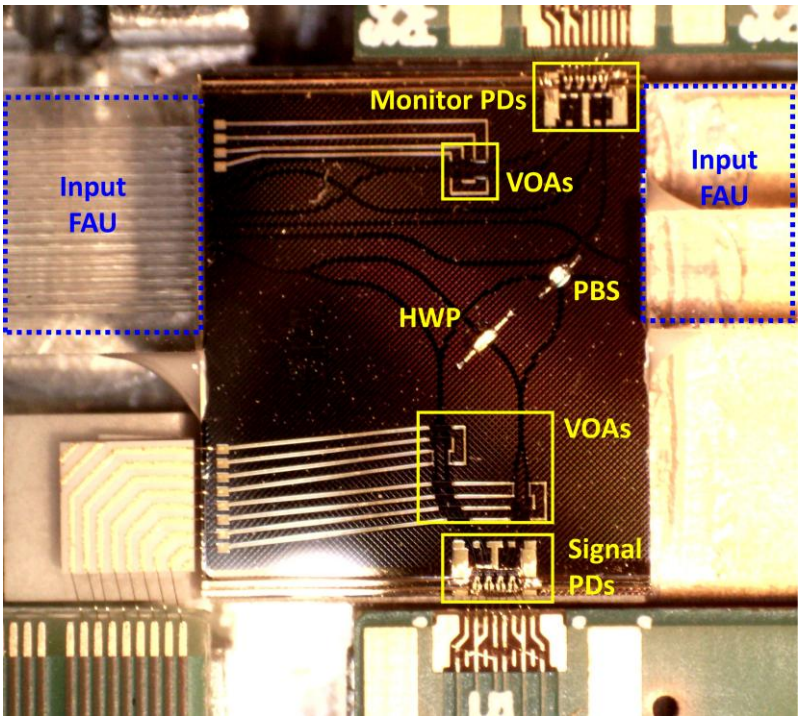

Figure 1.18: Top view photograph of the packaged PolyBoard PIC for dual-pol coherent detection. The micro-optic elements of the polarization beam splitter (PBS) and the half-wave plate (HWP) are visible on the chip.

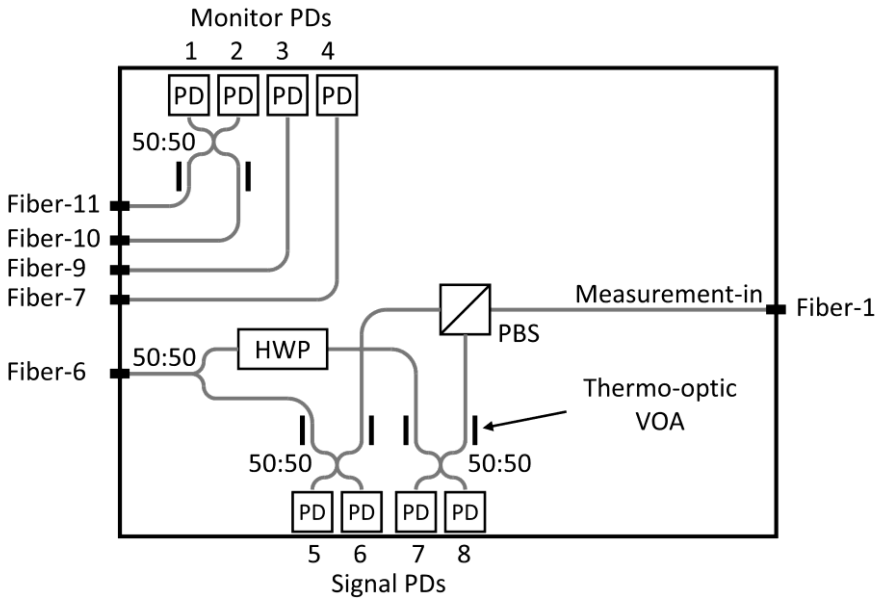

Figure 1.19: Schematic of the dual-pol coherent detection circuit in PolyBoard.

		Optical Loss (dB)
Monitor PDs	Balanced pair PD 1-2	20
	Monitor PDs, single PD-3	15
	Monitor PDs, single PD-4	16
Signal PDs	Balanced pair PD 5-6 (input from fiber port 1)	11
	Balanced pair PD 5-6 (input from fiber port 6)	15
	Balanced pair PD 7-8 (input from fiber port 1)	11
	Balanced pair PD 7-8 (input from fiber port 6)	24

*PD responsivity: ~1 A/W

Table 1: Optical losses of the PolyBoard dual-pol coherent detector PIC

1.5 System Demonstration of LDV

1.5.1 Experimental setup

A complete LDV system was implemented using the OFS and coherent receiver PICs described in the preceding sections and was tested in collaboration with Polytec. A schematic representation of the system is shown in Figure 1.20. A low-linewidth, fiber-coupled laser provided 10.8 dBm (12 mW) of optical power at 1550.12 nm, which was split into two branches. In the first branch, TE-polarized light with approximately 7 dBm (5 mW) of optical power was coupled into the TriPleX PIC, which incorporated the optical frequency shifter. A frequency shift of 2.5 MHz was introduced using the SSB-OFS. The second branch served as the reference beam for coherent detection in the PolyBoard PIC. Input and output coupling to the PICs was achieved using fiber-array units (FAUs). The frequency-shifted output from the TriPleX PIC, serving as the measurement beam, was routed via fiber to Polytec's probe-head, which focused the beam onto the vibrating surface under inspection and collected the reflected light through the same lens system. The measured optical power available for the probe beam was -14 dBm (40 µW). The theoretically inherent loss from the frequency conversion process is 14.7 dB for a 0.25π peak-to-peak phase shift, while an additional 6.3 dB corresponds to optical coupling and propagation losses. The light collected back from the probe-head was coupled into the PolyBoard PIC where the optical phase information from both TE and TM polarization was detected. Detection electronics and demodulation software from Polytec were used for the

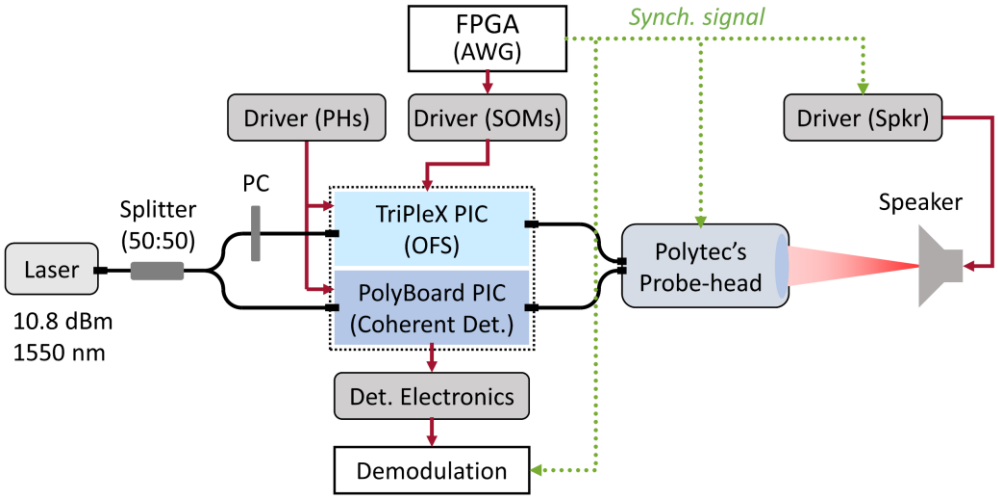

Figure 1.20: Schematic of the LDV system. Polytec's probe-head focused the beam on the vibrating surface and collected the back-scattered light. For real-time demodulation a synchronization signal was shared between the driver of the speaker and the demodulation circuit. PC: Polarization controller, PHs: Phase heaters, AWG: Arbitrary waveform generator

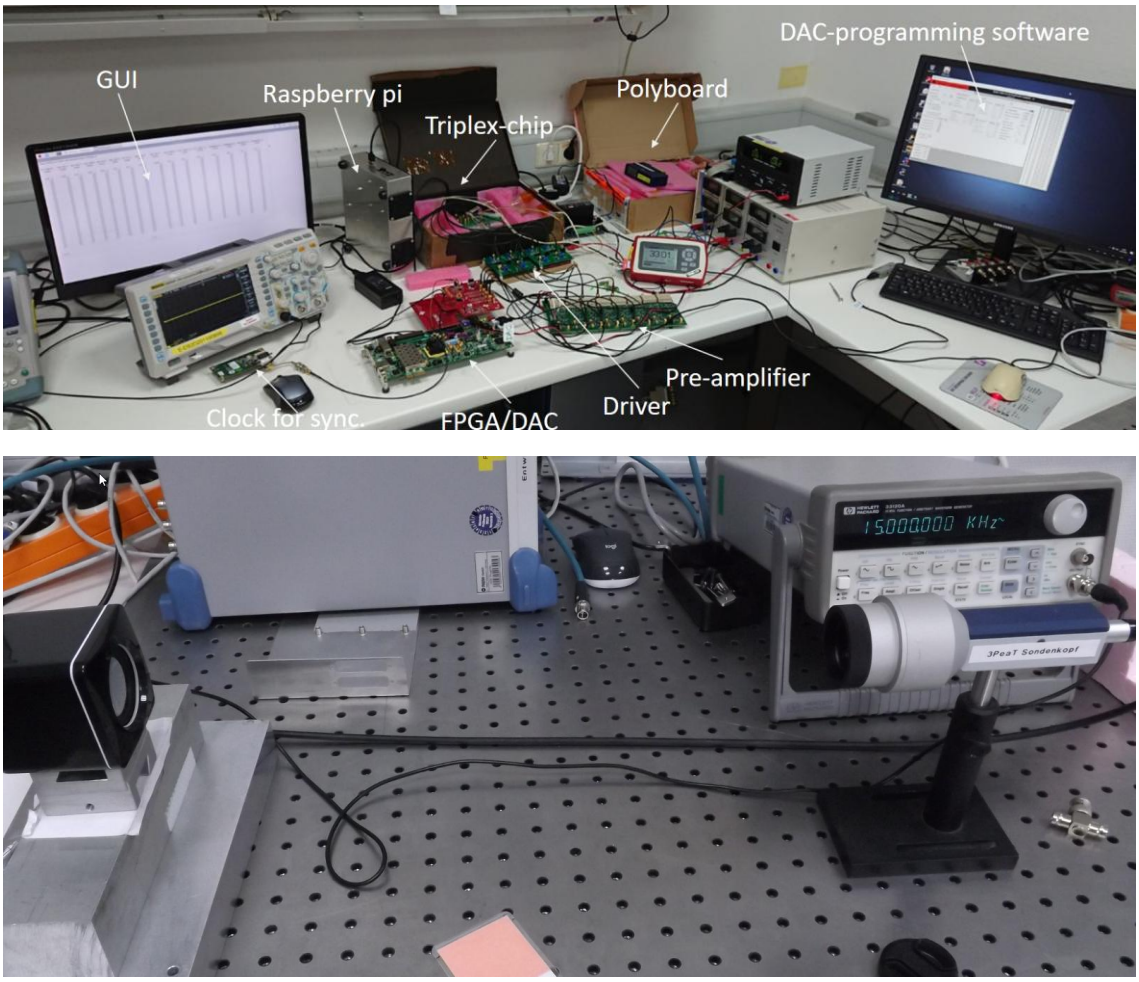

Figure 1.21: Photograph of (Top) the setup for vibration measurements and (Bottom) Polytec's probe-head targeting the speaker.

processing of the raw signals. Custom electronics were used to control the phase-heaters on both PICs and to provide the driving signals to the stress-optic modulators in TriPleX. The latter circuit was based on a field programmable gate array (FPGA) to generate the signals and to provide the necessary clock signals for the synchronization of the driving and detection electronics with the excitation signal of the vibrating surface. The total optical loss in the PolyBoard PIC, including coupling and insertion loss for all optical components in the paths from the fiber-input to the PDs, was estimated at approximately 11 dB for the measurement input, at 15 dB for the optical reference input and at around 15 dB on average for the monitor PDs, assuming PD responsivity of 1 A/W (see Table 1). An additional 9 dB loss was measured in the path of the HWP. The extinction ratio of the PBS was 15 dB.

Figure 1.22 shows a block diagram of the electronic modules used to control the PICs and drive the stress-optic modulators. A thermoelectric (TEC) controller was used to keep

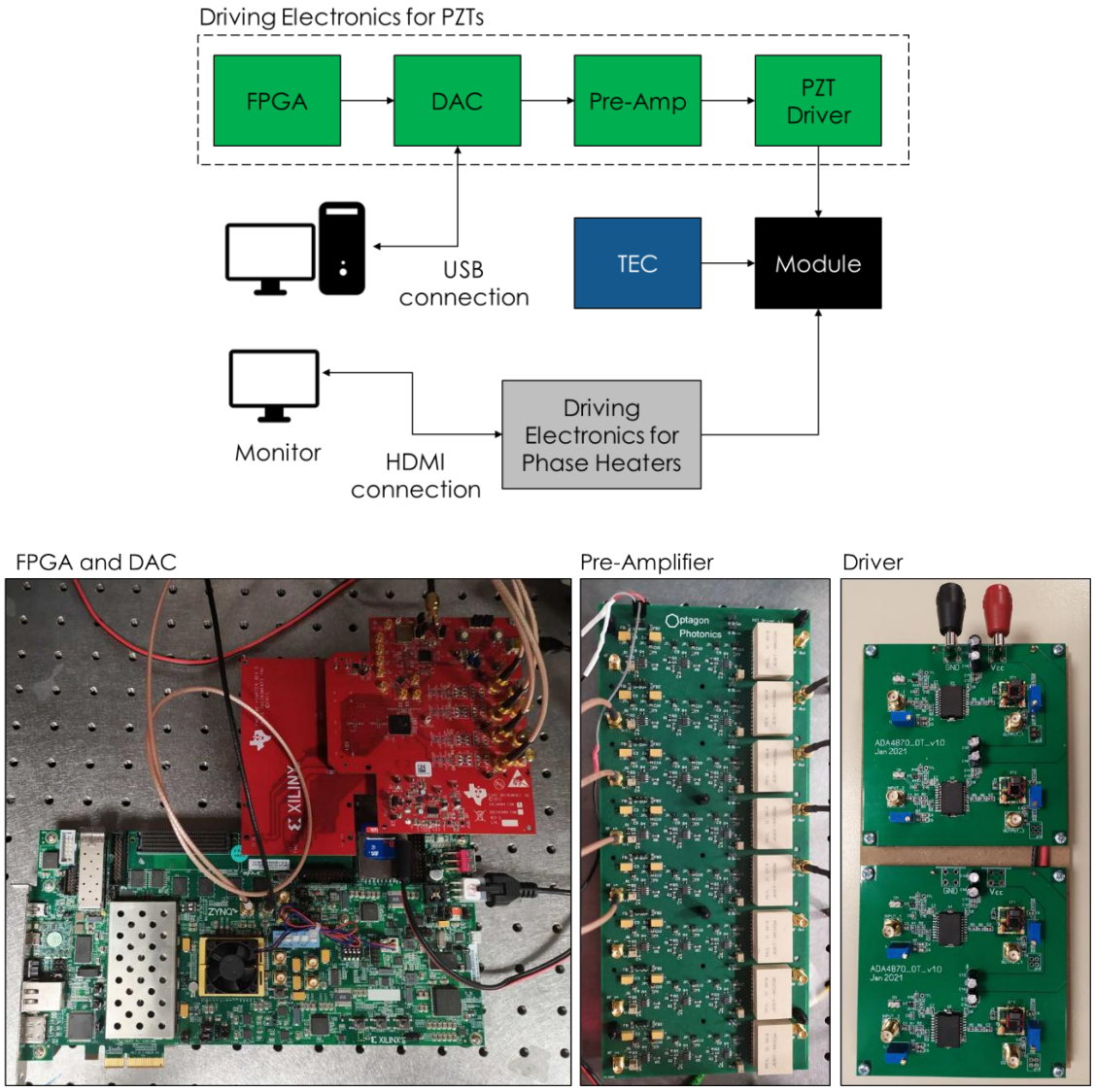

Figure 1.22: (Top) Block diagram of the electronic modules that were used to control the PICs and (Bottom) the driving electronics for the PZT-based stress-optic modulators.

the temperature of the TriPleX PIC at 25 ºC. The FPGA provided four sinusoidal signals with appropriate phase differences to drive the IQM (SSB modulator), as discussed in paragraph 1.3.1.2. A DAC was employed to produce LVDS signals with an amplitude of 390 mV. However, single-ended signaling was used, with the complementary LVDS output terminated using a 50 Ω load. A pre-amplification stage adjusted the signal levels to the range of 1 V to 5 V prior to entering the fixed-gain (~11.7 dB) driver circuit. Table 2 summarizes the measured output levels at each stage of the signal chain. Both the driving system for stress-optic modulators and the heater control module were developed by the start-up company Optagon Photonics.

	DAC	Pre-Amplifier	Driver
Supply voltage	+6V	±15V	+40V
Supply current (idle)	590mA	230mA	150mA
Supply current (all channels on)	630mA	-15V: 215mA, +15V: 260mA	270mA
Output Amplitude per channel (peak-to-peak) *SSB modulator	IA: 390mVpp IB: 390mVpp IC: 390mVpp ID: 390mVpp	RFout2: 4.78Vpp RFout3: 3.62Vpp RFout4: 1.61Vpp RFout5: 2.85Vpp	Channel 1: 71.2Vpp, offset: 39V Channel 2: 54.3Vpp, offset: 39V Channel 3: 24.1Vpp, offset: 39V Channel 4: 42.6Vpp, offset: 39V

Table 2: Configuration of the driving electronics for the PZT-based modulators.

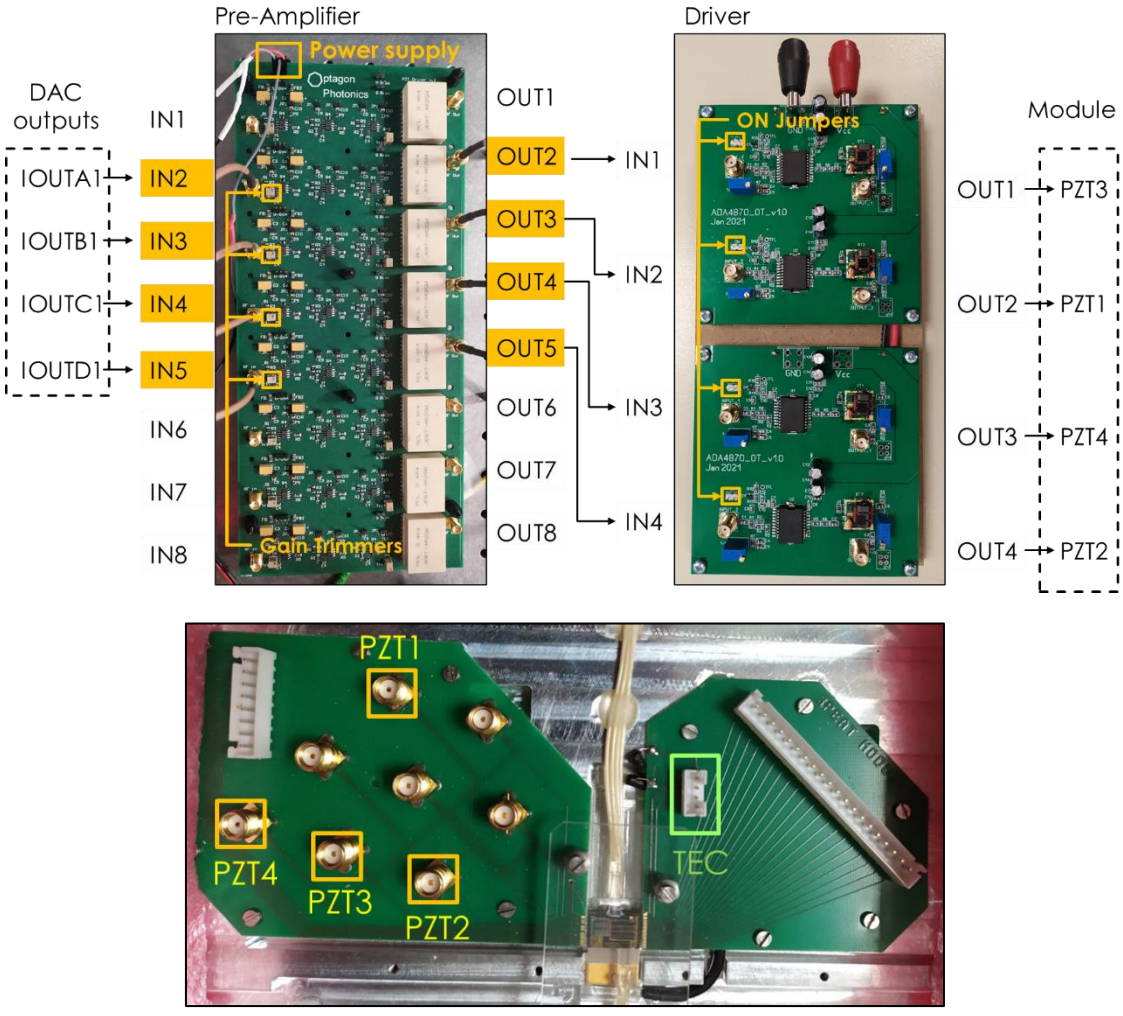

Figure 1.23: (Top) Pre-amplifier and driver boards for the PZT-based stress-optic modulators. The outputs of the DAC are connected to the pre-amplifier; pre-amplifier's outputs are connected to the driver and finally the outputs of the driver are connected to the stress-optic modulators' RF inputs in the packaged PIC. (Bottom) Packaged TriPeX PIC implementing the OFS.

1.5.2 Experimental results

To evaluate the accuracy and stability of the complete LDV setup, we performed measurements using a vibration calibrator. The calibrator generated a sinusoidal vibration at 159.15 Hz with a peak-to-peak displacement amplitude of 14.142 μm (10 μm RMS). After digital demodulation of the raw signal, a stable sinusoidal waveform with a displacement amplitude of 14.1 μm was recovered. The displacement spectrum obtained via FFT of the time-domain signal is shown in Figure 1.24(Top), clearly exhibiting a sharp spectral peak at 159 Hz, corresponding to the periodic motion of the calibrator. An elevated noise floor extending up to ~35 kHz is likely caused by intermodulation with spurious components at the electrical carrier frequency of 2.5 MHz. The excellent agreement between the measured amplitude and frequency and the calibrator's nominal values confirms the accuracy of the LDV system. To assess the resolution limits of the system, we conducted measurements on a membrane loudspeaker, which produces displacements in the nanometer range. The loudspeaker was driven with a sinusoidal signal at 15 kHz. The demodulated output was passed through a 1 MHz bandpass filter centered on the 2.5 MHz carrier frequency to suppress in-band noise and enhance resolution. The resulting displacement spectrum is shown in Figure 1.24(Bottom), where the 15 kHz excitation peak is clearly visible, corresponding to a displacement amplitude of approximately 5 nm. From the spectral data, we estimate that the noise-limited resolution of the system is around 10 pm for frequencies above 1 kHz, where the noise spectrum is white and the baseline remains flat. For frequencies below 200 Hz, the resolution is limited to a few nanometers (< 10 nm) due to increased low-frequency electronic noise from the detection and digitization circuitry, as well as environmental vibrations. These measurements were initially performed with offline signal demodulation. However, real-time demodulation is highly advantageous in scenarios requiring immediate feedback for system or sample adjustments. To demonstrate this, we carried out measurements on the loudspeaker using real-time demodulation, recording and analyzing both orthogonal polarization channels. The resulting displacement spectrum is shown in Figure 1.25. Due to memory constraints in the real-time processor, the observation window was limited to 20 kHz. Both polarization channels carried the same signal content, revealing a displacement amplitude of 5 nm at 10 kHz, matching the loudspeaker's excitation. The system demonstrated a displacement resolution of approximately 10 pm under these conditions.

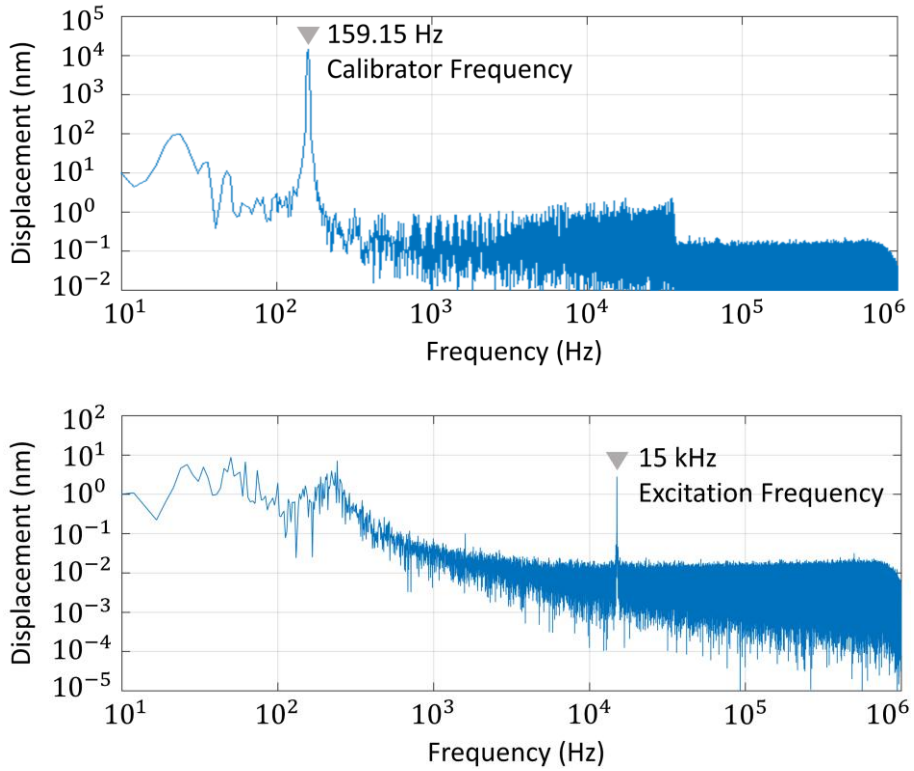

Figure 1.24: (Top) Spectrum from the calibration measurement with a sinusoidal vibration frequency at 159.15 Hz with a peak-to-peak displacement amplitude of 14.142 µm. (Bottom) Displacement spectrum from a loudspeaker using a sinusoidal excitation signal at 15 kHz. Bandpass filtering is applied to improve the resolution of the measurement (achievable noise floor around 10 pm/√Hz)

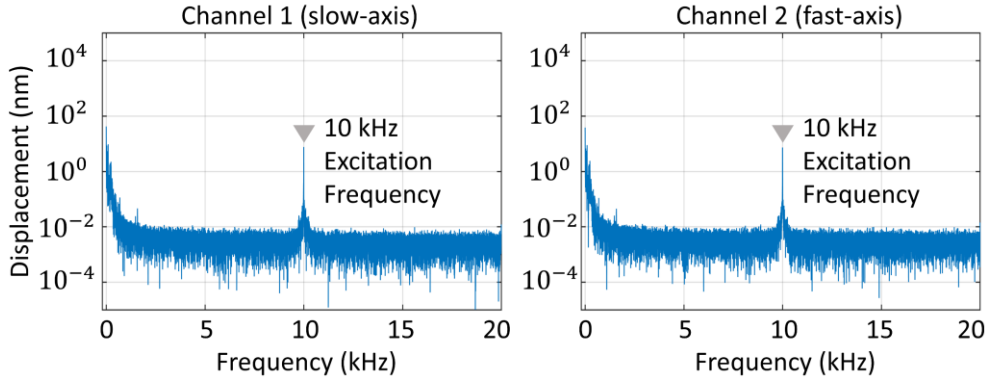

Figure 1.25: Displacement spectrum from a loudspeaker using 10 kHz excitation. The two channels correspond to the two independent polarization channels and carry the same information. The achievable displacement resolution is below 10 pm

1.6Hybrid 3D photonic integration

In the previous sections, we presented an LDV system that utilized two separately packaged PICs, implemented on distinct platforms: the Si3N4 (SiN) platform from LioniX (TriPleX) and the polymer-based platform from FhG-HHI (PolyBoard). In this section, we describe our work on a fully integrated LDV system that leverages hybrid integration of these two platforms into a single photonic chip. The hybrid PIC supports all essential functionalities of a heterodyne LDV system, including splitting the input light into measurement and reference paths, introducing an optical frequency shift to the one path, managing polarization, and detecting the reflected measurement beam. The optical frequency shift is implemented in the TriPleX section using a serrodyne modulation scheme, where a phase modulator is driven by a 100 kHz sawtooth waveform (see paragraph 1.3.3.1). The modulation of the optical field is based on the stress-optic modulators implemented on the TriPleX platform (see paragraph 1.3.2). The PolyBoard section provides polarization control and heterodyne detection of the reflected beam. It integrates on-chip micro-optic components including a polarization beam splitter (PBS), a half-wave plate (HWP), and a pair of balanced detectors composed of four flip-chip bonded InP-based photodiodes. An additional pair of monitor PDs are used to track the optical modulation. Optical I/O to the chip is facilitated by fiber arrays edge-coupled to both TriPleX and PolyBoard sections, where in the TriPleX side, tapers structures are used for efficient fiber coupling. The schematic of the circuit is shown in Figure 1.26.

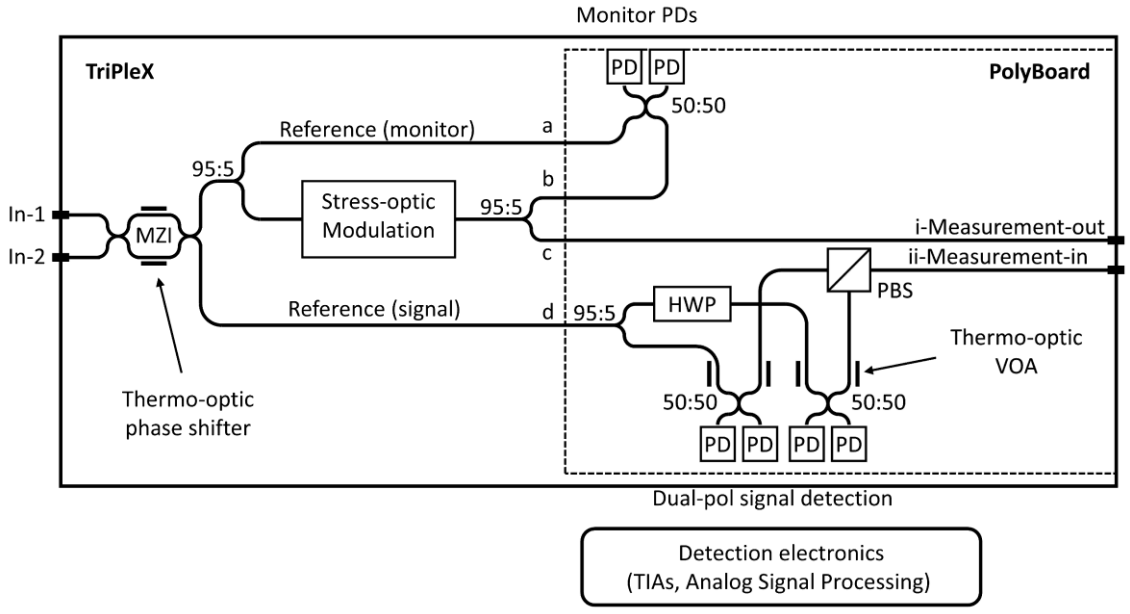

Figure 1.26: Functional layout of the fully integrated LDV module. Interfaces between the TriPleX and the PolyBoard are labeled with a-d.

1.6.1 Integration concept

PolyBoard waveguides can be fabricated on nearly any flat substrate capable of supporting the spin-coating techniques used for polymer layer deposition. Owing to this versatility, a TriPleX wafer can be employed as the process substrate for the realization of PolyBoard circuits. The TriPleX and PolyBoard platforms are inherently compatible, as both utilize silicon wafers as their mechanical foundation. Our goal was to combine the two platforms with a wafer-level process to reduce the complexity and cost of the assembly. The hybrid integration concept is illustrated in Figure 1.27. The TriPleX platform facilitates the integration of the PZT-based modulators, while the PolyBoard platform accommodates the thin-film filters (TFFs) in etched slots, the 45° mirrors and the InP-based PDs to support the dual-pol detection as described in section 1.4.

To enable the integration of optical circuits from the TriPleX and PolyBoard platforms, efficient optical coupling between the two must be established. For this purpose, vertical couplers are employed. On the TriPleX side, the asymmetric double stripe (ADS) waveguide geometry is used, as it provides low-loss propagation and supports tight bends at a 1550 nm wavelength due to strong mode confinement. This geometry consists of two Si3N4 stripes, 180 nm (top stripe) and 75 nm (bottom stripe) in height, separated by 100 nm SiO2 cladding layer, as described in paragraph 1.3.2. On the PolyBoard side, the standard 3.2 µm height and 3.2 µm width waveguide is employed. Efficient coupling requires effective index matching between the TriPleX and PolyBoard waveguides. Since the ADS geometry exhibits a higher effective index than the PolyBoard waveguide, the top

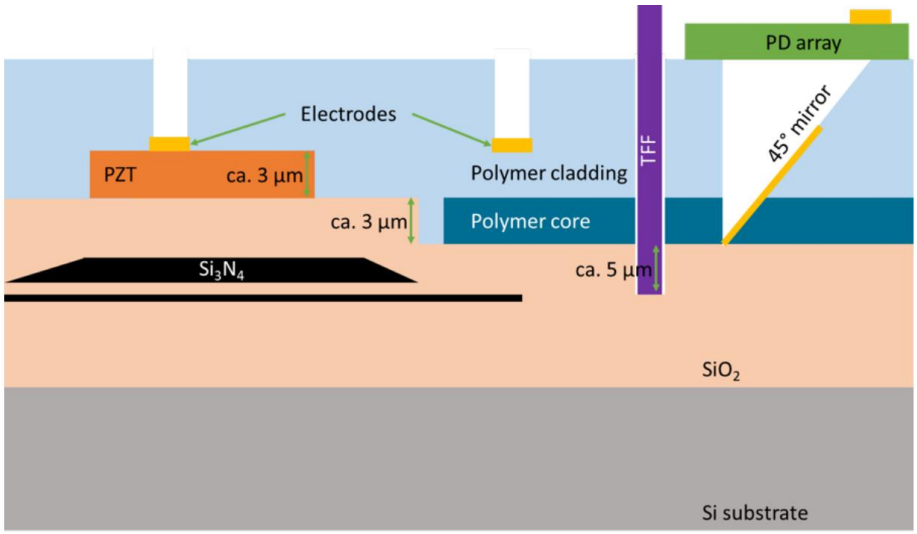

Figure 1.27: Longitudinal cross section summarizing the technologies used in the TriPleX and the PolyBoard platform.

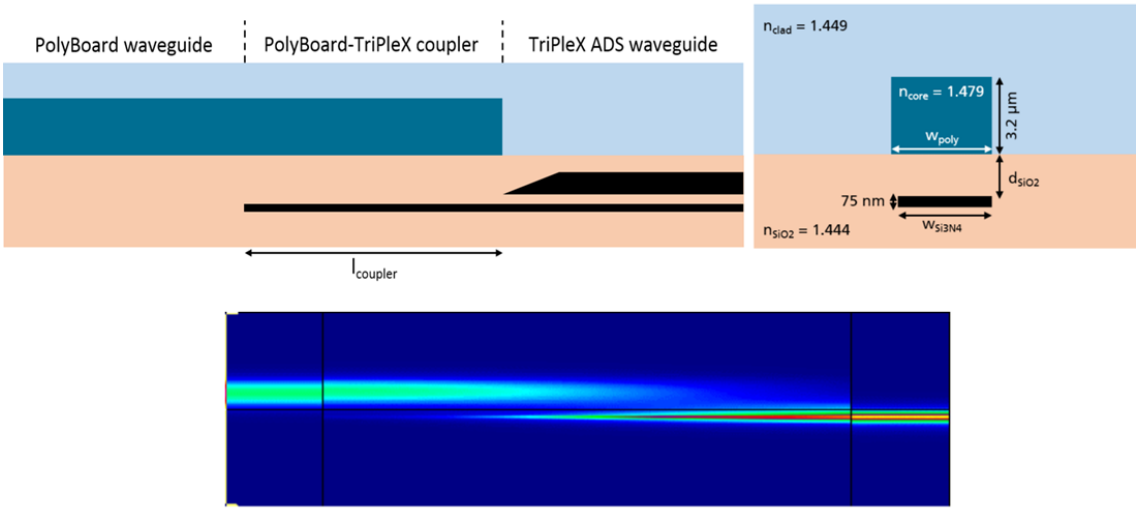

Figure 1.28: (Left) Longitudinal and (Right) lateral cross section of the TriPleX-PolyBoard coupler. (Bottom) Color-coded light intensity in the coupling region (longitudinal cross section).

high-contrast stripe is adiabatically tapered to zero, allowing only the lower-contrast bottom stripe to couple light into the PolyBoard waveguide. The vertical coupler geometry was optimized analytically, with the key parameters being the TriPleX waveguide width w_{Si3N4}, the SiO2 spacer thickness d_{SiO2} between the two waveguides, and the overlapping length $I_{coupler}$, as illustrated in Figure 1.28. The optimal parameters, as derived from simulations, are summarized in Table 3. In this design, the PolyBoard waveguide width remains identical to the standard value for this refractive index contrast, while the TriPleX waveguides are laterally tapered to 2.6 µm and the SiO thickness is set to 750 nm. At a coupler length of 71.8 µm, simulations predict a coupling loss of only 0.3 dB for TE polarization. TM polarization is not considered, as the TriPleX waveguides are specifically optimized for TE-polarized light. Finally, it should be noted that the top Si3N4 stripe is also tapered down to zero in the regions requiring edge coupling to the fiber, so that only the bottom Si3N4 stripe remains to match the 9-µm mode field diameter (MFD) of the fiber.

Design parameter	Symbol	Value (µm)
PolyBoard waveguide width	w_{poly}	3.2
TriPlex waveguide width	w_{Si3N4}	2.6
Silicon dioxide thickness	d_{SiO2}	0.75
Coupler length	$I_{coupler}$	71.8

Table 3: Optimal design parameters of TriPleX-PolyBoard couplers.

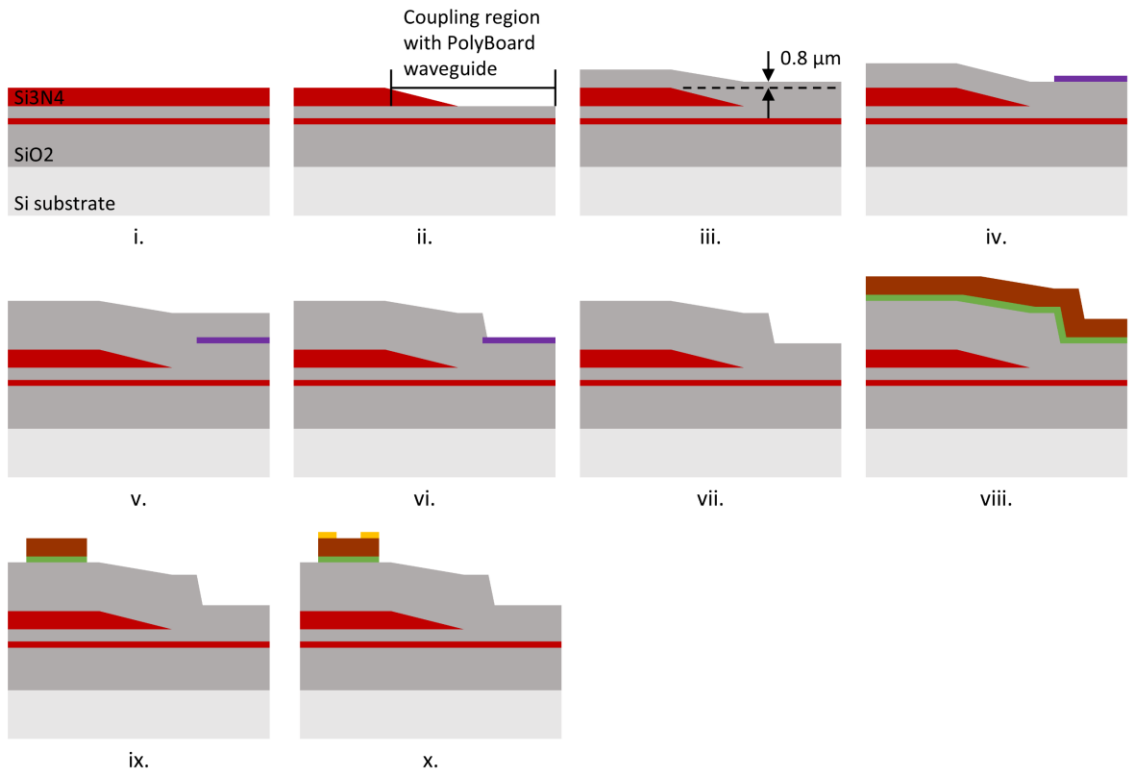

Figure 1.29: Process steps for fabrication of TriPleX PIC. An etching stopper (purple) was used to enable precise control of the etching in the coupling region with the PolyBoard.

Efficient evanescent coupling between PolyBoard and TriPleX waveguides requires an intermediate oxide layer of approximately 0.75 µm between the two platforms. Conversely, to integrate the PZT layer for the stress-optic modulators described in section 1.3.2, while minimizing propagation loss, a SiO2 top cladding layer of roughly 3 µm is required above the high-contrast top stripe of the TriPleX waveguides. This necessitates precise control of the SiO2 top cladding thickness in the vertical coupling regions. A well-defined oxide thickness for the coupling zone with the PolyBoard can be achieved across the entire TriPleX wafer by introducing a selective etch stop. The process is illustrated in Figure 1.29. After defining the buried stop layer (Figure 1.29 (iv)), a 3.3 µm-thick SiO2 layer is deposited using a TEOS LPCVD process. Subsequent annealing at 1150 °C reduces the thickness by approximately 10%, resulting in a final thickness of about 3 µm on top of the TriPleX structure after deposition and back-thinning (Figure 1.29 (v)). A new etching mask, which is an inverted replica of the etch-stop mask, is then used to selectively remove excess oxide from the PolyBoard coupling region. Following lithography, the oxide is dry etched to a depth of about 2.2 µm, stopping precisely at the buried stop layer, leaving the required 0.8 µm thickness (Figure 1.29 (vi)). The stop layer is then selectively removed without etching the underlying SiO2 (Figure 1.29 (vii)). Next, a PZT layer is deposited via PLD,

using a barium titanate (BTO) seeding layer to promote high-quality growth on the SiO2 surface (Figure 1.29 (viii)), following a process optimized by SolMateS [51]. A wet etch step removes the BTO/PZT layers from unwanted regions of the wafer, so that the stress-optic modulators can be formed (Figure 1.29 (ix)). Lift-off lithography is then employed to deposit a Ti (20 nm) / Pt (40 nm) / Au (300 nm) metal stack by evaporation, defining the coarse electrode layout. Due to limitations in the minimum feature size achievable with lift-off, a second etching step, using RIBE, is performed to narrow the electrodes from 20 µm to 5 µm, a critical adjustment for the electrodes above the PZT actuators (Figure 1.29 (x)).

The key fabrication steps of the PolyBoard-on-TriPleX platform are illustrated in Figure 1.29: (i) The process begins with a pre-structured TriPleX wafer obtained from the process described above (see Figure 1.29). (ii) A thick polymer waveguide layer is deposited onto the wafer; this layer is significantly thicker than the final waveguide height to fully cover the TriPleX structures. (iii) PolyBoard waveguides are defined by lithography and dry etching. The titanium etch mask used for patterning is subsequently removed with hydrofluoric acid. To protect the PZT structures from hydrofluoric acid, all TriPleX features must remain covered by the polymer layer during this step. (iv) The polymer waveguide is then dry etched to its final height, thereby exposing the TriPleX structures. (v) A thick cladding polymer layer is deposited, transferring the underlying TriPleX topography to the cladding surface. (vi) The polymer surface is planarized to reduce this topography. (vii) The cladding is dry etched down to the TriPleX electrodes, after which electrodes are deposited on the PolyBoard layer. (viii) An additional cladding polymer layer is deposited. (ix) Openings for electrode pads and slots are dry etched, and the PolyBoard electrodes are reinforced by galvanic deposition. (x) The titanium mask for the slots is removed, and the polymer stack is thinned until the slots reach the underlying SiO2 surface. (xi) Finally, the slots are further etched into the SiO2 using a different dry etching chemistry. The fabricated wafer, after completion of all steps, is shown in Figure 1.31. Subsequent back-end processes, including singulation, photodetector attachment, and insertion of TFFs, were performed by FhG-HHI. Fiber array units were then attached to the diced chips, and initial PZT performance tests were conducted by LioniX. The complete assembly and packaging of the module were carried out by Cordon Electronics.

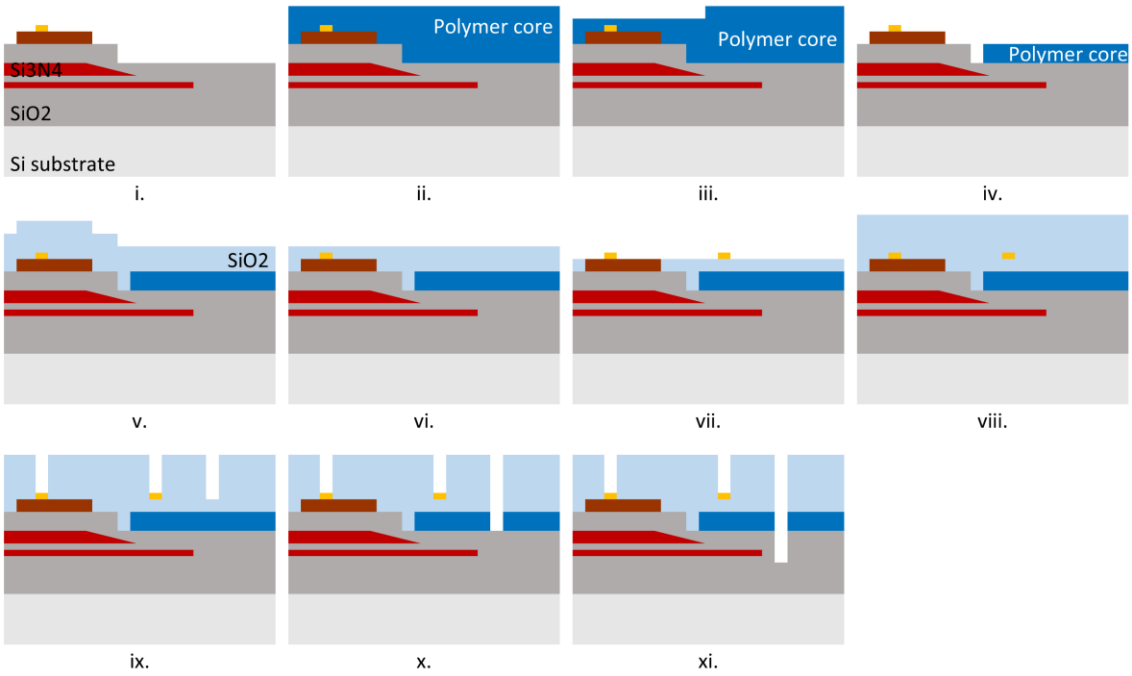

Figure 1.30: Fabrication steps for the integration of PolyBoard on top of TriPleX.

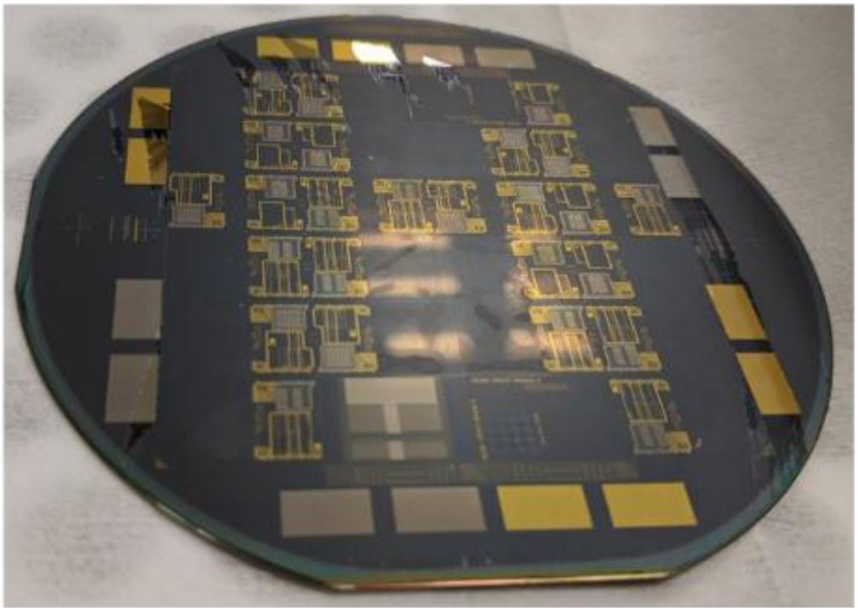

Figure 1.31: Photograph of the first wafer realizing TriPleX-PolyBoard hybrid integration.

1.6.2 Experimental results

The fabricated device was evaluated by applying a sawtooth driving signal to the stress-optic PZT modulator in order to demonstrate serrodyne optical frequency shifting. The coherent detection circuit integrated in the module enabled observation of the on-chip beating between the frequency-shifted carrier and an optical reference, as illustrated in Figure 1.32. For the experiments, a narrow-linewidth CW laser source delivered 10 dBm of optical power at 1550.12 nm, which was coupled into the TriPleX section of the LDV module via a single-mode fiber and a polarization controller (PC) [57]. Optical in- and out-coupling were facilitated by two fiber-array units (FAUs) attached to the east and west facets of the chip. As shown schematically in Figure 1.26, an on-chip Mach–Zehnder interferometer (MZI) divides the input signal into a measurement path and a reference path. The reference branch is routed to the PolyBoard section for coherent detection, while the measurement branch passes through the stress-optic PZT modulator, which introduces the serrodyne frequency shift. A 100 kHz sawtooth waveform was applied to the PZT elements to generate the shift. The frequency-shifted light at the device output was then fed back into the measurement input of the dual-polarization coherent detection circuit in the PolyBoard region. By adjusting the PC, the launched optical field could be switched between the fast and slow axes of the integrated PBS, corresponding to the two orthogonal polarization states in the dual-pol scheme. The photocurrents from the on-chip detectors were amplified by dedicated analog electronics and monitored in the time domain with a real-time oscilloscope. The measured optical output power was −8.5 dBm, corresponding to an overall insertion loss of 18.5 dB. This includes FAU coupling losses, propagation losses in

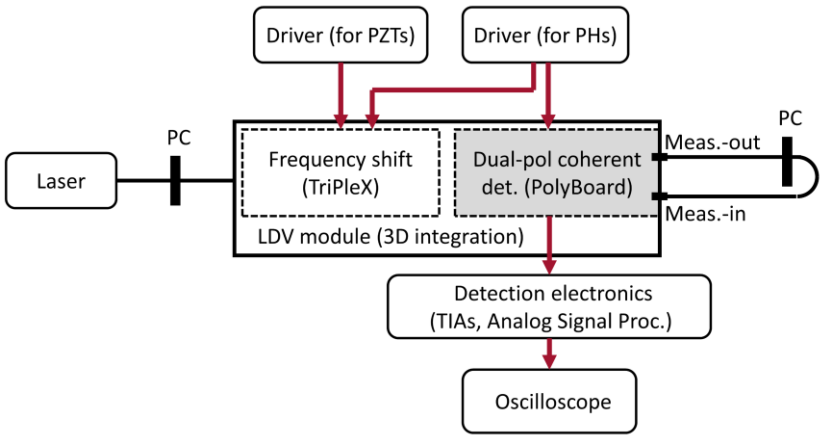

Figure 1.32: Displacement spectrum from a loudspeaker using 10 kHz excitation. The two channels correspond to the two independent polarization channels and carry the same information. The achievable displacement resolution is below 10 pm.

both TriPleX and PolyBoard waveguides, and the coupling loss introduced by the vertical couplers. Independent test structures indicate that the latter contributes < 1 dB, while the combined propagation and coupling losses of the individual platforms remain below 6 dB. The excess loss is attributed mainly to misalignment between the two integrated platforms, highlighting the need for further refinement of the alignment and fabrication procedure to ensure reproducibility in the 3D integration process.

Figure 1.33 shows the applied sawtooth driving waveform together with the detected signals for the case where all optical power is aligned to the fast-axis polarization of the PBS. A linear voltage ramp from 0 to 100 V, generated by a custom driver, was applied to two cascaded stress-optic PZT phase shifters in order to achieve a full 2π optical phase shift. The interference between the frequency-shifted carrier and the optical reference produced a sinusoidal signal, whose frequency corresponds to the applied frequency shift of 100 kHz and thus acts as the carrier. If vibration-induced modulation were present on the measurement path, it would appear as a phase modulation superimposed on this sinusoid. The measured beating signal also reveals a phase discontinuity, originating from the finite fall time of the sawtooth drive. This discontinuity effectively introduces an inverted modulation during the falling edge, as discussed in 1.3.3.1. Ideally, the fall time should be negligible compared to the modulation period. In our experiment, the fall time accounts for approximately 6% of the period, which results in harmonic sidebands appearing about 23 dB below the fundamental tone according to our analysis in 1.3.1.1.

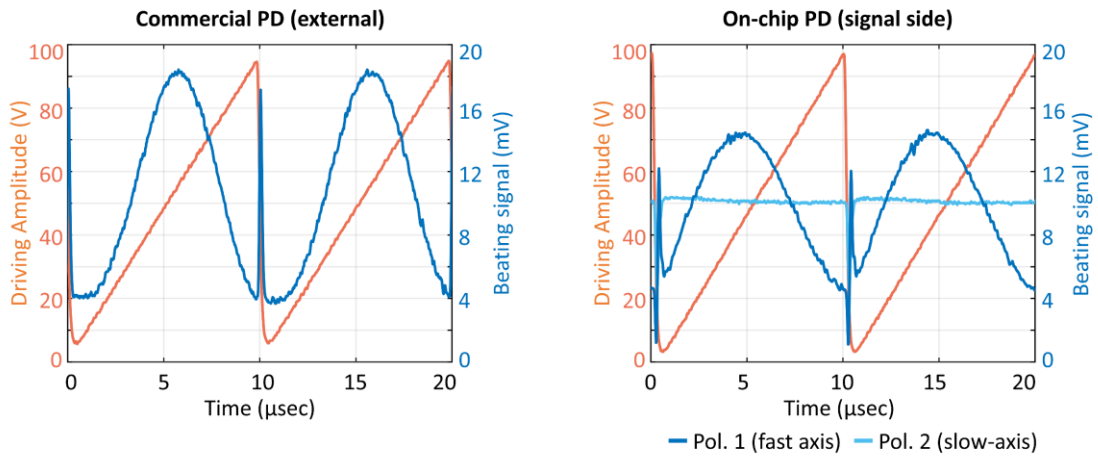

Figure 1.33: Measurement of the beating signal (blue) obtained after combining the modulated and the reference beam. Measurements were taken using (Left) a commercial external photodetector and (Right) the on-chip photodetectors. The ramp driving signal of the PZT-based serrodyne optical frequency shifter is shown (orange).

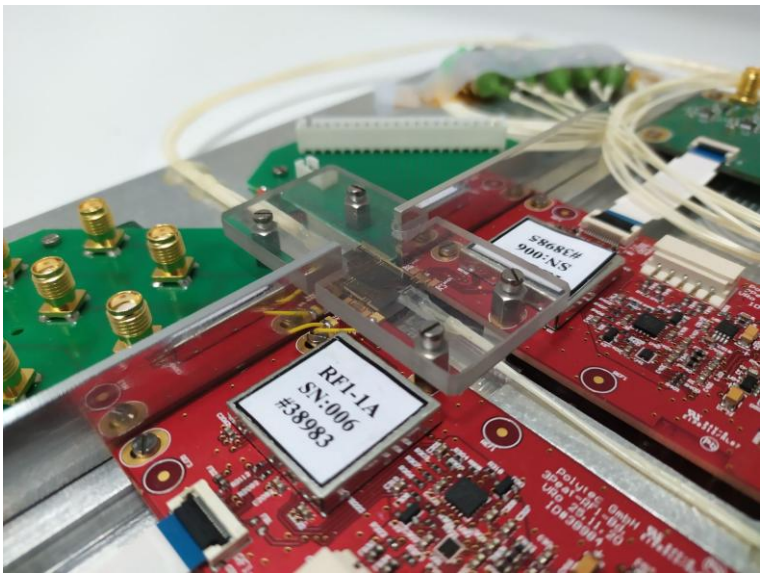

Figure 1.34: Assembly of the 3D photonic integrated LDV PIC.

1.7Summary

In this part we worked towards the development of a PIC-based heterodyne LDV system, with an emphasis on the implementation of optical frequency shift in the silicon nitride platform of LioniX. The frequency shifting was realized through stress-optic index modulation in the TriPleX platform, enabled by piezoelectric actuation of a PZT layer deposited on top of the waveguides and driven via an applied electric field between electrodes. We demonstrated for the first time a top-top electrode configuration, in which both electrodes are positioned on top of the PZT layer to generate a horizontal electric field across it. Regarding device performance, we achieved a sinusoidal phase shift of 0.25π peak-to-peak at 2.5 MHz with a power dissipation of 156 mW, with the best-performing device. The average power consumption across all fabricated modulators was 660 mW for the same induced phase shift. The modulators required relatively long electrodes (~15 mm) and high-voltage drive signals (>100 Vpp), which makes them less competitive compared with LiNbO3 or plasma dispersion modulators in silicon photonics. Nevertheless, achieving MHz-range modulation bandwidth within a wafer-scale SiN process constitutes an important milestone toward the development of large-scale optical circuits incorporating multiple integrated modulators, with potential applications in multi-channel sensing and microwave photonics. Further enhancement of modulation efficiency can be pursued by optimizing stress distribution within the waveguide geometry and by improving PZT

material quality, particularly crystal uniformity and piezoelectric response. A key benefit of the top-top electrode layout compared with the conventional top-bottom design is that it enables the PZT thickness to be increased without reducing the effective field density. This flexibility allows independent optimization of PZT thickness, potentially leading to higher stress-optic efficiency and lower power consumption.

We have demonstrated optical frequency shift (OFS) of a 1550 nm carrier in the MHz regime, employing stress-optic phase modulation. Theoretical analysis was performed to evaluate the performance of both serrodyne and single-sideband (SSB) OFS schemes, highlighting their practical limitations in terms of conversion efficiency (CE) and suppression of unwanted sidebands (SBSR). Experimental validation on the TriPleX platform confirmed frequency shifts of 100 kHz and 2.5 MHz, with corresponding SBSR values of 22.1 dB and 39 dB. A major advantage of implementing OFS in TriPleX is its capability for high optical power handling, in contrast to silicon photonics where two-photon absorption imposes a fundamental limitation. The SSB-OFS was integrated into a miniaturized laser Doppler vibrometer (LDV) operating at 1550 nm. Vibration measurements were demonstrated up to 15 kHz, with the system capable of detecting frequencies up to 1 MHz, while maintaining a displacement resolution of 10 pm. Signal detection was performed using a dual-polarization coherent receiver realized in the PolyBoard platform, incorporating InP-based photodiodes. In this proof-of-concept implementation, the TriPleX and PolyBoard PICs were packaged separately and interconnected via fiber arrays. More compact solutions are possible, either by hybrid edge-coupling of the two units or by adopting wafer-level 3D integration methods for monolithic assembly. Furthermore, the TriPleX platform supports hybrid integration of semiconductor laser sources with ultra-narrow spectral linewidths [57], providing a promising route towards fully integrated, on-chip light generation.

A novel approach for 3D hybrid integration of the silicon nitride (TriPleX) and polymer (PolyBoard) platform into single 3D-PICs was presented, where the polymer material is placed inside etched windows on TriPleX. With this approach a fully integrated heterodyne LDV module was realized, comprising an optical frequency shifter (OFS) and on-chip polarization handing elements for dual-pol coherent detection. Serrodyne frequency shift of 100 kHz based on stress-optic modulation in TriPleX was demonstrated, showcasing the potential for real-world LDV applications. Although the measured coupling loss between the two platforms was in the order of 15 dB, simulation results suggest that the losses can

be minimized to < 1 dB with the corresponding improvements in the fabrication process. We have demonstrated that the stress-optic modulators of the current work can be successfully integrated in a fully functional LDV system that allows the measurement of vibration frequencies at least two orders of magnitude higher from what is possible with the conventional thermo-optic phase shifters of the SiN platform. The realization of efficient OFS functionality in the SiN platform with a wafer-scale process is a significant achievement, as it can open the way to the combination of heterodyne interferometric principles and solid-state scanning units (such as OPAs) through monolithic integration, enabling low-cost and compact sensor systems.

References

[1] Y. Li, E. Dieussaert, and R. Baets, “Miniaturization of Laser Doppler Vibrometers—A Review,” Sensors, vol. 22, no. 13, p. 4735, Jun. 2022, doi: 10.3390/s22134735.

[2] S. J. Rothberg et al., “An international review of laser Doppler vibrometry: Making light work of vibration measurement,” Opt. Lasers Eng., vol. 99, pp. 11–22, Dec. 2017, doi: 10.1016/j.optlaseng.2016.10.023.

[3] J. Yang, T. Yang, Z. Wang, D. Jia, and C. Ge, “A Novel Method of Measuring Instantaneous Frequency of an Ultrafast Frequency Modulated Continuous-Wave Laser,” Sensors, vol. 20, no. 14, p. 3834, Jul. 2020, doi: 10.3390/s20143834.

[4] C. Rogers et al., “A universal 3D imaging sensor on a silicon photonics platform,” Nature, vol. 590, no. 7845, pp. 256–261, Feb. 2021, doi: 10.1038/s41586-021-03259-y.

[5] Y. Park and K. Cho, “Heterodyne interferometer scheme using a double pass in an acousto-optic modulator,” Opt. Lett., vol. 36, no. 3, p. 331, Feb. 2011, doi: 10.1364/OL.36.000331.

[6] A. G. Mychkovsky, N. A. Chang, and S. L. Ceccio, “Bragg cell laser intensity modulation: effect on laser Doppler velocimetry measurements,” Appl. Opt., vol. 48, no. 18, p. 3468, Jun. 2009, doi: 10.1364/AO.48.003468.

[7] H. Toda, M. Haruna, and H. Nishihara, “Integrated-optic heterodyne interferometer for displacement measurement,” J. Lightwave Technol., vol. 9, no. 5, pp. 683–687, May 1991, doi: 10.1109/50.79546.

[8] Y. Li, S. Meersman, and R. Baets, “Optical frequency shifter on SOI using thermo-optic serrodyne modulation,” in 7th IEEE International Conference on Group IV Photonics, Beijing, China, Sep. 2010, pp. 75–77. doi: 10.1109/GROUP4.2010.5643423.

[9] Y. Li et al., “Heterodyne laser Doppler vibrometers integrated on silicon-on-insulator based on serrodyne thermo-optic frequency shifters,” Appl. Opt., vol. 52, no. 10, p. 2145, Apr. 2013, doi: 10.1364/AO.52.002145.

[10] D. B. Cole, C. Sorace-Agaskar, M. Moresco, G. Leake, D. Coolbaugh, and M. R. Watts, “Integrated heterodyne interferometer with on-chip modulators and detectors,” Opt. Lett., vol. 40, no. 13, p. 3097, Jul. 2015, doi: 10.1364/OL.40.003097.

[11] Y. Li, E. Dieussaert, and R. Baets, “Miniaturization of Laser Doppler Vibrometers—A Review,” Sensors, vol. 22, no. 13, p. 4735, Jun. 2022, doi: 10.3390/s22134735.

[12] M. Izutsu, S. Shikama, and T. Sueta, “Integrated optical SSB modulator/frequency shifter,” IEEE J. Quantum Electron., vol. 17, no. 11, pp. 2225–2227, Nov. 1981, doi: 10.1109/JQE.1981.1070678.

[13] S. Shimotsu et al., “Single side-band modulation performance of a LiNbO 3 integrated modulator consisting of four-phase modulator waveguides,” IEEE Photonics Technol. Lett., vol. 13, no. 4, pp. 364–366, Apr. 2001, doi: 10.1109/68.917854.

[14] H. Yamazaki, T. Saida, T. Goh, A. Mori, and S. Mino, “Dual-carrier IQ modulator with a complementary frequency shifter,” Opt. Express, vol. 19, no. 26, p. B69, Dec. 2011, doi: 10.1364/OE.19.000B69.

[15] A. Kodigala et al., “Silicon Photonic Single-Sideband Generation with Dual-Parallel Mach-Zehnder Modulators,” in Conference on Lasers and Electro-Optics, San Jose, California, 2019, p. STh4N.6. doi: 10.1364/CLEO_SI.2019.STh4N.6.

[16] G. M. Hasan, M. Hasan, and T. J. Hall, “Performance Analysis of a Multi-Function Mach-Zehnder Interferometer Based Photonic Architecture on SOI Acting as a Frequency Shifter,” Photonics, vol. 8, no. 12, p. 561, Dec. 2021, doi: 10.3390/photonics8120561.

[17] K. Alexander et al., “Nanophotonic Pockels modulators on a silicon nitride platform,” Nat Commun, vol. 9, no. 1, p. 3444, Dec. 2018, doi: 10.1038/s41467-018-05846-6.

[18] M. Lauermann et al., “Integrated optical frequency shifter in silicon-organic hybrid (SOH) technology,” Opt. Express, vol. 24, no. 11, p. 11694, May 2016, doi: 10.1364/OE.24.011694.

[19] G. T. Reed et al., “Recent breakthroughs in carrier depletion based silicon optical modulators,” Nanophotonics, vol. 3, no. 4–5, pp. 229–245, Aug. 2014, doi: 10.1515/nanoph-2013-0016.

[20] T. Spuesens et al., “Integrated Optical Frequency Shifter on a Silicon Platform,” in Conference on Lasers and Electro-Optics, San Jose, California, 2016, p. SF2G.1. doi: 10.1364/CLEO_SI.2016.SF2G.1.

[21] Y. Yamaguchi, A. Kanno, T. Kawanishi, M. Izutsu, and H. Nakajima, “Pure Single-Sideband Modulation Using High Extinction-Ratio Parallel Mach-Zehnder Modulator with Third-Order Harmonics Superposition Technique,” in CLEO: 2015, San Jose, California: OSA, 2015, p. JTh2A.40. doi: 10.1364/CLEO_AT.2015.JTh2A.40.

[22] A. Rubiyanto, H. Herrmann, R. Ricken, F. Tian, and W. Sohler, “Integrated optical heterodyne interferometer in lithium niobate,” J. Nonlinear Optic. Phys. Mat., vol. 10, no. 02, pp. 163–168, Jun. 2001, doi: 10.1142/S0218863501000516.

[23] P. Edinger et al., “Silicon photonic microelectromechanical phase shifters for scalable programmable photonics,” Opt. Lett., vol. 46, no. 22, p. 5671, Nov. 2021, doi: 10.1364/OL.436288.

[24] W. Jin, R. G. Polcawich, P. A. Morton, and J. E. Bowers, “Piezoelectrically tuned silicon nitride ring resonator,” p. 14, 2018.

[25] M. Huang, “Stress effects on the performance of optical waveguides,” International Journal of Solids and Structures, vol. 40, no. 7, pp. 1615–1632, Apr. 2003, doi: 10.1016/S0020-7683(03)00037-4.

[26] S. Donati, L. Barbieri, and G. Martini, “Piezoelectric actuation of silica-on-silicon waveguide devices,” IEEE Photon. Technol. Lett., vol. 10, no. 10, pp. 1428–1430, Oct. 1998, doi: 10.1109/68.720283.

[27] K. K. Tsia, S. Fathpour, and B. Jalali, “Electrical tuning of birefringence in silicon waveguides,” Appl. Phys. Lett., vol. 92, no. 6, p. 061109, Feb. 2008, doi: 10.1063/1.2883925.

[28] Y. Sebbag et al., “Bistability in silicon microring resonator based on strain induced by a piezoelectric lead zirconate titanate thin film,” Appl. Phys. Lett., vol. 100, no. 14, p. 141107, Apr. 2012, doi: 10.1063/1.3701587.

[29] C. Schriever, C. Bohley, J. Schilling, and R. B. Wehrspohn, “Strained Silicon Photonics,” Materials, vol. 5, no. 12, pp. 889–908, May 2012, doi: 10.3390/ma5050889.

[30] N. Hosseini et al., “Stress-optic modulator in TriPleX platform using a piezoelectric lead zirconate titanate (PZT) thin film,” Opt. Express, vol. 23, no. 11, p. 14018, Jun. 2015, doi: 10.1364/OE.23.014018.

[31] J. P. Epping et al., “Ultra-low-power stress-optics modulator for microwave photonics,” presented at the SPIE OPTO, San Francisco, California, United States, Feb. 2017, p. 101060F. doi: 10.1117/12.2266170.

[32] J. P. Epping et al., “Ultra-low-power stress-based integrated photonic phase actuator,” p. 3, 2018.

[33] A. Everhardt et al., “Ultra-low power stress-based phase actuation in TriPleX photonic circuits,” in Integrated Optics: Devices, Materials, and Technologies XXVI, San Francisco, United States, Mar. 2022, p. 11. doi: 10.1117/12.2609405.

[34] F. Casset et al., “Stress optic modulator using thin-film PZT for LIDAR applications,” in 2019 IEEE SENSORS, Montreal, QC, Canada: IEEE, Oct. 2019, pp. 1–4. doi: 10.1109/SENSORS43011.2019.8956537.

[35] J. Wang, K. Liu, M. W. Harrington, R. Q. Rudy, and D. J. Blumenthal, “Silicon nitride stress-optic microresonator modulator for optical control applications,” Opt. Express, vol. 30, no. 18, p. 31816, Aug. 2022, doi: 10.1364/OE.467721.

[36] P. J. M. van der Slot, M. A. G. Porcel, and K.-J. Boller, “Surface acoustic waves for acousto-optic modulation in buried silicon nitride waveguides,” Opt. Express, vol. 27, no. 2, p. 1433, Jan. 2019, doi: 10.1364/OE.27.001433.

[37] I. Ansari et al., “Light modulation in Silicon photonics by PZT actuated acoustic waves,” ArXiv211207988 Phys., Dec. 2021, Accessed: Jan. 30, 2022. [Online]. Available: http://arxiv.org/abs/2112.07988

[38] https://www.lionix-international.com/forms/triplex-silicon-nitride-whitepaper/

[39] C. Tsokos et al., “True Time Delay Optical Beamforming Network Based on Hybrid Inp-Silicon Nitride Integration,” J. Lightwave Technol., vol. 39, no. 18, pp. 5845–5854, Sep. 2021, doi: 10.1109/JLT.2021.3089881.

[40] M. D. Nguyen, R. Tiggelaar, T. Aukes, G. Rijnders, and G. Roelof, “Wafer-scale growth of highly textured piezoelectric thin films by pulsed laser deposition for micro-scale sensors and actuators,” J. Phys. Conf. Ser., vol. 922, p. 012022, Nov. 2017, doi: 10.1088/1742-6596/922/1/012022.

[41] M. D. Nguyen, E. P. Houwman, M. Dekkers, and G. Rijnders, “Strongly Enhanced Piezoelectric Response in Lead Zirconate Titanate Films with Vertically Aligned Columnar Grains,” ACS Appl. Mater. Interfaces, vol. 9, no. 11, pp. 9849–9861, Mar. 2017, doi: 10.1021/acsami.6b16470.

[42] D. de Felipe et al., “Recent Developments in Polymer-Based Photonic Components for Disruptive Capacity Upgrade in Data Centers,” J. Light. Technol., vol. 35, no. 4, pp. 683–689, Feb. 2017, doi: 10.1109/JLT.2016.2611240.

[43] Z. Zhang et al, “Hybrid Photonic Integration on a Polymer Platform,” MDPI Photonics, Vol. 2, Issue 3, pp. 1005-1026, Sept. 2015.

[44] V. Katopodis et al., “Multi-Flow Transmitter Based on Polarization and Optical Carrier Management on Optical Polymers,” IEEE Photonics Technology Letters, vol. 28, no. 11, pp. 1169-1172, June 2016.

[45] V. Katopodis et al, “Polymer enabled 100 Gbaud connectivity for datacom applications,” Elsevier Optics Communications, Vol. 362, pp. 13-21, March 2016.

[46] M. Johansmann, G. Siegmund, and M. Pineda, “Targeting the Limits of Laser Doppler Vibrometry” 2005.

[47] G. Siegmund, “Sources of measurement error in laser Doppler vibrometers and proposal for unified specifications,” presented at the Eighth International Conference on Vibration Measurements by Laser Techniques: Advances and Applications, Ancona, Italy, Jun. 2008, p. 70980Y. doi: 10.1117/12.803150.

[48] Y. Li, S. Meersman, and R. Baets, “Realization of fiber-based laser Doppler vibrometer with serrodyne frequency shifting,” Appl. Opt., vol. 50, no. 17, p. 2809, Jun. 2011, doi: 10.1364/AO.50.002809.

[49] L. M. Johnson and C. H. Cox, “Serrodyne optical frequency translation with high sideband suppression,” J. Light. Technol., vol. 6, no. 1, pp. 109–112, Jan. 1988, doi: 10.1109/50.3974.

[50] C. G. H. Roeloffzen et al., “Low-Loss Si3N4 TriPleX Optical Waveguides: Technology and Applications Overview,” IEEE J. Sel. Top. Quantum Electron., vol. 24, no. 4, pp. 1–21, Jul. 2018, doi: 10.1109/JSTQE.2018.2793945.

[51] Solmates B.V., website: http://www.solmates-pld.com

[52] D. H. A. Blank, M. Dekkers, and G. Rijnders, “Pulsed laser deposition in Twente: from research tool towards industrial deposition,” J. Phys. Appl. Phys., vol. 47, no. 3, p. 034006, Jan. 2014, doi: 10.1088/0022-3727/47/3/034006.

[53] M. Kleinert et al., “Photonic integrated devices and functions on hybrid polymer platform,” presented at the SPIE OPTO, San Francisco, California, United States, Feb. 2017, p. 100981A. doi: 10.1117/12.2256987.

[54] A. Maese-Novo et al., “Thermally optimized variable optical attenuators on a polymer platform,” Appl. Opt., vol. 54, no. 3, p. 569, Jan. 2015, doi: 10.1364/AO.54.000569.

[55] Polytec GmbH., website: https://www.polytec.com/

[56] M. Dekkers et al., “The significance of the piezoelectric coefficient d 31,eff determined from cantilever structures,” J. Micromechanics Microengineering, vol. 23, no. 2, p. 025008, Feb. 2013, doi: 10.1088/0960-1317/23/2/025008.

[57] K.-J. Boller *et al.*, “Hybrid Integrated Semiconductor Lasers with Silicon Nitride Feedback Circuits,” *Photonics*, vol. 7, no. 1, p. 4, Dec. 2019, doi: 10.3390/photonics7010004.

Part 2

Polymer-based Optical Phased Arrays

In this part, we present our work on the development of optical phased arrays (OPAs) in the polymer-based photonic integration platform of the Heinrich Hertz Institute (HHI). Our key concept involves utilizing the 3D integration capability of polymeric materials to form two-dimensional (2D) edge-emitting OPAs for achieving 2D beam steering. To validate this concept, a 2×4 OPA was realized and experimentally tested. To the best of our knowledge, this work represents the first 3D photonic integrated edge-emitting OPA with monolithic integration of the tuning section. Furthermore, we explore the potential of non-uniform element spacing in linear OPAs to suppress grating lobes and enhance the field of view (FOV). We also investigate algorithms for phase calibration of the fabricated OPA chips and present our findings.

2.1Introduction

Optical phased arrays (OPAs) have attracted significant research interest over the past decade for two main reasons. Firstly, emerging applications such as light detection and ranging (LiDAR), optical wireless communications (OWC), holographic displays, and biomedical imaging have created a demand for compact and cost-effective beam scanning devices. Most current devices rely on opto-mechanical components, such as moving mirrors, to direct beams in various directions. These mechanical parts are bulky, expensive, and prone to wear and tear, making them unsuitable for integration into moving vehicles such as cars or drones due to their mass and mechanical complexity. Moreover, the scanning speed and precision of those devices are limited by the mass of their moving components. Contrarily, OPAs can perform beam steering without the need for moving parts, by utilizing an array of coherent emitters and adjusting their phases electronically. Thus, they offer the possibility for dramatic reduction in size, weight, power consumption and cost (SWaP-C). The second reason for OPAs' gaining popularity in recent years is the progress of photonic integration technology. Advancements in the fabrication and packaging of photonic integrated circuits (PICs), largely driven by the datacom market, have paved the way for the creation of more sophisticated circuits and their seamless

integration with electronic ICs. These innovations have led to the development of highly functional devices for real-world applications.

2.1.1 Fabrication platforms

OPAs have been implemented on nearly every existing photonic integration platform, each characterized by its own benefits and shortcomings. Relevant features to consider for the implementation of an OPA circuit, include: i) the integration density of the platform (component footprint, minimum bending radius, etc.), ii) the index contrast of the platform, which affects the outcoupling beam divergence, iii) the phase modulation technology (tuning speed, power consumption), iv) the propagation loss (associated with circuit scalability) and v) the coupling to fiber loss (interfacing), vi) the optical power handling capability, vii) the possibility for hosting active components for light generation and amplification (monolithically or via hybrid integration), and viii) the compatibility of the platform with CMOS foundries (CMOS compatibility). In the present paragraph, we briefly discuss some of the frequently used platforms for demonstrating OPAs in literature. It should be noted that this paragraph does not attempt to provide a comprehensive analysis or comparison of fabrication platforms. Instead, it aims to highlight the diversity of available options and emphasize the fact that the responsibility of selecting the appropriate platform for a particular application lies with the designer, based on the specific requirements of the application.

Silicon on insulator (SOI) has been the most prevalent platform for the realization of large-scale OPAs, due to its high integration density and its compatibility with the mature CMOS fabrication process. First demonstrations took place in the beginning of the previous decade, comprising a few tens of channels [1]-[12], but within a few years, implementations with hundreds [13]-[18], and even thousands [19]-[22] of tunable elements were made possible. A few works also showcase co-integration with driving electronics [9][14][15][20] or hybrid integration with active components utilizing III-V materials [11][12][23]. One limitation of SOI is the significant power consumption of thermo-optic (TO) phase shifters. Typical power efficiency ranges between 20 to 30 mW/π [15][24], although less than 2 mW/π has been achieved with more elaborate heating structures [18]. Minimizing the power consumption of tuning elements is essential for the scalability of OPAs. To address this limitation, and also improve on the actuation response time, alternative phase tuning technologies utilizing electro-optical (EO) mechanisms [5][16] or

opto-electromechanical (OEM) tuning [25]-[27] have been proposed in SOI. However, OEM tuning necessitates a more complex fabrication process, which has not yet reached the maturity level of the simpler and more established thermo-optic devices. On the other hand, EO Si phase shifters based on free-carrier injection or depletion offer high bandwidth and low power consumption. Nonetheless, they introduce significant residual amplitude modulation (RAM) due to the plasma dispersion effect in silicon, which adversely affects the performance of OPAs. Alternatively, EO modulation can be achieved through hybrid integration with III-V materials, though this comes at the cost of a more complex fabrication process [23]. Additional challenges in the SOI platform include managing high optical power levels, typically limited to 20 mW [28], and cost-effective interfacing with optical fibers. Coupling to fibers is accomplished using grating couplers, which increase packaging complexity and typically introduce a coupling loss in the order of a few dB. Another platform, that has gained momentum in recent years is lithium niobate on insulator (LNOI) [29]. Its exceptional electro-optic (EO) properties make it highly attractive for fast scanning applications [30]-[33]. For instance, in [33], LNOI modulators were utilized in an

		Silicon dioxide (Silica)	Silicon photonics (SOI)	Silicon Nitride (Si3N4)	III-V (GaAs, InP)	Lithium niobate (LNOI)	Polymer photonics
Transparency window		0.2-2.7 µm	1.0-3.6 µm	0.4-3.6 µm	0.6-0.9 µm 0.9-1.6 µm	0.3-4.0 µm	0.4-1.6 µm
Integration density		Multiple layers (3D)	***	*	*	*	Multiple layers (3D)
Index contrast (FOV)			***	*	*	*	
Phase tuning	TO	**	**	*	*	*	**
	EO		*		**	***	**
	OEM		*	*			
Propagation loss		**		***			*
Coupling to fibers		**		**			***
Power handling		**		**			***
Light generation & amplification			Hybrid integration	Hybrid integration	***	Hybrid integration	Hybrid integration
CMOS compatibility			***	**	*		

TO: Thermo-optic, EO: Electro-optic, OEM: Opto-electromechanical effect

Table 4: Comparison of photonic integration platforms

OPA to demonstrate nanosecond-scale phase tuning with power consumption on the order of pJ/π. Similar to the SOI platform, optical interfacing in the LNOI platform is facilitated by grating couplers. Fast tuning rates can also be achieved with III-V materials, such as indium phosphide (InP) [34]-[38] or gallium arsenide (GaAs) [39][40]. These typically offer power efficiency in the order of hundreds of μW/π. A notable advantage of platforms based on III-V materials is their ability to support the monolithic integration of active components for on-chip light generation and amplification. Despite these benefits, neither LNOI nor III-V material-based platforms can match the integration density provided by the SOI process. Silicon nitride (SiN) has emerged as a promising alternative to SOI, offering CMOS compatibility and exceptionally low propagation loss [41]. Its wide transparency window makes it suitable for applications in both the near-infrared (NIR) [42]-[44] and visible [45][46] spectral regions. Furthermore, SiN offers high power handling capability due to its inherent lower optical nonlinearity and larger core size compared to SOI. However, it demonstrates relatively poor performance in thermo-optic (TO) tuning due to its low thermo-optic coefficient (TOC) and thermal conductivity, which are both lower than those of silicon. Power consumption of ~30 mW/π and time response of 20 μs have been demonstrated at blue wavelengths (~488 nm) [46], while power efficiency decreases further in the NIR (~40 mW/π at 1550 nm). Consequently, alternative methods have emerged to enable efficient phase tuning. Among the most notable is the use of lead zirconate titanate (PZT) thin films, which leverage refractive index modulation [47][48] or geometric deformation [49] through the stress-optic effect. Although these solutions have demonstrated significant improvements in recent years, substantial effort is still required to meet the industry standards for yield and reliability. Another platform proposed for OPA implementation is silicon dioxide, commonly known as silica, particularly for its ability to create 2D end-fire OPAs by inscribing 3D waveguiding paths within the bulk silica structure [50]. In one of the most interesting efforts, a 4×4 OPA was developed [51], using ultra-fast laser inscription (ULI) method to inscribe the waveguiding paths [52]. Polymer-based photonic circuits also enable the formation of multiple waveguiding layers, offering significant flexibility in design. Furthermore, polymer PICs can incorporate a variety of additional functionalities, making them a compelling option for realizing OPAs. The concept of 3D photonic integration for OPA formation will be described in detail in a subsequent section. The following paragraph will focus on the advantages and limitations of polymer-based photonic integration. Table 4 presents a qualitative comparison of the platforms discussed.

2.1.2 Polymer-based photonic integration

Polymer optical materials are an attractive option for the development of OPAs for several reasons. Firstly, the fabrication of polymer photonic devices utilizes techniques like spin coating and UV lithography, which offer a flexible and cost-effective manufacturing process [53]. This is also the case for PolyBoard, the photonic integration platform of HHI, which is based on commercially available polymer materials from ChemOptics Inc. (ZPU-12 series) and has been utilized in the present work. Because of their simplicity, the same fabrication steps can be repeated to develop 3D PICs which comprise multiple waveguiding layers, as shown in Figure 2.1. To facilitate the transition of light between adjacent waveguiding layers, vertical couplers have been developed on PolyBoard [54]-[57]. Initially envisioned for coupling to multi-core fibers [58] and later for constructing large-scale switching circuits without waveguide crossings [59][60], these 3D PolyBoard PICs represent also a viable solution for implementing 2D OPAs with end-fire waveguides to support two-dimension beam steering. This application of 3D PolyBoard PICs is proposed and evaluated for the first time within this work.

Furthermore, polymer-based platforms support highly efficient thermo-optic devices, due to the inherently high thermo-optic coefficient, ranging from $-1 \times 10^{-4}\,K^{-1}$ to $-3 \times 10^{-4}\,K^{-1}$, and low thermal conductivity (~0.3 W/m/K) of polymer materials [61][62]. The low thermal conductivity contributes to reduced power consumption of polymer TO devices (<10 mW) compared to SOI, but it also results in increased response times (in the order of milliseconds). While thermal confinement benefits power consumption and minimizes thermal crosstalk, it negatively impacts response speed. Therefore, polymer-based thermo-optic devices are suitable candidates in scenarios where tuning speeds of a few kilohertz are sufficient. Although not being explored in this work, the potential of polymer materials for high-speed modulation should not be overlooked. Polymer-based modulators have been extensively studied due to their exceptional electro-optic (EO) properties, offering large modulation bandwidth (>100 GHz) [63]-[65]. However, they face manufacturing challenges, which are still to be resolved to support high-volume production [66]. In order for the material to gain the desirable electro-optic properties alignment of its chromophore dipoles is required. This is achieved through a poling process where an electric field is applied while heating the material to its glass transition temperature. A scalable solution for such post-processing steps is yet to be demonstrated. Additional challenges pose the aging and long-term reliability of such EO

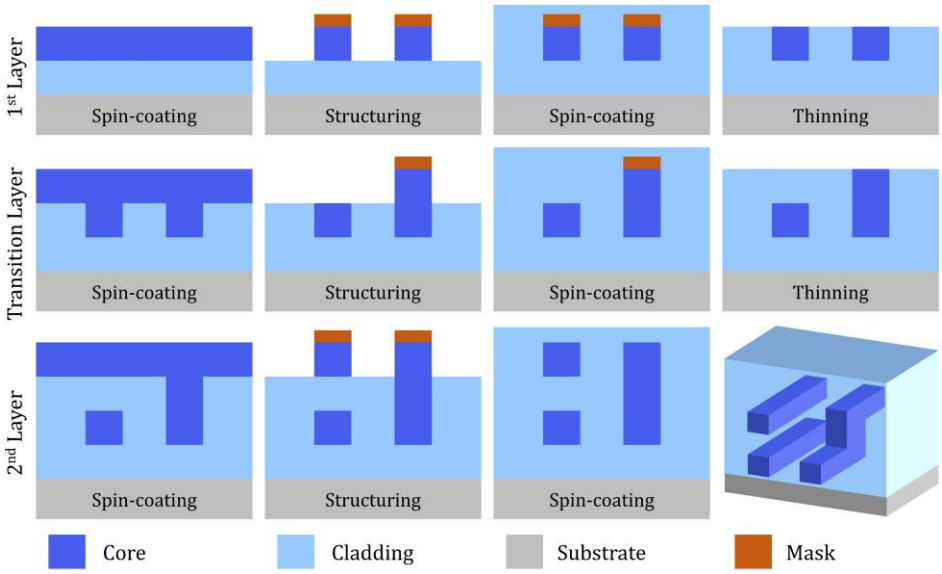

Figure 2.1: Fabrication processing steps for the formation of multiple waveguiding layers in the polymer photonic integration platform. By repeating the same fabrication steps multiple waveguiding layers can be formed. Multi-layer devices such as vertical MMI couplers are used to transfer the light between different waveguiding layers.

devices. Nevertheless, in this work we solely rely on thermo-optic tuning for phase control in the OPAs.

Polymer waveguides exhibit high optical power handling capability. Unlike silicon, which exhibits a strong two-photon absorption (TPA) effect when operating at wavelengths below 2.2 μm, polymeric waveguides do not suffer from TPA. Previous reliability tests in the PolyBoard platform have proven the capability of the waveguides to handle up to 23 dBm (~200 mW) optical power for long periods of time under a wide range of temperature conditions without demonstrating additional propagation loss or refractive index change [53]. In comparison, SOI waveguides struggle to propagate several tens of milliwatts of optical power for more than a few millimeters without significant power degradation due to two-photon absorption [67]. While the performance of rib waveguides is significantly better, they are characterized by a larger bending radius, which compromises the compactness of the routing. Another noteworthy aspect is that polymer platforms, developed during the rise of wavelength division multiplexing (WDM) passive optical networks (PONs), have evolved to encompass a wide range of functionalities. The device portfolio of PolyBoard includes tunable lasers [68], optical isolators [69] and polarization manipulators [59], variable optical attenuators [70], optical switches [60], dual-pol coherent receivers [71], and high-speed modulators [63], which could be utilized in emerging beam-scanning applications. Many of the capabilities rely on the hybrid integration of indium

phosphide elements such as gain sections, modulators and photodiodes, and on the assembly of thin films and micro-optic elements inside etched-slots and grooves on the surface of the polymer platform. Lastly, due to the symmetry of the cross-section of the single-mode PolyBoard waveguide, the supported mode is hybrid with both transverse electric (TE) and transverse magnetic (TM) components. This characteristic is a clear advantage when the PolyBoard device functions as a receiver.

On the other hand, there are challenges associated with polymer-based OPAs, primarily due to the low index contrast characteristic of polymer materials [53]. This presents two issues: first, low index contrast leads to weak confinement of the propagating mode within the waveguiding structure, preventing waveguides from being placed closely together without experiencing cross-coupling. As we will discuss in the next paragraph, which analyzes the basic theory of OPAs, this results in the formation of undesirable copies of the main lobe in the radiation pattern, effectively limiting the steering range. However, this limitation can be mitigated through various strategies, such as designing waveguides to reduce cross-coupling via phase mismatch or placing emitters with aperiodic spacing. The latter approach is investigated within this work. The low index contrast results in the beam outcoupled from the edge-emitting facet of a single waveguide exhibiting low divergence. As we will see in the next paragraph, the radiation pattern of the elementary emitter acts as an envelope that defines the field of view (FOV) of the OPA. Therefore, the high directivity of a single element limits the OPA's steering range. To address this issue, one can either tweak the platform's index contrast or improve the radiation characteristics of single waveguides through elaborate designφ. Another challenge concerns the scalability of 3D PICs, which is intricately tied to the control of the fabrication process. The maximum number of waveguiding layers that can be manufactured depends on the alignment precision of the masks applied between successive layer fabrications. Since 2014, the possibility of manufacturing up to five separate waveguiding layers has been demonstrated [58]. In recent years, efforts have focused more on the development of vertical MMI structures for interconnecting layers rather than increasing the total number of layers [54]-[57][60]. Given the current capabilities and the progress made in recent years, we estimate that doubling the number of waveguiding layers is a realistic scenario. However, surpassing ten waveguiding layers presents a significant challenge based on the current fabrication capabilities. Next, we summarize the features of PolyBoard, the polymer-based photonic

integration platform of the Heinrich Hertz Institute (HHI), that make it an attractive platform for developing OPAs, as well as the challenges.

Advantages of polymer-based OPAs

5. Simplified and cost-effective manufacturing process
6. Capacity for 3D photonic integration (2D end-fire OPAs)
7. Power-efficient thermo-optic devices: phase shifters, VOAs, tunable ECLs (Best recorded P_π in this work ~1.3 mW)
8. High optical power handling capability (up to 200 mW CW)
9. Basic waveguide structure equally supports TE and TM components
10. Hybrid integration with InP elements (on-chip light generation & detection)
11. Integration of optical isolation and polarization handling elements
12. Easy fiber-to-chip coupling (using U-grooves)
13. Broad transparency (wavelength windows around 850 nm, 1310 nm, 1550 nm)

Challenges of polymer-based OPAs

- □ Limited FOV (due to the high directivity of the edge-emitting waveguide)
- □ Response time of thermo-optic devices in the order of ms
- □ Scalability of 3D PICs (current status: 5 w/g layers)

2.1.3 Optical Phased Array circuit

The circuit of an optical phased array (OPA) can be broadly divided into three subsections: i) the power distribution network, ii) the phase tuning section and iii) the emitting aperture. There are several variations on the implementation of each section. In this paragraph we aim to summarize the different design choices and present the associated challenges.

2.1.3.1 Power distribution network

The optical distribution network is the circuit responsible for converting the single-mode input waveguide to a set of N channels. This can be performed by using either an MMI splitting tree or a star coupler. The MMI coupler tree is a robust way to achieve splitting among elements as it is characterized by broadband operation and scales nicely to

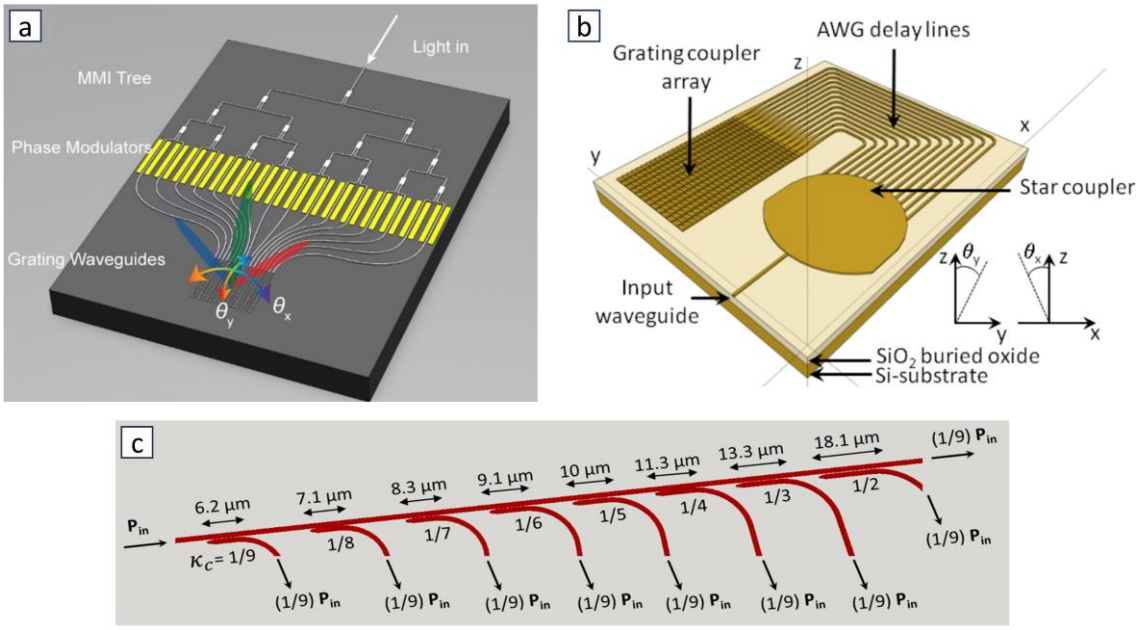

Figure 2.2: Examples of the three typically used power distribution networks: (a) the MMI splitting tree [31], (b) the star coupler [3], and (c) the cascaded directional couplers [20].

high channel counts with small pitch. A potential benefit of MMI tree is the uniform phase delay among the channels due to equal path lengths. The power distribution is also uniform, which can be an advantage or a drawback. A star coupler is preferred in cases where array tapering is desirable for reducing the sidelobe level, at the expense of main lobe beamwidth, as it naturally produces a gaussian amplitude weighting among the channels [13][22]. Additionally, star couplers are broadband and offer a more compact footprint relative to the MMI tree for the same channel count [23]. A potential shortcoming of star couplers is that they are not path-length matched and thus produce unequal phase distribution between the outputs. A possible solution to achieve phase matching at the output is to vary the widths of the output waveguides. A third alternative would be a cascaded direction coupler scheme with gradually increasing splitting ratios. The main drawback of directional couplers is their strong wavelength dependence, which makes them unsuitable for applications requiring large optical bandwidths (e.g. when wavelength tuning is performed). Moreover, compared to MMIs directional couplers are more susceptible to fabrication errors.

2.1.3.2 Phase tuning and driving schemes

The phase tuning (or modulation) section is the part of the OPA where the appropriate phase difference between the channels is applied to create the desired phase profile at the output of the array to perform beam-steering. There are four factors associated with the performance of the phase modulation technology in an OPA: i) modulation bandwidth, ii)

insertion loss, iii) power consumption and iv) footprint. The modulation bandwidth determines the scanning speed of the OPA, while the scalability of the system is mainly related to power consumption, the insertion loss and the footprint of the phase shifter device. The phase modulation mechanisms can be broadly categorized into four categories: i) thermo-optic (TO) modulation, ii) free-carrier or plasma dispersion (PD) modulation based on carrier injection, carrier depletion or carrier accumulation, iii) electro-optic (EO) modulation based on Pockels effect, and iv) opto-electromechanical (OEM) modulation.

As we briefly discussed in paragraph 2.1.1, each platform offers different possibilities for phase modulation. The simplest phase shifting technology, shared among all platforms, is the one based on thermo-optic (TO) tuning. Silicon platform exhibits a TO coefficient of ~$1.8 \times 10^{-4}\ K^{-1}$ and thermal conductivity 163 W/(m·K) [62], offering a typical TO phase shifter efficiency of 20 to 30 mW/π. Efforts have been made to reduce the power consumption and footprint of the thermal phase shifters in SOI. Some notable examples are the work of Sun *et al.* from 2014 [8], demonstrating a compact TO phase shifter based on an S-shaped doped waveguide with 8.5 mW/π efficiency, and the work of Miller *et al.* from 2020 [18], presenting a multi-pass structure with 1.7 mW/π efficiency. However, the multi-pass phase shifter presented significant insertion losses, in the order of a few dB (2-3 dB). On the other hand, polymer-based photonic integration platforms present more efficient thermo-optic effect, primarily due to the lower thermal conductivity of polymer materials relative to silicon (0.1-0.3 W/(m·K)) [62]. One limitation of TO tuning is its restricted modulation bandwidth. In silicon the bandwidth of TO phase shifters is usually limited to a few tens of kHz [6], while in silicon nitride and polymer-based platforms, which exhibit lower thermal conductivity than silicon, the bandwidth is an order of magnitude lower (<1 kHz). An alternative to thermo-optic (TO) tuning in silicon is opto-electromechanical tuning. MEMS-based phase shifters provide tuning speeds in the range of several hundred kilohertz to a few megahertz, coupled with relatively low insertion loss. A large microelectro-mechanical-system (MEMS)-based 2D array, demonstrated by Wang *et al.*, comprising 160×160 elements, achieves a response time of a few microseconds [72]. However, these devices often require high driving voltages and still encounter challenges related to yield and wear over time.

Higher modulation bandwidths can be achieved with the use of EO phase shifters. Silicon EO phase shifters are based on free-carrier dispersion effect, since electro-optic effect (Pockels or Kerr effect) is negligible in silicon. In [16], Poulton *et al.* demonstrated

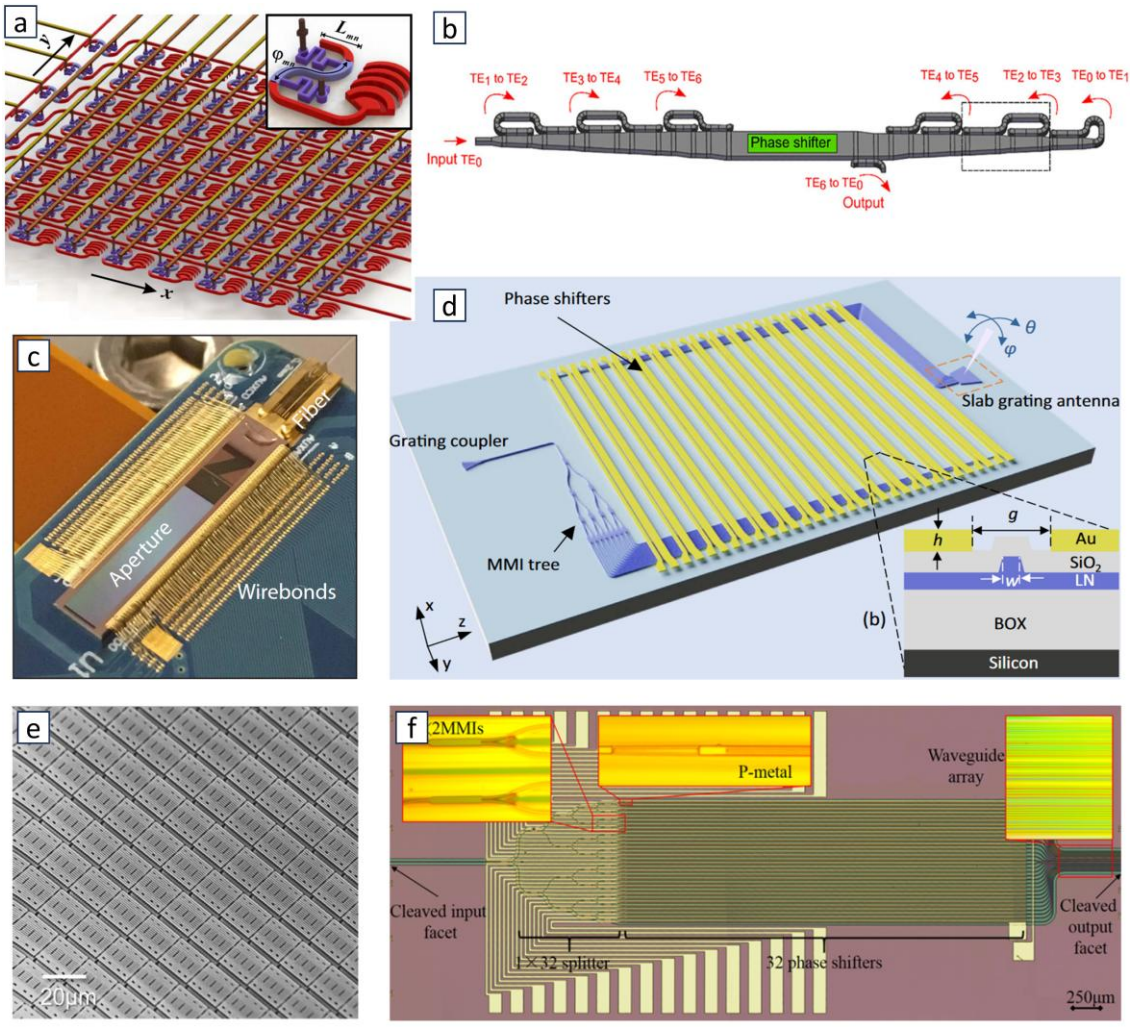

Figure 2.3: Phase modulation technologies: (a) 8×8 OPA in SOI utilizing a compact TO phase shifter design by Sun *et al.* [8], (b) Multi-pass TO phase shifter in SOI for reduced power consumption by Miller *et al.* [18], (c) 1D 512 channel OPA in silicon based on EO tuning by Poulton *et al.* [16], (d) 1D OPA thin-film lithium niobate based on EO tuning with bandwidth in the GHz range by Li *et al.* [30], (e) MEMS-based 160×160 OPA in SOI by Wang *et al.* [72], (f) InP-based OPA with 32 EO modulators by Tan *et al.* [38].

a 512-channel silicon OPA with EO phase shifters, achieving a time constant of 10 ns (equivalent to a bandwidth of several MHz) and power consumption on the order of a few μW/π. A drawback of plasma dispersion modulators (PDMs) is that the change in refractive index is accompanied by a detrimental change in intensity due to the absorption via free carriers, resulting in a residual amplitude modulation (RAM). To address this challenge, hybrid integration of III-V materials in the silicon platform has been proposed to realize more efficient EO phase modulation. With this approach Xie *et al.* demonstrated a 32-channel OPA based on III-V/Si heterogeneous phase shifters with low RAM (< 0.2 dB), full-wavelength phase shift voltage ($V_{2\pi}$) of less than 1.5 V and bandwidth in the GHz range [23]. Tan *et al.* utilized the electro-optic effect in InP platform to realize a 32-channel

OPA with total power consumption of less than 7.5 mW [38]. The p-i-n phase shifters were operated in reverse biasing to achieve power consumption of 0.1 mW/π. Hirano *et al.* utilized EO modulation in a polymer-based OPA to achieve a scanning speed of 2 MHz and power consumption of less than 1 mW [72]. On the other hand, Pockels modulators in the LNOI platform can provide bandwidth in the order of several GHz. For example, in [30], Li *et al.* demonstrated a 1D thin-film lithium niobate (TFLN) OPA based on EO modulators with 2.5 GHz bandwidth. However, the scalability of OPAs in LNOI is constrained by the large half-wave voltage-length product (6-7 V·cm), which necessitates modulator lengths of approximately 1 cm. Apart from their fast response time, another advantage of EO phase shifters is their ability to be placed in proximity without impacting adjacent channels. In contrast, TO phase shifters require wider spacing to mitigate thermal crosstalk and often necessitate fan-in and fan-out sections before and after the phase tuning section, as the pitch of the phase modulators is larger than that of the waveguides in the emitting section. By utilizing EO phase shifters in silicon, Poulton *et al.* demonstrated an OPA in which the modulators were arranged with an inline pitch of just 1 μm [21], effectively eliminating the need for fan-in and fan-out sections.

Another important aspect of OPAs is their control signals and the necessary driving channels. In its simplest form, each channel of an OPA is independently controlled by a phase shifter, which, in turn, is controlled by a dedicated DAC channel. Several architectures have been proposed to simplify the driving of OPAs. In 2009, Acoleyen *et al*. proposed the use of proportional heaters to apply different phase shift between the channels with the same control signal [1], a concept that has also been investigated in subsequent works [74][75]. In this way, a single DAC channel is sufficient to perform beam scanning in one dimension in a continuous manner. A limitation of this approach is that phase errors due to fabrication cannot be eliminated since there is no independent channel control. However, as the number of elements increases the effect of the phase errors becomes less significant [19]. A different approach to achieve continuous beam scanning has been proposed in 2014 by Yaacobi *et al.*, which places the optical phase shifters in a cascaded splitting architecture, while additional phase shifters are used to compensate for the fabrication-induced phase errors [6]. In 2018 Chung *et al* extended this concept to present a scalable architecture for the formation of 2D arrays with a reduced number of DAC channels [20]. Cascaded driving to reduce the number of control signals, and consequently, the required DAC channels can also be applied in a tree architecture, as demonstrated in

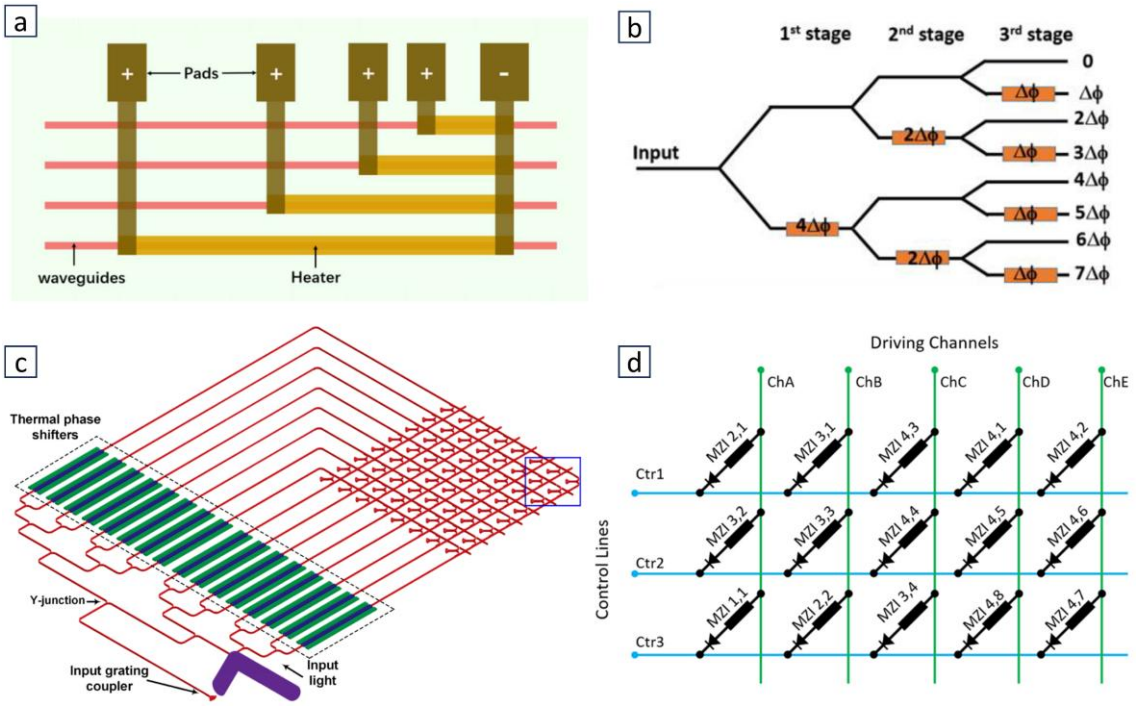

Figure 2.4: Driving architectures that have been proposed to reduce the number of control signals: (a) Proportional heaters by Wang *et al.* [75], (b) Cascaded tree architecture by Zhu *et al.* [76], (c) Mode interference method by Ashtiani and Aflatouni [80], and (d) column-row addressing with PWM drive by Ribeiro *et al.* [79].

[76]-[78]. Another method for reducing the number of control signals is to arrange the phase shifters in an array and employ column-row addressing [14][22][79]. However, this method requires more complicated PWM driving signals. Ashtiani *et al.* have proposed an entirely different approach, based on mode interference within a larger interference array circuit, to control an $N \times N$ array with $2N$ control signals. The operational principle is analogous to the Blass matrix architecture commonly employed in microwave photonics [81]. A drawback of this method is its susceptibility to fabrication-induced phase errors. Minimizing the complexity and power consumption of driving and control electronics is essential for compact OPA systems. Under this context, Kjellman *et al.* have investigated the impact of DAC resolution on OPA performance [82], while Chung *et al.* have proposed optimized phase assignment strategies to reduce power consumption[20].

2.1.3.3 Emitting aperture

The radiation characteristics of an OPA are primarily determined by the type of emitters and their spatial arrangement. Based on their aperture type, OPAs can be broadly classified into three categories: i) Edge-emitting OPAs, also known as end-fire OPAs, ii) Nano-antenna array OPAs, which utilize compact grating antennas to form 2D planar arrays, and iii) waveguide grating OPAs. The key performance metrics associated with the aperture

include a wide field of view (FOV), ideally spanning up to 180º, a narrow beamwidth corresponding to high directivity, and effective suppression of unwanted lobes in the radiation pattern. Achieving a FOV of 180º requires an emitter pitch of half-wavelength. For OPAs operating around 1.55 μm, this corresponds to submicron emitter pitch, which introduces significant design challenges. An alternative approach to achieving a wide FOV is to arrange the emitters in a non-uniform way, creating what is known as a sparse aperiodic array [83]. Beamwidth is directly influenced by the size of the emitting aperture, which is related to the total number of channels in the array.

The end-fire configuration represents the simplest design for an emitter array [24][46][84]-[88]. In this setup, waveguides are routed to the edge of the chip, where light is outcoupled in-plane into free space. A notable advantage of this approach is that light emission is not reliant on diffraction, enabling high efficiency across a broad spectrum. Additionally, the radiation profile is a uniform Gaussian beam, as it is directly determined by the waveguided mode. The widest FOV with an end-fire OPA was achieved in 2018 by Phare *et al.* [24], attaining a theoretical FOV of 180º by placing the emitters with a half-wavelength pitch (775 nm). This was made possible by introducing a variation in the waveguide width to achieve mode mismatching and thus suppress optical crosstalk between adjacent waveguides [89]. However, the practical FOV was limited to 120º due to the element factor. Half-wavelength pitch has also been demonstrated by Kossey *et al.* [85] but the FOV was limited to 64º by the element factor. The dependence of the FOV on the element factor is presented in detail in paragraph 2.2, where we introduce the basic theory of antenna arrays. Optimizing the FOV in end-fire OPAs has also been investigated by employing aperiodic arrangement of the emitters, in the silicon [84], silicon nitride [46], and InP platform [38]. The largest 1D end-fire arrays, have been demonstrated by Komatsu *et al.* in InP [36], and Kohno *et al.* in SOI [86], comprising 100 and 128 channels respectively. However, a significant limitation of the end-fire configuration is the difficulty in forming 2D planar arrays. Since most photonic integrated circuits (PICs) consist of a single waveguide layer, edge-emitting OPAs are typically constrained to 1×N arrays, resulting in a strip-like radiation pattern. Consequently, they function primarily as line beam scanners and beam steering is limited only to a single plane.

Formation of 2D planar arrays is possible by using nano-antenna elements which are based on diffraction gratings to emit light vertically to the chip plane. In this way 2D arrays can be formed within a single waveguide layer. The concept was first introduced in 2010

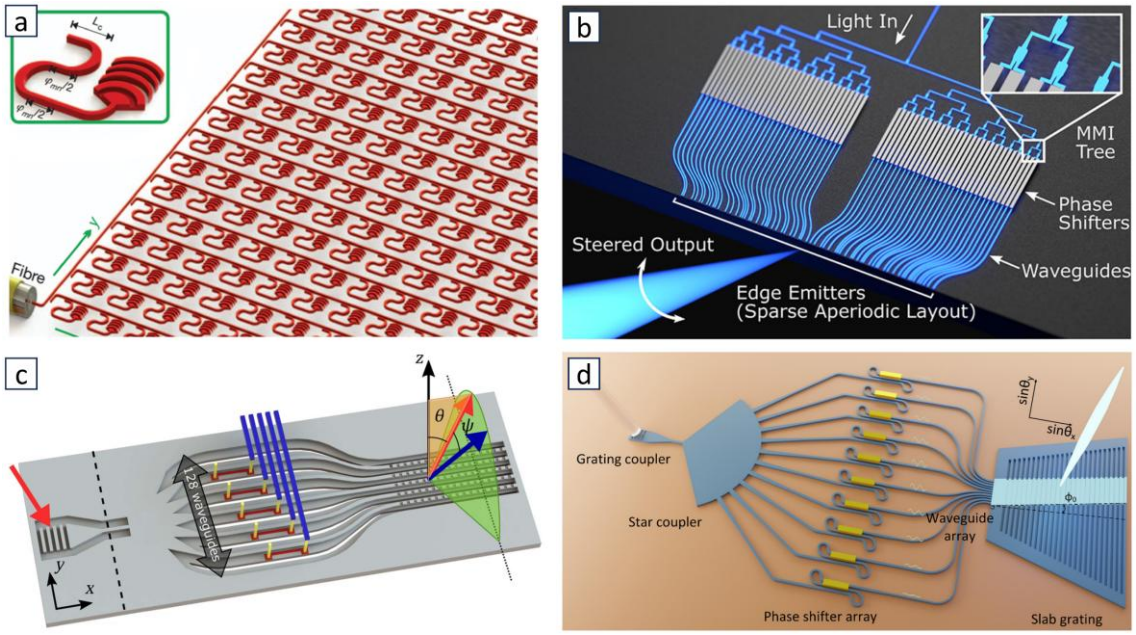

Figure 2.5: OPA aperture configurations: (a) nano-antenna array based on grating emitters, (b) end-fire array based on edge-emitting waveguides, (c) long waveguide gratings aperture, and (d) emission is based in a slab grating region, shared among all channels.

by Acoleyen *et al.*, by presenting a 4×4 array in silicon, but without the possibility for active phase tuning. In 2014, Sun *et al.* demonstrated a passive 64×64 array that could form the 'MIT' logo by inscribing suitable phase difference between the channels (phase control from the fabrication). In the same year Sun *et al.* also presented an 8×8 array that could be actively tuned to accomplish 2D beam steering within a 10º FOV. The following years 8×8 nano-antenna arrays have been demonstrated also by Abediasl and Hashemi [9], Ashtiani and Aflatouni [80], and Zhang *et al.* [90], although with a narrower FOV. To achieve wide FOV the emitters must be placed closely together, which presents a significant challenge in 2D nano-antenna arrays due to the size of the antenna element and the real estate needed for the optical routing. The larger FOV demonstrated with a 2D OPA to date is 16º×16º by Fatemi *et al.* [14], where the positions of the 128 elements were optimized in a non-uniform arrangement. Similarly, Fukui *et al.* [91] demonstrated a non-uniform 2D OPA utilizing a Costas array, achieving approximately 19000 resolvable points within a 5.9º×5.9º FOV.

The third type of emitter is the waveguide grating. The OPA circuit closely resembles that of the edge-emitting OPA, with a key distinction: instead of terminating the waveguides at the edge of the chip, waveguide gratings are used to emit light perpendicular to the chip's surface, as show in Figure 2.5(c). Two-dimensional beam steering is accomplished by tuning the laser source's wavelength, exploiting the wavelength dependence of the diffraction grating structures. By using wavelength tuning for scanning

in one direction, the control complexity of OPAs is significantly reduced. For example, achieving 2D beam steering in $N \times N$ nano-antenna arrays require N^2 phase tuning elements. In contrast, waveguide grating OPAs reduce this requirement to just N phase tuning elements, resulting in a linear scaling with the size of the array. Because of this advantage, the waveguide grating configuration has been extensively studied, leading to the demonstration of OPAs with hundreds and thousands of elements. In 2016 Hutchison *et al.* demonstrated a 128-channel OPA with an 80º FOV in the OPA axis using a non-uniform aperture and 17º in the other axis via 100 nm wavelength tuning around 1310 nm [13]. In 2020, Millet *et al.* achieved a FOV of 6º×70º with a uniform OPA of 512 waveguide gratings placed with 1.3 μm pitch [18]. That same year, Poulton *et al.* showcased an 8196-channel uniform array with 1 μm element pitch, achieving 100º FOV in the OPA axis and 17º via 120 nm wavelength tuning (0.14º/nm) [21]. To manage the large number of tuning elements, CMOS DACs were directly flipped onto the PIC. The largest FOV with a waveguide grating OPA to date was demonstrated by Li *et al.* in 2021, achieving a 19.2º×140º FOV [92]. This was accomplished by employing non-uniform element pitch with an average distance of ~19λ and wavelength tuning across 280 nm. A slightly different approach to achieve a wide FOV, is the use of a slab grating region [93]. Instead of patterning individual waveguide gratings, all waveguides share a common grating region, as shown in Figure 2.5(d). Wang *el al.* used this approach to place 32 waveguides with 1 μm pitch, connected to a Si slab grating, and achieve a 96º FOV in the OPA axis [75]. Liu and Hu used a similar approach, but they were able to achieve half-wavelength spacing by employing phase mismatching between adjacent waveguides before entering the slab region. Their 64-channel array could achieve in theory 180 º FOV [94]. One year later they extended their design to 1000 channels, demonstrating a FOV 10.8°×140° by combining wavelength tuning [22]. One limitation of waveguide gratings is their reduced emitting efficiency, as they generate both upward and downward beams due to diffraction, with the downward beam leaking into the silicon substrate. However, various methods have been proposed to enhance the efficiency of these structures by either minimizing the leakage beam or redirecting it toward the desired direction [95]. Another drawback of diffraction gratings is their wavelength dependency, which can limit performance in systems requiring broad-spectrum emission, such as FMCW LiDAR. This dependency may compromise the system's resolution, affecting overall accuracy.

2.1.4 3D integration for 2D end-fire OPAs

2.1.4.1 Previous works

Forming 2D end-fire OPAs is challenging as it requires the fabrication of multiple waveguiding layers. The concept of using 3D photonic integration to create end-fire arrays was introduced by Hosseini *et al.* in 2009 [96]. This was a collaborative effort, aiming to explore fabrication techniques for multi-layer PICs, between research groups at the University of Texas and Stanford University, working on sequential transfer printing of silicon nanomembranes to realize multi-layer stacks [97]. The study highlighted the key challenge of achieving precise alignment accuracy across layers, identifying alignment tolerance of less than 10 nm as critical for high-performance devices, when using a silicon waveguide with 500 nm width and 230 nm thickness. They assert that their proposed fabrication scheme offers advantages in achieving this level of accuracy. However, their demonstration is limited to a single-layer 1×12 OPA with unequally spaced edge-emitting waveguides [84]. An alternative approach for the realization of 3D circuits is the use of ultra-fast laser inscription (ULI). This method was proposed by Gross and Withford in 2015 [52], and one year later by Yoo *et al.* [50], to form 2D end-fire OPAs by engraving waveguide patterns in glass. Guan *et al.* used this method to fabricate a 4×4 aperture in silica, which was integrated with a silica planar light-wave circuit (PLC) that incorporated thermal phase shifters to provide active phase control of the 16 channels of the array [51]. With this technique, a femtosecond laser beam is locally focused to introduce a permanent refractive index increase in the glass. As the beam travels through the material a higher-index path is formed, which acts as a waveguide. One drawback of this technique is the low index contrast, which results in weak mode confinement. To ensure a 20 dB separation between adjacent waveguides in [51], the center-to-center waveguide spacing at the emitting edge was set to 18 μm, limiting the FOV to 4.9º×4.9º due to the formation of grating lobes. A similar structure of 16×16 has been also fabricated by the same group, leveraging on the flexibility offered by this method, without, however, demonstrating active phase control [50]. A more recent work on the fabrication of 3D PICs for OPA devices is the one from Wu *et al.* [98]-[100], where he proposes a method based on the deposition of multiple silicon nitride (SiN) layers between silicon oxide (SiO2) cladding.

To address the challenges of precision alignment and accurate spacing control between layers, commonly encountered in the fabrication of 3D PICs, a fabrication process involving a single lithographic step was proposed. However, this method is only applicable for OPA designs that share the same pattern between different layers and poses a limit to the flexibility of the specific approach. Using this technique the fabrication and experimental testing of a 4-layer OPA was demonstrated, comprising 16 channels per layer. The thickness of the SiN core and silicon oxide cladding layers was 800 nm and 500 nm, respectively, resulting in a vertical pitch of 1.3 μm between waveguides in different layers. The thickness of the silicon oxide cladding layer was not sufficient to eliminate crosstalk between waveguides of different layers and ensure independent phase control between the channels, further restricting the design flexibility. In addition, the lateral pitch between the waveguides at the emitting edge was set to 8 μm to guarantee the etching depth. This indicates a trade-off between the number of layers that can be etched in a single step, to maintain vertical alignment, and the minimum spacing between waveguides within the

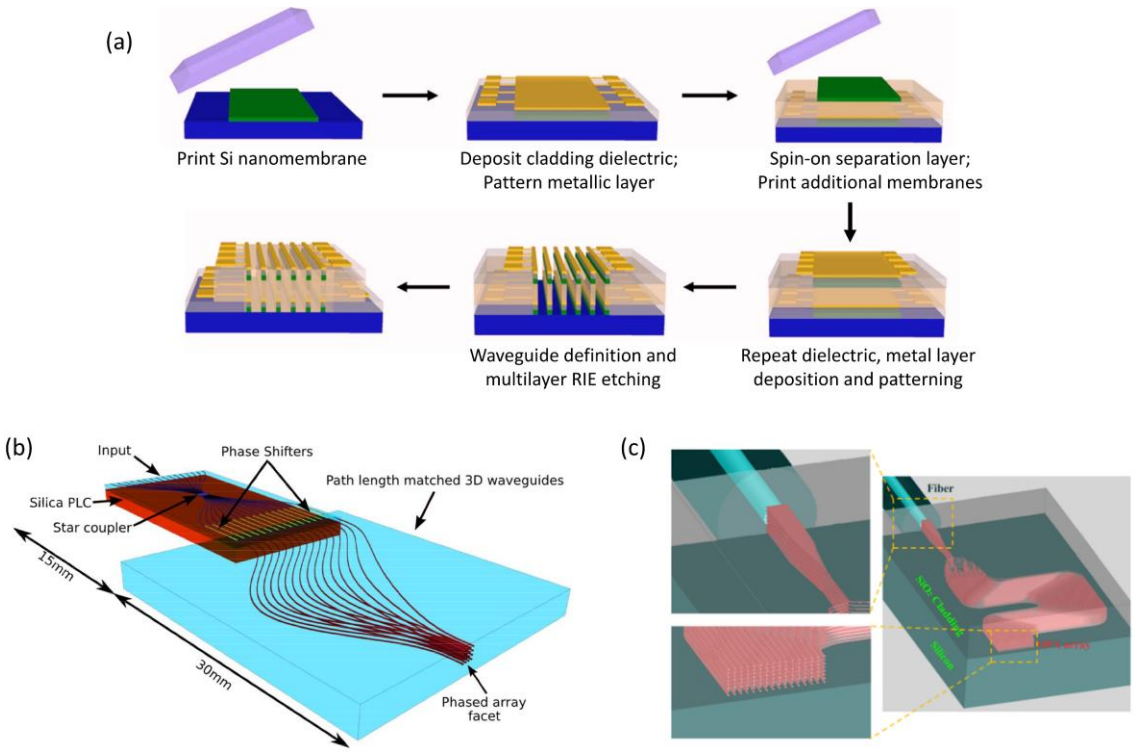

Figure 2.6: Works on 3D PICs for the realization of 2D end-fire OPAs: (a) Fabrication technique proposed by Hosseini *et al.* for the flexible manufacturing of 3D PICs. Fabrication steps include transfer printing of Si nanomembranes, electron beam lithography for waveguide definition, and reactive ion etching (RIE) [97]. (b) 4×4 hybrid OPA based on ultra-fast laser inscription (ULI) in silica by Guan *et al.* [51] (c) Illustration of a dispersive passive 8×16 OPA based on multi-layer SiN/SiO2 structure by Wu *et al.* [99]. The authors proposed a self-aligning fabrication technique with a single etching step [100]. The actual fabricated device was a 4×16 OPA.

same layer. Furthermore, beam-steering is achieved by introducing a path difference between channels and employing wavelength tuning, so no active phase control was demonstrated in the specific work.

Recently, polymer-based OPAs have attracted attention from research groups at Kwangwoon University and Pusan National University in South Korea, primarily due to their high optical power handling capability, the efficient thermo-optic phase shifters, and their flexible fabrication techniques [101]-[104]. In [102], Kim *et al.* combined a 32-channel 1D OPA with a tunable laser source and a Bragg-grating to demonstrate 2D beam scanning across a 3.9°×8.9° FOV. Leveraging on the high-thermal confinement of polymer platform, thermo-optic phase shifters exhibited a 2 mW/π tuning efficiency. In later works, polymer waveguides were integrated with silicon nitride waveguides to improve the radiation characteristics of the OPA [103]. The aperture of the OPA, as well as the power distribution network, were transferred to the SiN platform, while the phase modulation part remained in the polymer. Moreover, control of the elementary emitter radiation pattern was demonstrated by introducing tapered waveguides in the emitting edge of the SiN section, and a complete scanning system comprising a 64-channel 1D hybrid OPA packaged with optics was presented [104]. Although discussing the fabrication flexibility offered by polymer-based photonic integration, none of the above works in polymer focuses on the fabrication of multi-layer PICs for the realization of 2D OPAs.

2.1.4.2 Our concept

To the best of our knowledge, the present work is the first to present 3D polymer OPAs for 2D beam steering. Our concept utilizes PolyBoard, the polymer-based platform of Fraunhofer Heinrich-Hertz Institute (HHI), to form multiple waveguiding layers, based on the repetition of the conventional fabrication steps. These steps utilize two polymer resins, the core and the cladding resin, and involve: i) spin-coating of the cladding resin on a silicon (Si) substrate, ii) spin-coating of the waveguide resin, iii) structuring of the waveguiding layer using ultra-violet (UV) lithography and reactive ion etching (RIE), and iv) spin-coating of the cladding resin to form the top cladding layer. This process is repeated several times with different masks for each waveguiding layer, resulting in polymer-based PICs with multiple, and completely independent, waveguiding layers. An illustration of the fabrication steps is depicted in Figure 2.1. The light is transferred between the different waveguiding layers using vertical MMI structures, that have been developed in the PolyBoard platform [54]-[57], while power splitting in the same layer is facilitated by

conventional single-layer MMIs. Figure 2.7 depicts an envisioned passive 4×4 OPA based on 1×8 lateral MMIs and 1×1 vertical MMIs to distribute the optical power among the channels. For active tuning, phase heaters can be integrated either on the top layer, above the top cladding, or between waveguiding layers by incorporating additional metallization layers into the stack. However, the latter approach is not explored in this work. In all fabricated PICs, the heating electrodes are positioned above the top cladding. A drawback of this configuration is that the phase-shift efficiency reduces for lower waveguiding layers, as more power is required to transfer the same amount of heat to waveguides buried deeper in the structure. A third approach is to implement the power distribution network and phase tuning section in the top layer, with the light subsequently distributed to the other layers via vertical MMIs. Finally, in the last part of the circuit, the waveguides are brought closer together to form the emitting aperture of the OPA.

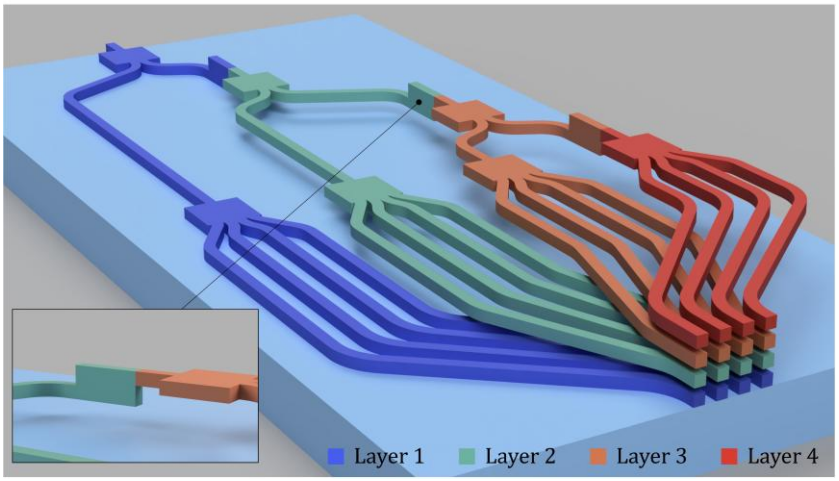

Figure 2.7: Concept of 2D OPAs based on PolyBoard platform with multiple waveguiding layers and vertical MMI couplers for light coupling between adjacent layers. End-fire single-mode waveguides serve as optical antenna elements at the end-facet of the PolyBoard PIC (cladding material omitted for illustration purposes). A 4 × 4 OPA is shown as example. Inset: Close view of a vertical MMI coupler followed by a lateral one.

2.1.5 Work outline

Four different types of PICs were realized within this work. First, uniform single-layer 1×4 OPAs and double-layer 2×4 OPAs with active phase tuning are presented, and beam-steering in one and two dimensions is demonstrated accordingly. These initial implementations served as a reference for validating our modeling, presented in paragraph 2.3.1, and identifying the limitations of uniform OPAs in PolyBoard. Additionally, they facilitated the development of our characterization setup, including the lens system for far-field imaging, software for data acquisition, image processing, as well as algorithms, for

precise control of the OPAs. Subsequently, linear non-uniform OPAs are theoretically investigated to enhance the field-of-view and reduce the channel count compared to uniform arrays. Single-layer non-uniform 1×16 OPAs were fabricated and experimentally evaluated. This technique can be easily extended to multi-layer structures, along with its benefits. In addition, algorithms were developed to facilitate the calibration and control of these PICs. Finally, a passive multi-layer 4×8 OPA was fabricated as a stand-alone PIC. An additional single-layer PIC with a 1-to-32 splitting tree and 32 thermal phase-shifters was fabricated to enable active phase tuning of the passive 4×8 OPA through edge-coupling. Assembly and packaging of the two PICs was not completed, and experimental results remain unavailable to date. However, the possibility of 3D photonic integration in PolyBoard is demonstrated and our conclusions remain valid. This work serves as a proof of concept for 2D end-fire polymer-based OPAs. We discuss the current limitations and propose a 4-layer non-uniform OPA, which we believe represents the best achievable design given the current fabrication capabilities. As technology advances, realizing an 8×8 OPA could become feasible, and we believe that the present work represents a significant step in moving this concept from possibility to reality. We finally note that the OPAs in the present work are operated only as emitters, and no signal reception is demonstrated.

Objectives

1. Develop a modelling framework for far-field radiation patterns, integrating electromagnetic (EM) simulation with MATLAB-based tools.
2. Demonstrate 2D optical beam-steering using multi-layer PolyBoard OPAs.
3. Develop a far/near-field characterization setup (including control software, GUI, image processing techniques, etc.)
4. Develop an optimization platform for the design of non-uniform OPAs.
5. Develop OPA calibration techniques.

2.2 Theoretical aspects

The phased array concept was originally introduced by the physicist Ferdinand Braun at the beginning of the 20th century, and it has been extensively utilized in radar systems ever since. The basic theory can be found in any standard microwave radar book [105]. In this paragraph we present a brief overview of the main concepts, with an emphasis on the optical domain, and we introduce the tools for the analysis of optical phased arrays (OPAs). According to the pattern multiplication principle, the total far field radiation of an antenna array is equal to the product of the field of the elementary emitter, and the array factor, under the assumption that the elements that compose the array are identical emitters

$$\text{Total pattern} = [\text{Element pattern}] \cdot [\text{Array Factor}]. \tag{2.1}$$

Therefore, the analysis of the array can be decomposed to the modelling of the single emitter and the array factor (AF). Moreover, the conclusions drawn from the analysis of the array factor are, to some extent, applicable regardless of the type of emitter used in the array. In this paragraph we focus on the concepts and trade-offs that are associated with the array factor, which is a function of the number of elements, their geometrical arrangement (linear, rectangular, circular, etc.), their spacing, their relative excitation magnitude and phase. The modelling of the radiation pattern of the elementary emitter is presented in the modelling section of the next paragraph.

2.2.1 Array factor

The total electric field of an N-element array at an observation point P in the far-field at (θ, φ) direction, is the superposition of the waves produced by each individual emitter

$$\begin{aligned} E(\theta,\varphi) &= \mathbf{f}(\theta,\varphi)\cdot a_1 e^{-j\boldsymbol{k}\cdot\boldsymbol{r_1}} + \cdots + \mathbf{f}(\theta,\varphi)\cdot a_N e^{-j\boldsymbol{k}\cdot\boldsymbol{r_N}} \\ &= \sum_{i=1}^{N} \mathbf{f}(\theta,\varphi)\cdot a_i e^{-j\boldsymbol{k}\cdot\boldsymbol{r_i}} \\ &= \mathbf{f}(\theta,\varphi)\cdot \sum_{i=1}^{N} a_i e^{-j\boldsymbol{k}\cdot\boldsymbol{r_i}} \end{aligned} \tag{2.2}$$

, where $\mathbf{f}(\theta,\varphi)$ is the element pattern, a_i the complex weight coefficient applied to each emitter, and $\boldsymbol{r_n}$ the spatial vectors. We define "array factor" (AF) the summation term

$$AF = \sum_{i=1}^{N} a_i e^{-j\boldsymbol{k}\cdot\boldsymbol{r_n}}. \tag{2.3}$$

To find the radiation intensity $U(\theta,\varphi)$ we use the absolute square of the array factor

$$U(\theta,\varphi) = U_{element}(\theta,\varphi) \cdot |AF(\theta,\varphi)|^2 \tag{2.4}$$

and

$$U_{element}(\theta,\varphi) = \mathbf{f}(\theta,\varphi) \cdot \mathbf{f}^*(\theta,\varphi) \tag{2.5}$$

2.2.2 Directivity, Beamwidth and Effective Aperture

The directivity D of an antenna is the ratio of the radiation intensity $U(\theta,\varphi)$ in a given direction, i.e., the radiated power per unit solid angle at this direction, over the radiation intensity averaged over all directions. If the direction is not specified, the direction of maximum directivity D_{max} is implied. The average radiation intensity is equal to the total power P_{rad} radiated by the antenna divided by 4π, which is the radiation intensity of an isotropic source, denoted here as U_0. Hence,

$$D_{max} = \frac{U_{max}}{U_0} = 4\pi \frac{U_{max}}{P_{rad}} \tag{2.6}$$

$$P_{rad} = \oiint_{\Omega} U d\Omega = \int_0^{2\pi} \int_0^{\pi} U(\theta,\varphi) \sin\theta \, d\theta d\varphi \tag{2.7}$$

where $d\Omega = \sin\theta \, d\theta d\varphi$. By defining the beam solid Ω_A angle as

$$\Omega_A = \frac{1}{U_{max}} \int_0^{2\pi} \int_0^{\pi} U(\theta,\varphi) \sin\theta \, d\theta d\varphi \tag{2.8}$$

directivity can be rewritten as

$$D_{max} = \frac{4\pi}{\Omega_A} \cong \frac{4\pi}{\theta_x \theta_y} \tag{2.9}$$

A usual approximation is $\Omega_A \cong \theta_x \theta_y$, where θ_x and θ_y is the half-power beamwidth (full-angle in radians) in two perpendicular planes. The approximation is more accurate for radiation patterns that present a narrow major lobe and very negligible minor lobes, which is usually the case in phased arrays. The (maximum) effective aperture of an antenna is related to its (maximum) directivity by

$$A_{eff} = \frac{\lambda^2}{4\pi} D_{max} \tag{2.10}$$

Therefore,

$$\theta_x \theta_y \cong \frac{4\pi}{A_{eff}} \tag{2.11}$$

The last relationship shows that the beamwidth is directly proportional to the emitting aperture, describing the design principle that narrower beams require larger apertures.

2.2.3 Linear array

The array factor of a linear N-element array with uniform spacing d between the elements, uniform excitation amplitude $|\alpha|$ (equal to unity), and progressive phase excitation between the elements $\Delta\phi = \phi_a$, is given by the expression

$$AF = \sum_{n=0}^{N-1} |\alpha| \cdot e^{jn(kd\sin\theta + \phi_a)} = \sum_{n=0}^{N-1} e^{jn\,\xi} \tag{2.12}$$

where $\xi = kd\sin\theta + \phi_a$ and k is the wave number. Assuming the reference point at the physical center of the array, the normalized array factor can be simplified as

$$AF = \frac{1}{N}\left[\frac{\sin\left(N\frac{\xi}{2}\right)}{\sin\left(\frac{\xi}{2}\right)}\right] \tag{2.13}$$

According to L'Hôpital's rule the maxima occur when both the denominator and numerator of equation (2.13) are zeros

$$\frac{\xi}{2} = \pm m\pi \tag{2.14}$$

Solving for θ in the case of no steering ($\phi_a = 0$) yields

$$\theta_m = \sin^{-1}\left(\pm m\frac{\lambda}{d}\right), \qquad m = 0,1,2,\ldots \tag{2.15}$$

where m is used as maxima indicator. The first maximum occurs at $\theta_0 = 0$, and is referred to as the main lobe. All the other maxima occurring at $m \geq 1$ are called grating lobes (or ghost lobes). In beam steering grating lobes are highly undesirable as they limit the steering range. The beam can be unambiguously steered within the angular range between the main lobe to the first grating lobe, referred to as field of view (FOV). To steer the beam to a specific direction θ_0, the same phase difference ϕ_a should be applied between the successive elements of a uniform array, equal to

$$\phi_a = kd\sin\theta_0 \tag{2.16}$$

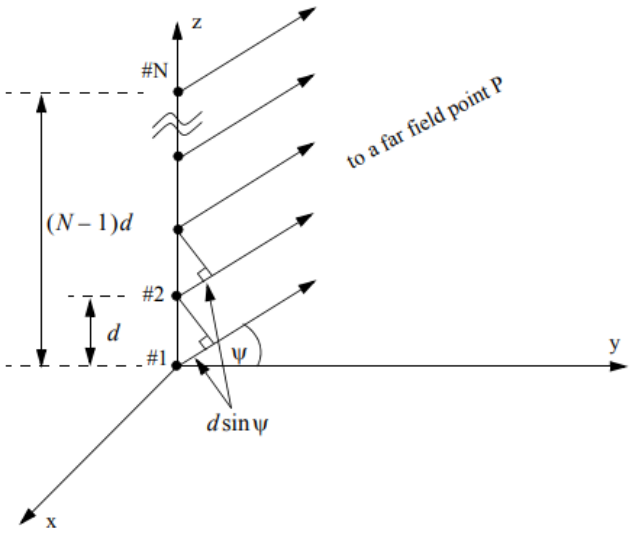

Figure 2.8: Linear array of equally space elements.

where k is the wavenumber and d the distance between the elements. Therefore, the total applied phase shift to the N-th element equals to $(N-1)\phi_a$. When beam steering is considered ($\phi_a = kd\sin\theta_0$) the grating lobes occur at

$$|\sin\theta - \sin\theta_0| = \pm n\frac{\lambda}{d}, \qquad n = 0,1,2,\ldots \tag{2.17}$$

where θ_0 is the beam target angle. Thus, the emitter spacing should be $d < \lambda/2$ to prevent grating lobes from occurring between $\pm 90^{\circ}$. This is a practical challenge for OPAs that operate in the NIR region ($\lambda \cong 1.55$ μm), as $\lambda/2$ emitter pitch is prohibited due to cross-coupling between adjacent channels. There are different approaches to address this challenge that we discuss in the next paragraph.

For a symmetrical pattern, the half-power beamwidth θ_{3dB} (full-angle) is given as

$$\theta_{3dB} = 2|\theta_m - \theta_h| \tag{2.18}$$

where θ_m is the first maximum and θ_h is the half-power point. To determine θ_h equation (2.13) is approximated by $\mathrm{sinc}(N\xi/2) = \sin(N\xi/2)/(N\xi/2)$ for small values of θ. Thus, by solving $|\mathrm{sinc}(N\xi/2)|^2 = 1/2$, we find that the 3 dB point of the array factor occurs at

$$N\frac{\xi}{2} = \pm 1.391 \tag{2.19}$$

Solving for θ_h yields

$$\theta_h = \sin^{-1}\left[\frac{1}{kd}\left(-\phi_a \pm \frac{2\times 1.391}{N}\right)\right] \tag{2.20}$$

and by subtituting $\phi_a = kd\sin\theta_0$ and $k = 2\pi/\lambda$

$$\theta_h = \sin^{-1}\left(-\sin\theta_0 \pm 0.443\frac{\lambda}{L}\right) \tag{2.21}$$

where $L = Nd$ the length of the linear aperture. For large values of L and $\theta_0 = 0$ (no beam steering) the half-power beamwidth is

$$\theta_{3dB} = 2\theta_h = 0.886\frac{\lambda}{L} \tag{2.22}$$

The above expression is valid when the array is uniformly illuminated. However, if tapering is applied, it is modified by a factor that accounts for beam broadening.

In the case of beam scanning, the half-power beamwidth is described by

$$\theta_{3dB\ (scanning)} = \sin^{-1}\left(\sin\theta_0 + 0.443\frac{\lambda}{L}\right) - \sin^{-1}\left(\sin\theta_0 - 0.443\frac{\lambda}{L}\right). \tag{2.23}$$

For a large array, the beamwidth computed from the above expression increases approximately as $1/\cos\theta$, and thus it can be approximated as

$$\theta_{3dB\ (scanning)} \cong \frac{\theta_{3dB}}{\cos\theta_0} \tag{2.24}$$

Figure 2.8 shows the array factor of a uniform linear array for $\phi_a = \pm\pi/2$ with emitter pitch of d = 2, 6 and 10 μm and operating wavelength λ = 1.55 μm, as well as the corresponding applied phase shift to each element of the array. Higher order lobes (grating lobes) are formed in all the cases, although in the case of d= 2 μm, there are not visible within the FOV of ± 20 degrees. In the cases of $d = 6$ μm and $d = 10$ μm, the higher order grating lobes fall within the presented FOV. The following points can be noted:

- The far-field intensity lobes can be directed at different angles by adjusting the phase configuration. This is the basic concept of beam steering with phased arrays.
- Grating lobes are formed when $d > \lambda/2$. As the distance between the emitters increases the grating lobes move closer to the main lobe, reducing the FOV.
- The lobes become narrower as the element spacing increases. This is because the total emitting aperture of the array becomes larger.
- Low intensity sidelobes are formed around the main lobe. This is due to the discrete nature of the array, which forms a wavefront with discretized phase gradient [106].
- The total radiation intensity is the outcome of the multiplication of the array factor with the pattern of the elementary emitter.

When beam steering is applied the phase difference ϕ_a takes values in the range $[-\pi,\ \pi]$. From (2.17) follows that for $\phi_a = \pm\pi$, the 1st order grating lobe appears at the angle of the main lobe's direction with the opposite sign, i.e., the main lobe and the 1st grating lobe are symmetrical around 0. Thus, steering beyond $\phi_a = \pm\pi$ will push the 1st grating lobe into the steering range of the main lobe and will make beam steering

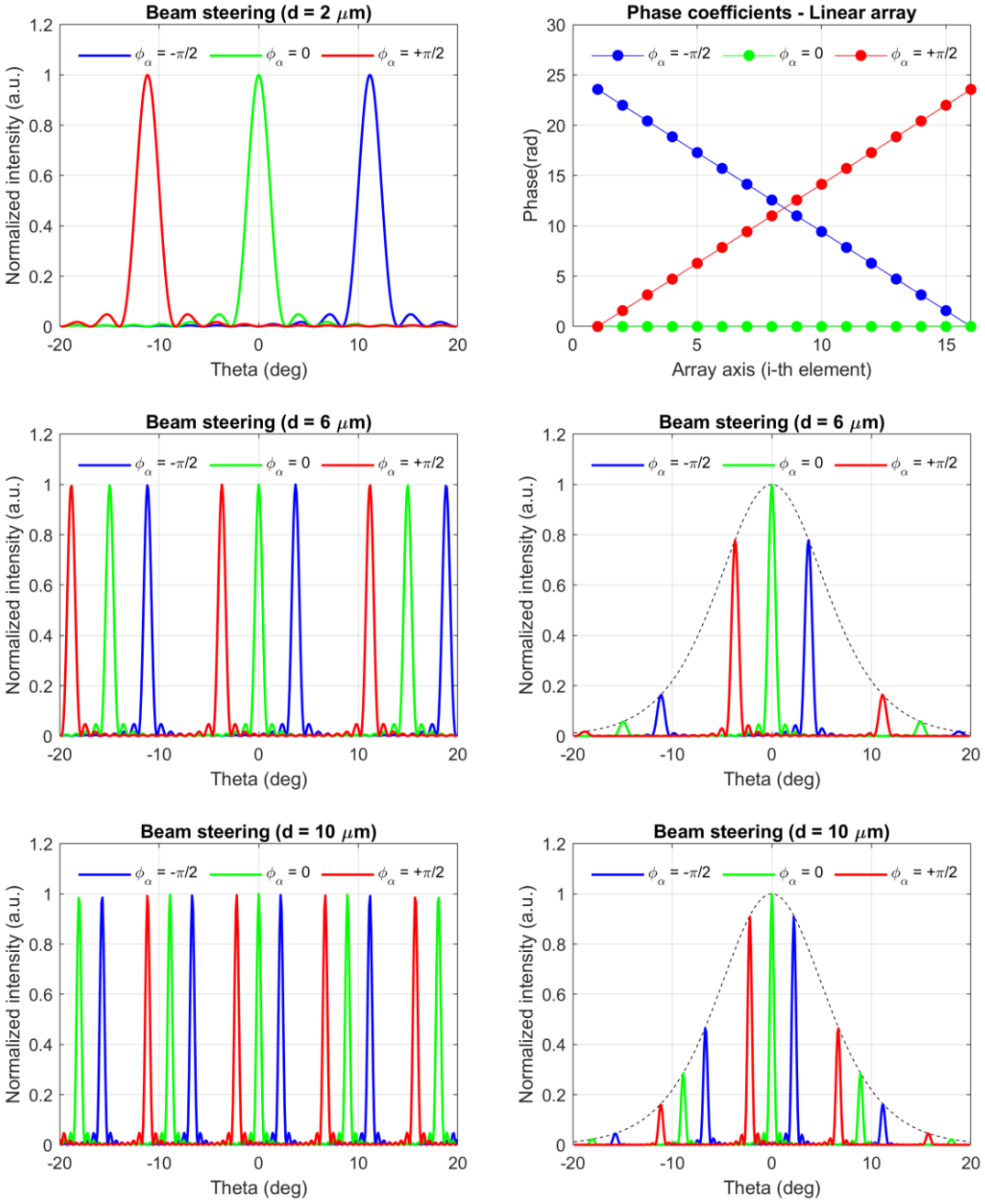

Figure 2.9: Beam steering in a linear 16-channel array with element pitch d = 2 μm, 6 μm and 10 μm, operating wavelength 1.55 μm, and progressive phase excitation between the elements $\Delta\phi = \phi_a$. (Left) Array factor for $\phi_a = 0$ and $\phi_a = \pm\pi/2$. (Top Right) Phase applied to each element of the array. The phase shift applied to the 16th element equals to $15\pi/2$. (Middle and Bottom Right) An example radiation pattern as formed after the multiplication of the array factor with the element pattern. The element pattern is shown with dotted line.

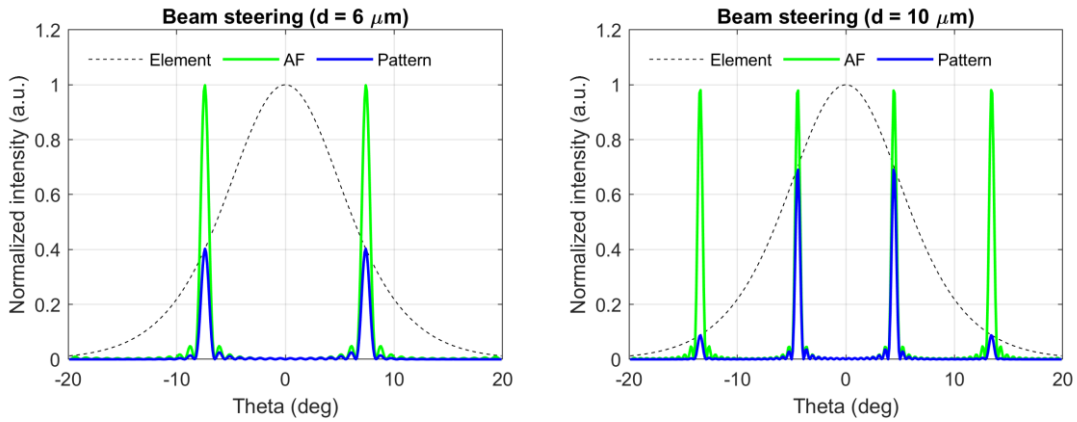

Figure 2.10: The phase difference $\Delta\phi(=\phi_a)$ between the elements takes values within $[-\pi,\ \pi]$ to achieve beam steering within the ambiguous-free FOV. The radiation pattern of a linear 16-channel array is shown when $\phi_a = \pi$, for element pitch (Left) d = 6 μm and (Right) d = 10 μm. The main lobe and the first order grating lobe are formed symmetrically around 0º. Operating wavelength is 1.55 μm wavelength.

unambiguous. Figure 2.10 shows an example radiation pattern where $\phi_a = \pi$. Finally, except from the grating lobes also sidelobes are present in the radiation pattern, where the theoretical sidelobe suppression ration (SLSR) between the main lobe and the first sidelobe is 13.26 dB [108].

2.2.4 Rectangular array

The array factor is essentially the far field of the array when each antenna is considered as an ideal point source. The concept of the linear array in the x-axis of Figure 2.8 can be extended to a rectangular $M \times N$ array in the x-y plane. The array factor in this 2-D case is

$$AF = \sum_{n=0}^{N-1}\sum_{m=0}^{M-1} \alpha_{mn} \cdot e^{jk(md_x \sin\theta\cos\varphi + nd_y \sin\theta\sin\varphi)} \tag{2.25}$$

where $\alpha_{mn} = |\alpha_{mn}|e^{j\phi_{mn}}$ is a complex number which defines the emission amplitude $|\alpha_{mn}|$ and the emission phase ϕ_{mn} of the antenna. The above expression can be decomposed into the components

$$S_x(\theta,\varphi) = \sum_{m=0}^{M-1} \alpha_m e^{jmkd_x \sin\theta\cos\varphi} \tag{2.26}$$

$$S_y(\theta,\varphi) = \sum_{n=0}^{N-1} a_n e^{jnkd_y \sin\theta\sin\varphi} \tag{2.27}$$

so that the total array factor is given as the product

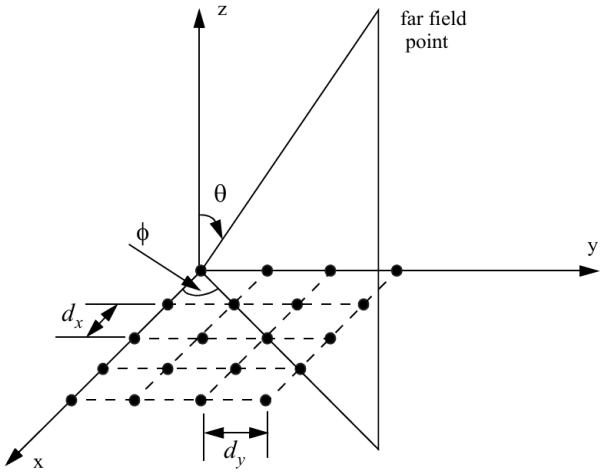

Figure 2.11: Linear array of equally space elements.

$$AF = S_x S_y. \tag{2.28}$$

The last equation indicates that the pattern of a rectangular array is the product of the array factor of the arrays in the x- and y- directions when assuming a uniform element grid. When dealing with 2D arrays it is common to use the u-v coordinates, where

$$u = \sin\theta \cos\varphi \tag{2.29}$$

$$v = \sin\theta \sin\varphi \tag{2.30}$$

and

$$\varphi = \tan^{-1}(u/v) \tag{2.31}$$

$$\theta = \sin^{-1}\sqrt{u^2 + v^2} \tag{2.32}$$

where the visible region is defined by $\sqrt{u^2 + v^2} \leq 1$. Using u-v coordinates the array factor in the more general case is written as

$$AF = \sum_{n=1}^{N}\sum_{m=1}^{M} \alpha_{mn} \cdot e^{jk(x_m u + y_n v)} \tag{2.33}$$

where (x_m, y_n) the position of the elements in the x-y plane. Figure 2.12 presents beam-steering with a rectangular 8×8 array, using a MATLAB implementation of the above equation. The lateral and vertical element pitch is set to 6 μm, which, as a result, creates grating lobes at ~15º angular distance from the main lobe. The grating lobes become more evident as the main lobe is directed to (0,5º), (5º,0) and (5º, 5º) in azimuth and elevation planes.

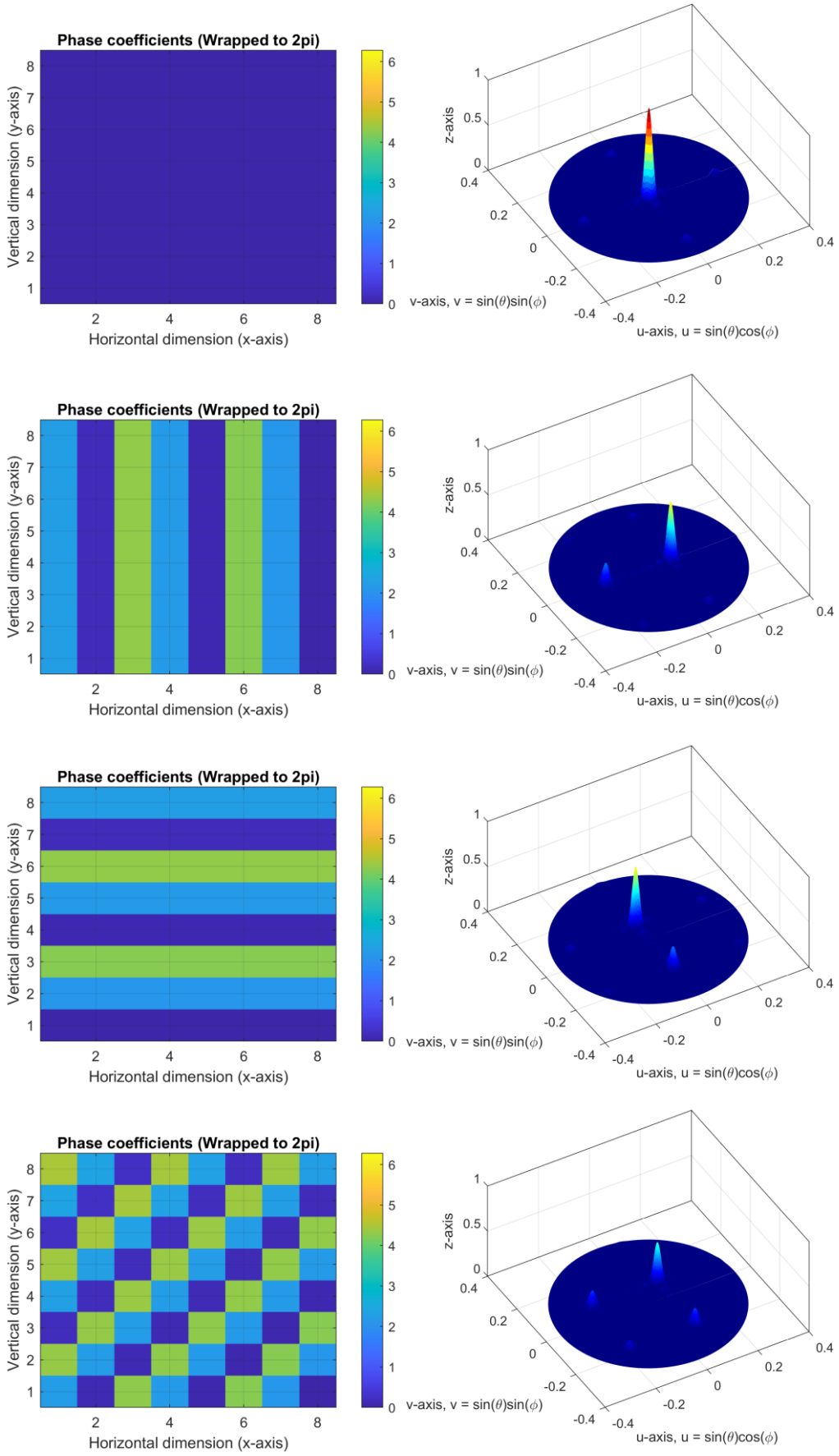

Figure 2.12: Four beam-steering scenarios with a rectangular 8×8 array operating at 1550 nm wavelength. The vertical and lateral pitch of the elements is set to 6 μm.

2.2.5 Aperture design fundamentals

Three key specifications are associated with the aperture of an OPA: (i) the beamwidth angle, (ii) the field-of-view (FOV), also referred to as the steering or scanning range, and (iii) the number of resolvable spots, defined as the ratio of the FOV to the beamwidth. Instead of beamwidth, sometimes the spot size at a certain distance is specified. Depending on the range requirement of the application the beam diameter or beamwidth is calculated, and the size of the aperture is determined. Next, based on the required FOV, the pitch between the elements is determined. The FOV is essentially the separation between the main lobe and the first grating lobe, as we discussed in 2.2.3. Ideally the elements are placed as close as possible to maximize the FOV. The required number of channels is calculated by dividing the aperture size with the pitch. Alternatively, if an aperiodic arrangement of the elements is used, the size of the aperture is divided by the average element pitch. As an example, Table 5, presents the calculated beamwidth and aperture size corresponding to a beam diameter of 10 cm at a specific distance D, ranging from 10 m to 100 m. To achieve 20 m, a beamwidth of 0.286º is required, which necessitates an aperture of approximately 177λ, or 274 μm at 1.55 μm wavelength, as calculated using equation (2.23). Assuming a uniform emitter pitch of 6 μm, a total of 46 channels would be required. Figure 2.13 illustrates the relationship between beamwidth and aperture size based on equation (2.23), as well as the FOV relative to the emitter pitch according to equation (2.17), for 1.55 μm wavelength. Figure 2.15 shows the direct relationship between beamwidth and element pitch in a uniform array. It also depicts the number of resolvable spots relative to the emitter pitch. The figure reveals that increasing the emitter pitch does not increase the number of resolvable spots, as both the beamwidth and the FOV decrease at the same rate.

Distance [m]	**Beamwidth (Half angle) [mrad](º)**	**Beamwidth (Full angle) [mrad](º)**	**Aperture size (uniform) [λ] (μm) ***
10	5.0 (0.286º)	10 (0.573º)	88 (136 μm)
20	2.5 (0.143º)	5.0 (0.286º)	177 (274 μm)
50	1.0 (0.057º)	2.0 (0.115º)	441 (684 μm)
100	0.5 (0.0286º)	1.0 (0.0573º)	886 (1373 μm)

* λ = 1.55 μm

Table 5: Calculated aperture to achieve a beam diameter of 10 cm at distance D.

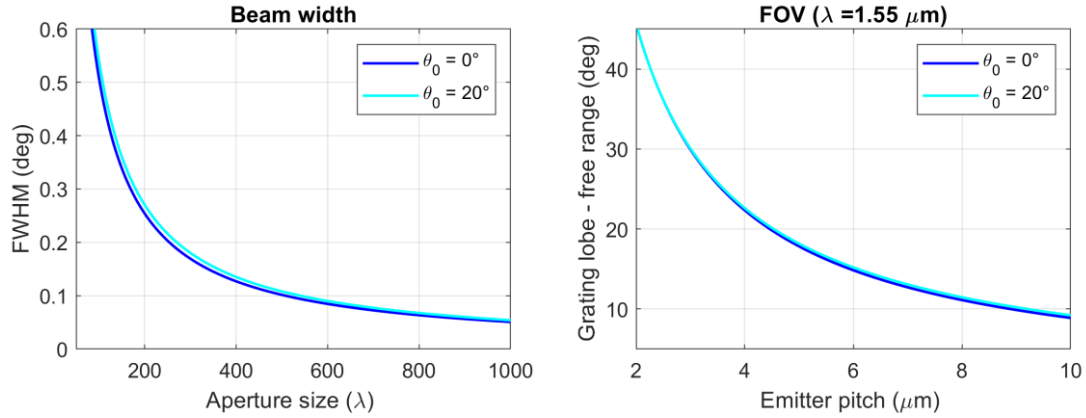

Figure 2.13: The two basic figures associated with the far-field characteristics of an OPA, described by the array factor: beamwidth and field-of-view (FOV). (Left) The beamwidth is determined by the size of the emitting aperture. (Right) The grating-lobe-free scanning range (FOV) is determined by the element pitch.

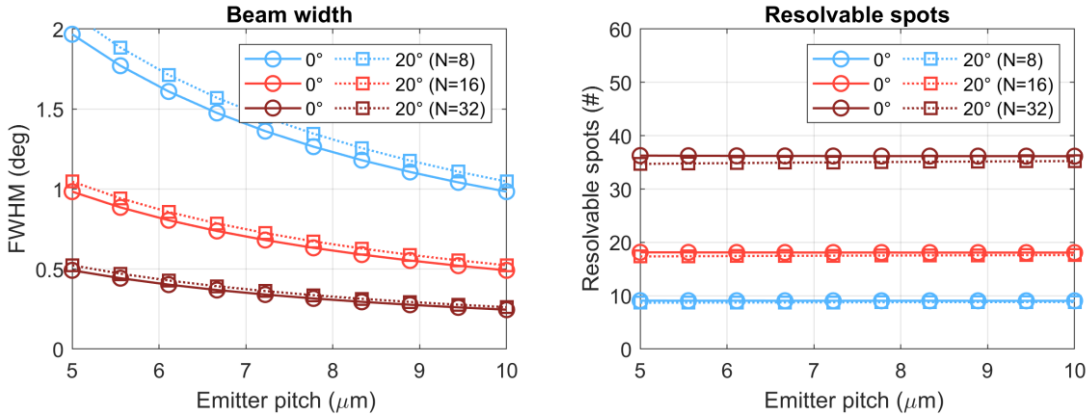

Figure 2.14: Calculated beamwidth and number of resolvable spots (i.e. field-of-view divided by beam width) relative to the emitter pitch, for unform linear arrays with N elements.

Aperture design steps

1. Define beamwidth based on range specification
2. Calculate aperture size based on beamwidth
3. Define element pitch based on FOV specification
4. Calculate the number of channels based on the aperture size and element pitch
5. Find the resolvable spots based on the beamwidth and the FOV

2.3Uniform OPAs

2.3.1 Modelling

2.3.1.1 Radiation pattern of the elementary emitter

Under the assumption that all emitters have the same radiation characteristics, the modelling of an OPA starts from the modelling of the elementary emitter. In our case the light is outcoupled to free space by the edge of the standard waveguide structure of the PolyBoard platform. The following specifications need to be determined regarding the elementary emitter: (i) the outcoupling power efficiency, (ii) the supported modes' polarization, and (iii) the divergence of the outcoupled beam. The first of the above is known; the power of the waveguided mode is emitted in-plane, i.e. along the principal axis of the waveguide. Because the beam is end-fired to the air, the backward emitting is highly suppressed. This is not always the case. For example, in the case of diffraction gratings, used as optical emitters, the optical power is outcoupled in both top and bottom out-of-plane directions, i.e. perpendicular to the grating structure. In the absence of any selectivity, only half the power is outcoupled towards the useful (top) direction and more elaborate structures are needed to redirect the bottom emitted power towards the top, to improve optical power efficiency. For the remaining two parameters (polarization dependency and beam divergence) we need to study the modes which are supported by the PolyBoard waveguide, and the corresponding free space emission pattern. To do so we use RSoft's photonic device simulation tools and MATLAB.

The geometry of the PolyBoard waveguide is shown in Figure 2.15. The cross-section is a square with a side of 3.2 μm and the refractive index of the core and the cladding is 1.48 and 1.45 respectively. This geometry provides single mode operation at 1550 nm with equally supported TE and TM components due to its symmetry. We calculate the supported modes using the finite element method (FEM) mode solver of RSoft Synopsys (FemSIM). A mode is guided when its effective index is bounded by the refractive indices of the core and the cladding [107]:

$$n_{clad} < n_{eff} < n_{core} \tag{2.34}$$

The above criterion is only satisfied by the fundamental mode, having an effective index of $n_{eff} = 1.4637$. All the higher modes have an effective index lower than the refractive index of the cladding and thus are not guided. The fundamental mode is hybrid TE and TM,

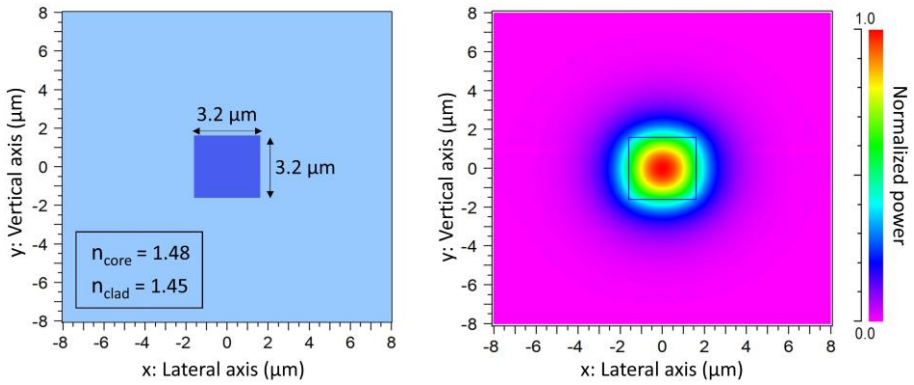

Figure 2.15: PolyBoard single mode waveguide.

as both E_x and E_y components of the electric field are equally present, and the same is true for the components of the magnetic field (we assume propagation on the z-axis). We then excite the waveguide with the calculated fundamental mode, and we record the amplitude and phase of the field after some propagation distance L, at the end-facet of the waveguide. Apart from power attenuation no other effects are observed on the propagating mode. For the calculation we employ the beam propagation method (BPM) using RSoft's BeamPROP tool. The field recorded by the monitor is then used to derive the radiation pattern of the waveguide as described next.

To calculate the far-field radiation of the edge-emitting waveguide we borrow a method from microwave antennas, which is based on the Field Equivalence Principle [108]. This method makes use of the idea that the fields outside an imaginary closed surface can be obtained by placing suitable electric- and magnetic-current densities on the surface, which satisfy the boundary conditions, and yield the same fields outside the surface as the actual radiation source within the volume enclosed by the surface. In the case of rectangular aperture antennas, the imaginary surface S is assumed to be on the plane of the antenna aperture, in our case the end-facet of the waveguide, enclosing the radiation source by extending to the infinity. This geometry is illustrated in Figure 2.16. An electric current density $\boldsymbol{J}_S$ and a magnetic current density $\boldsymbol{M}_S$ reside on the surface S and yield the fields $\boldsymbol{E}_1$ and $\boldsymbol{H}_1$ on the region outside the surface, i.e., at the front of the waveguide's facet, which is in fact the region of interest. Since the region enclosed by S, i.e. the region behind the waveguide facet, is out of interest, the fields $\boldsymbol{E}_0$ and $\boldsymbol{H}_0$ within S can be assumed to take any value, and it is obviously convenient to assume that they are zero (Love's Equivalence Principle). In this way, the boundary conditions for the tangential field components on the surface S can be written:

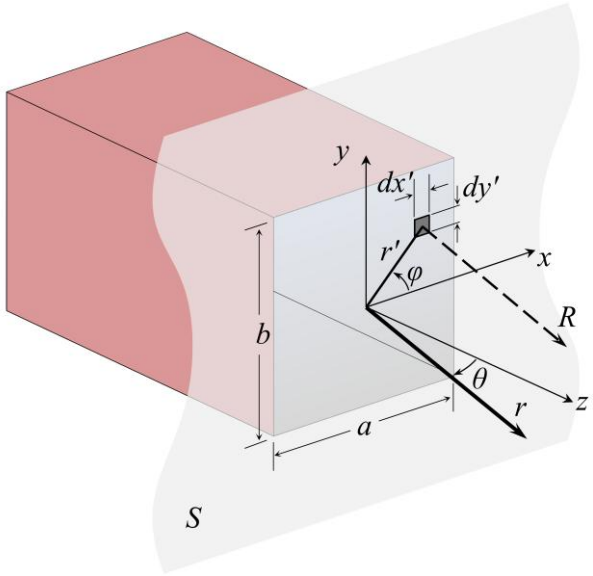

Figure 2.16: Modelling of the PolyBoard waveguide as an aperture antenna using the field equivalence principle. The imaginary surface S extends to the infinity.

$$\boldsymbol{J}_S = \hat{n} \times (\boldsymbol{H}_1 - \boldsymbol{H}_0)|_{H_0=0} = \hat{n} \times \boldsymbol{H}_1$$
$$= \hat{z} \times \left(\hat{x}H_{1x} + \hat{y}H_{1y}\right) = \hat{y}H_{1x} - \hat{x}H_{1y} \quad (2.35)$$

$$\boldsymbol{M}_S = -\hat{n} \times (\boldsymbol{E}_1 - \boldsymbol{E}_0)|_{E_0=0} = -\hat{n} \times \boldsymbol{E}_1$$
$$= -\hat{z} \times \left(\hat{x}E_{1x} + \hat{y}E_{1y}\right) = -\hat{y}E_{1x} + \hat{x}E_{1y} \quad (2.36)$$

where $\hat{n}$ the unit vector normal to S. The components E_{1x}, E_{1y}, H_{1x}, H_{1y} at the outer side of the surface can be connected in a straightforward way to the components E_x, E_y, H_x, H_y measured at the waveguide's facet. The refractive index change is also taken into account as the mode leaves the dielectric waveguide and propagates into the air. Since the TE mode has non-zero only the E_x and H_y components and the TM mode only the E_y and H_x components, equations (2.35) and (2.36) can be further simplified if the propagating mode inside the optical waveguide has only TE or TM polarization:

$$\boldsymbol{J}_S^{TE} = -\hat{x}H_{1y} \quad (2.37)$$

$$\boldsymbol{J}_S^{TM} = \hat{y}H_{1x} \quad (2.38)$$

$$\boldsymbol{M}_S^{TE} = -\hat{y}E_{1x} \quad (2.39)$$

$$\boldsymbol{M}_S^{TM} = \hat{x}E_{1y} \quad (2.40)$$

In either polarization case, the equivalent sources $\boldsymbol{J}_S$ and $\boldsymbol{M}_S$ derived from the above equations can be used for the calculation of the normalized magnetic and electric vector potentials $\boldsymbol{N}$ and $\boldsymbol{L}$ related to the far-field radiation. Using again the geometry of Figure

2.16, and working with spherical coordinates, the relations between the equivalent sources and the $\hat{\theta}$ and $\hat{\varphi}$ components of the vector potentials take the following form:

$$N_\theta(\theta,\varphi) = \iint_S \left[J_x \cdot cos\theta \cdot cos\varphi + J_y \cdot cos\theta \cdot sin\varphi\right] e^{jkr'cos\psi} ds' \tag{2.41}$$

$$N_\varphi(\theta,\varphi) = \iint_S \left[-J_x \cdot sin\varphi + J_y \cdot cos\varphi\right] e^{jkr'cos\psi} ds' \tag{2.42}$$

$$L_\theta(\theta,\varphi) = \iint_S \left[M_x \cdot cos\theta cos\varphi + M_y \cdot cos\theta sin\varphi\right] e^{jkr'cos\psi} ds' \tag{2.43}$$

$$L_\varphi(\theta,\varphi) = \iint_S \left[-M_x \cdot sin\varphi + M_y \cdot cos\varphi\right] e^{jkr'cos\psi} ds' \tag{2.44}$$

In equations (2.41)-(2.44), the parameters θ and φ are the spherical coordinates of the observation point in the far-field, k is the wavenumber in free space, $ds' = dx' \cdot dy'$ is the differential area on the surface S of the integration, r' is the amplitude of the vector corresponding to the differential area, and ψ the angle between the vectors $\boldsymbol{r'}$ and $\boldsymbol{r}$ that correspond to the differential area and the observation point, respectively. For the selected geometry, the factor $r'cos\psi$ takes the form:

$$r'cos\psi = x' \cdot sin\theta cos\varphi + y' \cdot sin\theta sin\varphi \tag{2.45}$$

Finally, the electric and magnetic fields that are radiated by the rectangular aperture antenna in the far-field can be calculated using the vector potentials from equations (2.41)-(2.44) accordingly:

$$E_r(\theta,\varphi) \cong 0 \tag{2.46}$$

$$E_\theta(\theta,\varphi) \cong -\frac{i \cdot k \cdot e^{-i \cdot k \cdot r}}{4\pi r}\left[L_\varphi(\theta,\varphi) + \eta \cdot N_\theta(\theta,\varphi)\right] \tag{2.47}$$

$$E_\varphi(\theta,\varphi) \cong \frac{i \cdot k \cdot e^{-i \cdot k \cdot r}}{4\pi r}\left[L_\theta(\theta,\varphi) - \eta \cdot N_\varphi(\theta,\varphi)\right] \tag{2.48}$$

$$H_r(\theta,\varphi) \cong 0 \tag{2.49}$$

$$H_\theta(\theta,\varphi) \cong \frac{i \cdot k \cdot e^{-i \cdot k \cdot r}}{4\pi r}\left[N_\varphi(\theta,\varphi) - \frac{L_\theta(\theta,\varphi)}{\eta}\right] \tag{2.50}$$

$$E_\varphi(\theta,\varphi) \cong -\frac{i \cdot k \cdot e^{-i \cdot k \cdot r}}{4\pi r}\left[N_\theta(\theta,\varphi) + \frac{L_\varphi(\theta,\varphi)}{\eta}\right] \tag{2.51}$$

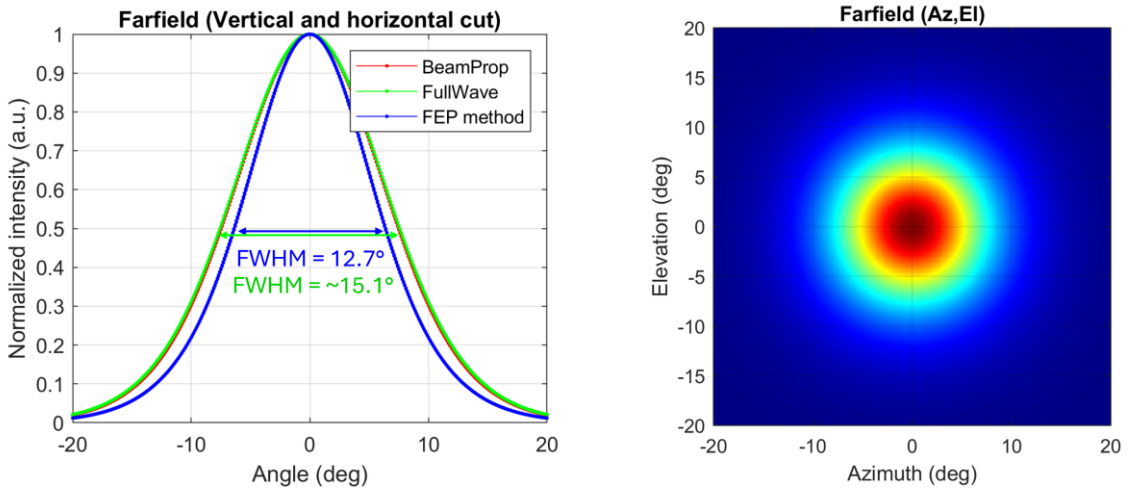

Figure 2.17: (Left) Calculated far-field radiation of the PolyBoard edge-emitting waveguide based on the modelling of the waveguide as an aperture antenna and using the field equivalence principle (FEP). For comparison the far-field calculated by Rsoft's BeamProp and FullWave simulation tool is presented (spatial grid size 0.1 μm). As we will see in the next paragraph the calculation based on our custom modelling shows better agreement with the experimental results. (Right) Far-field radiation presented in azimuth-elevation plot.

The calculation of the $\boldsymbol{E}$ and $\boldsymbol{H}$ fields can be used in turn for the estimation of other important antenna parameters such as the Poynting vector and the radiation intensity. In more detail, the time average Poynting vector is calculated as follows:

$$\boldsymbol{W}_{av}(\theta,\varphi) = \frac{1}{2}\mathrm{Re}[\boldsymbol{E} \times \boldsymbol{H}^*] \tag{2.52}$$

Taking into account that the radial components of the $\boldsymbol{E}$ and $\boldsymbol{H}$ fields are practically zero, equation (2.52) can be written as:

$$\boldsymbol{W}_{av}(\theta,\varphi) = \frac{1}{2}\mathrm{Re}\left[E_\theta \cdot H_\varphi^* - E_\varphi \cdot H_\theta^*\right] \cdot \hat{r} \tag{2.53}$$

The magnitude of the time average Poynting vector in the far-field is denoted as W_{rad} and describes the radiated power density (or radiation density) in W/m^2. Finally, the far-field parameter that we want to derive is the radiation intensity U_0, which describes the power radiated by an antenna per unit solid angle. It is expressed in W/unit solid angle, and is associated with the radiation density via the following mathematical expression:

$$U_0 = r^2 \cdot W_{rad}(\theta,\varphi) \tag{2.54}$$

Although the solution is analytical, equations (2.41)-(2.44) show that integration over the defined surface is required, and thus the degree of accuracy depends on the resolution of the fields over the surface. The calculation is implemented in a MATLAB script, which

takes as input the $\boldsymbol{E}$ and $\boldsymbol{H}$ fields at the end-facet of the waveguide (near field) and calculates the far-field radiation intensity based on the equations presented above.

The motivation for adopting the above method, derived from microwave theory, lies in its higher accuracy, despite requiring longer computation times. Most commercially available photonic simulation tools, such as RSoft and Lumerical, use Fourier transforms of the near-field to generate far-field radiation patterns. Figure 2.17 compares our modeling with the far-field calculation tools provided by RSoft (BeamProp and FullWave). In the following section, where experimental results are presented, it will become evident that our model shows better agreement with the measurements.

2.3.1.2 Minimum waveguide spacing

The ideal spacing between emitters is half the operation wavelength (λ/2), otherwise grating lobes are formed in the radiation pattern, that limit the ambiguity-free scanning range. Another drawback from the formation of grating lobes is that part of the outcoupled optical power is directed to angles other than the desired one, i.e., the angles of the grating lobes. Ideally, we would like to have all the optical power concentrated inside one lobe, i.e., the main lobe. Half-wavelength spacing though is often unachievable due to cross-coupling between optical waveguides. Therefore, if the grating lobes cannot be avoided altogether, the goal becomes to push them to the widest possible angle by placing the emitters as close as possible. To do so we investigate the minimum acceptable distance between two waveguides for a given co-propagation distance, so that the fields propagating through the waveguides remain relatively isolated. This practically means that the interaction between the two co-propagating fields does not alter their amplitude and phase by a significant amount. The last point is crucial since the OPA works under the assumption that every emitter acts independently, with a well-controlled amplitude and phase.

The power exchange between two parallel single-mode waveguides in proximity is described by coupled-mode theory. The power that is transferred from a waveguide "A" to a parallel waveguide "B" after some propagation distance z, assuming that only waveguide "A" is excited, is given by the following equations:

$$P_A(z) = P_0 - P_B(z) \tag{2.55}$$

$$P_B(z) = P_0 \frac{\kappa^2}{\kappa^2 + \delta^2} \sin^2\left(\sqrt{\kappa^2 + \delta^2} \cdot z\right) \tag{2.56}$$

, where κ is the coupling constant and δ is the phase mismatch,

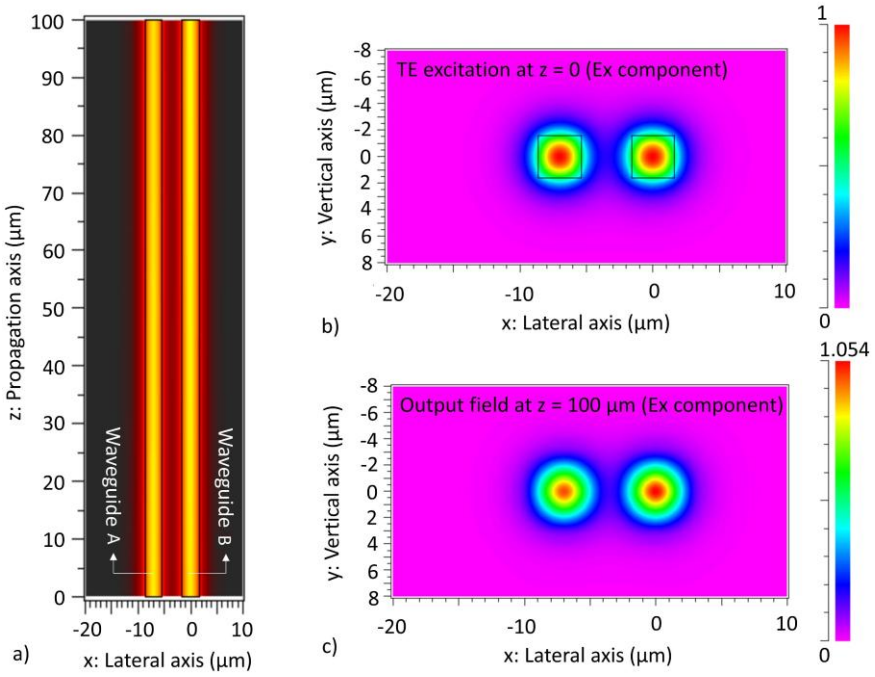

Figure 2.18: (a) Simulation of cross-coupling between two PolyBoard waveguides with 7 µm distance. (b) Excitation of the waveguides with equal amplitude TE modes. The phase of excitation of waveguide "A" is swept from -180º to 150°, while the phase of excitation of waveguide "B" is kept constant at 0º. (c) Output fields at z = 100 µm for the case of 30º phase excitation difference. The asymmetry in the amplitude due to cross-coupling is clear.

$$\kappa = \kappa_{AB} = \kappa_{BA} = \frac{\omega}{4}\iint (\varepsilon' - \varepsilon)(\boldsymbol{\mathcal{E}}_A^* \cdot \boldsymbol{\mathcal{E}}_B)dxdy \tag{2.57}$$

$$2\delta = (\beta_A - \beta_B) = \Delta\beta \tag{2.58}$$

, $\varepsilon'(x,y) - \varepsilon(x,y) = \Delta\varepsilon(x,y)$ is the dielectric perturbation due to the presence of the other waveguide, and $\boldsymbol{\mathcal{E}}_A$ and $\boldsymbol{\mathcal{E}}_B$ the amplitude of the propagating field in the corresponding waveguide [109]. For identical waveguides $\Delta\beta \cong 0$. The coupling constant is analytically calculated for a specific waveguide geometry. In addition to coupled mode analysis, a method known as super-mode analysis can be used for approximate solutions [109][110].

Another approach to study cross-coupling between waveguiding structures is to use a numerical simulation tool. In our study we used BPM (RSoft's BeamPROP). To evaluate the strength of the waveguide coupling in relation to the pitch we take the simplest case of two parallel PolyBoard waveguides with co-propagation distance of 100 µm. The specific length had been chosen according to the length of the s-bends that are required for reducing the waveguide pitch at the emitting edge of the chip. The length of the s-bends is associated with the number of waveguides in the OPA, i.e., number of channels, which in our case is four per waveguiding layer (see Figure 2.25). Both waveguides are excited by their fundamental eigenmode with TE polarization and peak amplitude normalized to unity. The

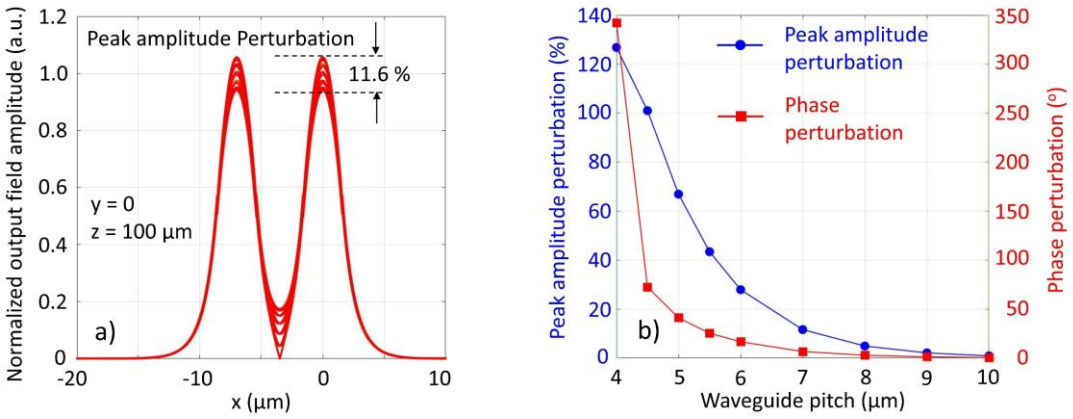

Figure 2.19: (a) Example of amplitude perturbation in the output field of waveguide "B" (after 100 μm propagation) due to the phase variation in the excitation of waveguide "A" placed at 7 μm distance. (b) Amplitude and phase perturbation at the center of the output of waveguide "B" as a function of the pitch.

phase of the excitation field in waveguide "*B*" is zero, whereas the phase of the excitation field in waveguide "*A*" varies from -180° to +150°. The simulation setup is shown in Figure 2.18, for the example case of 7 μm waveguide pitch and 30° phase excitation difference. The beam propagation pattern is shown, as well as the distribution of the excitation fields ($z = 0$) and output fields ($z = 100$ μm). The perturbation of the amplitude and the phase of the output field of waveguide "B" with respect to the corresponding amplitude and phase when the waveguide is alone, depends on the pitch, as well as on the phase, of the excitation field at the input of waveguide "A". Thus, the perturbation level at the center of cross-section of waveguide "B" serves as a metric for the assessment of the isolation between the waveguides (see Figure 2.19(a)). Figure 2.19(b) summarises our results for pitch values from 4 μm up to 10 μm. As shown, for pitch equal or larger than 8 μm, the perturbation is negligible, and the waveguides remain practically decoupled. For pitch between 8 and 6 μm, the perturbations start rising, but remain moderate, whereas for pitch below 6 μm, the rise becomes much more abrupt. Based on these observations, we concluded that the value of 6 μm is a safe lower limit for the waveguide pitch.

To evaluate the effect of cross-coupling on the radiation pattern we extend our study in the following way. At $z = 100$ μm we introduce a free space section in our simulation domain, and we use a monitor to capture the near-field from the emission of the two waveguides into the free space. Subsequently, we use the recorded field (amplitude and

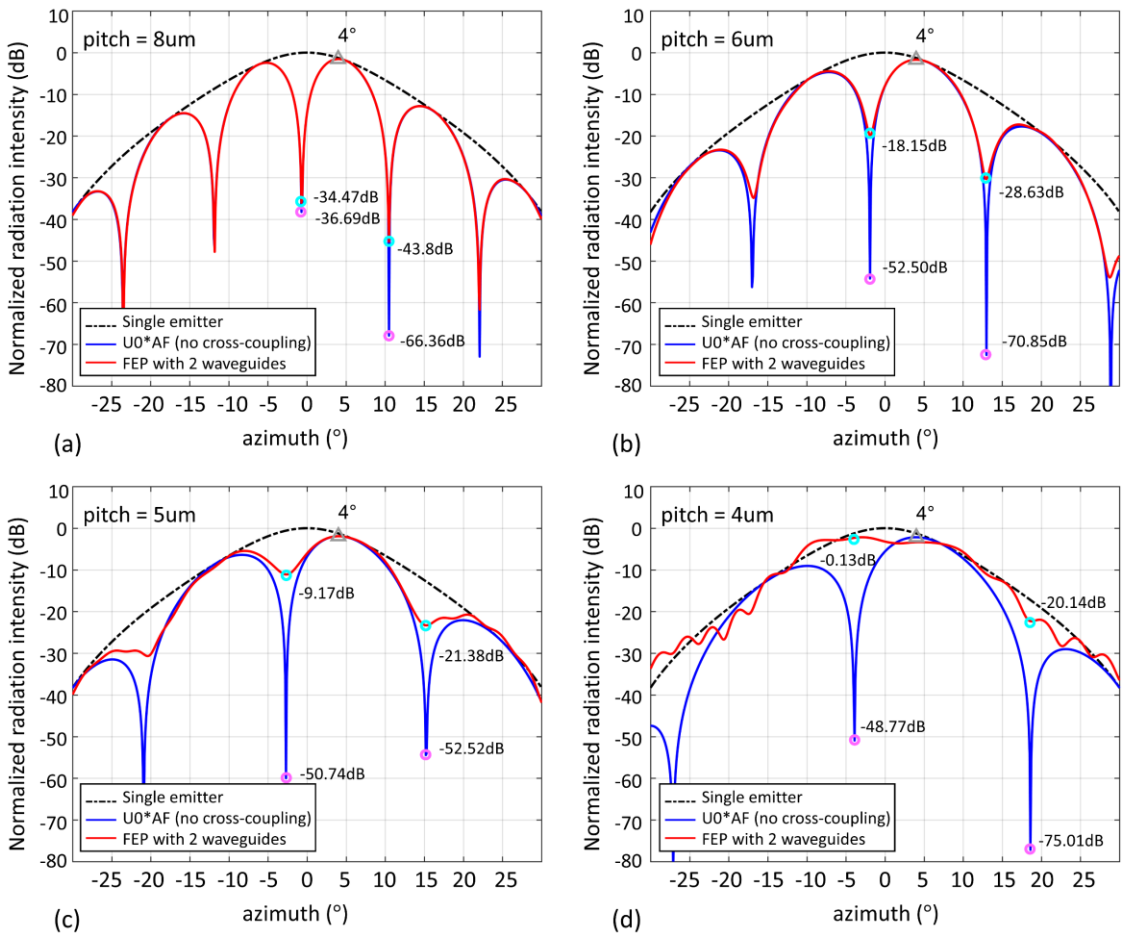

Figure 2.20: Computed far-field of two edge-emitting PolyBoard waveguides for different spacing between the waveguides to demonstrate the effect of cross-coupling. The quality of the radiation pattern degrades as the spacing between the waveguides decreases. In the case of 4 μm spacing the cross-coupling is so severe that lobe formation is completely prevented.

phase) to calculate the far-field with the method described in 2.3.1.1. Since the field that serves as input to the method is the result of the propagation of the optical waves inside the two parallel waveguides, this method clearly takes into account the effect of cross-coupling. For reference, we calculate the far-field using equation (2.33), which assumes independent antenna elements, and thus, no cross-coupling is considered. Therefore, any difference between the results from the two methods can be attributed to the impact of optical crosstalk. The plots in Figure 2.20 present in logarithmic scale the normalized radiation intensity for different waveguide pitch. The angles where destructive interference occurs ("nulls") are the most indicative points for the comparison. As observed, for 8 μm pitch the radiation pattern remains almost unaffected by cross-coupling, whereas the difference between the two curves becomes substantially larger as the pitch decreases. In the case of 4 μm pitch where formation of lobes is entirely prevented. The relative excitation phase difference between the two waveguides is configured for beam steering at 4°.

2.3.2 Experimental results

2.3.2.1 Experimental setup

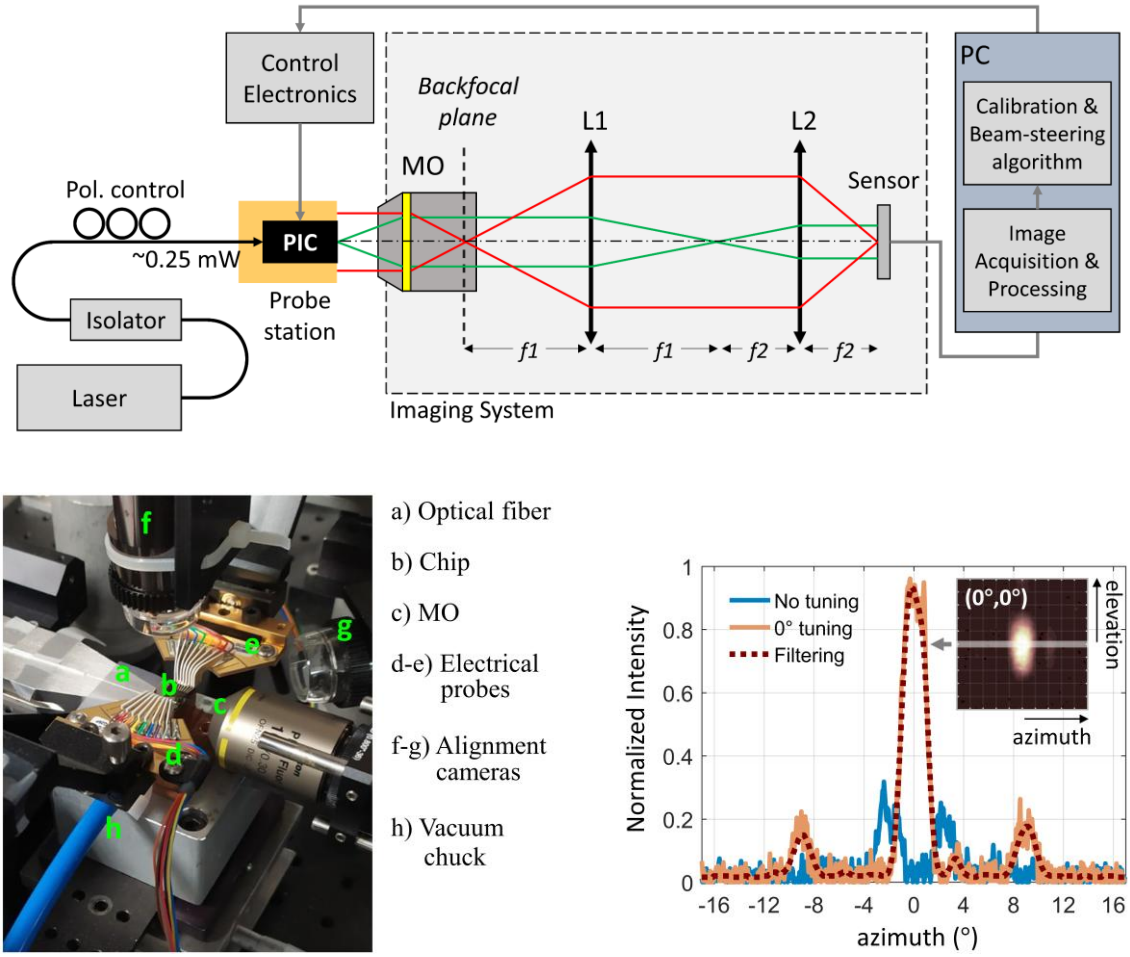

Figure 2.21: (Top) Illustration of the setup for characterizing the radiation pattern. (Left) Picture of the probe station that facilitated the optical coupling and provided access to the electrical pads of the chip via electrical probes. The microscope objective (MO) that collects the outcoupling light from the chip is also visible. (Right) Example radiation pattern captured with the CCD sensor. The line plot corresponds to the zero-elevation row from the captured frame. The pattern before tuning the phase heaters of the chip is random (blue curve), while after calibrating the phase heaters the output beam converges to 0 degrees (orange curve).

For the characterization of the radiation pattern of the fabricated OPA chips we developed the experimental setup presented in Figure 2.21. Coherent light in the C-band, provided by a pigtailed distributed feedback (DFB) laser, is coupled into the chip by means of an optical alignment stage. A fiber optic isolator is used to protect the laser source from any back reflections that may be present due to the edge-coupling between the fiber and the chip. Furthermore, a polarization controller is employed to manually adjust the polarization of light coupled into the chip. To achieve efficient coupling from the fiber to the PolyBoard waveguide a lensed tip fiber with 6 μm focal length and 6 μm mode field diameter (MFD)

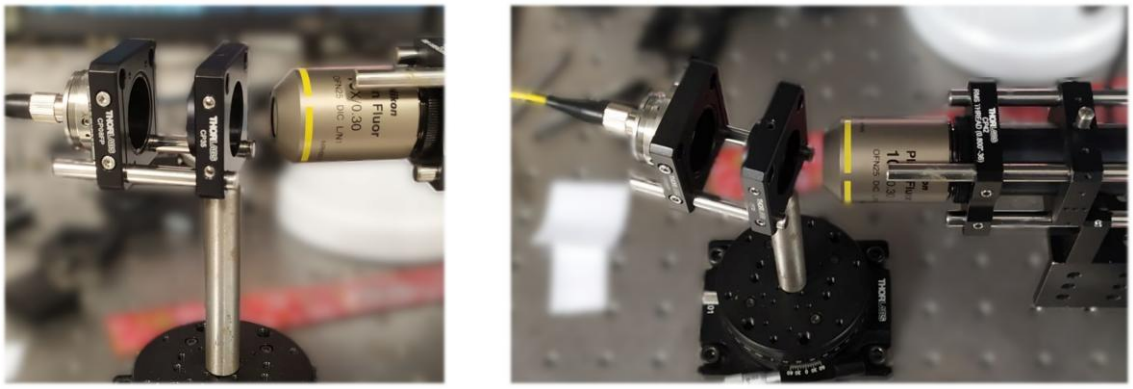

Figure 2.22: (Left) Close-up and (Right) top view of the setup for the calibration of the imaging system. A collimated fiber output is aligned with the principal axis of the imaging system. The collimated beam can be rotated by a known amount with the help of a rotation stage while the rotation axis is positioned on the focal point of the microscope objective (MO). By rotating the beam and marking the illuminated pixels in the captured image we can calibrate the image in terms of angle of acceptance. The procedure is performed twice: for the horizontal (azimuth) and vertical (elevation) axis of the image.

is employed. To perform the edge-coupling between the fiber and the chip we use a six-axis positioning stage with sub-micron resolution, although control of the three axes (XYZ) is sufficient for the alignment. Light outcoupled from the opposite edge of the chip is collected by an imaging system that can facilitate either far-field or near field imaging. The captured data are digitized and sent to a PC. The heating elements on the chip are accessed via probe tips connected to a multi-channel current driver, which can be controlled via the PC. By running python scripts on the PC we are able to program the chip and converge the output beam to the desired outcoupling angle.

The imaging system comprises a microscope objective (MO), a pair of lenses and a charge-coupled device (CCD) sensor. The pair of lenses forms a 4-f (Fourier) system that transfers the rear focal plane of the MO (i.e., the Fourier image) to the camera with a defined image ratio, enabling far-field measurements [111]. Moreover, by removing lens “1” we can record the near field (i.e., the real image). Therefore, the specific system offers flexibility, as far as the selection between far-field and near-field imaging is concerned. Near-field imaging is useful when we perform optical alignment, either between the fiber and the chip, or between the chip and the imaging system. The lenses of the 4-f system are achromatic doublets with focal length 100 mm and 50 mm, creating an image ratio of 1:2. By selecting the appropriate image ratio we can utilize the entire area of the sensor and achieve optimum resolution in our imaging. The sensor is a 1/2” format CCD near infra-red (NIR) analog camera by Edmund Optics with a sensing area 6.4×4.8 mm and pixel size 8.4 μm × 9.8 μm. An additional video capture device is used to convert the camera’s analog

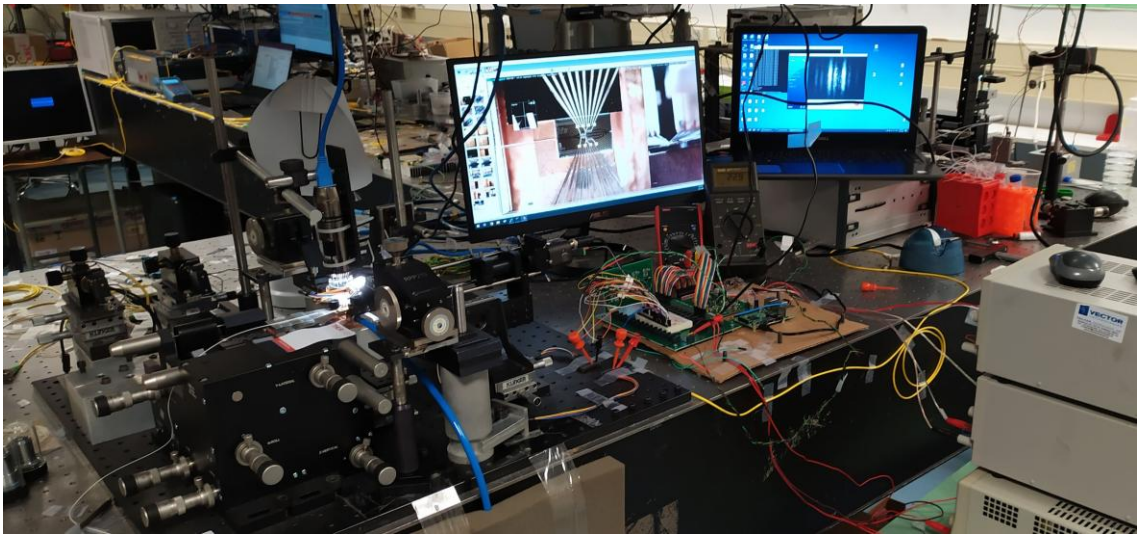

Figure 2.23: Photograph of the experimental setup.

signal to a digital signal that can be read on a PC through a usb port. The FOV of our system is 34°×28° (azimuth × elevation), defined by the 0.3 numerical aperture (NA) of the MO, while we achieve angular resolution <0.1°. The entire imaging system can be freely moved in the XYZ plane by means of a 3-axis micro-positioning stage, so that optical alignment with the chip can be accomplished. Prior to the installation of the imaging system in our setup, a characterization of the system was carried out to map each pixel of the captured image to a specific angle of acceptance, according to the method described in [112]. The angle is measured from the focal point of the MO and a zero angle corresponds to the principal axis of the optical system. For this characterization an auxiliary laser source with a collimated output beam was mounted on a rotational stage. The rotation axis of the stage was placed exactly at the focal point of the MO, where the end-facet of the chip is expected to be in the actual measurement. The spot size was adequately small to illuminate only a few pixels on the sensor. Via the rotation of the collimated beam by a known angle, it is possible to calibrate the image in terms of acceptance angle and light intensity, and to compensate for any image distortion effects originating from the lenses. In our case, however, no significant distortion was observed, except from near the image edges.

The far-field measurement procedure is the following: First, the chip is positioned on a vacuum chuck, that keeps it securly in place, and light is coupled into it with the lensed tip fiber. During this optical alignment the far-field is observed on the CCD sensor. When proper coupling is achieved a distinctive interference pattern can be observed. Next, since simply positioning the chip on the vacuum chuck does not ensure perfect alignment with the imaging system in front of the chip, further adjustment is needed. Optical alignment

between the chip and the imaging system is performed with the 3-axis positioning stage, on which the imaging system is mounted. For this alignment, lens "1" of the 4-f system is removed so that the near field is observed. Consequently, the electric probes are attached to the chip to provide access to the integrated phase heaters. Then, we run the calibration algorithm in our PC that is connected to the control electronics, and by reading the feedback from the sensor we can extract the initial phase difference between the optical paths on the chip (due to fabrication errors). After the calibration, we can employ the beam-steering algorithm to perform beam steering. We elaborate on the calibration and beam-steering algorithms in section 2.5.

2.3.2.2 Sensor noise and image processing

The sensor acquires grayscale frames of size 576 × 646, which correspond to a FOV of 28°×34° (elevation×azimuth), as defined from the optical system. The processing of the data is broadly divided into three stages: i) Noise reduction (using Gaussian filtering [113]), ii) detection of the strongest lobe, and iii) data visulization using surface and line plots. To evaluate the noise of the camera we performed a number of measurements, which we summarize in Figure 2.26. First, under conditions of total absence of illumination, we derive the average pixel value of 100 frames. We calculated that the average value of the resulting frame is ~6.3. In addition, we evaluated the spatial symmetry (horizontaly and vertically) of the sensor noise by calculating the average pixel value per column and row. Subsequently, we evaluated the noise under illumination conditions, by performing differentialmeasurements in approximately 760 frames. By subtracting two subsequent frames it is possible to cancel the contribution of the signal and measure the random fluctuations due to the noise of the sensor [114]. We derive an average pixel value of ~2.5 which suggests that the temporal fluctuation of the noise in each pixel is less than the mean value as calculated above.

Next, we evaluated the effect of Gaussian filtering on the image by varying the kernel size and the standard deviation of the distribution. Our goal is to suppress the image noise without distorting the measured beam, so that we can accurately measure its characteristics, such as shape and width. The dark noise of the camera per frame follows a gaussian distribution with mean pixel value 5.5 and standard deviation 5.8. For our image processing we selected a Gaussian filter of σ=2 and kernel size 9×9, which reduces the standard deviation to 1.3 around the mean pixel value, thus achieving a noise floor of approximately

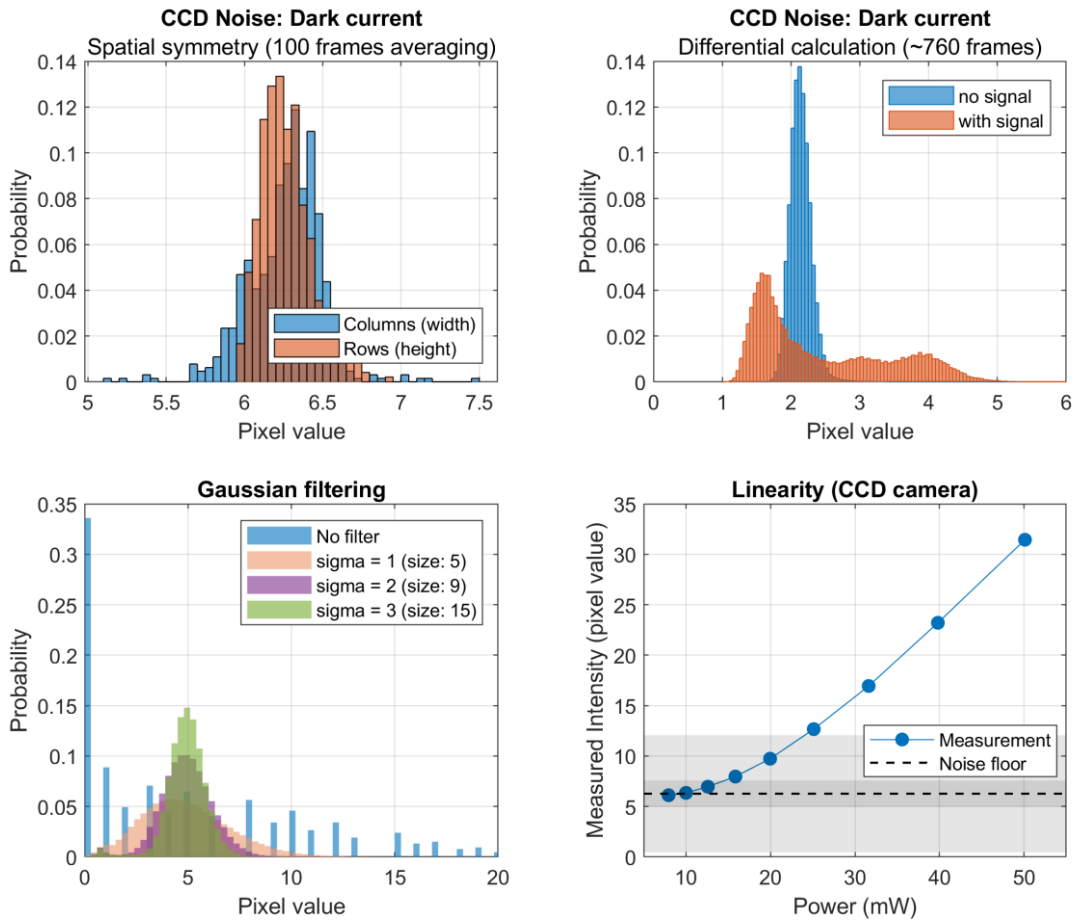

Figure 2.24: (Top Left) Spatial symmetry of the sensor noise. (Top Right) Differential calculation of the sensor noise under illumination conditions. (Bottom Left) Effect of image filtering. (Bottom Right) Characterization of the linearity of the CCD sensor (no filtering). The dotted line indicates the mean value and the gray area the standard deviation of the noise distribution. The darker gray area shows the standard deviation after applying the gaussian filtering.

-15.7 dB. Finally, we examined the linearity of the sensor and estimated its noise floor. This is important for relative measurements, such as the suppression ratio of the sidelobes, i.e., the power ratio between the main lobe and the maximum sidelobe. If the sensor is not linear then the measured suppression will be a function of the incident power to the sensor, or, equivalently, a function of the input power to the chip. Despite the fact that CCD sensors are highly linear [113], the presence of noise affects their linearity when the signal power is low. To perform the characterization we swept the laser's output power that is coupled into the chip and we integrated the pixels to derive a number corresponding to the average incident power. The resulted plot is shown in Figure 2.26. We concluded that for low intensity (< 10) noise dominates the signal zand the linearity is not ensured. However, by applying Gaussian filtering we can significantly reduce the standard deviation of the noise, as mentioned above, and lower this limit to pixel values of ~8.

2.3.2.3 Single layer OPAs

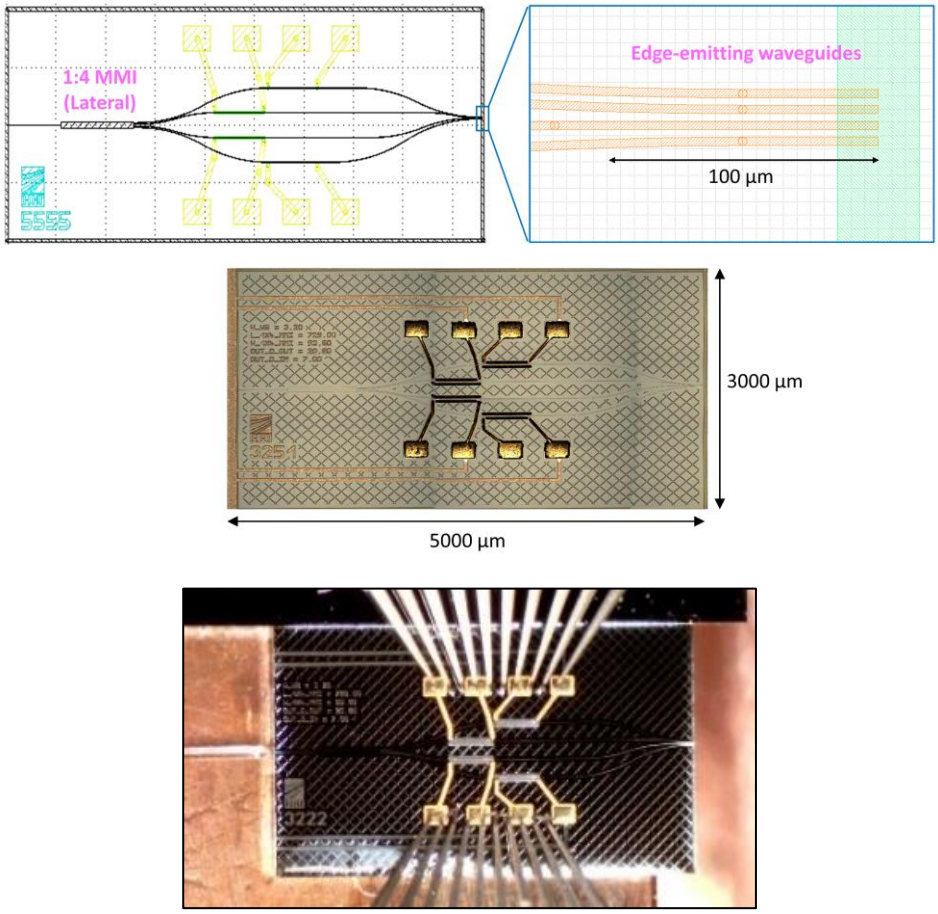

Figure 2.25: (Top Left) Mask layout of the single-layer OPAs, and (Top Right) detail of the layout at the east end of the chip, where the four emitting waveguides run in parallel, and (Middle) a photograph of the respective PolyBoard PIC. (Bottom) The PIC placed on the alignment stage. The optical fiber that is used to couple light into the chip, as well as the electrical probes to access the heaters are visible.

The first type of chips that were fabricated to showcase the potential of the PolyBoard platform for implementing OPAs were conventional single waveguiding layer PICs, comprising four-element linear OPAs. Three versions of these PICs were designed with waveguide pitch equal to 6, 8 and 10 μm, in order to experimentally validate our theoretical calculations regarding the impact of the pitch on the beam profile and FOV. Figure 2.25 presents the mask layout and a photograph of the specific version that corresponds to 6 μm waveguide pitch. On the west side of the circuit, the input light is split into four equal parts by a lateral 1:4 MMI coupler. In the output waveguides of the coupler, heating electrodes with around 20 Ohm resistance serve as thermal phase shifters for adjustment of the phase relation between the array elements. The required current at each heating electrode for half-wave phase shift is approximately 16 mA. Finally, in the east part of the circuit, the four

waveguides are brought in proximity via S-bends and run in parallel towards the end-facet of the PIC. The length of this very last section is kept short to avoid cross-coupling between the parallel waveguides. The size of the chip is 3 mm × 5 mm. Figure 2.26 presents the profile of the radiated beam for all the fabricated versions of the PolyBoard OPAs. The beamwidth, defined as the FWHM of the beam intensity, was measured 3.3°×12.7°, 2.6°×12.4° and 2.1°×12.9° for lateral pitch equal to 6 μm, 8 μm and 10 μm, respectively. As observed, the beamwidth on the elevation plane approximates the beamwidth of the single waveguide emitter, as there are no additional waveguides in the vertical direction to act on the array factor. On the azimuthal plane on the other hand, the beam width is becoming narrower as the pitch increases, which is related to the increased aperture size of the OPA, as we discussed in 2.2.5.

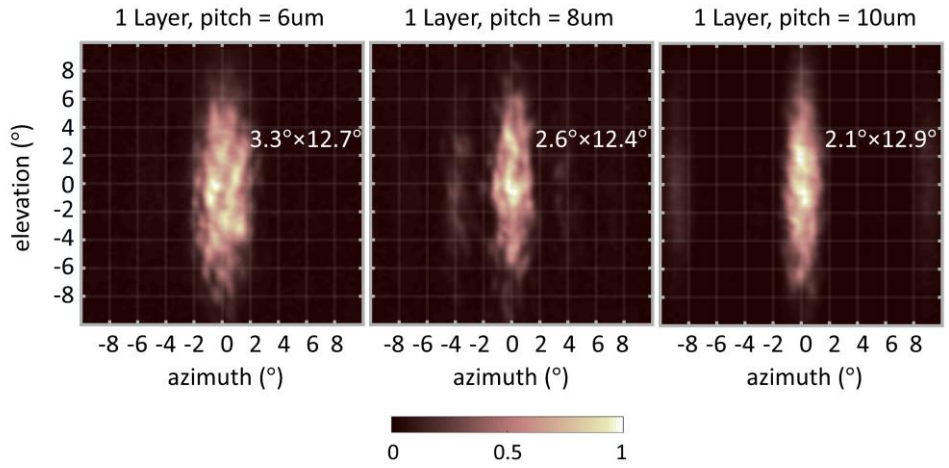

Figure 2.26: Measured beam profile of the 1×4 single-layer OPAs.

2.3.2.4 Double-layer OPAs

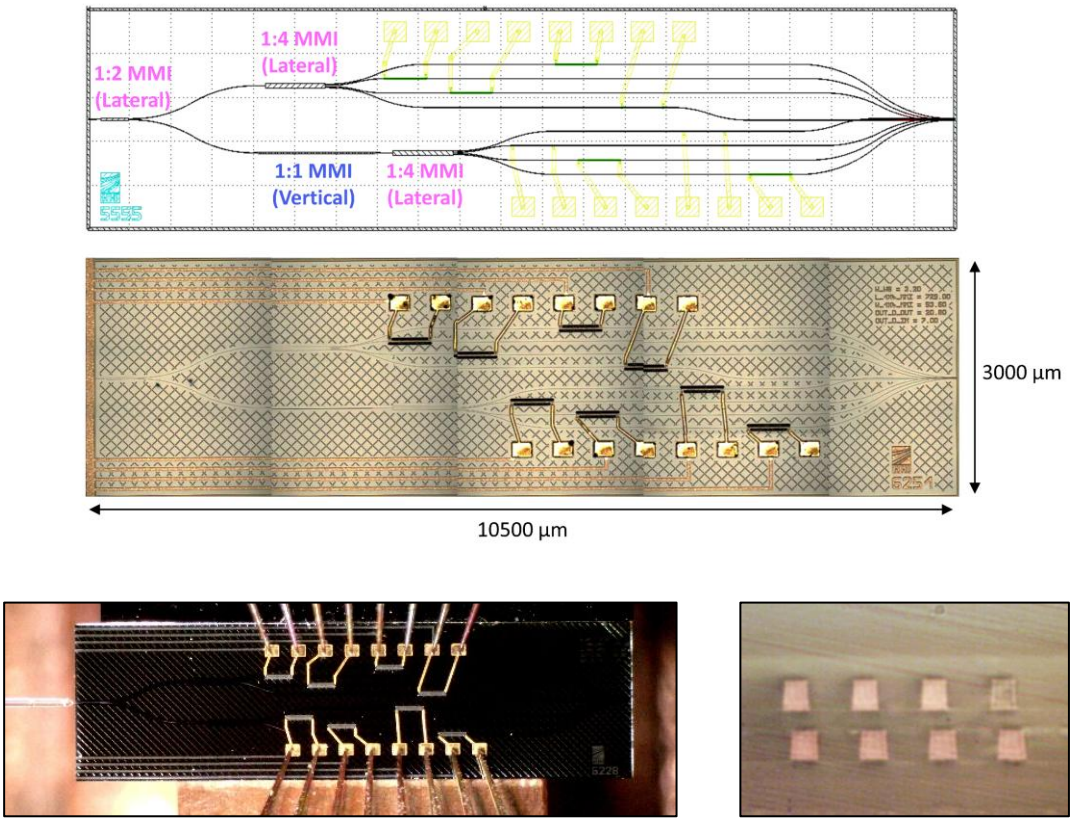

Figure 2.27: (Top) Mask layout for the fabrication of 2×4 OPAs, and (Middle) photograph of a respective PolyBoard PIC. (Bottom left) The PIC positioned on the alignment stage to perform optical coupling via a lensed optical fiber and accessed the heaters with electrical probes (500 μm pitch). (Bottom right) Micro-photograph of the end-facet of the PIC, where the edge of the waveguides that act as the optical antennas are clearly visible. The lateral pitch is 10 μm and the vertical pitch between the two waveguiding layers is 7.2 μm.

The second type of PolyBoard PICs that were fabricated comprised two waveguiding layers to accommodate the formation of 2×4 OPAs. Again, three versions of these PICs were designed, each with different lateral pitch between the waveguides at the emitting edge, equal to 6, 8 and 10 μm. The vertical pitch was 7.2 μm in all versions. Figure 2.27 presents the mask layout and a photograph of the version with 10 μm lateral pitch. On the west side of the circuit the input signal is split into two parts by a lateral 1:2 MMI coupler. The light at the second output of this coupler is transferred to the upper waveguiding layer by means of a vertical MMI coupler with 1350 μm length and 10.4 μm height. At both layers, the rest of the optical circuit is practically the same as the circuit of the single layer PICs described in the previous paragraph: the light at each layer is split into four equal parts by a lateral 1:4 MMI coupler and the optical phase inside the output waveguides is adjusted by thermo-optic phase shifters. Finally, the four waveguides are brought in proximity by

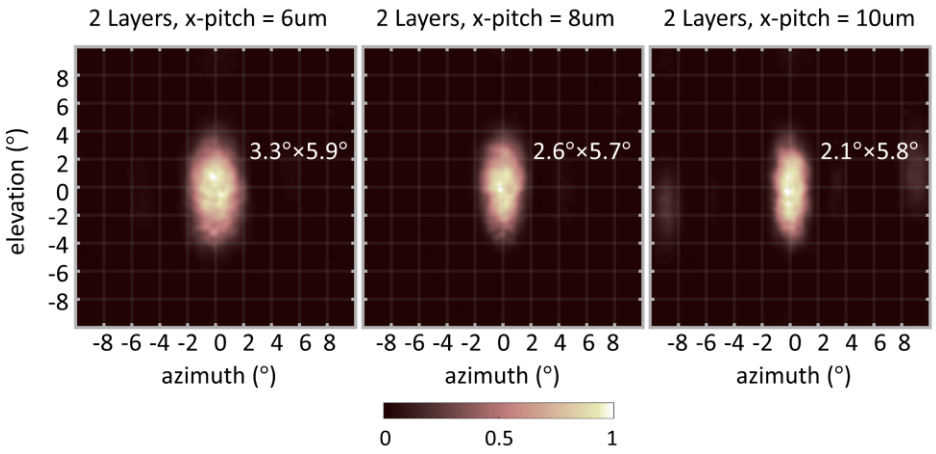

Figure 2.28: Comparison between the simulation (upper row) and the experimental (lower row) radiation patterns in the case of the 2×4 OPA and 8 μm lateral pitch in four beam steering scenarios. The intended main lobe steering angle is displayed in each frame at the top-left: 1st column scenario: (0o, 0o). 2nd column scenario: (4o, 0o). 3rd column scenario: (0o, 4o). 4th column scenario: (4o, 4o).

means of S-bends and run in parallel till the end-facet of the PIC. The linear 1×4 OPAs at the two layers are laterally aligned to each other to form a rectangular 2×4 OPA. However, an offset between the two layers is present due to fabrication errors, as it is shown in the photograph of Figure 2.27, depicting the end-facet of the chip with 10 μm lateral pitch. If needed, this fabrication error can be compensated by applying appropriate phase difference between the elements, providing that the phase of each element can be individually controlled (which is true in our case).

The formation of multiple waveguiding layers is based on the repetition of the standard steps of PolyBoard technology; a sequence of spin-coating, structuring (using UV lithography) and removal steps, as shown in Figure 2.1. It should be noted that the heating electrodes were placed over the cladding of the top layer. This suggests that the heaters controlling the top layer waveguides are situated closer to them, and thus, are more energy-efficient compared to the heaters that control the bottom layer waveguides. Consequently, placing the heaters in a single layer (for example above the top waveguiding layer, as shown here) limits the number of waveguiding layers that can be controlled, as the energy produced by the heating electrodes is dissipated in the structure. In order to scale the circuit, the phase control of the waveguides can be implemented on the top layer, before the light is transferred to subsequent layers deep in the photonic structure. A more detailed discussion regarding the scalability of such structures is included in 2.6. The measured current for half-wave phase shift was measured 16 mA and 20 mA, for the upper and lower waveguide layer, respectively. Figure 2.28 presents the measured beam profile of the 2×4

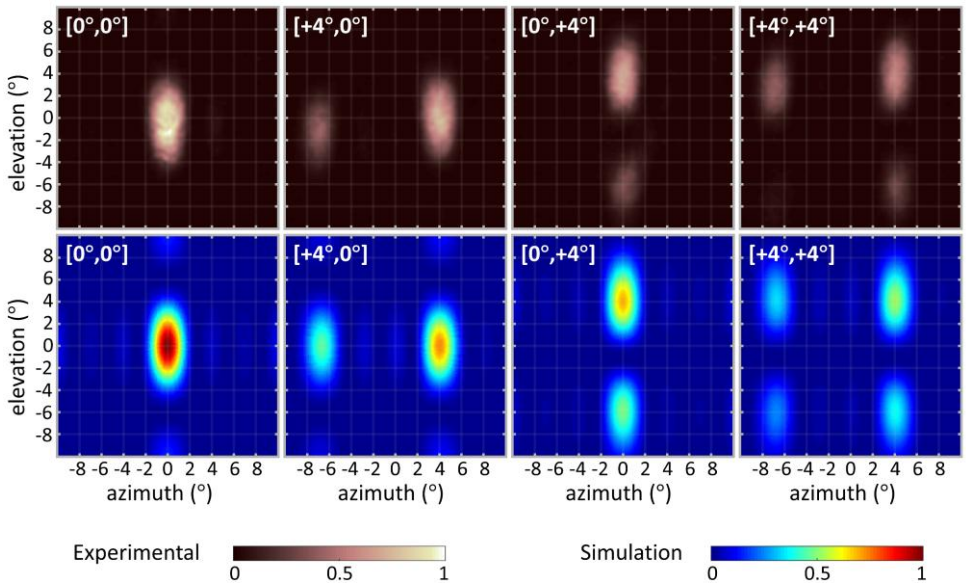

Figure 2.29: Comparison between measured (top row) and simulated (bottom row) radiation patterns in four beam steering scenarios, for the case of the 2×4 OPA with 8 μm lateral pitch.

OPA chips. The beamwidth is 3.3°×5.9°, 2.6°×5.7° and 2.1°×5.8° for lateral pitch equal to 6 μm, 8 μm and 10 μm, respectively. As observed, the addition of the second waveguide layer decreases drastically the beam width in the vertical direction. In the lateral direction, the beam is becoming narrower as the pitch increases and the overall emitting aperture becomes larger.

Figure 2.29 presents a comparison between experimental and simulation results. The experimental images (top row) are from the testing of the 2×4 OPA with 8 μm lateral pitch, and the simulation results (bottom row) are from the simulation of the far-field pattern of the same structure. According to theory, two elements with 7.2 μm pitch, and four elements with 8 μm pitch, are expected to give grating lobes at approximately 9.9° away from the main lobe in the vertical direction and 10.7° in the lateral direction. Four beam steering scenarios are presented. The first one (shown in the first column) corresponds to beam convergence at 0° both on the azimuthal and the elevation plane [0°, 0°]. No grating lobes are present in the experimental image. The second scenario (shown in the second column) corresponds to targeted beam direction at +4° on the azimuthal and 0° on the elevation plane [+4°, 0°]. A grating lobe is now present at [-6.7°, 0°], as expected. The third scenario (shown in the third column) corresponds to targeted beam direction at 0° on the azimuthal and +4° on the elevation plane [0°, +4°]. The fourth scenario (shown in the last column) corresponds to beam convergence at +4° both on the azimuthal and the elevation plane [+4°, +4°]. In this case, grating lobes are present both in the lateral and vertical direction at

azimuthal and elevation angles that are practically equal to the expected ones. The similarity of the experimental images with the simulated ones demonstrates the quality of the fabricated 3D PolyBoard chips and validates the 2D beam scanning concept.

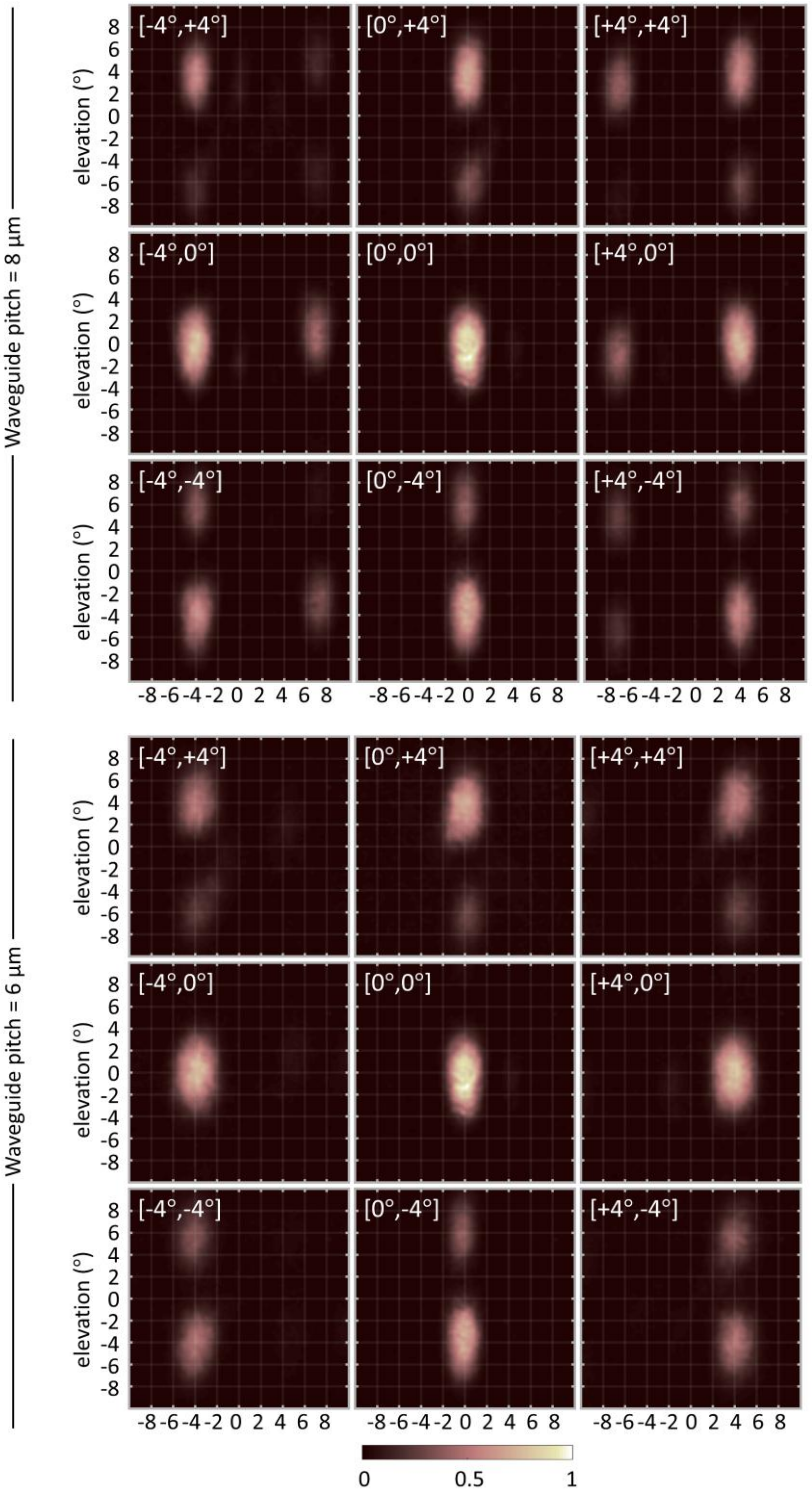

Figure 2.30: Raw images of two-dimensional beam steering with the 2×4 OPAs with (Top) 8 µm and (Bottom) 6 µm lateral pitch, spanning 8º in azimuth and elevation plane.

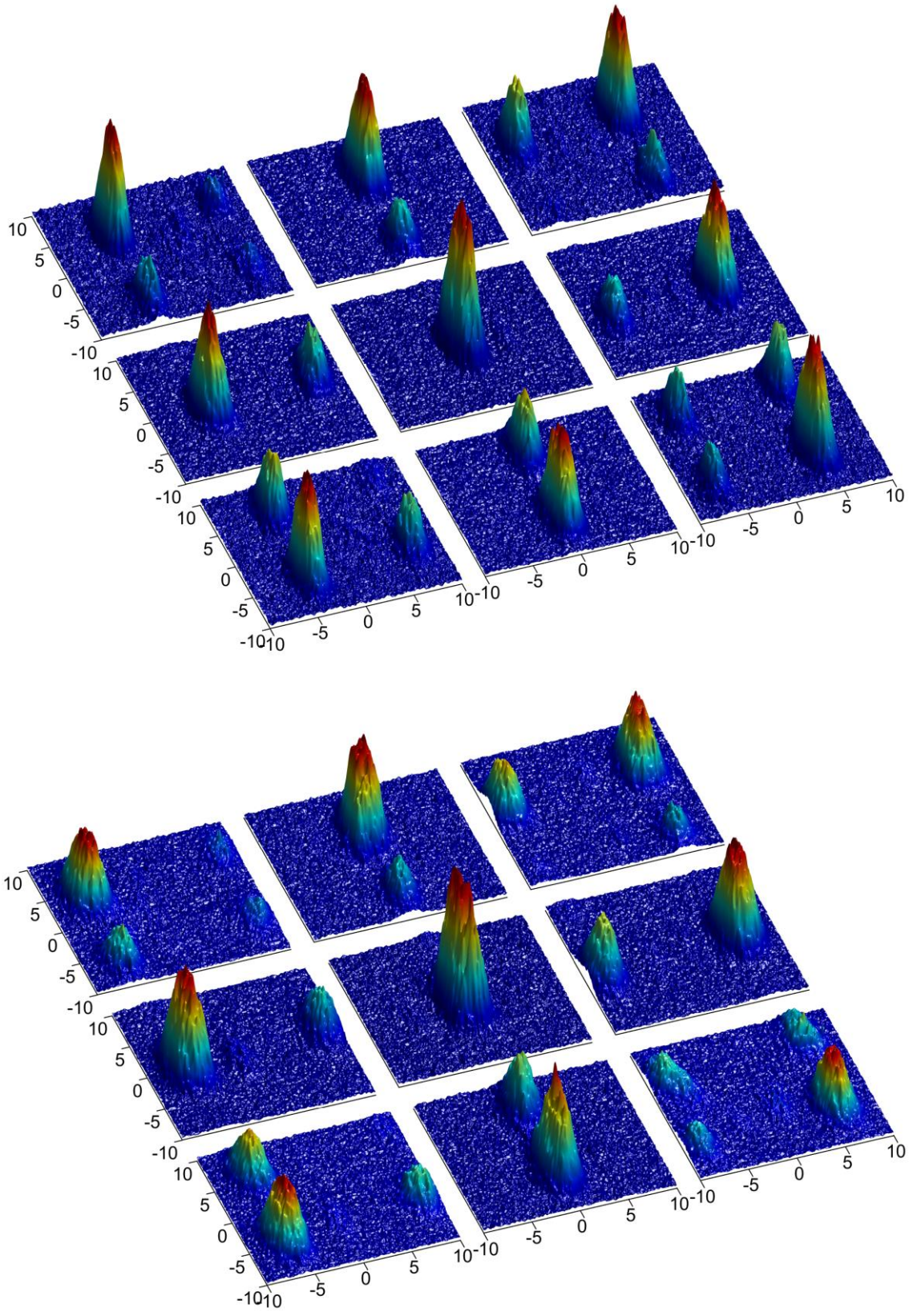

Figure 2.31: Two-dimensional beam steering with the 2×4 OPAs, with (Top) 8 µm lateral pitch, spanning 8º in the azimuth and elevation plane, and (Bottom) with 6 µm lateral pitch, spanning 12º in the azimuth and 8º in the elevation plane.

Figure 2.30 presents an additional compendium of captured images from the testing of the 2×4 OPAs with 8 μm and 6 μm lateral waveguide pitch, divided into two subgroups accordingly. The beam is targeted at -4°, 0°, +4° on the azimuthal and the elevation planes. According to equation (2.17), the expected spacing between the main and the grating lobes in the case of 6 μm spacing is approximately 9.9° in the vertical and 14.0° in the lateral direction. The angular spacing between the main and the grating lobe in the vertical direction is approximately 9.9° in all the images of the first and the third row of both subgroups. This result is expected since the OPAs have the same number of elements (two) and the same pitch (7.2 μm) in the vertical direction. In the lateral direction on the other hand, we can observe a significant difference due to the different pitch between the two OPAs. While in the images of the first and the third column of the first subgroup (8 μm pitch) the angular distance between the main and the grating lobes is 10.7°, in the corresponding images of the second subgroup (6 μm pitch) no grating lobes are present. The reason is that an angular clearance of 14° is expected between the main lobe and first order grating lobe, and thus the latter appears at ±10° in the lateral direction (when the main lobe is targeted at ±4°), where it is strongly suppressed by the envelope of the single waveguide emitter. In Figure 2.32 we summarize our results from the characterization of the three fabricated designs of the two-layer uniform OPAs, with 10 μm, 8 μm, and 6 μm lateral waveguide pitch. For the characterization we scanned the beam along the azimuthal and elevation plane with an angle step of 2°. As the beam was scanned along the azimuthal plane its elevation angle was kept at 0°. Each line in the plot represents the slice of the corresponding image at 0° elevation angle. Similarly, when the beam was scanned along the elevation plane, its azimuth angle was kept at 0°. In this case each line represents the slice of the corresponding image at 0° azimuth angle. In all these figures, the theoretical radiation pattern of the elementary emitter is drawn to make obvious that its distribution serves as an envelope that suppresses the OPA lobes at large angles. As observed, the experimentally measured lobe intensity matches the theoretical envelope both in the azimuthal and the elevation plane.

Finally, as far as a metric for the overall power efficiency of our OPAs is concerned, we can define the optical throughput as the ratio between the optical power inside the main lobe (at the reference radiation angle of 0° on the azimuthal and the elevation angle) and the input optical power. Clearly, this ratio depends on the coupling loss, the insertion loss of the optical circuit, the outcoupling efficiency of the optical antennas (practically unity

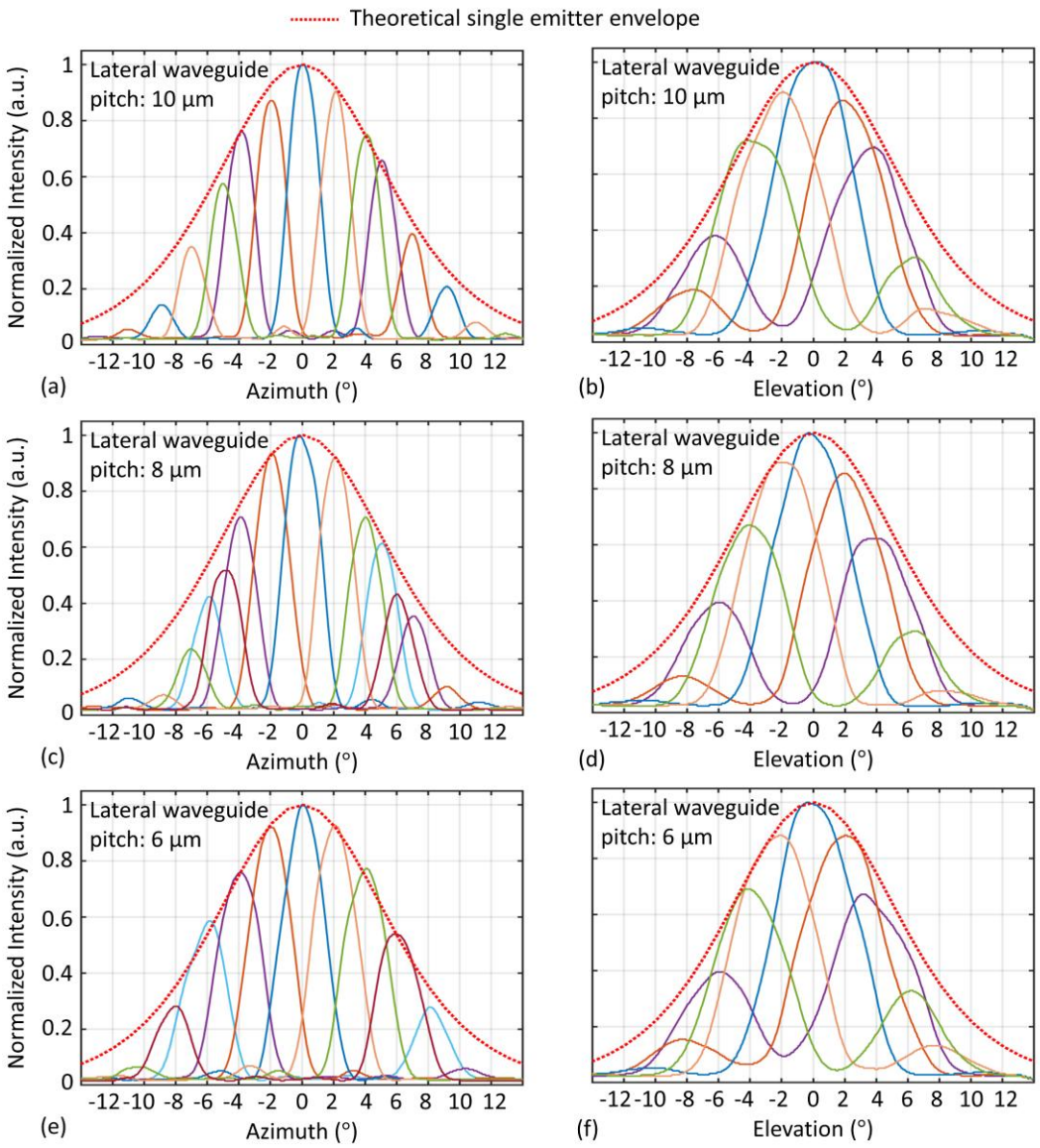

Figure 2.32: Experimental results demonstrating 2D beam steering with the fabricated 2×4 uniform OPAs. Each row corresponds to different design, with 10 µm, 8 µm, and 6 µm waveguide lateral pitch. Beam steering along the azimuthal and the elevation plane is demonstrated. The beam width is significantly larger along the elevation plane due to the fewer antenna elements along the vertical axis of the array (only two elements).

due to the use of end-fire waveguides), and the power ratio between the main and the total radiated power. The latter depends on the target angle as the main lobe is suppressed at wider angles due to the elementary emitter envelope (see Figure 2.32). According to theory the power concentrated in the main lobe formed by the 2×4 OPA with 6 µm lateral waveguide pitch at [0°, 0°] is 0.8 of the total radiated power (equivalently ~1 dB loss). Taking into account an insertion loss of ~3 dB, and ~1.5 dB coupling loss we get ~5.5 dB total optical loss, which corresponds to an optical power efficiency of roughly 28%. By integrating the pixel values in our sensor, we verified experimentally the main lobe to total

radiation power ratio, while the coupling and insertion loss were measured independently using test structures.

2.3.2.5 Power distribution network

In our implementation we use lateral and vertical MMI structures to distribute the optical power uniformly among the emitting waveguides. Any power imbalance among the elements results in non-optimum performance of the phased array since this error cannot be compensated with phase adjustments. Additional structures, such as MZIs, are needed to calibrate the power in each emitting waveguide. Therefore, in the absence of any means to actively regulate the optical power in each emitting waveguide we rely on the performance of the passive components to achieve uniform power distribution. To characterize the power distribution network a single-mode fiber was used to collect the light that was out-coupled from each end-fire waveguide. In more detail, the characterization involved measurements for the estimation of the insertion loss and the polarization dependence of the MMIs by controlling the input light polarization. The results showed that at 1550 nm wavelength the average power imbalance at the eight outputs of the chip is less than 2 dB, both for TE and TM input polarization (see Figure 2.33). The imbalance is calculated as the difference between the maximum and the minimum measured power at the chips' outputs. The total insertion loss measured from fiber to fiber was approximately 13 dB, averaging over a wavelength range from 1500 nm to 1600 nm. This value includes the in-coupling and out-coupling loss, which is ideally ~1.5 dB/facet when simple SMF is used [53], the standard propagation loss of the waveguides (0.7 dB/cm), the insertion loss of the lateral 1×2 MMI and 1×4 MMI couplers, which is ~1 dB [53], and the insertion loss of the vertical MMI coupler. Previous measurements with test structures have shown that the insertion loss of the vertical coupler is ~1 dB, both in the TE and in the TM case [54]. Any excess loss is attributable to poor optical alignment between the fibers and the chip. The average optical loss in the upper layer is slightly higher than the lower layer due to the presence of the vertical MMI coupler along the respective optical paths. The typical imbalance of the horizontal couplers is ~0.8 dB (both for TE and TM polarization) [53], while the typical insertion loss of the vertical coupler is not higher than 1 dB (both for TE and TM polarization). Therefore, the maximum power deviation between the elements should be ~1.8 dB. Any additional variation should be attributed to the optical crosstalk between the waveguides, which, as discussed in paragraph 2.3.1.2, can result in optical power transfer between waveguides, and to measurement error. It is noted that the heating

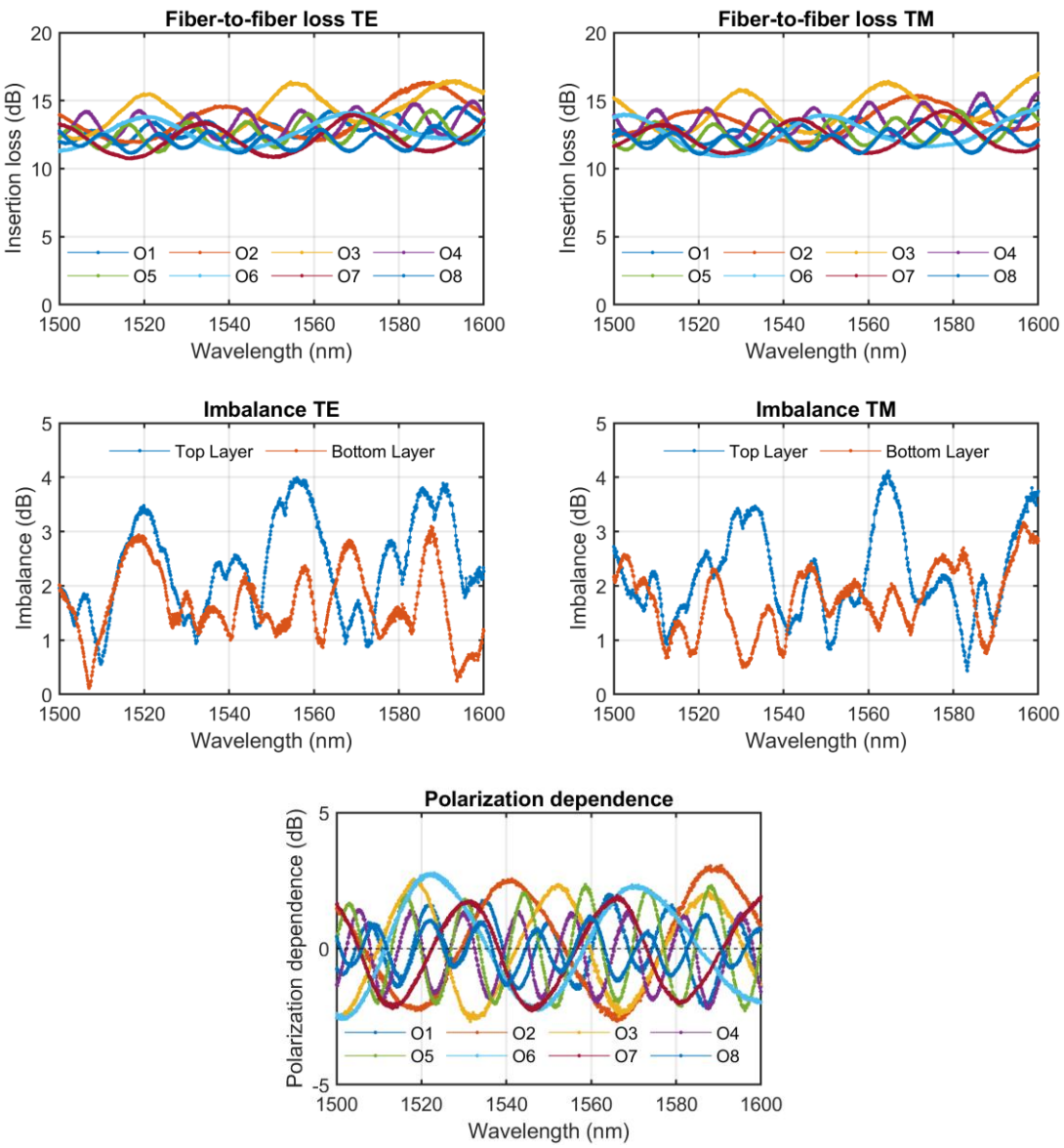

Figure 2.33: Measurements of the insertion loss, power imbalance and polarization dependence of the 2×4 OPA with 10 μm lateral waveguide spacing.

electrodes were not active during this set of measurements, thus the relative phases between the waveguides were random, leading in turn to a random transfer of optical power between the waveguides. Overall, the power imbalance is acceptable and does not deteriorate the performance of the phased array around 1550 nm. Mitigating the imbalance would require better control over the fabrication process to ensure the MMIs' performance, as well as the inclusion of VOAs to offer the possibility of active power calibration, at the expense of increased circuit complexity and power consumption.

2.4Non-uniform linear OPAs

In the previous paragraph we presented the design and experimental testing of OPAs with four and eight uniformly arranged elements, either in a linear way (1D) or in a 2D plane, leveraging the potential of the PolyBoard platform for multiple waveguiding layers. In this paragraph we expand our study to 16-channel linear arrays with unequal spacing between the elements. The motivation to implement non-uniform array arises from the fact that they can effectively suppress the grating lobes that are formed when the emitters are sparsely positioned, i.e., with larger than half the wavelength pitch. By suppressing the grating lobes aperiodic configurations can significantly expand the FOV, so that is limited only by the envelope of the elementary emitter. This approach has been successfully demonstrated in the silicon [12]-[14][84][91] and silicon nitride [46] platforms, as well as in InP [38]. Aperiodic placement of the elements is particularly useful in applications in the visible spectrum, where subwavelength emitter pitch is entirely unfeasible. For instance, in [46] the authors used this technique to realize an OPA operating with blue light. Apart from expanding the FOV, aperiodic emitter spacing provides additional benefits that should be considered when designing an OPA. Firstly, it can relax emitter pitch requirements. In a uniform array the distance between the emitters is the shortest possible that is allowed by cross-coupling restrictions in the specific integration platform. In all photonic platforms this spacing is greater than λ/2, leading to the formation of grating lobes. There are works that demonstrate subwavelength waveguide pitch at the expense of lower cross-coupling suppression ratio [43][85], or by introducing waveguide width variations to achieve phase mismatching between adjacent waveguides [24][89][94]. In an aperiodic array most of the emitters can be placed with much larger spacing (several multiples of λ), which facilitates the minimization of cross-coupling between adjacent channels. Another important aspect is the channel count reduction. Since the beamwidth is only determined by the aperture size of an OPA, using a sparser array means fewer elements are needed to fill a specific aperture. Larger spacing between emitters in a uniform array brings grating lobes closer to the main lobe in the radiation pattern, and thus, limits the FOV. Contrarily, in an aperiodic array sparsity does not affect the FOV (providing that the position of the emitters is optimized accordingly). Fewer channels, i.e. emitters, lead to fewer phase tuning elements on the photonic chip and thus fewer electronic channels for driving (DACs), reducing the overall complexity and power consumption of the system. As we will present within this paragraph, to achieve the same beamwidth with a 16-channel aperiodic array (specifically the one

based on an ordered cubic pattern which has FWHM of 0.45°), approximately 30 channels would be necessary with a uniform array of 6 μm emitter spacing; that is almost twice the number of channels. As a final remark, we would like to note that the optimized aperiodic patterns are agnostic to the radiation pattern of the elementary emitter as they are associated with the array factor. This implies that if an improved edge-emitting structure is introduced, characterized by a larger FWHM, the very same aperiodic designs could be employed to achieve an even larger FOV, under the assumption that the physical dimensions of the single element are not dramatically altered. Followingly, we summarize the key benefits and shortcomings of using unequal emitter spacing relative to uniform spacing.

Advantages of non-uniform arrays

1. Improved field-of-view by suppression of grating lobes
2. Relaxed design constraints in spacing due to sparse placement of the emitters
3. Reduced number of emitters to cover a specific aperture size
4. Reduced system complexity and power consumption due to the above

Limitations of non-uniform arrays

- □ Higher sidelobe levels
- □ Increased design complexity due to the use of optimization algorithms
- □ Individual channel control is necessary, limiting the flexibility of available control schemes

2.4.1 Aperture design

The elementary emitter of the aperiodic OPAs is the PolyBoard waveguide, the modelling of which is presented in paragraph 2.3.1.1. Here we describe the design of the aperiodic aperture, which is essentially identifying the position of the emitters, such that the design criteria are met. We use three different methods of placing the emitters, described in detail in [83]: (i) ordered spacing based on a function (linear, quadratic, cubic, etc.), (ii) random spacing using random offsets around a uniform grid, and (iii) random spacing using stepwise positioning of the emitters. In cases (ii) and (iii), where the spacing between the emitters is random, an optimization process is needed to optimize the element position. Various algorithms have been proposed to perform this task, with the particle swarm optimization (PSO) [116]-[118] and the genetic algorithm (GA) [119]-[122] being the most

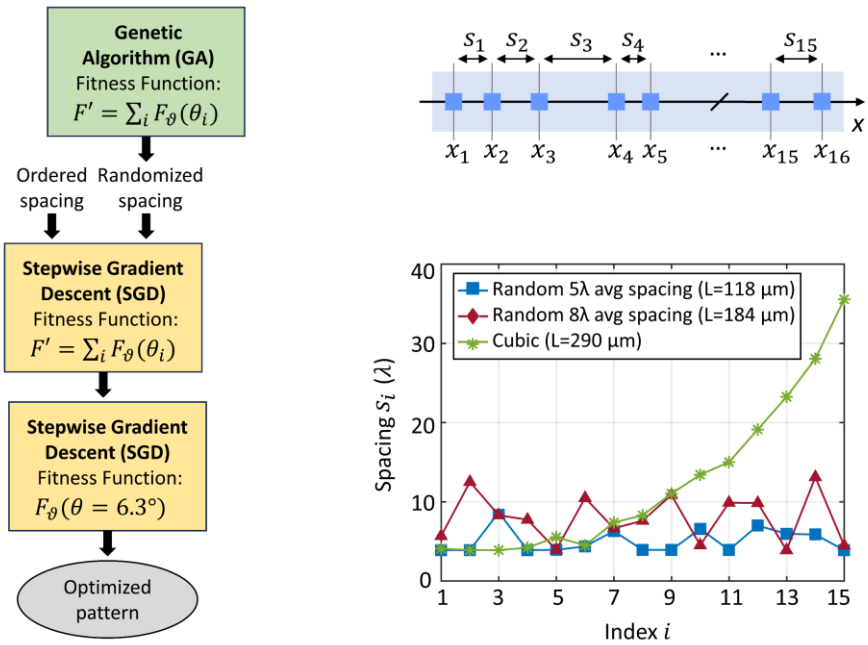

Figure 2.34: (Left) Flowchart of the optimization process. (Top-right) Linear array geometry under optimization. (c) Three example designs with optimized emitter spacing.

widely used. In our approach, a genetic algorithm is employed to explore the vast design space, followed by a batch gradient descent (BGD) algorithm to fine-tune the spacing between the elements. The same stepwise BGD algorithm is also used to optimize the ordered spacing layouts. The flowchart of the design process is shown in Figure 2.34. A commonly used fitness function in the literature is the sidelobe suppression (SLS) at a given target angle θ, noted here as $F_\vartheta(\theta)$. However, since this function only provides information for the specific target angle θ, it cannot capture the performance of the OPA in the entire region of interest (ROI). In our study, we define a ROI of 20°, symmetrically around 0°, i.e. [-10°, 10°]. Furthermore, we define an additional fitness function F', which is the sum of the $F_\vartheta(\theta)$ for all target angles in ROI. To reduce the calculation time of F', only positive target angles are considered in the calculation since the radiation pattern is symmetric around 0°, hence, $F' = \sum_i F_\vartheta(\theta_i)$, $\theta_i \in [0, 10]$. The resolution of the θ_i vector can be configured according to the desired simulation time. We set a resolution of 0.1° resulting in a θ_i vector of 101 points in total. The population consists of 100 members, with 20 members undergoing mutation in each generation. Crossover is performed exclusively between the two best-performing members. Of the 15 bits of information (representing the spacing between the 16 emitters), 3 bits are used in the crossover process, and 6 bits in mutation. A new member is added to the population only if its fitness exceeds 10% of the population's average fitness. The BGD algorithm is applied with the fitness function F',

and consequently, with $F_{\vartheta}(\theta_{3dB})$, where $\theta_{3dB} = 6.3°$ is the half-angle of the power of the elementary emitter. Optimization using this function can yield aperiodic layouts with smaller variations in side-lobe suppression (SLS) across a wider range of angles, outperforming patterns with higher SLS near 0° but significantly degraded performance at larger angles. In each evaluation cycle, the BGD algorithm shifts the position of each array element along the x-axis by the same random step (uniformly distributed) in either direction. Element positions are updated only at the end of the cycle, followed by a reduction of the maximum step size by a factor of 0.99. The BGD algorithm is detailed in paragraph 2.5.1.3. The algorithm stops after a total of 10^6 evaluation cycles and the best structure is saved. The intensity of the radiated far-field is calculated by equation (2.33), simplified for a linear array, given as

$$\mathrm{I}_{FF}(\theta, \varphi = 0) = \mathrm{I}_0(\theta, \varphi) \left| \sum_{i=1}^{N} exp[jk_0 x_i (sin\theta - sin\theta_0)] \right|^2 \tag{2.59}$$

where I_0 is the far-field radiation intensity of the individual emitter, k_0 is the wavenumber of the light in the vacuum, x_i is the position of the i-th emitter, and θ_0 is the target angle in the azimuthal (x-z) plane ($\varphi = 0$). The radiation pattern for the 16 emitters, consisting of 400 points, is calculated in ~0.5 msec using matrix operations in MATLAB.

The results of our study are summarized in Figure 2.35 and Figure 2.36. In Figure 2.35 we plot the SLS, defined as the ratio between the main lobe and the highest sidelobe, across the steering range of 0º to 10º. To quantify the SLS performance for the entire steering range with a single metric, we calculate the area under the SLS curve. For reference, we plot the theoretical SLS curve of the best-performing uniform array, which features 6 μm element pitch. However, in uniform arrays the highest sidelobe is the grating lobe, making the SLS essentially the ratio between the main lobe and the grating lobe. The heights of the two lobes (main and grating lobe) become equal when the main lobe is directed at ~7.6º, marking the FOV of the unform array. Within the ambiguity-free FOV, where the grating lobe is not present, the SLS is determined by the highest sidelobe and is theoretically equal to 13.26 dB [108]. By employing non-uniform spacing we can achieve SLS > 2 dB for target angles up to 10º. However, most applications require an SLS greater than 8 dB. Therefore, we focus on a target angle span up to ~6.3º, which corresponds to the 3 dB point of the elementary emitter's radiation pattern (FWHM of 12.7º). In the first row of Figure 2.35 we present the performance of the structures based on ordered aperiodic patterns, such

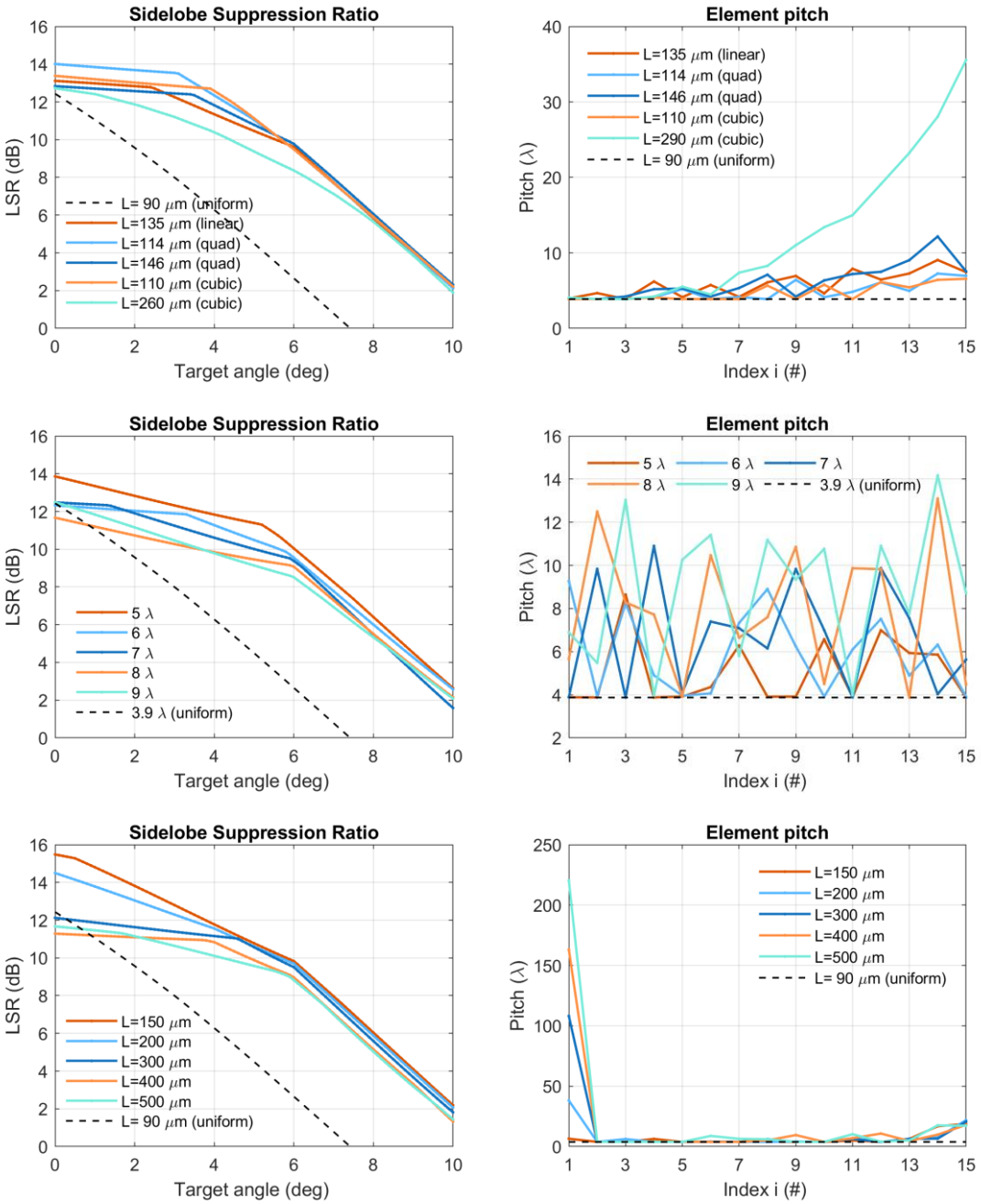

Figure 2.35: Summary of the simulation results. In the left column, the sidelobe suppression ratio (LSR) with respect to the target angle is presented, while performing beam-steering from 0º to 10º. In the right column the corresponding element pitch is plotted. From top to bottom the element placement methods are: (Top) ordered spacing, (Middle) random offsets around a uniform grid, and (Bottom) stepwise positioning.

as linear, quadratic or uniform functions. In the second row, we present the structures designed with a randomized spacing around a uniform grid, and in the last row, the structures based on randomized spacing formed with a step-by-step placement strategy. Figure 2.36 presents the same results, organized according to three key performance indicators: i) the SLS at 6º, ii) the beamwidth, and iii) the power concentrated in the main lobe. We consider a maximum steering angle of 6º, because of the 3dB point of the

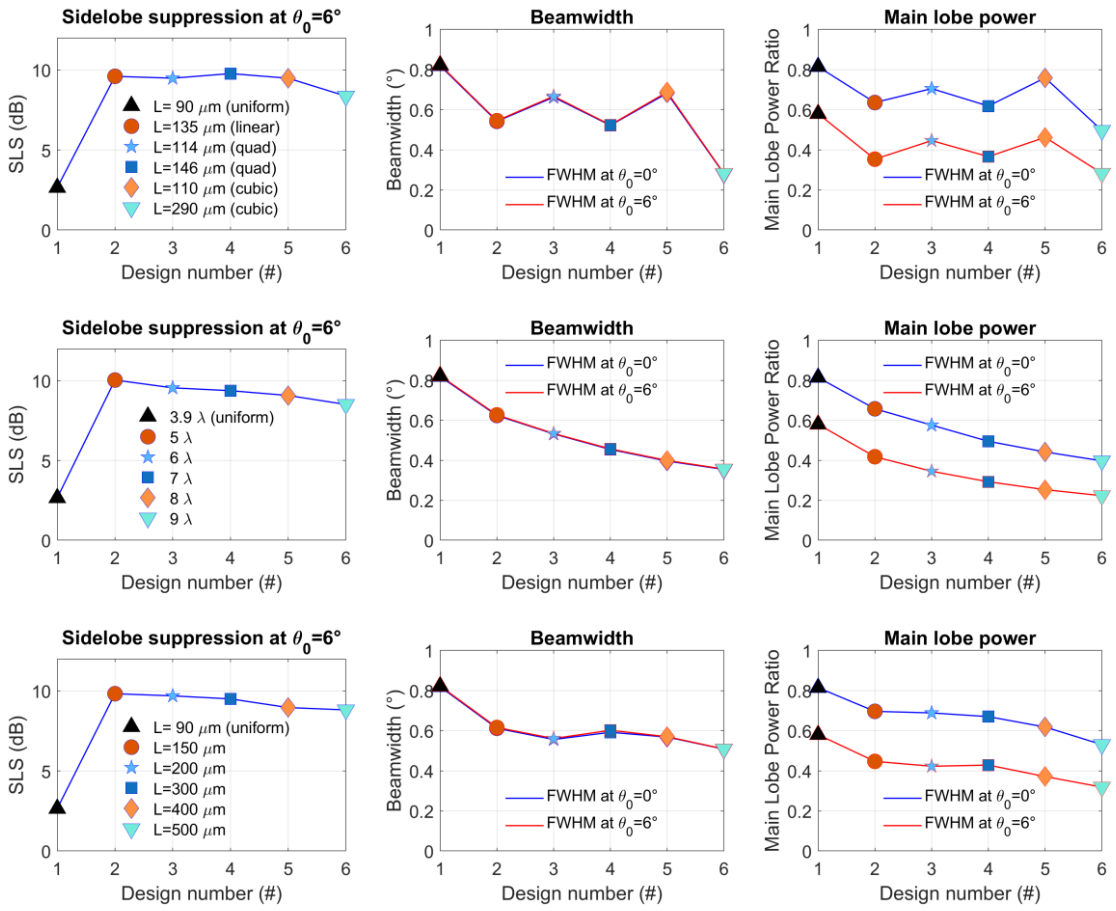

Figure 2.36: Simulated performance of the top five designs from each placement strategy. The uniform design with 6 μm pitch is also plotted for reference. From top to bottom the element placement methods are: (Top) ordered spacing, (Middle) random offsets around a uniform grid, and (Bottom) stepwise positioning.

elementary emitter, as mentioned above. We plot both the beamwidth and the power in the main lobe at a target angle of 0º and 6º. The designs selected for fabrication are presented in Table 6, sorted from the largest to the narrowest beamwidth, or equivalently, from the shortest to the largest aperture. The total aperture sizes are 118 μm, 146 μm, 184 μm, and 290 μm, respectively. Designs 1 and 3 are based on the random offset element placement strategy, optimized with the genetic algorithm, while designs 2 and 4 are based on a function. The selection was based primarily on the beamwidth and the SLS. No design from the third placement strategy was selected for fabrication, as the designs from the first two categories demonstrated a better trade-off between SLS and beamwidth. For the ordered spacing, the quadratic and cubic functions were slightly modified during optimization with the BGD algorithm. In Table 6 we compare the theoretical beamwidth of the aperiodic apertures with that of the 16-channel uniform array. The best-performing structure in this regard is the one based on the cubic function, with an aperture size of 290 μm, demonstrating a reduction in beamwidth by over 65%.

#	Design	Placement Strategy	SLS at 6º	Main lobe power ratio at 0º	Beamwidth at 0º (º)	*Beamwidth reduction at 0º (%)
1	5λ average spacing	Random offset	10.04 dB	0.6576	0.627	24.00
2	L=146 μm quadratic	Ordered	9.774 dB	0.6182	0.522	36.72
3	8λ average spacing	Random offset	9.075 dB	0.4415	0.399	51.64
4	L=290 μm cubic	Ordered	8.366 dB	0.4964	0.282	65.82
*	L=90 μm uniform pitch 6 μm	Uniform	2.653 dB	0.8144	0.825	_

Table 6: Summary of the aperiodic designs selected for fabrication.

2.4.2 Experimental results

2.4.2.1 OPA PIC

The 16-channel aperiodic OPAs were designed and fabricated using the polymer-based platform of HHI based on commercially available polymer materials (ZPU-12 series from ChemOptics Inc.) [53]. The cladding and core indices are 1.45 and 1.48 respectively at a wavelength of 1550 nm and provide a propagation loss of ~0.7 dB/cm. As mentioned in the modelling of the elementary emitter in section 2.3.1.1, the core of the single-mode waveguide, has a square cross section of 3.2 μm × 3.2 μm, resulting in a mode field diameter of around 4.2 μm. Moreover, both TE and TM components of the single mode are equally supported due to the symmetry of the waveguide cross-section. The optical power inserted to the chip is distributed among the 16 channels of the OPA by two stages of 1x4 MMI couplers of 700 μm length and 53.6 μm width. The pitch between adjacent channels in the phase tuning section of the chips is 178 μm to eliminate thermal crosstalk. Due to the low thermal conductivity of the polymer platform ($\sim 0.3\ W/m/K$) thermal crosstalk of less than 5% is expected for distances greater than 60 μm between adjacent waveguides, while even better isolation can be achieved by forming air trenches next to the heater and waveguide. The heaters were implemented with 120 nm-thick Au on top of the waveguides, measuring 500 μm length and 15 μm width. The waveguides are brought closer together on the emitting side of the PIC with a fan-in section to form the desired aperiodic pattern. Figure 2.37 presents the 16-channel OPA chips with dimensions 7 mm × 13.5 mm.

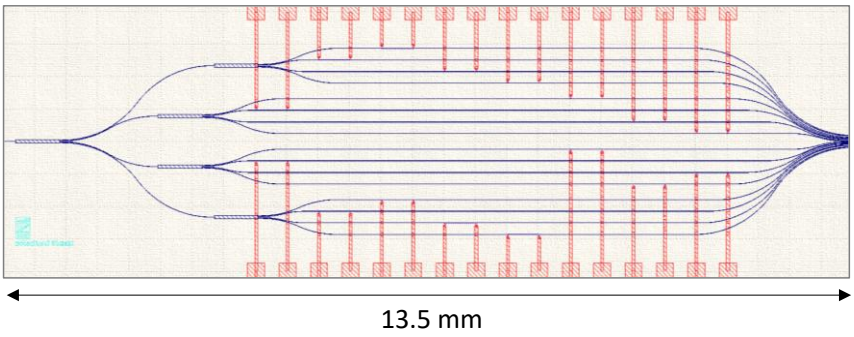

Figure 2.37: Circuit of the 16-channel PolyBoard OPAs. The waveguide spacing at the east side is different for each aperture design.

2.4.2.2 Beam-steering with suppressed grating lobes

To characterize the radiation pattern of the fabricated devices we used our standard camera setup presented in paragraph 2.3.2.1. The chip was placed on a probe station with a passive heat sink. We used a fiber-pigtailed distributed feedback (DFB) laser at 1553 nm wavelength and a lensed fiber to couple 5 dBm of power into the chip. The initial phased array emission was random due to the random initial phases of the emitters, as we explain in section 2.5. To extract the initial phase mismatch between the emitting waveguides, a stochastic parallel gradient-descent (SPGD) algorithm is used to converge the beam at 0° emission (along the z-axis), using feedback from the camera. Beam steering in the azimuth plane is achieved through a combination of deterministic and search-based approaches. Equation (2.58) is used to direct the beam to the desired azimuth angle, while the SPGD algorithm further optimizes the radiation pattern to enhance the SLS. On average, 35 evaluations were sufficient to accurately determine the initial phases, corresponding to a maximum fitness of 0.85, which reflected the similarity with the theoretical radiation pattern. The evaluation time was set to approximately 1 second, primarily constrained by the timing limitations of the control electronics, though further optimization is possible with the current setup. The heating elements of the polymer platform support tuning in the millisecond range (~2 ms). Further details on OPA calibration are discussed in section 2.5.

Example far-field images, captured with our imaging system, are shown in Figure 2.38, demonstrating beam-steering between ±6º with resolution of 1º. The data correspond to the PIC with the aperiodic pattern of 5λ average spacing (design #1 in Table 6). Figure 2.39 summarizes the measurement results from the characterization of the fabricated samples. The PIC with the ordered spacing based on the quadratic function (design #2 in Table 6) was electrically damaged during testing and became non-operational. As a result, three of

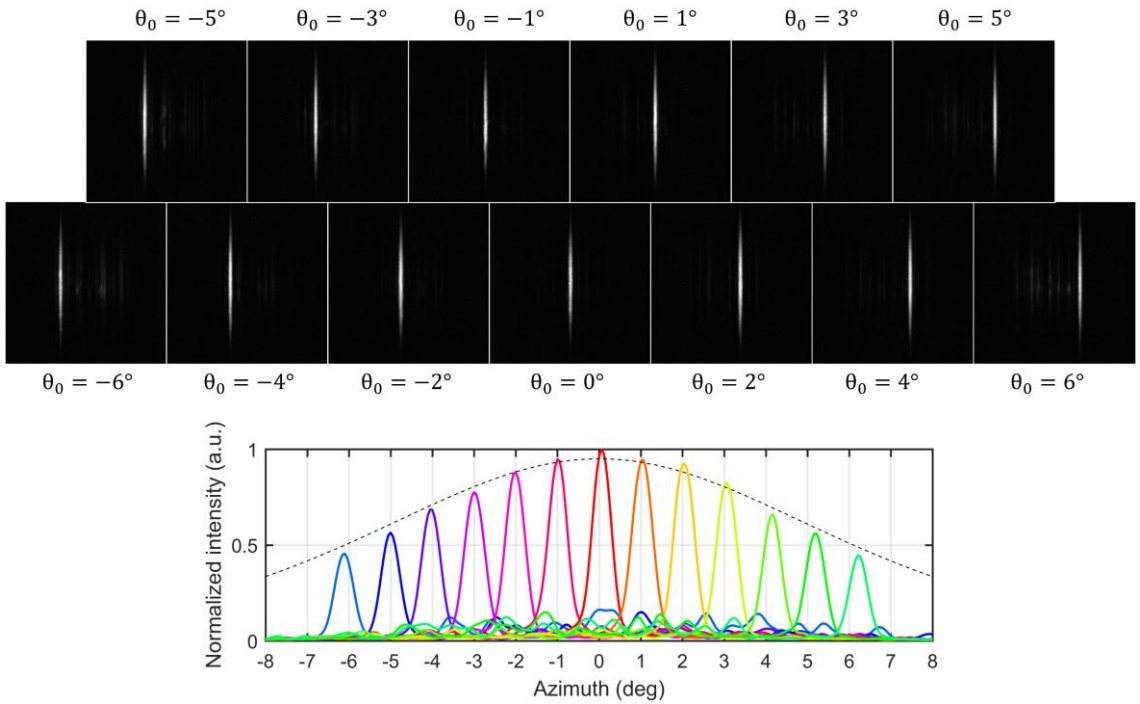

Figure 2.38: Beam-steering experimental results. (Top) Normalized captured frames of the far-field from the CCD camera demonstrating scanning in the range ±6° with a step of 1°. (Bottom) Cross section of frames showing measurements with an angle step of 1°. The measurements correspond to the randomized pattern of 5λ average pitch.

the four fabricated samples were successfully characterized and are presented here. We measured the SLS, the beam FWHM in the beam-steering plane (azimuth) and the power of the main lobe relative to the total radiated power for a scan range of ±10°. For conciseness, we fold the horizontal axis and present the positive and negative target angles with light and dark blue color respectively. We indicate the measurements with markers and the corresponding theoretical values using a dotted line. The randomized pattern with an average distance of 5λ has a side lobe suppression of more than 11 dB up to a steering angle of 5°, i.e. for a FOV of ±5°, while for the same FOV the cubic pattern has more than 8.7 dB. To calculate the total radiated power, we integrate the pixels over the entire frame captured by our imaging system, which corresponds to a FOV of ±17° in the azimuth plane. The best performing structure in terms of power in the main lobe is the pattern with 5λ average spacing, due to its smaller aperture size. The average values of the measured beam FWHM were 0.69° and 0.52° for the randomized 5λ and 8λ average spacing patterns accordingly, and 0.45° for the ordered cubic pattern. To achieve the same beamwidth as the latter using a uniform array with 6 μm spacing, nearly twice the number of channels (~30 channels) would be required (see Figure 2.14). The wider measured beamwidth may be attributed to the resolution of our imaging system (~0.05°/pix) combined with camera

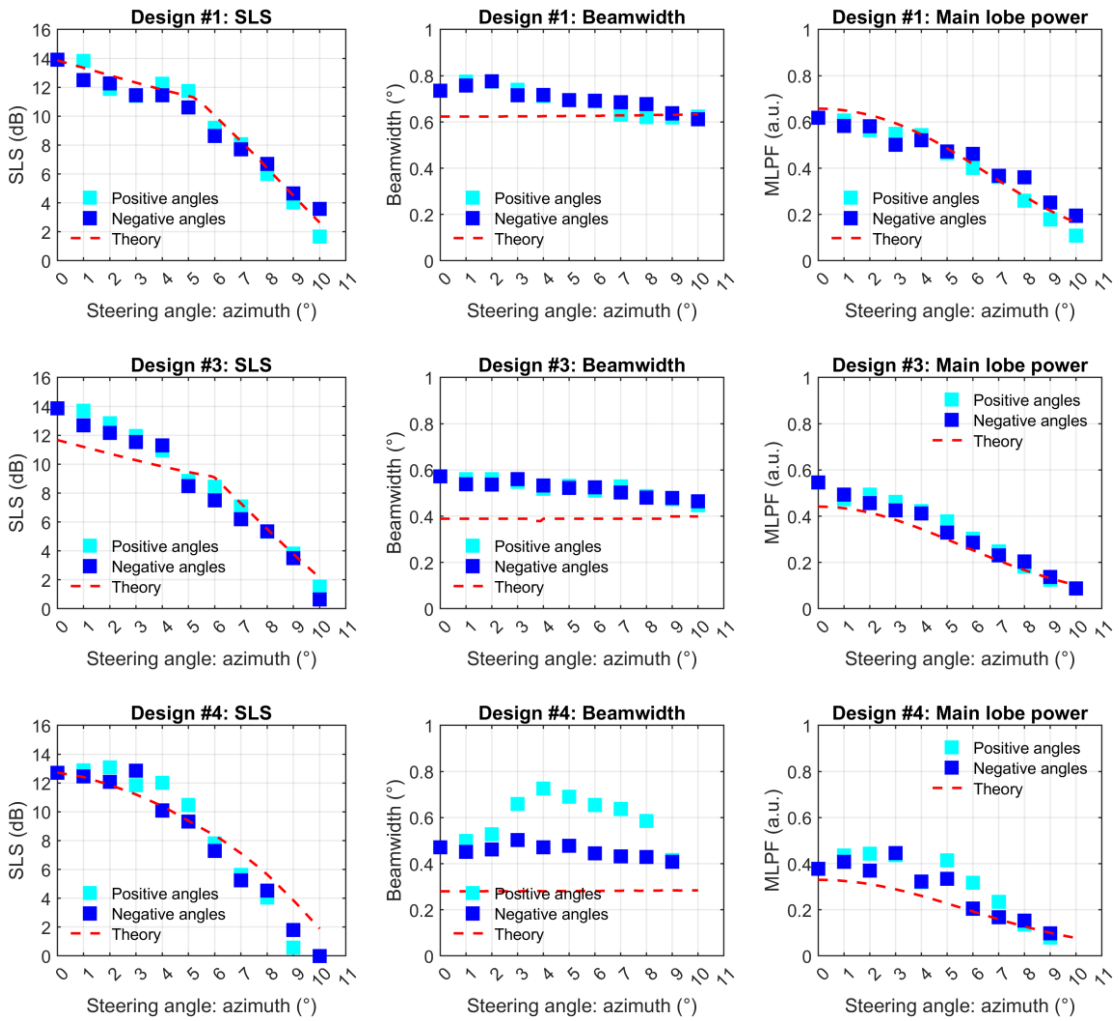

Figure 2.39: Measured performance of the 1×16 aperiodic OPAs in terms of (Left) sidelobe suppression (SLS), (Middle) beamwidth, and (Right) power in the main lobe over the total radiated power. Beam steering is performed from -10 to 10 degrees.

noise. Another factor may be the limitation of the converging algorithm to form a very sharp beam with the selected angular step ($\Delta\phi = 15°$). The FOV is currently limited by the beam divergence of the elementary emitter, the edge-emitting waveguide demonstrating a 3dB beamwidth of ~12.7°. Further improvement can be possible by slight modifications on the waveguide cross-section size or the refractive index contrast, although not without adversely affecting the propagation loss of the platform. In Figure 2.39, we present the data from the three different designs in the same figure for comparison. We again fold the horizontal axis and record the average value between the measurement at the positive and negative target angles. Although the measurements were not completely symmetrical around 0°, their difference was less than 0.5% for SLS and less than 8% and 13%, for the beamwidth and main lobe power ratio, respectively. For comparison, we also plot the corresponding performance of the uniform pattern with 6 μm pitch.

2.5Phase calibration

In its default state, an integrated OPA exhibits a random emission pattern when no phase tuning is applied, meaning the antenna elements have a random phase distribution. This is primarily due to unavoidable variations in waveguide dimensions, resulting from fabrication imperfections [115]. Additionally, phase variations are introduced when the optical paths of the waveguides in the power distribution network are not equal by design. Therefore, a phase calibration process is needed to determine the initial phase error and compensate for it by applying the appropriate phase shift to each element. Considering that the phase tuning of each element is facilitated by a DAC channel with up to 16-bit resolution (thus 2^{16} levels) and considering that OPAs can consist of hundreds to thousands of elements, it becomes apparent that the search space is incredibly vast. The total number of possible states is $2^{N \cdot B}$, where N is the number of OPA channels (emitting elements) and B is the DAC bit-resolution. For example, the number of states for a 64-channel array controlled by an 8-bit resolution DAC is equal to $2^{512} \cong 2^{10 \cdot 51} \cong 10^{153}$. To address this problem, optimization-based methods have been proposed. Conventional algorithms for phase calibration include the hill-climbing algorithm [10][12], particle swarm optimization (PSO) algorithm [34][116]-[118], genetic algorithm [119]-[122], and a number of variations of the gradient descent algorithm [5][23][43][75][123]-[126]. These iterative search algorithms can effectively align the wavefront and generate a converged beam at the target direction. More recently, neural networks have been utilized to facilitate the calibration process. The neural network can be trained to determine the phase errors directly from the initial random far-field pattern, without the need for iterations, which offers a significant acceleration of the calibration process [127]-[129].

The calibration process extends beyond correcting fabrication-induced phase errors. For example, factors such as temperature variations can influence calibration outcomes. To account for these changes look-up tables are employed, although this further slows down the calibration process. Alternatively, active thermal control of the chip is implemented [125]. However, even at the same temperature and wavelength, knowledge of the initial phase error alone cannot ensure optimal beam convergence at all target angles. In other words, equation (2.59) is not sufficient to determine the tuning vector for precise beam steering. Fabrication-induced imperfections in the array geometry, along with inhomogeneities in the phase shifter efficiency introduce errors to the array factor. Performance variation among phase tuning elements is a common source of error, requiring

individual characterization for accurate phase control. In thermo-optic tuning, additional challenges such as nonlinear resistance caused by self-heating and thermal crosstalk must also be addressed. Therefore, look-up tables are typically extended to cover multiple target angles with a defined grid resolution. The typical calibration method is to use a camera to record the radiation pattern in a laboratory setup as the one presented in paragraph 2.3.2.1. However, a lot of research effort has been made to implement OPA calibration on wafer scale [130] or to develop techniques for on-chip calibration [44][131]-[134].

The goal in an optimization problem is the optimization of the objective function (OF). The terms *fitness* or *profit* function are used when the goal is to maximize OF, while when the goal is the minimization of the OF, the terms *loss* or *cost* function are used. Several figures of merit have been proposed in the literature as objective functions for the calibration. One approach is to optimize the directivity of the OPA, by measuring the radiation intensity at a specific target direction and dividing it by the total radiated power. Another method is the optimization of the sidelobe suppression ratio (SLSR). A third figure of merit is the level of similarity of the measured radiation intensity pattern with the theoretical one. The level of similarity can be quantified by taking the pixel-wise Euclidean distance between the measured and the simulated far-field pattern, or the overlap coefficient, which is basically the common area under the two surfaces of the measured and the simulated radiation pattern. In many cases the objective function is defined as a combination of the above figures [131]. In this section we present the algorithms that we implemented for calibrating the fabricated OPAs, their simulated performance and the corresponding experimental measurements.

2.5.1 Modelling

We consider a given channel i of the array, controlled by a thermal phase shifter. The phase φ_i before the emitting aperture is defined by the accumulated phase error $\varphi_{error,i}$ in the optical path, and by an induced phase change by the heater. The latter is dependent on the applied electrical power P_i and the thermo-optic proportionality constant k_i, thus

$$\varphi_i = \varphi_{error,i} + k_i P_i. \tag{2.60}$$

When using a current source to drive the heating electrode, we can decompose the applied electrical power as

$$P_i = R(I_i) \times I_i^2 = \left(R_{0,i} + a_{R,i} I_i^2\right) \times I_i^2 \tag{2.61}$$

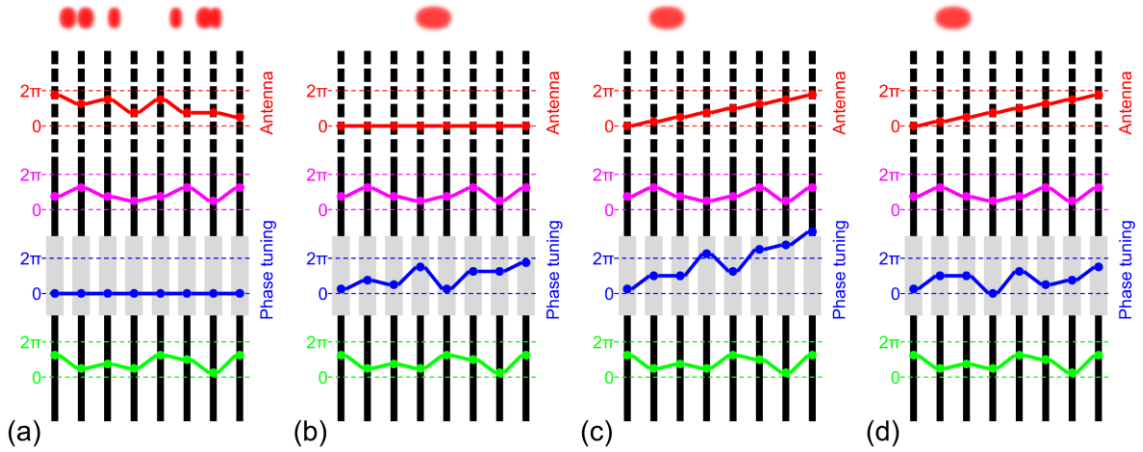

Figure 2.40: Schematic representation of the phase profile before and after the calibration. (a) Uncalibrated OPA, (b) calibrated for $\varphi = 0$, (c) application of a linear phase gradient for beam steering and (d) application of modulo 2π function. Phase perturbations in the optical path before and after the tuning section are assumed. The phase variations before and after the tuning section are indicated with green and magenta lines respectively.

, where $R_{0,i}$ and $a_{R,i}$ are the parameters to model the nonlinear behavior of the resistance due to self-heating. If the applied power P_i is such that φ_i equals 2π, for every channel of the array, then the beam will converge at 0° and the values of $\varphi_{error,i}$ can be extracted. While the beam can be directed to any target angle, convergence at 0° is chosen for simplicity. Figure 2.40 illustrates the phase profile of the array during this calibration procedure. Additionally, in an array of N channels, the phase error for $N-1$ channels must be determined, with one channel serving as the phase reference. Consequently, since any channel can be chosen as reference, there are essentially N different solutions to the calibration problem -one for each channel in the array. The calibration is performed in two stages: first, we calibrate the tuning elements by finding the $P_{2\pi,i}$ for each channel, and consequently, we extract the $\varphi_{error,i}$ by employing a calibration algorithm. In this work we investigate three popular iterative search algorithms for the calibration: a) hill-climbing algorithm, b) batch gradient descent (BGD) and c) stochastic parallel gradient descent (SPGC) algorithm. We compare the performance of the algorithms in terms of execution time as the number of channels increases. Furthermore, we improve the BGD algorithm by introducing deterministic features and make it faster than SPGD for a small number of channels.

2.5.1.1 Fitness functions

As mentioned above, there are several different fitness functions that can be used for the optimization, which can broadly be categorized into two types: those based on the

power measured in a specific direction (directivity) and those that quantify the similarity between the measured radiation pattern and the theoretical one. In our study, we employ fitness functions of both types. The primary fitness function is the overlap coefficient, a quantity that gives the degree of similarity between two vectors, defined as

$$c_{OVL} = \frac{\left|\sum U_{meas} \cdot U_{target}\right|^2}{\sum|U_{meas}|^2 \cdot \sum\left|U_{target}\right|^2} \tag{2.62}$$

, where U_{meas} is the normalized measured radiation intensity and U_{target} the corresponding theoretical radiation pattern at the target angle. The overlap coefficient, as defined above, is a modified form of the Pearson correlation coefficient [135], and can be viewed geometrically as the cosine angle of two vectors, closely related to the dot product:

$$cos\theta = \frac{u \cdot v}{\|u\| \cdot \|v\|} \tag{2.63}$$

, where $\|u\|$ and $\|v\|$ denote the magnitude of the vectors, and θ the angle between them. For completeness we also mention here the Euclidean distance, which is the most widely used measure of similarity between two vectors u and v in the two-dimensional space:

$$d(u,v) = \sqrt{\sum_k (u_k - v_k)^2} = \|u - v\|. \tag{2.64}$$

The second fitness function that we make use of is the intensity over a defined region of interest (ROI), e.g. at a square area of side a around 0°, and is calculated as the sum of all pixel values $p_{i,j}$ inside the ROI:

$$I_{ROI} = \sum_{i,j} p_{i,j} \tag{2.65}$$

, where i and j are the pixels' coordinates. The intensity I_{ROI} can also be divided by the sum of all the pixels in the captured far-field image I_{total}, resembling the directivity of the OPA. An alternative ROI is the area within the 3 dB beam width of the main lobe. Finally, a very useful fitness function is the sidelobe suppression ratio (LSR), defined as the ratio between the peak of the main lobe h_{main} and the peak of the highest sidelobe:

$$LSR = \frac{h_{main\_lobe}}{max(\boldsymbol{h}_{sidelobes})} \tag{2.66}$$

, where $\boldsymbol{h}_{sidelobes}$ the vector containing all the sidelobes in the radiation pattern above a certain threshold.

2.5.1.2 Parallel hill-climbing algorithm

The simplest calibration algorithm is the hill climbing type. A deterministic version of the algorithm is described in [122], which is basically a brute force approach. The phase of each optical channel is swept from 0 to 2π with a defined DAC step, and the fitness function in every step is evaluated. The value that provides the highest fitness is selected and the algorithm progresses to the next channel until all channels are optimized. In our study we use a different version of the algorithm, which relies on the calculation of the first and second order partial derivative of the fitness function to determine the direction and the magnitude of the step, as presented in [10]. The pseudocode of the algorithm is described in Table 7. We assume that the driving current of the phase heater in an optical channel i is controlled by the voltage u_i applied by a DAC channel, and thus, we can associate the applied optical phase shift to a vector $\boldsymbol{u} = (u_1, u_2, \dots, u_n)$ applied by the DAC, where n is the number of DAC channels, which in our case is the number of the optical channels. Accordingly, the phase step vector corresponds to a voltage vector $\boldsymbol{\delta u}$. In our implementation of the algorithm the elements of δu are random variables drawn from a uniform distribution ranging from 0 to a user-defined maximum step value. All channels are updated simultaneously, and this is why we call this variation of the algorithm parallel hill climbing (PHC). We test the performance of the algorithm by running 50 calibration runs for three different uniform OPA geometries: 1×16, 2×16 and 4×16, with pitch between the emitters $dx = 6\ \mu m$ and $dy = 7.2\ \mu m$. The results of the simulation are presented in Figure 2.41. We plot the number of evaluations that are needed to reach a specific fitness value between 80% and 98% as well as the evolution of the fitness function, selected here

```
1:  while F ≤ target_fitness or i ≤ max_iterations
2:      Generate δu
3:      for k in {−2, −1, 0, 1, 2}
4:          Set_DAC_voltages(u + k · δu)      # Write to DAC
5:          Read_from_camera()                # Read pattern from camera
6:          Evaluate F                        # Evaluate fitness
7:      Calculate ∂F/∂u and ∂²F/∂u²
8:      Choose n from the set {−2, −1, 0, 1, 2}
9:      Set_DAC_voltages(u + n · δu)          # Write to DAC
    end
```

Table 7: Pseudo-code of parallel hill-climbing algorithm

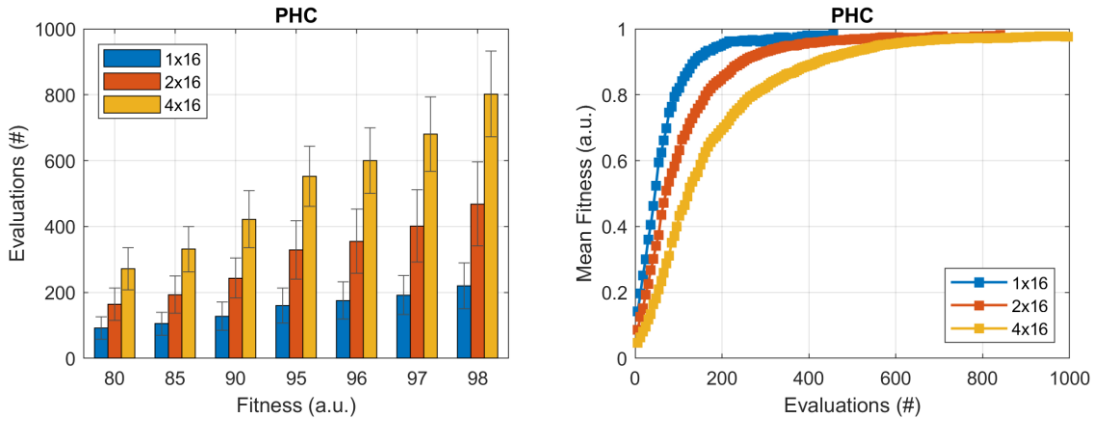

Figure 2.41: (Left) Number of evaluations needed to reach the indicated fitness value and (Right) the mean fitness evolution over time for the parallel hill climbing algorithm.

to be the overlap coefficient. The number of evaluations is directly related to the execution time of the algorithm, as each evaluation of the fitness function requires a DAC access to update the control voltages of the OPA and a camera read to get the current frame. In each algorithm cycle (epoch) there is a total of five evaluations of the fitness function plus one access to the DAC at the end of each cycle. In a practical implementation, factors such as the DAC write and settling time, the tuning technology's settling time in the OPA (e.g., heaters), and the camera's frame read time must be considered to accurately translate the number of evaluations into calibration time.

2.5.1.3 Batch gradient descent algorithm

Another family of algorithms that is broadly used for phase calibration is the gradient descent type. In this paragraph we present the batch gradient descent (BGD) algorithm, and we introduce two additional features on the basic algorithm to improve its performance. The name of the algorithm originates from the fact that the computation of an update is based on all the available *samples* (batch). In our application, this practically means that in each iteration of the algorithm (epoch), the fitness function is evaluated independently for every channel i of the OPA to determine the direction of the step δu_i. The overall update vector $\boldsymbol{\delta u}$ is applied at the end of the iteration, only after δu_i (magnitude and sign) has been identified for every channel. As in the case of the hill climbing algorithm presented in the previous paragraph δu_i is a random variable drawn from a uniform distribution. The pseudocode of the algorithm is presented in Table 8. As a next step in refining the basic algorithm, we introduce a shortcut by leveraging a deterministic aspect of the problem. As the algorithm iterates through different states to estimate the gradient, there are instances when the beam partially converges to a specific angle. Since the phase vector $\boldsymbol{\varphi_r}$ that targets

the beam to a particular angle can be calculated using the equation (2.59), we can subtract $\boldsymbol{\varphi_r}$ from the current state to redirect the beam towards (0°,0°) and resume optimization from that point. We use $\boldsymbol{r}$ to represent the appropriate voltage vector, which, when added on the current phases, shifts the beam towards (0°,0°). To implement this, a second fitness function based on the lobe power, is used. More specifically, the 3dB power of the brightest lobe on the captured image (I_{lobe}) is calculated and compared to a user defined threshold. The pseudocode of the algorithm is also presented in Table 8 where we indicate with green color the numbering of the lines associated with the deterministic part.

```
1:  while F ≤ target_fitness or i ≤ max_iterations
2:      Generate δu                          # Random vector
3:      Initialize n                         # Sign vector (zero initially)
4:      Initialize r                         # Redirection vector (zero initially)
5:      Initialize F^best, u^best            # Best fitness and corresponding
                                             # voltage vector (zero initially)
6:      for i = 1 to number_of_channels
7:          Set_DAC_voltage(u_i + δu_i)      # Write to DAC
8:          Read_from_camera()               # Read pattern from camera
9:          Evaluate F^+                     # Evaluate fitness
10:         Evaluate I^+_lobe                # Evaluate main lobe intensity
11:         Set_DAC_voltage(u_i − δu_i)      # Write to DAC
12:         Read_from_camera()               # Read pattern from camera
13:         Evaluate F^−                     # Evaluate fitness
14:         Evaluate I^−_lobe                # Evaluate main lobe intensity
15:         Choose n_i from the set {−1, 1}
16:         if max (I^+_lobe, I^−_lobe) > power_threshold
17:             Calculate r
18:             Break
19:         [F_i^best, u_i^best] ← max(F^+, F^−)
20:     Set_DAC_voltages(u + n · δu + r)     # Write to DAC
21:     Read_from_camera()                   # Read pattern from camera
22:     Evaluate F                           # Evaluate fitness
23:     if max(F_i^best) > F
24:         Set_DAC_voltages(u_i^best)       # Write to DAC
25: end
```

Table 8: Pseudo-code of the implemented batch gradient descent (BGD) algorithm, including two application specific features to improve convergence speed. The lines numbered with green color refer to the 'deterministic' expansion (BGD-1) and the ones numbered with red color to 'the jump-to-best' feature (BGD-2).

As a final improvement we take advantage of the iterative nature of the algorithm. Since each element of the array is iterated over, the total number of fitness evaluations is twice the number of elements -one for adding and one for subtracting the step from the voltage vector. Among all these steps, it is possible to pass from a state where the fitness function is sufficiently high. And in fact, the value of the fitness function might be higher than the one produced from the state chosen as next from basic BGD algorithm. Therefore, by saving all the calculated fitness values and their corresponding voltage vectors to achieve them, we can add an additional step outside the iteration loop to choose between the output of the basic algorithm and the best setting that was achieved during the iterations. We call this feature ‘jump-to-best’ as it ignores the state calculated by the BGD algorithm and jumps directly to the state that give the best fitness value. Since the calculated gradient is ignored, we can consider this addition as a kind of hill-climbing approach. A potential drawback of this implementation is the additional memory required to store all voltage vectors at each iteration, as well as the extra read-from-camera and write-to-DAC steps. However, since these extra steps occur outside the iteration loop, their impact on the algorithm's runtime is negligible. In Table 8 we indicate with red color the numbering of the lines that are associated with the ‘jump-to-best’ feature.

The performance of the algorithms is again tested on the three OPA geometries: 1×16, 2×16, and 4×16, by running 20 calibration runs for each geometry. The results are presented in Figure 2.42 and Figure 2.43. Both figures display the same set of results, albeit with different presentations. In Figure 2.42, the number of iterations of the algorithm is shown in cycles, or epochs (we use them as interchangeable terms). From this representation, it can be concluded that the number of cycles required for the algorithm to converge remains relatively unaffected by the number of channels. However, Figure 2.43 highlights how the algorithm's runtime scales with array geometry, as it displays the number of evaluations instead of cycles. Since BGD algorithm requires evaluating fitness separately for every array element before taking a decision, it becomes increasingly slow as the number of channels increases, making it unsuitable for large-scale arrays. For such cases, the stochastic parallel gradient descent (SPGD) algorithm introduced in the next section, is preferred. Nevertheless, it is evident that the features we introduced reduce the algorithm’s runtime. For example, in Figure 2.43, the number of evaluations required to reach 98% fitness with the 4×16 array decreases from nearly 1,000 to fewer than 800, resulting in an improvement of over 20%.

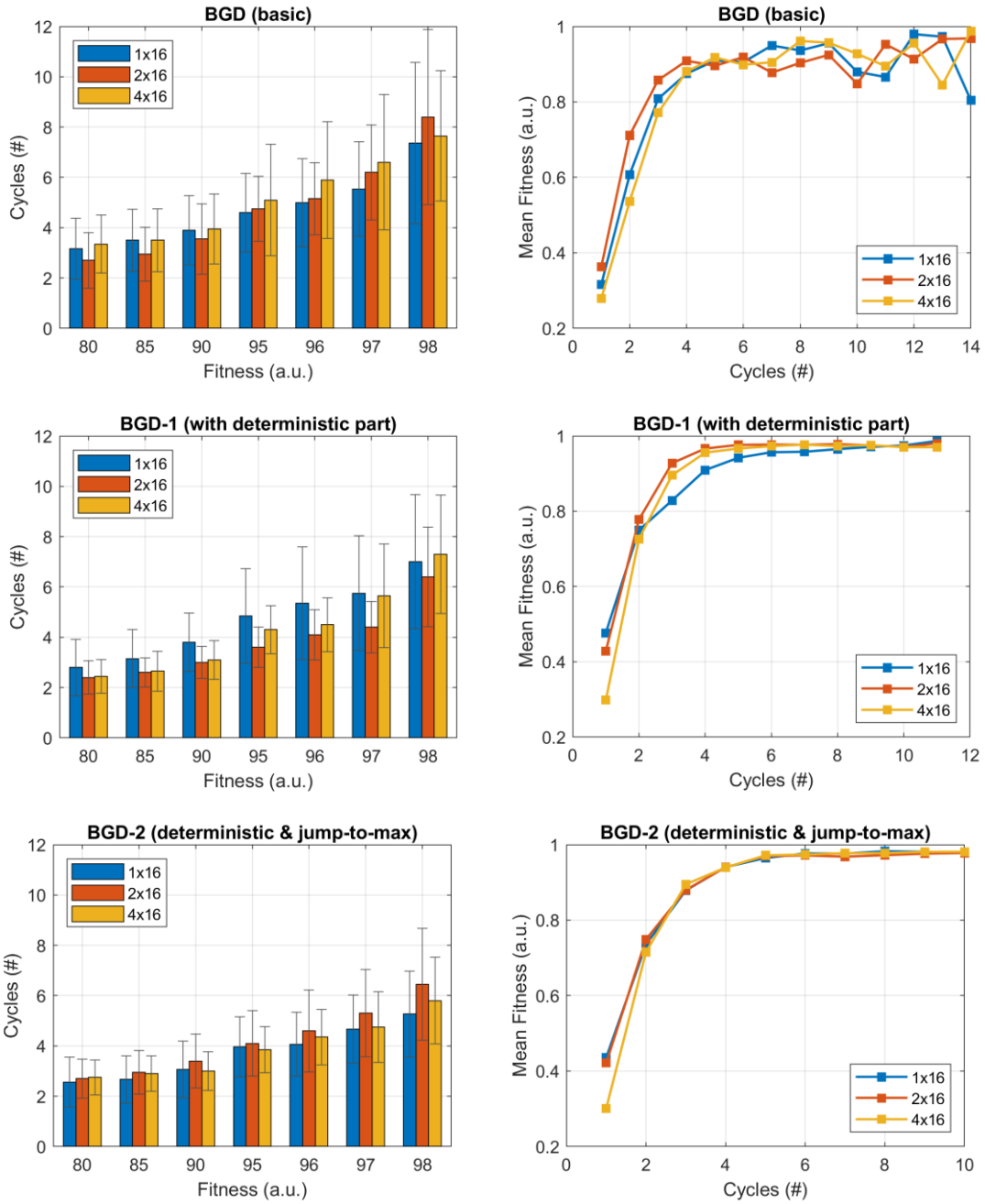

Figure 2.42: Theoretical performance of the basic batch gradient descent (BGD) algorithm and its two variations, ‘deterministic’ and ‘jump-to-max’, for three array geometries: 1, 2 and 4 waveguiding layers with 16 elements per layer. For each variation of the algorithm, we present (Left) the number of evaluations to reach a specific fitness level and (Right) the average fitness evolution out of 20 runs.

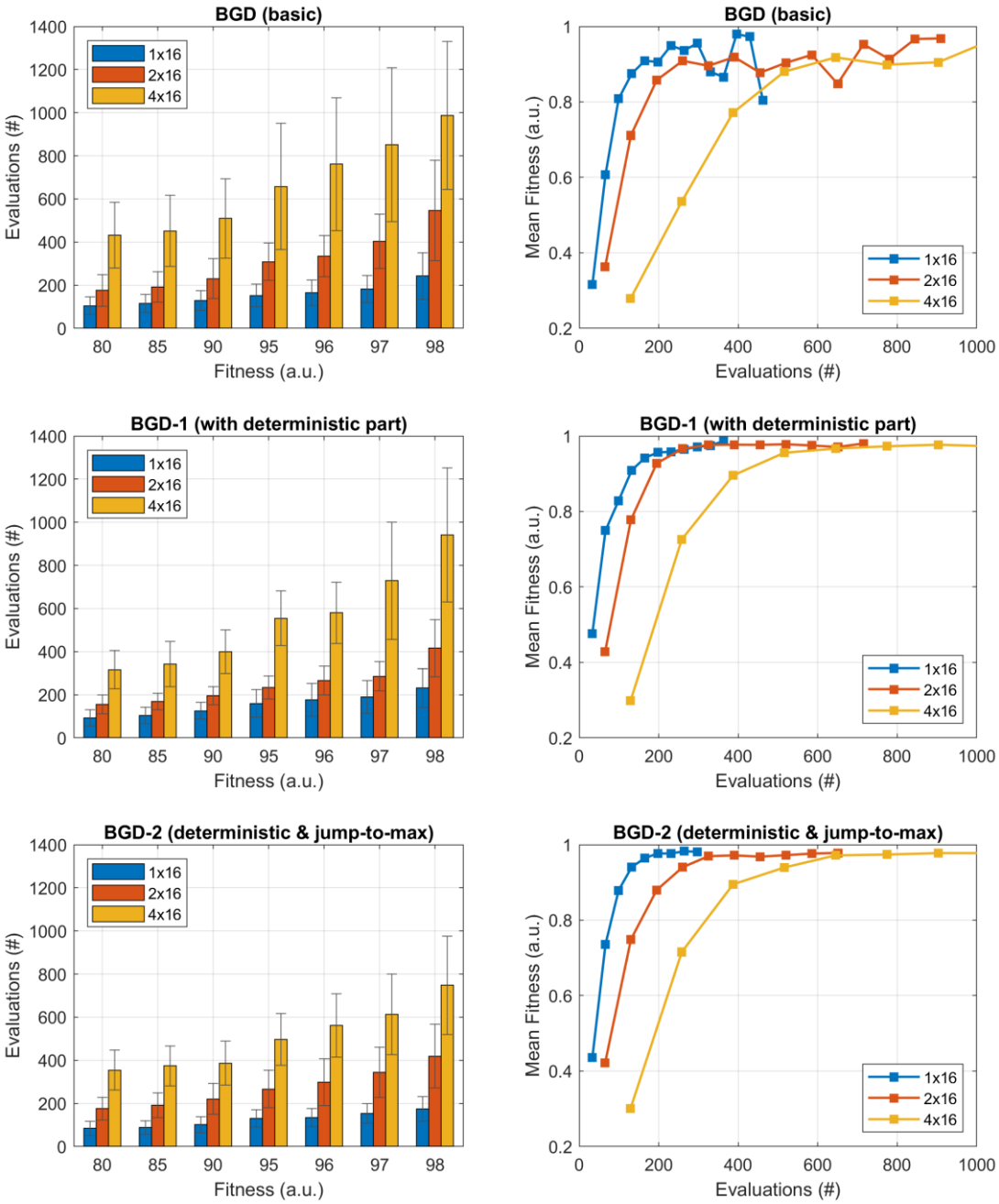

Figure 2.43: Theoretical performance of the basic batch gradient descent (BGD) algorithm and its two variations, ‘deterministic’ and ‘jump-to-max’, for three array geometries: 1, 2 and 4 waveguiding layers with 16 elements per layer. For each variation of the algorithm, we present (Left) the number of evaluations to reach a specific fitness level and (Right) the average fitness evolution out of 20 runs (Right). Each cycle corresponds to (2*N+1) evaluations, where N is the number of channels.

2.5.1.4 Stochastic parallel gradient descent (SPGD) algorithm

SPGD is a popular adaptive wave-front control technique originally proposed in [123]. The fitness function for a system with N control channels is defined as

$$\mathcal{F} = \mathcal{F}(u_1, u_2, \dots, u_N) = \mathcal{F}(\boldsymbol{u}) \tag{2.67}$$

, where u_i are the control parameters, i.e., the phase of the optical field in the i-th channel. In its original version, random perturbations δu_i with fixed amplitudes $|\delta u_i| = \delta u$ and random signs with equal probabilities $\delta u_i = +\delta u$ and $\delta u_i = -\delta u$ are applied in every channel simultaneously. Fitness perturbation is defined as $\delta\mathcal{F} = \mathcal{F}(\boldsymbol{u} + \boldsymbol{\delta u}) - \mathcal{F}(\boldsymbol{u})$, and the true gradient component $\partial\mathcal{F}/\partial u_i$ is approximated by $\delta\mathcal{F}/\delta u_i$. The benefit is that the stochastic gradient approximation $\delta\mathcal{F}/\delta u_i$ is calculated in a single step regardless of the number of dimensions of the system, i.e., the OPA channel, in opposition to the calculation of the true gradient scales linearly with the dimensions of the system. In our implementation we used a variation of the classical SPGD known as decoupled SPGD [124]. In that version small random perturbations δu_i with zero average value and equal variance, i.e.,

$$< \delta u_i > = 0 \tag{2.68}$$

$$\delta u_i \delta u_j = \sigma^2 \delta_{ij} \tag{2.69}$$

are applied to every channel simultaneously and the fitness perturbation is calculated as

$$\mathcal{F}^+ = \mathcal{F}(\boldsymbol{u} + \boldsymbol{\delta u}) \tag{2.70}$$

$$\mathcal{F}^- = \mathcal{F}(\boldsymbol{u} - \boldsymbol{\delta u}) \tag{2.71}$$

$$\delta\mathcal{F} = \mathcal{F}^+ - \mathcal{F}^- \tag{2.72}$$

, and thus, the stochastic approximation $\delta\mathcal{F}/\delta u_i$ of the true gradient component is calculated in two steps (calculation of $\mathcal{F}^+$ and $\mathcal{F}^-$). In each iteration $\boldsymbol{u}$ is updated as

$$\boldsymbol{u}^{(k+1)} = \boldsymbol{u}^{(k)} + \gamma \cdot \delta\mathcal{F}^{(k)} \cdot \boldsymbol{\delta u}^{(k)} \tag{2.73}$$

, where γ represents the learning rate and k is the number of iterations. An important parameter associated with $\boldsymbol{\delta u}$ is the maximum step size. Larger steps improve the convergence speed in the initial stages but they may lead in oscilations in later stages and make the progress slower. In Table 9 we present a pseudo-code of the implemented SPGD. Within each iteration the algorithm accesses the DAC three times and evaluates the radiation pattern twice, once for $\mathcal{F}^+$ and once for $\mathcal{F}^-$. As the algorithms presented above, we performed 20 runs of the SPGD algorithm for three OPA geometries and the result are shown in Figure 2.44. For the most complex geometry, the algorithm needs less than 700 evaluations to reach 98% fitness, which makes it the fastest converging algorithm among

```
while F ≤ target_fitness or i ≤ max_iterations
        Generate δu
        Set_DAC_voltages(u + δu)      # Write to DAC
        Read_from_camera()            # Read pattern from camera
        Evaluate F+                   # Evaluate fitness
        Set_DAC_voltages(u − δu)      # Write to DAC
        Read_from_camera()            # Read pattern from camera
        Evaluate F−                   # Evaluate fitness
        Calculate δF
        Calculate u^(k+1)
        Set_DAC_voltages(u^(k+1))     # Write to DAC
end
```

Table 9: Pseudo-code of the implemented stochastic parallel gradient descent (SPGD) algorithm.

the presented for the specific geometry. A drawback of SPGD is that its convergence speed can vary significantly based on the initial state, as it is shown in the fitness evolution plot in Figure 2.44. To address this limitation initial pre-alignment of the heaters using a deterministic hill-climbing algorithm has been proposed in [131]. However, no further improvement of the basic SPGD algorithm was investigated in this work, as small array geometries were fabricated and tested as proof-of-concept. In Figure 2.45 we perform a comparison between the SPGD algorithm and the best version of the BGD algorithm (BGD-2). To fully appreciate the scaling potential of each algorithm we extend our study to larger array geometries including the rectangular arrays 8×8 and 16×16. We plot the number of evaluations to reach fitness levels of 0.95 and 0.98 as a relation to the geometry, which can be either linear or rectangular. We conclude that BGD2 demonstrates faster

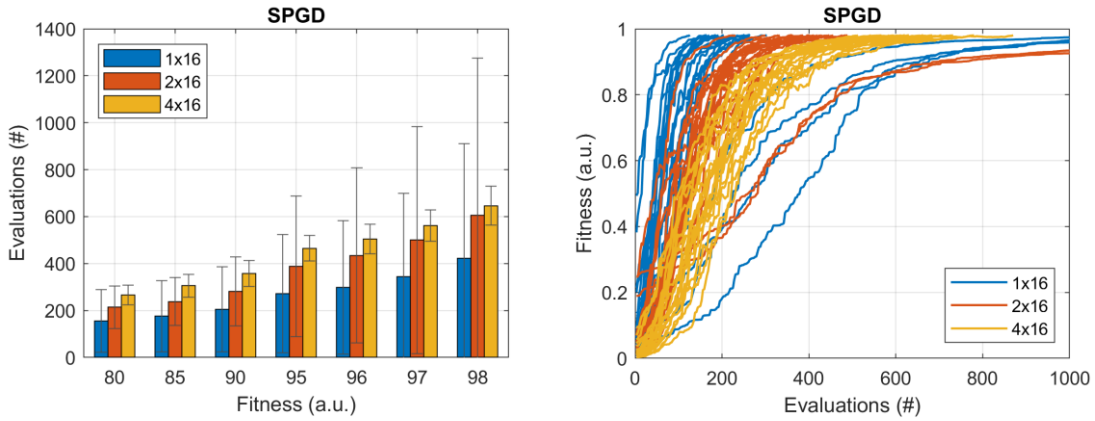

Figure 2.44: (Left) Number of evaluations needed to reach a specific fitness value and (Right) the mean fitness evolution over time for the stochastic parallel gradient descent (SPGD) algorithm.

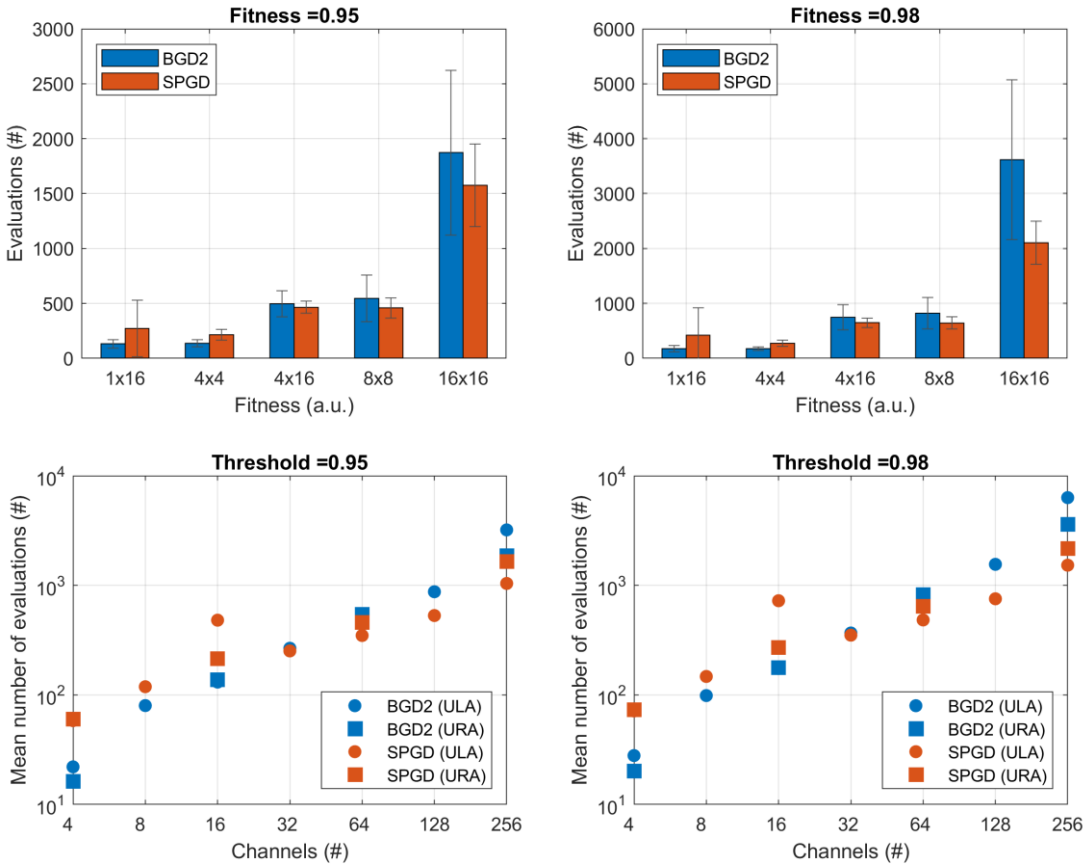

Figure 2.45: Comparison of SPGD and BGD-2 algorithms. The upper row shows the mean number and standard deviation of evaluations required to achieve a fitness of 0.95 (Left) and 0.98 (Right) for some selected geometries. The bottom row presents the mean number of evaluations as a function of the total number of channels for uniform linear arrays (ULA), i.e., of the form 1×N, and uniform rectangular arrays (URA) of the form N×N. The SPGD algorithm is more efficient for larger geometries, particularly when the number of channels exceeds 32.

convergence than SPGD when the number of channels is below 32, while for greater number of channels SPGD has a clear advantage.

2.5.2 Experimental results

2.5.2.1 Extraction of V-I characteristic

The algorithms presented in the previous paragraph were used for the testing of the uniform and aperiodic arrays. More specifically, we used the improved BGD algorithm (BGD-2) for the phase error calibration of the 1×4 and 2×4 OPAs, and the SPGD algorithm for the aperiodic 1×16 OPAs. The heating electrodes were driven by means of a programmable voltage controlled current source. Prior to employing the calibration algorithms, careful characterization of the heating electrodes was performed. First, the V-I characteristic of each heater is determined. We sweep the driving current from 0 to 20 mA and measure the voltage drop on the heating element. From the V-I curve, the dissipated

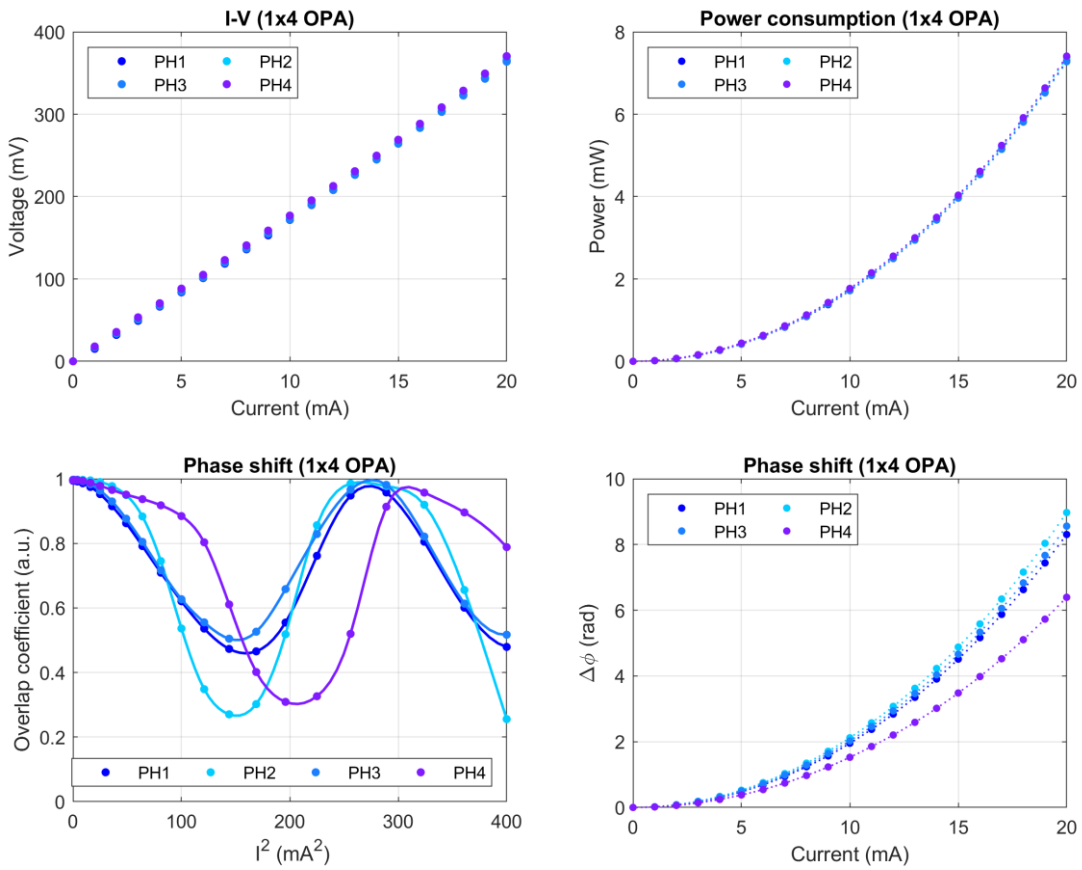

Figure 2.46: Calibration of the phase heaters of the uniform 1×4 OPA. (Top row) I-V characteristic and power dissipation of the phase heaters (PHs) as a function of the applied current. (Bottom left) Extraction of the half-wave phase shift current I_π based on the radiation pattern. The heater current is swept from 0 to 20 mA and the initial radiation pattern is repeated after a full 2π shift. (Bottom right) The applied phase shift with respect to driving current.

power, and consequently the phase shift, can be drawn as a function of the applied current (Figure 2.46 (Top)). As described in equation (2.60) there is a linear relationship between phase shift and dissipated power. With the above set of measurements, the non-linear behavior of the heater resistance due to self-heating is considered, providing more accurate control of the phase heaters (PHs). However, V-I curves do not provide any information about the introduced phase shift. To determine the half-wave phase shift (π) current I_π, we perform another characterization based on the radiation pattern as follows. The phase shifters are initially set to a random state that produces a distinguishable radiation pattern, which is stored as a reference. Next, the current in each phase heater is swept from 0 to 20 mA and the corresponding radiation pattern is captured. The similarity between the measured pattern and the reference pattern is quantified using the overlap coefficient. The point at which the initial radiation pattern appears once again indicates the 2π phase shift, while the point of least similarity corresponds to a π phase shift. The results of this characterization are shown in Figure 2.46 (Bottom). We should comment at this point, that

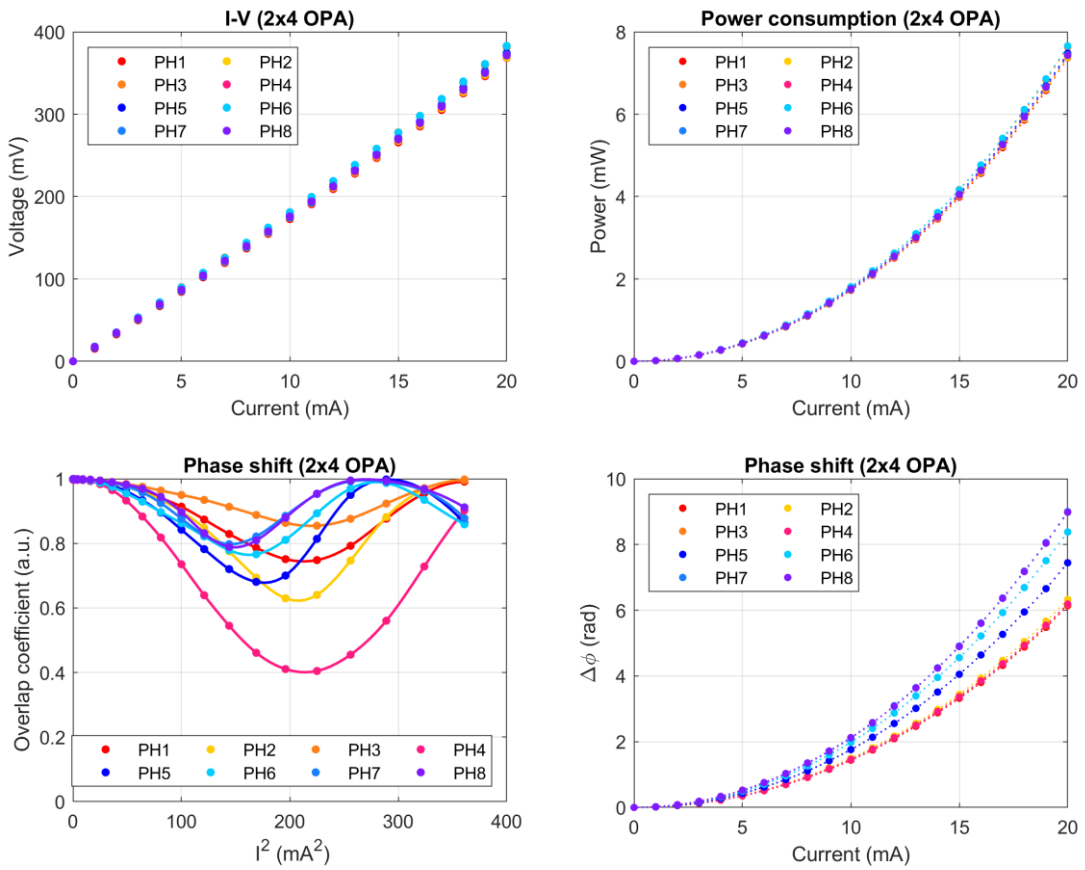

Figure 2.47: Calibration of the phase heaters of the uniform 2×4 OPA. (Top row) I-V characteristic and power dissipation of the phase heaters (PHs) as a function of the applied current. (Bottom left) Extraction of the half-wave phase shift current I_π based on the radiation pattern. The heater current is swept from 0 to 20 mA and the initial radiation pattern is repeated after a full 2π shift. (Bottom right) The applied phase shift with respect to driving current.

as the size of the array increases, the influence of a single element becomes increasingly smaller, limiting the applicability of the described method. However, a similar approach was successfully used to extract $I_{2\pi}$ in a 256-channel array [130]. In that study, the authors used the beam power as an indicator of the introduced phased shift. Consequently, the minimum detectable power swing was constrained only by the sensor's noise. The final step is to corelate the P-I curve obtained from the V-I characterization with the phase shift $\Delta\varphi$, or, equivalently, to determine the parameter k in equation (2.60). The initial phase error φ_{error} in equation (2.60) can be omitted and k can be calculated as π/P_π, where P_π is the half-wave power that corresponds to I_π, and can be determined from the P-I curve.

The characterization results of the 1×4 and 2×4 OPAs are presented in Figure 2.46 and Figure 2.47 respectively. In Figure 2.47 the different efficiencies of the upper layer (PH5-PH8) and bottom layer (PH1-PH4) phase heaters can be observed. The average P_π for the upper layer is ~2.8 mW, where for the bottom layer is ~3.8 mW. An exception in the upper

layer is heater PH4 of the 1×4 OPA that demonstrates P_π = 3.7 mW. However, it should be mentioned that the heaters were accessed with the help of electrical DC probes, which do not provide the same electrical conductivity. In fact, from a practical point of view, as the number of channels increases, it becomes increasingly difficult to access the pads of a chip in a uniform way. Consequently, the resistance between probe wires and chips' pads is not the same for all channels and can lead to different P_π measurements. Of course, this non-uniformity is not present in the case of wire-bonded chips. The larger amount of power that is needed to achieve a half-wave phase shift in waveguides of the bottom layer is related to the fact that there is a larger distance between the heating electrode and the waveguide structure. An improved version of Au heaters was used in the 16-channel aperiodic arrays that demonstrated an average P_π of ~1.3 mW (width = 15 μm, length = 500 μm).

2.5.2.2 Phase calibration

The BGD algorithm described in the previous section was applied to calibrate the actual PICs, specifically bare dies of the uniform 1×4 and 2×4 OPAs. Figure 2.48 presents the experimental results alongside the theoretical predictions from our modelling for the two best performing versions: BGD1 and BGD2. The plot illustrates the number of evaluations required to reach a specified fitness level, with the fitness function defined as the overlap coefficient. Each algorithm was executed 25 times for the two geometries. In the case of 2×4 OPAs, experimental performance closely aligns with the theoretical results. In contrast, for 1×4 OPAs, the experiment required more evaluations to achieve the same fitness level. The SPGD algorithm was employed to calibrate the PICs with the 1×16 non-uniform OPA. However, a comprehensive performance evaluation of the algorithm was not conducted. Figure 2.49 showcases three example runs of the implemented SPGD algorithm, using the PIC with the aperiodic OPA design #1 (see Table 6). The maximum fitness value achieved experimentally was 0.85, due to the errors introduced in the experimental setup. These errors were mainly attributed to camera noise and PIC fabrication imperfections, which caused deviations between the experimental pattern and the theoretical one. The algorithm demonstrated experimental performance similar to the average theoretical performance, as indicated by the black line in the corresponding figure.

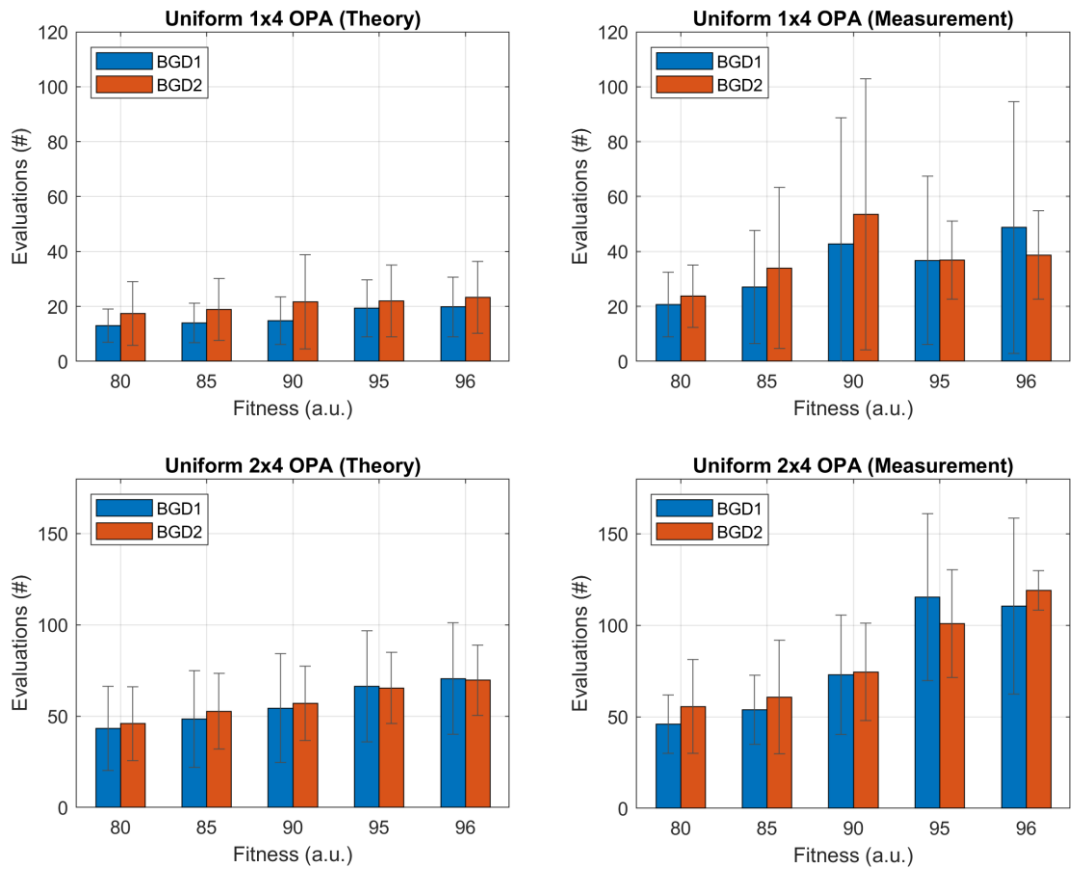

Figure 2.48: Comparison of the theoretical and experimental performance of the BGD algorithms (BGD1 and BGD2), based on 25 runs of each algorithm.

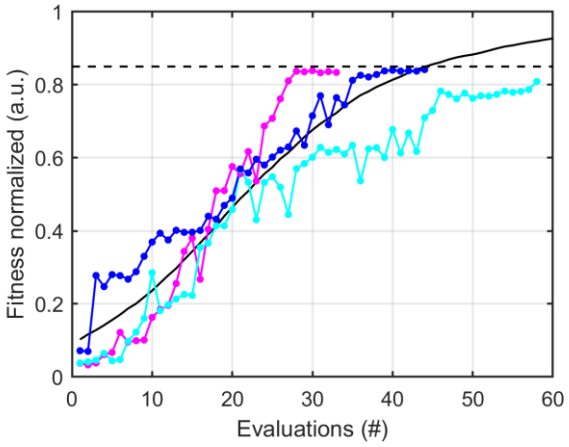

Figure 2.49: Example experimental runs from the SPGD algorithm with the first aperiodic design OPA PIC. The black curve shows the simulated performance of the algorithm. The maximum fitness values achieved experimentally was 0.85.

2.6Four-layer OPA

A passive multi-layer structure with four waveguide layers was fabricated on the PolyBoard platform to implement a 2D OPA at 1550 nm. Each layer comprised eight waveguides to form a 4×8 array with 32 independently controlled channels. In each layer, the waveguides are routed to the edge of the PIC for free space emission. To control the phase of each channel an additional PIC with an array of 32 phase heaters was fabricated also in PolyBoard, designed for edge-coupling with the passive 4×8 OPA PIC. An illustration of the PolyBoard PIC is shown in Figure 2.50.

2.6.1 PIC design and fabrication

2.6.1.1 Passive 4×8 array PIC

Figure 2.51 illustrates the waveguide routing in the 3D PIC in more detail. The light is coupled to the bottom layer of the PIC and is transferred to the corresponding layer using 1×1 vertical multi-mode interference couplers (vMMIs). The waveguide pitch at the input is 127 μm. Starting from the north side of the chip as shown in Figure 2.51, light from the 1st input remains to layer 1, light from the 2nd input is transferred to layer 2, from the 3rd input to layer 3, from the 4th input to layer 4, from the 5th input back to layer 1, and so on. The mapping of each channel to the aperture is shown in Figure 2.51. The vertical waveguide pitch is selected to be 7.2 μm, determined by the height of the 1×1 vMMI structure, which is designed to be 10.4 μm [54]. Additionally, this distance ensures suppressed optical crosstalk between the waveguides of different layers. To transfer light between multiple layers, a cascaded configuration of vMMIs is used [56]. The waveguide

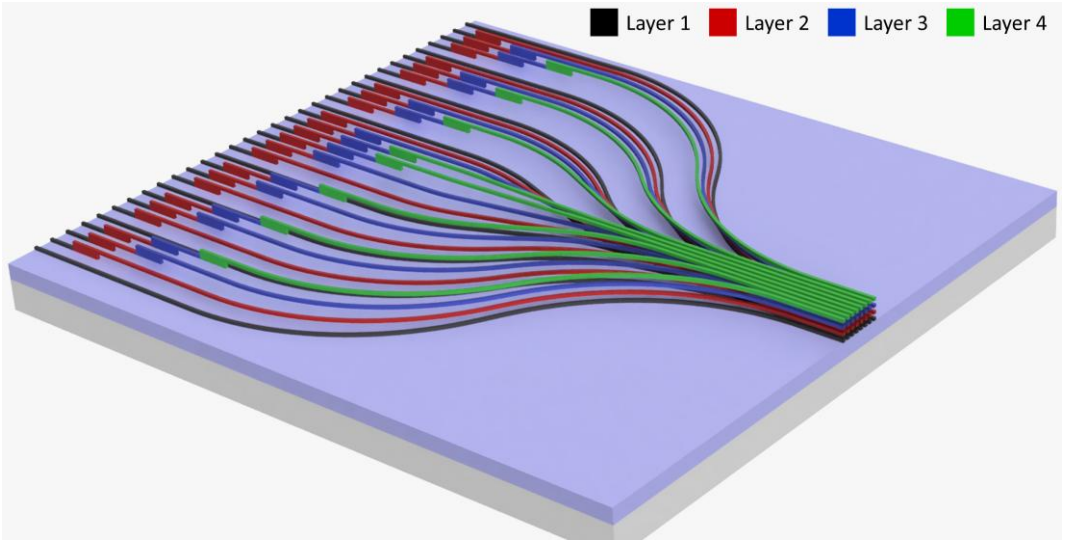

Figure 2.50: Illustration of the passive 4×8 OPA in the PolyBoard platform.

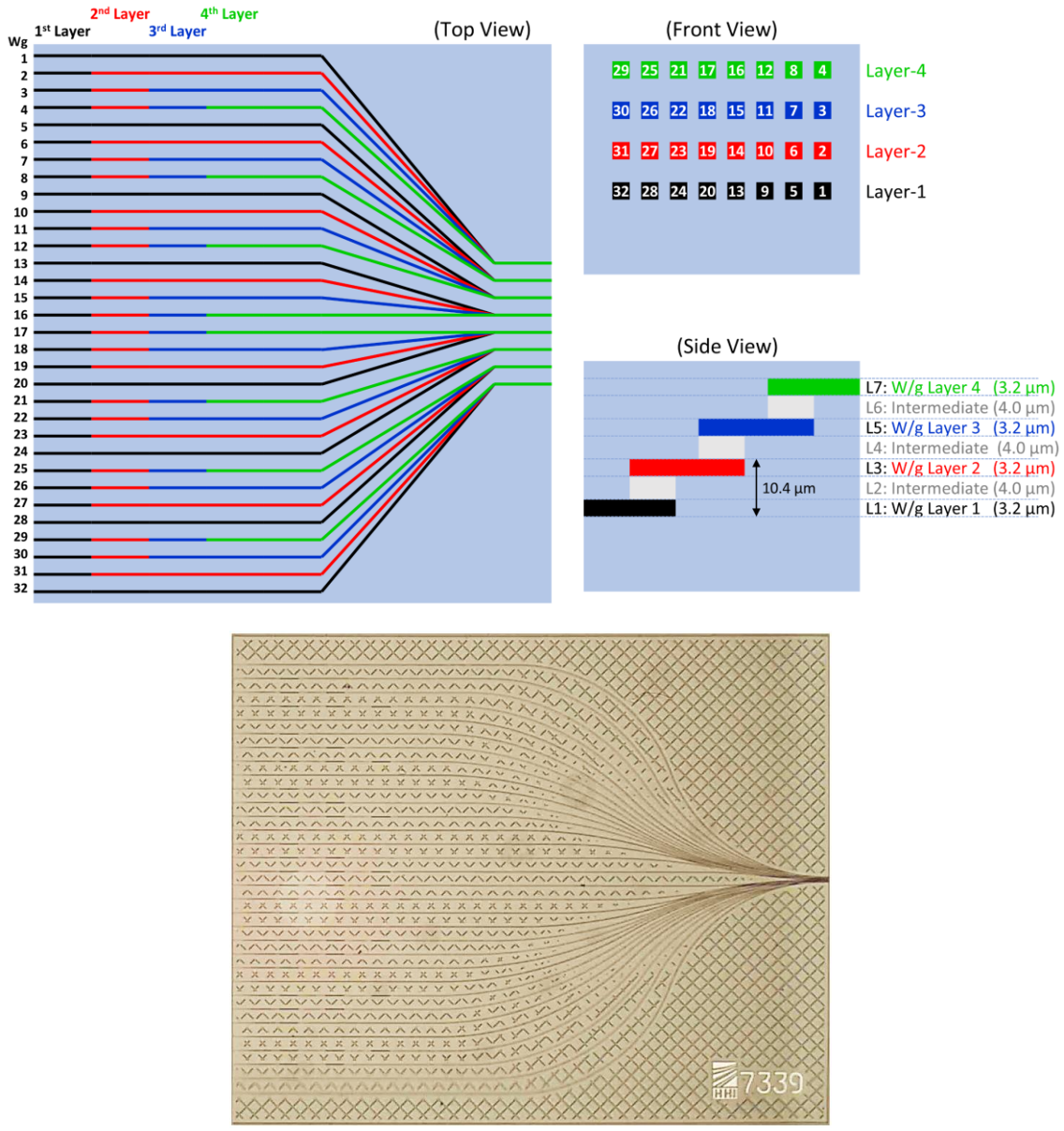

Figure 2.51: (Top) Schematic representation of the passive 4×8 OPA. The mapping of the 32 channels to the emitting aperture is shown. (Bottom) Fabricated PIC of the passive 4×8 OPA. The dimensions of the PIC are 5.5 mm × 4.5 mm.

dimensions are 3.2 µm × 3.2 µm, optimized for single mode operation around 1550 nm. We should note that the optical path lengths were not designed to be equal, so phase tuning is needed to converge the emitted power to a certatin angle.

To realize the specific multi-layer PIC the standard fabrication process of PolyBoard was optimized, primarily to address the challenge of wafer topography and improve the accuracy of the thinning process. The main fabrication steps for the formation of mutliple layers in PolyBoard are shown in Figure 2.1. Standard UV-photolithography and oxygen plasma reactive ion etching (RIE) is used to structure the waveguide layers. ChemOptics

ZPU-12 series material is used to fabricate waveguide core and cladding layers. The layer deposition alternates between these two materials. The uncured, liquid cladding material is spin-coated on a silicon substrate and cured by UV exposure. Subsequently, the same procedure is followed for the core layer. After the core layer is cured, it has to be structured to form waveguides. For this purpose, a photoresist is applied and exposed by means of UV lithography. The resist is developed and titanium (Ti) is evaporated onto the wafer surface. A lift-off process is carried out and the Ti remains in the areas above the waveguide, where it serves as an etching mask (Ti mask) that protects the underlying surface from the oxygen plasma etch. Another layer of cladding material is then applied on top of the waveguide. To ensure direct contact with the following waveguide plane the cladding has to be thinned down to the upper edge of the waveguide. In the standard fabrication process, the Ti mask is removed directly after the waveguide layer structuring. In the optimized process for the fabrication of multiple waveguide layers, the Ti mask is not removed before the cladding is applied [54]. This approach allows for precise control over the thinning process, enabling accurate determination of the cladding layer thickness above the waveguide using white light interferometry. Once the top cladding is etched, the Ti mask resurfaces and is subsequently removed to allow for the application of the next core material layer. During this step, the Ti mask also functions as a protective layer for the waveguide. This modification to the standard fabrication process on the PolyBoard platform results in a newly optimized workflow. The same procedure is followed for the topmost waveguide plane. However, in the final step, the Ti mask is removed before applying the cladding, and the cladding remains in place above the waveguide to serve as a protective layer.

The stacking of multiple waveguide layers creates significant surface topography, which can result in locally uneven thinning of the cladding. Figure 2.52 illustrates the effect of layer thickness variation across the wafer. Following thinning with oxygen plasma RIE, the Ti mask used for waveguide structuring is exposed and subsequently removed to continue the fabrication process. However, when the polymer cladding is slightly thicker, the thinning process may fail to fully expose the titanium hard mask on the waveguide. As a result, the mask cannot be removed, rendering the specific device unusable. Further etching is not feasible, as it would excessively reduce the cladding layer thickness around the functioning waveguides. The allowable thickness variation across the entire wafer is less than 500 nm. This issue becomes increasingly pronounced as the number of waveguiding layers increases. To tackle this challenge, a planarization process was

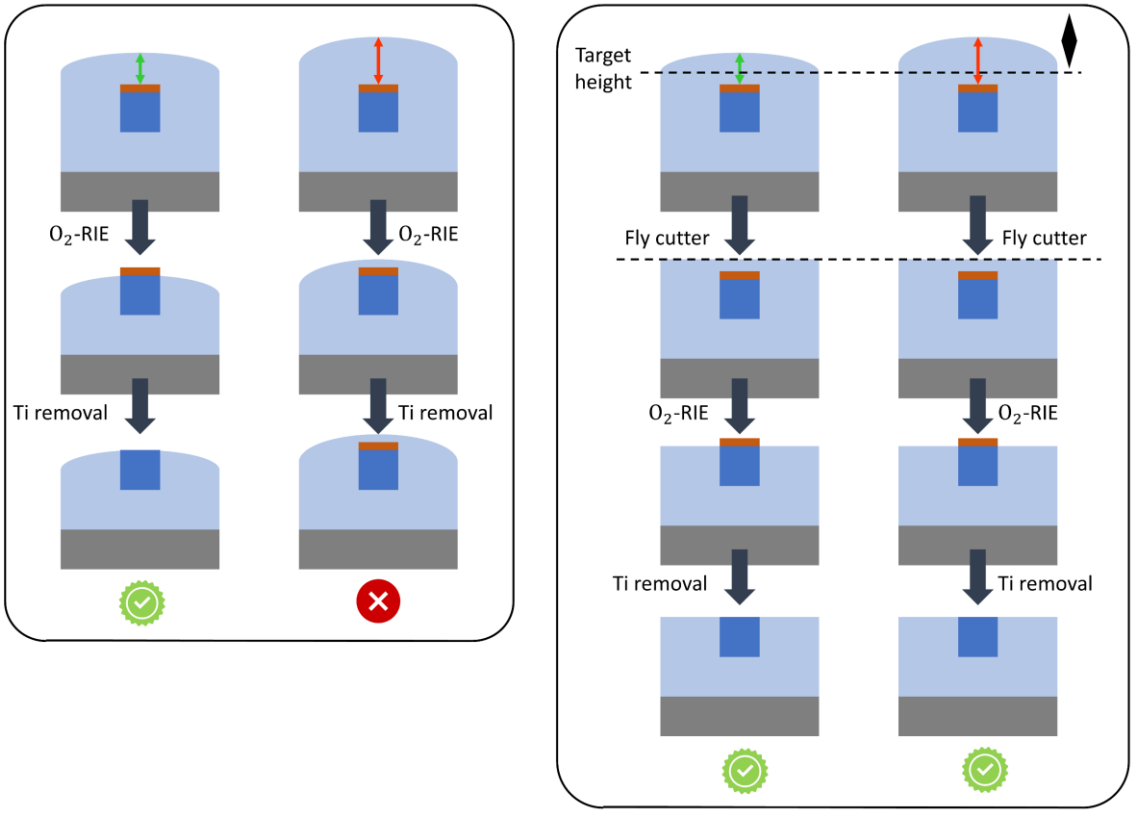

Figure 2.52: (Left box) Effect of variation of polymer cladding thickness across the wafer during the fabrication of vMMIs. The thickness difference causes some of the devices to be unusable, because the titanium (Ti) mask cannot be removed. (Right box) Wafer planarization for reliable fabrication of vertically connected polymer waveguide layers.

developed for the PolyBoard wafers. This process employs a fly cutter to level the wafer surface, reducing the polymer thickness to a predefined height. As shown in Figure 2.52, the fly cutter eliminates the topography and reduces the polymer layer thickness to the desired target height. This process ensures that the Ti mask maintains a consistent distance from the wafer surface across the entire wafer. This uniform distance serves as the target etch depth during the RIE process. As a result, the Ti layer is uniformly exposed on all structures. Finally, the Ti layer is removed from all structures.

Once planarization is completed, the entire wafer surface exhibits increased roughness due to the fly cutter. While this roughness provides immediate feedback that planarization has been successfully achieved, it is undesirable because it can increase optical losses from scattering. This issue can be mitigated by spin-coating a thin polymer cladding layer (a few micrometers thick) onto the wafer after planarization. The cladding layer does not reintroduce surface topography, as spin coating on a flat surface results in a highly uniform layer thickness, with variations on the order of 200 nm across the usable wafer area. However, the spin-coated layer also exhibits surface roughness similar to that of the initial

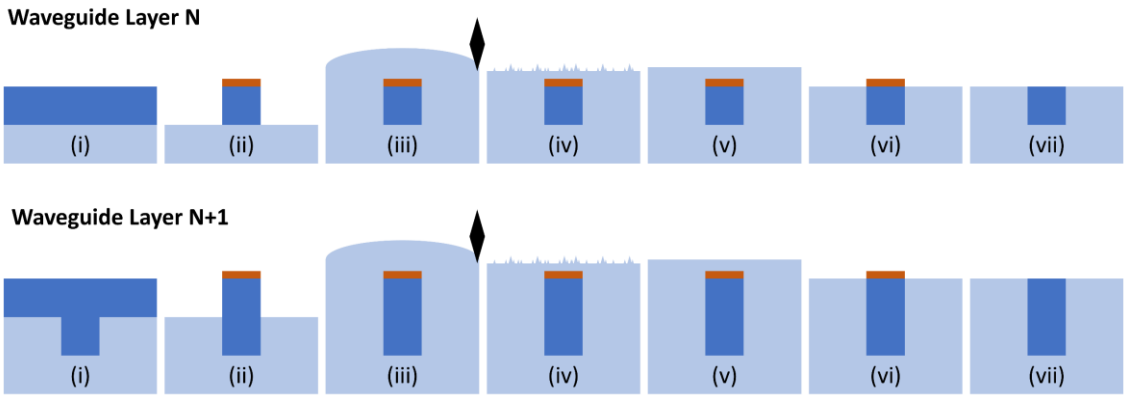

Figure 2.53: Final fabrication process developed for multilayer PolyBoard structures.

polymer layer before planarization. The final fabrication process of multi-layer PolyBoard structures is presented in Figure 2.53. The fabrication of the n-th waveguide layer begins with spin-coating a polymer core material layer onto a planar surface (i), which can be either an unstructured wafer with polymer cladding, or a planarized multilayer PolyBoard wafer with an existing waveguide layer beneath. Next, the waveguide core is patterned using a titanium mask and etched with RIE (ii). The wafer topography, resulting from the spin-coating of the polymer cladding layer, is then removed with the fly cutter (iii), leaving a rough wafer surface (iv). This roughness is smoothed out by spin-coating a thin polymer layer (v). After an additional RIE step, the Ti layer is exposed (vi) and finally removed from all structures (vii). The same process is repeated for the (n+1)-th waveguide layer, with the new waveguide layer aligned to the n-th layer to ensure proper coupling, with an alignment accuracy < 1 μm. The effect of the alignment accuracy is discussed in 2.6.2.

2.6.1.2 Phase control PIC

Phase tuning is supported by a different PIC which comprises 32 phase heaters. Figure 2.54 presents the mask of the PIC. The input optical power is distributed across the 32 channels using a plitting tree, based on a 1×2 MMI and two stages of 1×4 MMIs. The splitting tree has a total length of 7.5 mm. Each heater features a width of 15 μm and a length of 500 μm. To minimize the number of pads and electrical connections, a common ground pad is shared among all heaters. A U-groove is incorporated at the chip's input to facilitate optical fiber coupling. At the chip's output, the waveguides are designed with a 127 μm pitch to align with the input waveguides of the passive 4×8 OPA PIC.

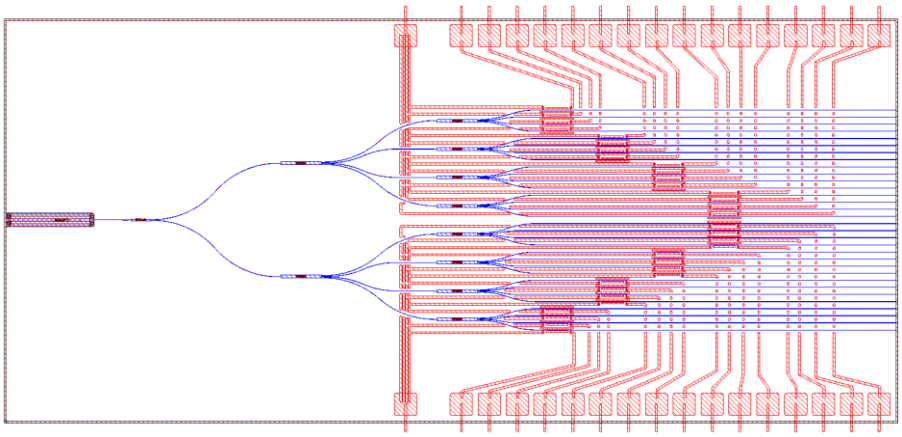

Figure 2.54: PolyBoard PIC comprising the splitting tree and 32 thermal phase shifters for the phase tuning of the passive 4×8 OPA. The dimensions of the PIC are 7.2 mm × 16 mm.

2.6.2 Modelling of excitation imbalance

A simulation of the radiation pattern of the 4×8 OPA was conducted to assess the impact of excitation amplitude imbalance caused by the insertion losses of the 1×1 vertical MMI (vMMI), introduced at each layer transition. The insertion loss of vMMIs has been extensively studied and reported [54][56][60]. As described in [54], the loss arises from layer misalignment within the vMMI structure due to process tolerances (see Figure 2.55). The width (W) and length (L) of the vMMI have been optimized to minimize these losses, assuming offset values below 2 µm [54]. The actual fabrication tolerances are less than 1 µm. Depending on the wavelength and polarization state, the vMMI insertion loss ranges from 1.0 to 1.5 dB (1520 nm to 1580 nm). In [56], the loss introduced by three cascaded vMMIs was measured to be between 2.5 and 4 dB (1500 nm to 1600 nm). These values have also been confirmed in a recent study on multi-layer PICs for switching applications [60]. In our study, we examined the impact of insertion loss, considering values ranging from 0.1 dB to 3 dB for a single vMMI structure, corresponding to each layer transition.

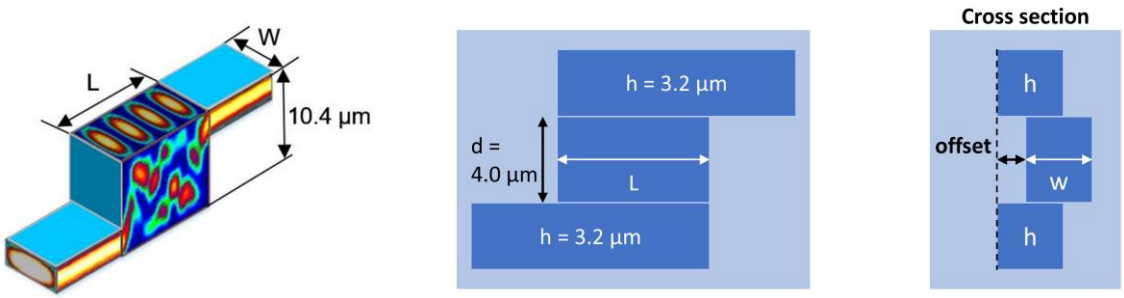

Figure 2.55: Vertical MMI coupler. The fabrication tolerances may lead to an offset between the individual layers of the MMI.

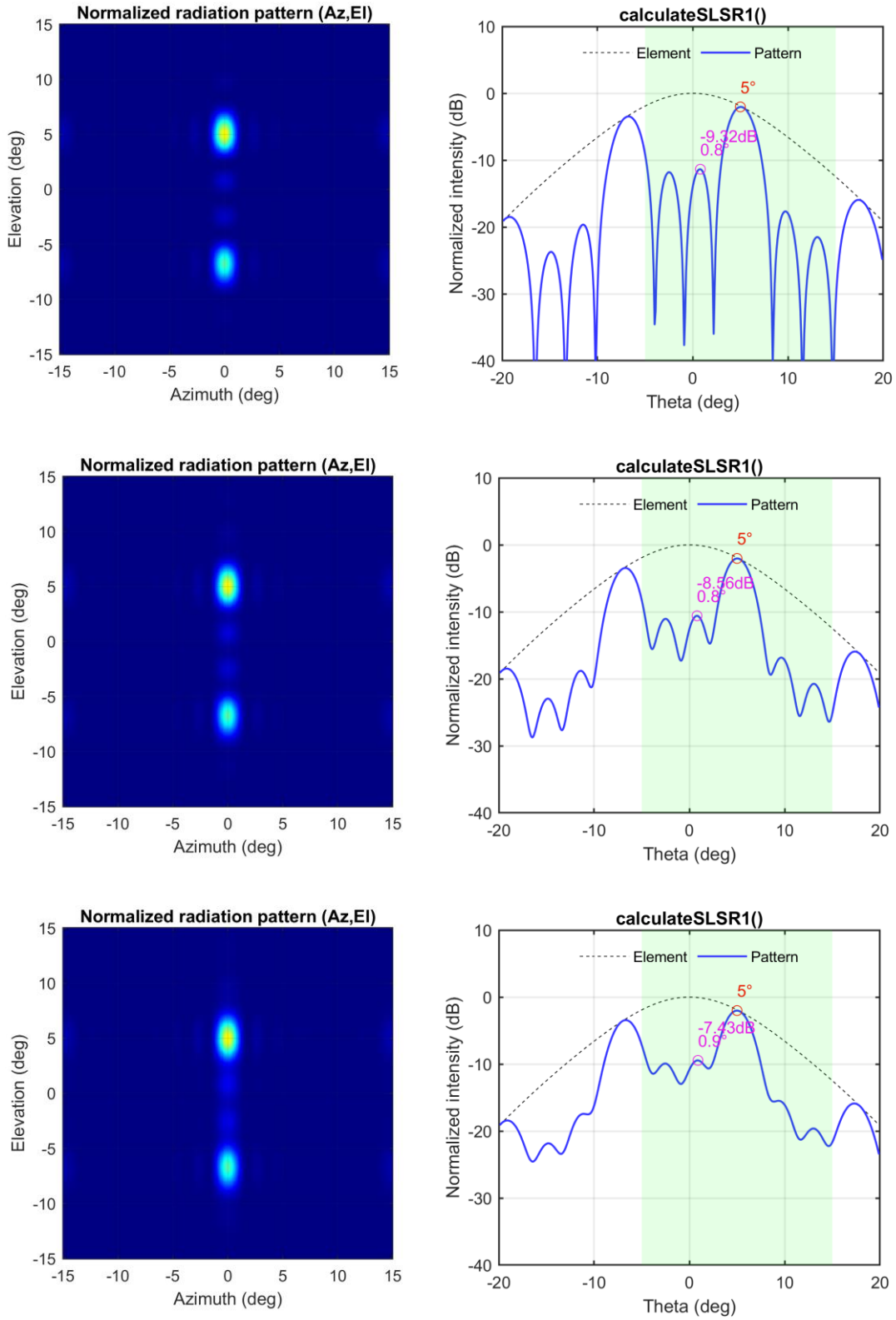

Figure 2.56: Radiation pattern of 4×8 uniform OPA with transition loss between the layers: (Top) 0.1 dB, (Middle) 1.2 dB and (Bottom) 2 dB. In the right column the slice at 0º azimuth is shown.

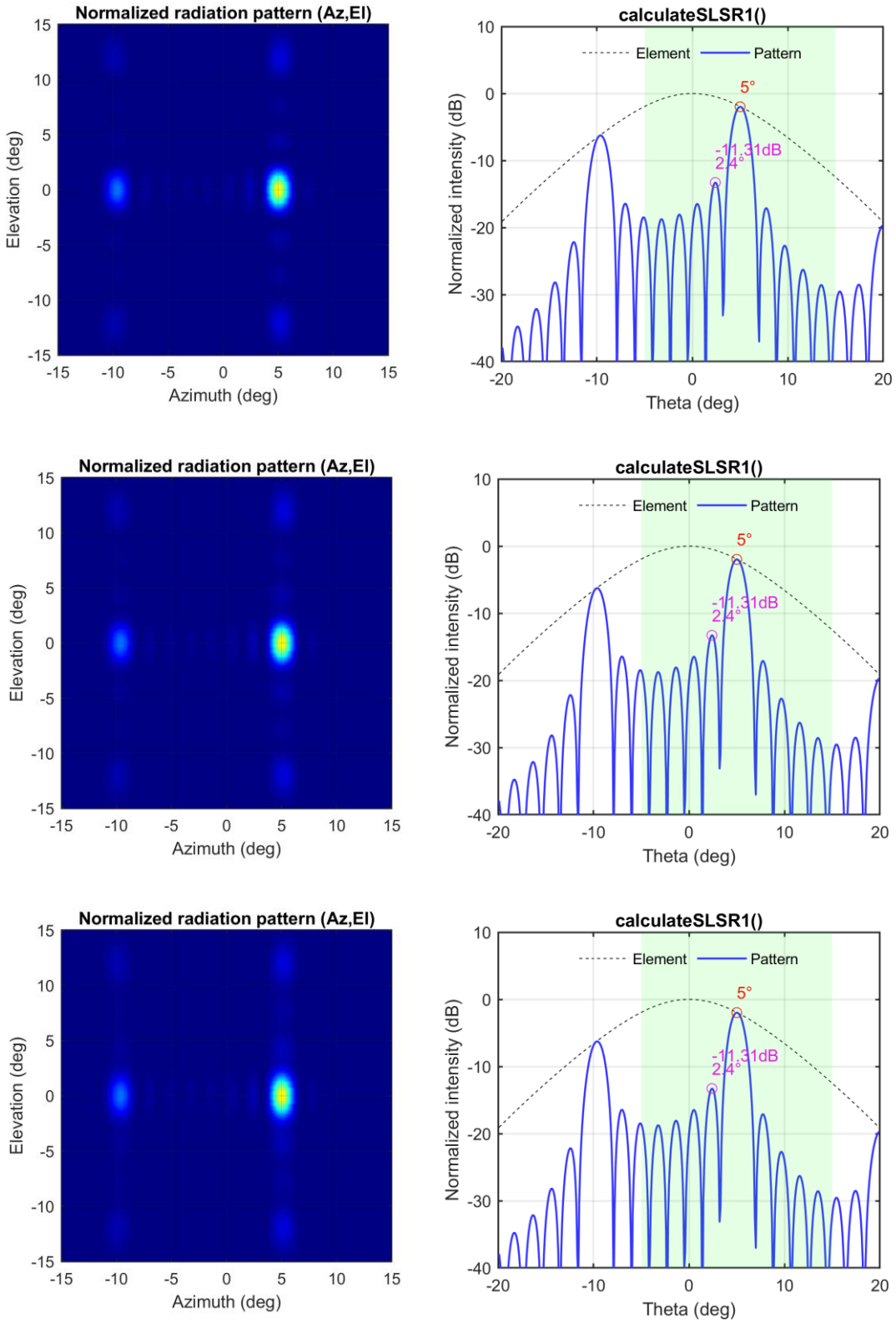

Figure 2.57: Radiation pattern of 4×8 uniform OPA with transition loss between the layers: (Top) 0.1 dB, (Middle) 1.2 dB and (Bottom) 2 dB. In the right column the slice at 0º elevation plane is shown. No difference is observed in the radiation pattern across the elevation plane.

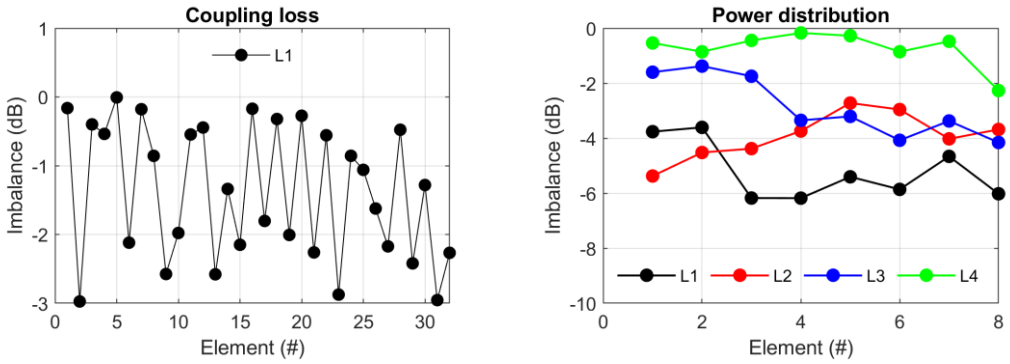

Figure 2.58: (Left) Power imbalance among the 32 channels due to couplings losses between the passive OPA and the control PIC. (Right) Power distribution among the elements in each of the four layers after taking account the coupling losses with the control PIC and the vertical MMIs.

In Figure 2.56, the beam is directed to $az = 0°$ and $el = 5°$. The operating wavelength is 1.55 μm. The grating lobe is visible since the vertical waveguide pitch is 7.2 μm. We plot a vertical slice of the radiation pattern at $az = 0°$ and calculate the suppression ratio of the 1st sidelobe relative to the main lobe for three different values of vMMI insertion loss: (Top) 0.1 dB, (Middle) 1.2 dB, and (Bottom) 2 dB. As the transition loss per layer increases, the suppression ratio decreases, and the overall noise floor rises, resulting in shallower nulls in the radiation pattern. In Figure 2.57, the beam is directed to $az = 5°$ and $el = 0°$. We plot a horizontal slice of the radiation pattern at $el = 0°$ and again calculate the suppression ratio of the 1st sidelobe relative to the main lobe. It is clear that the amplitude imbalance across the vertical axis of the array does not have an impact on the radiation pattern across the azimuth axis (horizontal). In our modelling we take into account the power imbalance among the 32 channels of the array due to the coupling losses between the 4×8 passive OPA PIC and the phase control PIC, assuming a maximum imbalance of 3 dB (see Figure 2.58). Figure 2.59 presents the suppression ratio of the 1st sidelobe for a 4-layer and an 8-layer OPA across the elevation axis ($az = 0°$), similar to Figure 2.56.

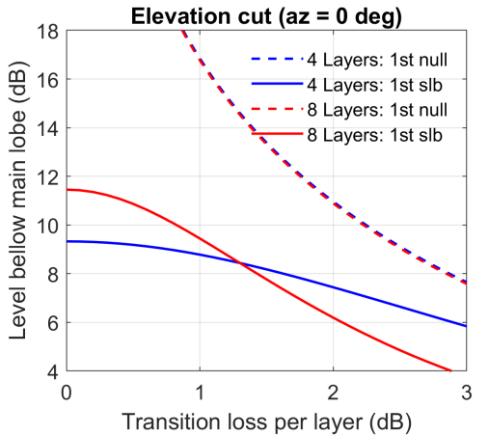

Figure 2.59: Suppression of the 1st sidelobe for a 4-layer and an 8-layer OPA.

2.7Summary

In this part, we presented our work on the design, modeling and characterization of polymer-based optical phased arrays (OPAs). We proposed and experimentally demonstrated a novel concept for 2D OPAs in support of laser beam scanning applications. Our solution is based on the formation of rectangular apertures at the edge of the chip using multiple waveguiding layers in 'PolyBoard', the polymer platform developed at Fraunhofer HHI. Our concept includes the use of vertical MMI structures to transfer the light between adjacent waveguiding layers and standard lateral MMIs to distribute optical power among waveguides of the same layer. The motivation to form edge-emitting OPAs is their high-power throughput and the potential for beam steering without the need for wavelength tuning. To the best of our knowledge this work is the first to demonstrate 2D edge-emitting (end-fire) OPAs based on 3D photonic integration with independent channel phase control.

First, the advantages and challenges of the proposed platform were discussed and the fundamental elements of OPA theory were introduced. Using the field equivalence principle, we calculated the far-field radiation of the standard 3.2 μm × 3.2 μm PolyBoard waveguide at 1550 nm, where the FWHM was calculated to be 12.7°. Subsequently, we assessed the impact of the waveguide pitch on the creation of grating lobes and the deterioration of the FOV. Using BPM simulations, we investigated the optical crosstalk between adjacent PolyBoard waveguides as a function of their spacing, and we concluded that 6 μm can be considered as a safe limit for the prevention of the detrimental coupling between waveguides at co-propagation distances of few hundred microns. We fabricated test structures of uniform linear (1D) and rectangular (2D) OPAs with lateral pitch of 6 μm, 8 μm and 10 μm and 4 waveguides per layer to validate experimentally our theoretical results. In the case of 2D arrays the vertical pitch of the waveguides was set to 7.2 μm, which was the distance between the different waveguiding layers, defined by the height of the vertical MMI structures. We measured the beam profiles of the 1×4 and 2×4 OPAs and demonstrated 2D beam-steering using the double layer OPAs. The widest FOV was 12º×8º (azimuth × elevation), measured with the 6 μm lateral pitch OPA, while the beamwidth was approximately 3.3º×5.9º. The smallest beamwidth was measured 2.1º×5.8º with the 10 μm lateral pitch OPA due to the larger aperture size. We described the development of our experimental setup, which was based on a 4-*f* optical system and a microscope objective to collect light and map the far-field radiation pattern on a sensor. The calibration procedure of our experimental setup is also discussed.

We then extended our work to non-uniform OPAs, where unequal emitter spacing was introduced to suppress grating lobes. Two optimization methods, a genetic algorithm and a gradient descent algorithm, were used to design 16-element linear aperiodic apertures, effectively eliminating grating lobes around 1.55 μm wavelength. By applying independent phase control to all 16 channels, we demonstrated 1D beam steering with side-lobe suppression ratios exceeding 11 dB within ±5°, and 6 dB within ±8°, steering range. Although aperiodicity was studied only in single-layer OPAs, the concept is directly applicable to our multi-layer 3D OPA concept. Phase tuning relied on thermo-optic (TO) phase shifters, which exhibited an efficiency of 1.28 mW/π. While TO shifters in PolyBoard typically offer reconfiguration times on the order of a few milliseconds [61], our designs were optimized for reduced power consumption and thermal crosstalk, resulting in reconfiguration times of ~15 ms. In practice, the tuning speed was limited by the software-controlled driving electronics.

We investigated phase calibration strategies for OPAs, comparing several algorithmic approaches. The stochastic parallel gradient descent (SPGD) method was found to be the most resource-efficient, offering faster convergence for OPAs with a large number of elements. Finally, we discussed the design of a 4×8 OPA comprising four stacked waveguiding layers, further extending the scalability of the proposed architecture.

References

[1] K. Van Acoleyen, W. Bogaerts, J. Jágerská, N. Le Thomas, R. Houdré, and R. Baets, "Off-chip beam steering with a one-dimensional optical phased array on silicon-on-insulator," *Opt. Lett.*, vol. 34, no. 9, p. 1477, May 2009, doi: 10.1364/OL.34.001477.

[2] K. Van Acoleyen, H. Rogier, and R. Baets, "Two-dimensional optical phased array antenna on silicon-on-Insulator," *Opt. Express*, vol. 18, no. 13, p. 13655, Jun. 2010, doi: 10.1364/OE.18.013655.

[3] K. Van Acoleyen, W. Bogaerts, and R. Baets, "Two-Dimensional Dispersive Off-Chip Beam Scanner Fabricated on Silicon-On-Insulator," *IEEE Photon. Technol. Lett.*, vol. 23, no. 17, pp. 1270–1272, Sep. 2011, doi: 10.1109/LPT.2011.2159785.

[4] K. Van Acoleyen, K. Komorowska, W. Bogaerts, and R. Baets, "One-Dimensional Off-Chip Beam Steering and Shaping Using Optical Phased Arrays on Silicon-on-Insulator," *J. Lightwave Technol.*, vol. 29, no. 23, pp. 3500–3505, Dec. 2011, doi: 10.1109/JLT.2011.2171477.

[5] F. Aflatouni, B. Abiri, A. Rekhi, and A. Hajimiri, "Nanophotonic projection system," *Opt. Express*, vol. 23, no. 16, p. 21012, Aug. 2015, doi: 10.1364/OE.23.021012.

[6] A. Yaacobi, J. Sun, M. Moresco, G. Leake, D. Coolbaugh, and M. R. Watts, "Integrated phased array for wide-angle beam steering," Opt. Lett., vol. 39, no. 15, p. 4575, Aug. 2014, doi: 10.1364/OL.39.004575.

[7] C. V. Poulton, A. Yaccobi, Z. Su, M. J. Byrd, and M. R. Watts, "Optical Phased Array with Small Spot Size, High Steering Range and Grouped Cascaded Phase Shifters," in *Advanced Photonics 2016 (IPR, NOMA, Sensors, Networks, SPPCom, SOF)*, Vancouver: OSA, 2016, p. IW1B.2. doi: 10.1364/IPRSN.2016.IW1B.2.

[8] J. Sun *et al.*, "Two-dimensional apodized silicon photonic phased arrays," *Opt. Lett.*, vol. 39, no. 2, p. 367, Jan. 2014, doi: 10.1364/OL.39.000367.

[9] H. Abediasl and H. Hashemi, "Monolithic optical phased-array transceiver in a standard SOI CMOS process," Opt. Express, vol. 23, no. 5, p. 6509, Mar. 2015, doi: 10.1364/OE.23.006509.

[10] J. K. Doylend, M. J. R. Heck, J. T. Bovington, J. D. Peters, L. A. Coldren, and J. E. Bowers, "Two-dimensional free-space beam steering with an optical phased array on silicon-on-insulator," *Opt. Express*, vol. 19, no. 22, p. 21595, Oct. 2011, doi: 10.1364/OE.19.021595.

[11] J. K. Doylend *et al.*, "Hybrid III/V silicon photonic source with integrated 1D free-space beam steering," *Opt. Lett.*, vol. 37, no. 20, p. 4257, Oct. 2012, doi: 10.1364/OL.37.004257.

[12] J. C. Hulme *et al.*, "Fully integrated hybrid silicon two dimensional beam scanner," *Opt. Express*, vol. 23, no. 5, p. 5861, Mar. 2015, doi: 10.1364/OE.23.005861.

[13] D. N. Hutchison *et al.*, "High-resolution aliasing-free optical beam steering," *Optica*, vol. 3, no. 8, p. 887, Aug. 2016, doi: 10.1364/OPTICA.3.000887.

[14] R. Fatemi, A. Khachaturian, and A. Hajimiri, "A Nonuniform Sparse 2-D Large-FOV Optical Phased Array With a Low-Power PWM Drive," *IEEE J. Solid-State Circuits*, vol. 54, no. 5, pp. 1200–1215, May 2019, doi: 10.1109/JSSC.2019.2896767.

[15] T. Kim *et al.*, "A Single-Chip Optical Phased Array in a Wafer-Scale Silicon Photonics/CMOS 3D-Integration Platform," *IEEE J. Solid-State Circuits*, vol. 54, no. 11, pp. 3061–3074, Nov. 2019, doi: 10.1109/JSSC.2019.2934601.

[16] C. V. Poulton, M. J. Byrd, E. Timurdogan, P. Russo, D. Vermeulen, and M. R. Watts, "Optical Phased Arrays for Integrated Beam Steering," in *2018 IEEE 15th International Conference on Group IV Photonics (GFP)*, Dec. 2018, pp. 1–2. doi: 10.1109/GROUP4.2018.8478729.

[17] C. V. Poulton *et al.*, "Long-Range LiDAR and Free-Space Data Communication With High-Performance Optical Phased Arrays," *IEEE J. Select. Topics Quantum Electron.*, vol. 25, no. 5, pp. 1–8, Sep. 2019, doi: 10.1109/JSTQE.2019.2908555.

[18] S. A. Miller *et al.*, "Large-scale optical phased array using a low-power multi-pass silicon photonic platform," *Optica*, vol. 7, no. 1, p. 3, Jan. 2020, doi: 10.1364/OPTICA.7.000003.

[19] J. Sun, E. Timurdogan, A. Yaacobi, E. S. Hosseini, and M. R. Watts, "Large-scale nanophotonic phased array," *Nature*, vol. 493, no. 7431, pp. 195–199, Jan. 2013, doi: 10.1038/nature11727.

[20] S. Chung, H. Abediasl, and H. Hashemi, "A Monolithically Integrated Large-Scale Optical Phased Array in Silicon-on-Insulator CMOS," *IEEE J. Solid-State Circuits*, vol. 53, no. 1, pp. 275–296, Jan. 2018, doi: 10.1109/JSSC.2017.2757009.

[21] C. V. Poulton, M. J. Byrd, B. Moss, E. Timurdogan, R. Millman, and M. R. Watts, "8192-Element Optical Phased Array with 100° Steering Range and Flip-Chip CMOS," in *Conference on Lasers and Electro-Optics*, Washington, DC: Optica Publishing Group, 2020, p. JTh4A.3. doi: 10.1364/CLEO_AT.2020.JTh4A.3.

[22] Y. Liu, X. Meng, and H. Hu, "1000-Element Silicon Optical Phased Array for Aliasing-Free 2D Optical Beam Steering," in *Conference on Lasers and Electro-Optics*, San Jose, California: Optica Publishing Group, 2022, p. JTh6C.3. doi: 10.1364/CLEO_AT.2022.JTh6C.3.

[23] W. Xie et al., "Heterogeneous silicon photonics sensing for autonomous cars [Invited]," Opt. Express, vol. 27, no. 3, p. 3642, Feb. 2019, doi: 10.1364/OE.27.003642.

[24] C. T. Phare, M. C. Shin, S. A. Miller, B. Stern, and M. Lipson, "Silicon Optical Phased Array with High-Efficiency Beam Formation over 180 Degree Field of View," p. 12, Feb. 2018.

[25] H. Sun, Q. Qiao, Q. Guan, and G. Zhou, "Silicon Photonic Phase Shifters and Their Applications: A Review," *Micromachines*, vol. 13, no. 9, p. 1509, Sep. 2022, doi: 10.3390/mi13091509

[26] R. Baghdadi *et al.*, "Dual slot-mode NOEM phase shifter," *Opt. Express*, vol. 29, no. 12, p. 19113, Jun. 2021, doi: 10.1364/OE.423949.

[27] P. Edinger *et al.*, "Silicon photonic microelectromechanical phase shifters for scalable programmable photonics," *Opt. Lett.*, vol. 46, no. 22, p. 5671, Nov. 2021, doi: 10.1364/OL.436288.

[28] A. Martin *et al.*, "Photonic Integrated Circuit-Based FMCW Coherent LiDAR," *J. Lightwave Technol.*, vol. 36, no. 19, pp. 4640–4645, Oct. 2018, doi: 10.1109/JLT.2018.2840223.

[29] C. Wang *et al.*, "Integrated lithium niobate electro-optic modulators operating at CMOS-compatible voltages," *Nature*, vol. 562, no. 7725, pp. 101–104, Oct. 2018, doi: 10.1038/s41586-018-0551-y.

[30] W. Li *et al.*, "High-speed 2D beam steering based on a thin-film lithium niobate optical phased array with a large field of view," *Photon. Res.*, vol. 11, no. 11, p. 1912, Nov. 2023, doi: 10.1364/PRJ.502439.

[31] G. Yue and Y. Li, "Integrated lithium niobate optical phased array for two-dimensional beam steering," *Opt. Lett.*, vol. 48, no. 14, p. 3633, Jul. 2023, doi: 10.1364/OL.491748.

[32] Z. Wang *et al.*, "Fast-speed and low-power-consumption optical phased array based on lithium niobate waveguides," *Nanophotonics*, vol. 13, no. 13, pp. 2429–2436, May 2024, doi: 10.1515/nanoph-2024-0066.

[33] W.-B. Lee, Y.-J. Kwon, D.-H. Kim, Y.-H. Sunwoo, and S.-S. Lee, "Hybrid integrated thin-film lithium niobate–silicon nitride electro-optical phased array incorporating silicon nitride grating antenna for two-dimensional beam steering," *Opt. Express*, vol. 32, no. 6, p. 9171, Mar. 2024, doi: 10.1364/OE.518961.

[34] W. Guo *et al.*, "Two-Dimensional Optical Beam Steering With InP-Based Photonic Integrated Circuits," *IEEE J. Select. Topics Quantum Electron.*, vol. 19, no. 4, pp. 6100212–6100212, Jul. 2013, doi: 10.1109/JSTQE.2013.2238218.

[35] J. Midkiff, K. M. Yoo, J.-D. Shin, H. Dalir, M. Teimourpour, and R. T. Chen, “Optical phased array beam steering in the mid-infrared on an InP-based platform,” *Optica*, vol. 7, no. 11, p. 1544, Nov. 2020, doi: 10.1364/OPTICA.400441.

[36] K. Komatsu, Y. Kohno, Y. Nakano, and T. Tanemura, “Large-Scale Monolithic InP-Based Optical Phased Array,” *IEEE Photon. Technol. Lett.*, vol. 33, no. 20, pp. 1123–1126, Oct. 2021, doi: 10.1109/LPT.2021.3107277.

[37] M. Gagino, M. B. J. Van Rijn, E. A. J. M. Bente, M. K. Smit, and V. Dolores-Calzadilla, “Broadband Operation of an InP Optical Phased Array,” IEEE Photon. Technol. Lett., vol. 34, no. 10, pp. 541–544, May 2022, doi: 10.1109/LPT.2022.3171979.

[38] S. Tan *et al.*, “Low-power consumption InP-based optical phase arrays with non-uniformly spaced output waveguides,” *Opt. Express*, vol. 31, no. 2, p. 3199, Jan. 2023, doi: 10.1364/OE.479334.

[39] Z. Wang, J. Liao, Y. Sun, X. Han, Y. Cao, and R. Zhao, “Chip scale GaAs optical phased arrays for high speed beam steering,” *Appl. Opt.*, vol. 59, no. 27, p. 8310, Sep. 2020, doi: 10.1364/AO.396524.

[40] M. Nickerson, B. Song, J. Brookhyser, G. Erwin, J. Kleinert, and J. Klamkin, “Gallium arsenide optical phased array photonic integrated circuit,” *Opt. Express*, vol. 31, no. 17, p. 27106, Aug. 2023, doi: 10.1364/OE.492556.

[41] C. G. H. Roeloffzen *et al.*, “Low-Loss Si3N4 TriPleX Optical Waveguides: Technology and Applications Overview,” *IEEE J. Select. Topics Quantum Electron.*, vol. 24, no. 4, pp. 1–21, Jul. 2018, doi: 10.1109/JSTQE.2018.2793945.

[42] N. A. Tyler *et al.*, “SiN integrated optical phased arrays for two-dimensional beam steering at a single near-infrared wavelength,” *Opt. Express*, vol. 27, no. 4, p. 5851, Feb. 2019, doi: 10.1364/OE.27.005851.

[43] Y. Zhang *et al.*, “Sub-wavelength-pitch silicon-photonic optical phased array for large field-of-regard coherent optical beam steering,” *Opt. Express*, vol. 27, no. 3, p. 1929, Feb. 2019, doi: 10.1364/OE.27.001929.

[44] M. Prost *et al.*, “Optical phased array with on-chip phase calibration,” *Opt. Lett.*, vol. 47, no. 23, p. 6081, Dec. 2022, doi: 10.1364/OL.467779.

[45] C. V. Poulton *et al.*, “Large-scale silicon nitride nanophotonic phased arrays at infrared and visible wavelengths,” *Opt. Lett.*, vol. 42, no. 1, p. 21, Jan. 2017, doi: 10.1364/OL.42.000021.

[46] M. Chul Shin *et al.*, “Chip-scale blue light phased array,” *Opt. Lett.*, vol. 45, no. 7, p. 1934, Apr. 2020, doi: 10.1364/OL.385201.

[47] J. Wang, K. Liu, M. W. Harrington, R. Q. Rudy, and D. J. Blumenthal, “Silicon nitride stress-optic microresonator modulator for optical control applications,” *Opt. Express*, vol. 30, no. 18, p. 31816, Aug. 2022, doi: 10.1364/OE.467721.

[48] A. Everhardt *et al.*, “Ultra-low power stress-based phase actuation in TriPleX photonic circuits,” in *Integrated Optics: Devices, Materials, and Technologies XXVI*, S. M. García-Blanco and P. Cheben, Eds., San Francisco, United States: SPIE, Mar. 2022, p. 11. doi: 10.1117/12.2609405.

[49] W. Jin, R. G. Polcawich, P. A. Morton, and J. E. Bowers, “Piezoelectrically tuned silicon nitride ring resonator,” p. 14, 2018.

[50] S. J. B. Yoo, B. Guan, and R. P. Scott, “Heterogeneous 2D/3D photonic integrated microsystems,” *Microsyst Nanoeng*, vol. 2, no. 1, p. 16030, Dec. 2016, doi: 10.1038/micronano.2016.30.

[51] B. Guan *et al.*, “Hybrid 3D Photonic Integrated Circuit for Optical Phased Array Beam Steering,” in *CLEO: 2015*, San Jose, California: OSA, 2015, p. STu2F.1. doi: 10.1364/CLEO_SI.2015.STu2F.1.

[52] S. Gross and M. J. Withford, “Ultrafast-laser-inscribed 3D integrated photonics: challenges and emerging applications,” *Nanophotonics*, vol. 4, no. 3, pp. 332–352, Nov. 2015, doi: 10.1515/nanoph-2015-0020.

[53] Z. Zhang and N. Keil, “Polymer Photonic Devices,” in *Nanomaterials, Polymers, and Devices*, 1st ed., E. S. W. Kong, Ed., Wiley, 2015, pp. 233–272. doi: 10.1002/9781118867204.ch9.

[54] M. Nuck *et al.*, “Low-Loss Vertical MMI Coupler for 3D Photonic Integration,” in *2018 European Conference on Optical Communication (ECOC)*, Rome, Italy: IEEE, Sep. 2018, pp. 1–3. doi: 10.1109/ECOC.2018.8535479.

[55] M. Nuck *et al.*, “3D photonic integrated 4x4 multi-mode interference coupler,” in *Integrated Optics: Devices, Materials, and Technologies XXIII*, SPIE, Mar. 2019, pp. 163–171. doi: 10.1117/12.2509776.

[56] M. Weigel *et al.*, “3D Photonic Integration: Cascaded 1x1 3D Multi-mode Interference Couplers for Vertical Multi-layer Connections,” 2020.

[57] M. Weigel *et al.*, “1x4 Vertical Power Splitter/Combiner: A Basic Building Block for Complex 3D Waveguide Routing Networks,” *th European Conference on Integrated Optics*, 2023.

[58] Ziyang Zhang *et al.*, “Multicore Polymer Waveguides and Multistep 45° Mirrors for 3D Photonic Integration,” *IEEE Photon. Technol. Lett.*, vol. 26, no. 19, pp. 1986–1989, Oct. 2014, doi: 10.1109/LPT.2014.2344116.

[59] D. de Felipe *et al.*, “Recent Developments in Polymer-Based Photonic Components for Disruptive Capacity Upgrade in Data Centers,” *J. Lightwave Technol.*, vol. 35, no. 4, pp. 683–689, Feb. 2017, doi: 10.1109/JLT.2016.2611240.

[60] M. Weigel *et al.*, “Design and Fabrication of Crossing-Free Waveguide Routing Networks Using a Multi-Layer Polymer-Based Photonic Integration Platform,” *J. Lightwave Technol.*, vol. 42, no. 5, pp. 1511–1517, Mar. 2024, doi: 10.1109/JLT.2023.3320908.

[61] Z. Zhang and N. Keil, “Thermo-optic devices on polymer platform,” *Optics Communications*, vol. 362, pp. 101–114, Mar. 2016, doi: 10.1016/j.optcom.2015.08.026.

[62] Y. Xie, L. Chen, H. Li, and Y. Yi, “Polymer and Hybrid Optical Devices Manipulated by the Thermo-Optic Effect,” *Polymers*, vol. 15, no. 18, p. 3721, Sep. 2023, doi: 10.3390/polym15183721.

[63] V. Katopodis *et al.*, “Polymer enabled 100Gbaud connectivity for datacom applications,” *Optics Communications*, vol. 362, pp. 13–21, Mar. 2016, doi: 10.1016/j.optcom.2015.07.064.

[64] V. Katopodis *et al.*, “Serial 100 Gb/s connectivity based on polymer photonics and InP-DHBT electronics,” *Opt. Express*, vol. 20, no. 27, p. 28538, Dec. 2012, doi: 10.1364/OE.20.028538.

[65] P. Groumas *et al.*, “Tunable 100 Gbaud Transmitter Based on Hybrid Polymer-to-Polymer Integration for Flexible Optical Interconnects,” *J. Lightwave Technol.*, vol. 34, no. 2, pp. 407–418, Jan. 2016, doi: 10.1109/JLT.2015.2463730.

[66] I. Taghavi et al., “Polymer modulators in silicon photonics: review and projections,” Nanophotonics, vol. 11, no. 17, pp. 3855–3871, Aug. 2022, doi: 10.1515/nanoph-2022-0141.

[67] J. Bass, H. Tran, W. Du, R. Soref, and S.-Q. Yu, “Impact of nonlinear effects in Si towards integrated microwave-photonic applications,” *Opt. Express*, vol. 29, no. 19, p. 30844, Sep. 2021, doi: 10.1364/OE.433646.

[68] D. De Felipe *et al.*, “Polymer-Based External Cavity Lasers: Tuning Efficiency, Reliability, and Polarization Diversity,” *IEEE Photon. Technol. Lett.*, vol. 26, no. 14, pp. 1391–1394, Jul. 2014, doi: 10.1109/LPT.2014.2324760.

[69] M. Happach *et al.*, “On-chip free beam optics on a polymer-based photonic integration platform,” *Opt. Express*, vol. 25, no. 22, p. 27665, Oct. 2017, doi: 10.1364/OE.25.027665.

[70] A. Maese-Novo *et al.*, “Thermally optimized variable optical attenuators on a polymer platform,” *Appl. Opt.*, vol. 54, no. 3, p. 569, Jan. 2015, doi: 10.1364/AO.54.000569.

[71] Z. Zhang *et al.*, “Hybrid Photonic Integration on a Polymer Platform,” *Photonics*, vol. 2, no. 3, pp. 1005–1026, Sep. 2015, doi: 10.3390/photonics2031005.

[72] Y. Wang *et al.*, “2D broadband beamsteering with large-scale MEMS optical phased array,” *Optica, OPTICA*, vol. 6, no. 5, pp. 557–562, May 2019, doi: 10.1364/OPTICA.6.000557.

[73] Y. Hirano et al., “High-Speed Optical-Beam Scanning by an Optical Phased Array Using Electro-Optic Polymer Waveguides,” IEEE Photonics J., vol. 12, no. 2, pp. 1–7, Apr. 2020, doi: 10.1109/JPHOT.2020.2981743.

[74] W. S. Rabinovich et al., “Free space optical communication link using a silicon photonic optical phased array,” presented at the SPIE LASE, H. Hemmati and D. M. Boroson, Eds., San Francisco, California, United States, Mar. 2015, p. 93540B. doi: 10.1117/12.2077222.

[75] P. Wang *et al.*, “Design and fabrication of a SiN-Si dual-layer optical phased array chip,” *Photon. Res.*, vol. 8, no. 6, p. 912, Jun. 2020, doi: 10.1364/PRJ.387376.

[76] S. Zhu et al., “Silicon Nitride Optical Phased Arrays with Cascaded Phase Shifters for Easy and Effective Electronic Control,” in 2019 Conference on Lasers and Electro-Optics (CLEO), Feb. 2019, pp. 1–2. doi: 10.1364/CLEO_AT.2019.AW4K.5.

[77] D. Fowler, S. Guerber, J. Faugier-Tovar, N. A. Tyler, and B. Szelag, “Integrated Optical Phased Array Based on a Binary Splitter Tree With Reduced Number of Control Voltages,” J. Lightwave Technol., vol. 40, no. 12, pp. 4027–4032, Jun. 2022, doi: 10.1109/JLT.2022.3154971.

[78] W. Li, J. Chen, D. Liang, D. Dai, and Y. Shi, “Silicon optical phased array with calibration-free phase shifters,” Opt. Express, OE, vol. 30, no. 24, pp. 44029–44038, Nov. 2022, doi: 10.1364/OE.475350.

[79] A. Ribeiro, S. Declercq, U. Khan, M. Wang, L. V. Iseghem, and W. Bogaerts, “Column-Row Addressing of Thermo-Optic Phase Shifters for Controlling Large Silicon Photonic Circuits,” *IEEE J. Select. Topics Quantum Electron.*, vol. 26, no. 5, pp. 1–8, Sep. 2020, doi: 10.1109/JSTQE.2020.2975669.

[80] F. Ashtiani and F. Aflatouni, “N × N optical phased array with 2N phase shifters,” Opt. Express, vol. 27, no. 19, p. 27183, Sep. 2019, doi: 10.1364/OE.27.027183.

[81] C. Tsokos et al., “True Time Delay Optical Beamforming Network Based on Hybrid Inp-Silicon Nitride Integration,” J. Lightwave Technol., vol. 39, no. 18, pp. 5845–5854, Sep. 2021, doi: 10.1109/JLT.2021.3089881

[82] J. O. Kjellman et al., “Minimizing DAC Complexity for Control of Optical Phased Arrays,” in 2019 IEEE Photonics Conference (IPC), San Antonio, TX, USA: IEEE, Sep. 2019, pp. 1–2. doi: 10.1109/IPCon.2019.8908515.

[83] T. Komljenovic, R. Helkey, and L. Coldren, “Sparse aperiodic arrays for optical beam forming and LIDAR,” vol. 25, no. 3, p. 18, Feb. 2017.

[84] D. Kwong et al., “1x12 Unequally spaced waveguide array for actively tuned optical phased array on a silicon nanomembrane,” Appl. Phys. Lett., p. 3, 2011.

[85] M. R. Kossey, C. Rizk, and A. C. Foster, “End-fire silicon optical phased array with half-wavelength spacing,” APL Photonics, vol. 3, no. 1, p. 011301, Jan. 2018, doi: 10.1063/1.5000741.

[86] Y. Kohno, K. Komatsu, R. Tang, Y. Ozeki, Y. Nakano, and T. Tanemura, “Ghost imaging using a large-scale silicon photonic phased array chip,” Opt. Express, vol. 27, no. 3, p. 3817, Feb. 2019, doi: 10.1364/OE.27.003817.

[87] W. Xu, L. Zhou, L. Lu, and J. Chen, “Aliasing-free optical phased array beam-steering with a plateau envelope,” Opt. Express, vol. 27, no. 3, p. 3354, Feb. 2019, doi: 10.1364/OE.27.003354.

[88] B. Bhandari et al., “Dispersive silicon–nitride optical phased array incorporating arrayed waveguide delay lines for passive line beam scanning,” Sci Rep, vol. 12, no. 1, p. 18759, Nov. 2022, doi: 10.1038/s41598-022-23456-7.

[89] W. Song et al., “High-density waveguide superlattices with low crosstalk,” Nat Commun 6, 7027 (2015).

[90] H. Zhang, Z. Zhang, J. Lv, C. Peng, and W. Hu, “Fast beam steering enabled by a chip-scale optical phased array with 8 × 8 elements,” Optics Communications, vol. 461, p. 125267, Apr. 2020, doi: 10.1016/j.optcom.2020.125267.

[91] T. Fukui et al., “Non-redundant optical phased array,” Optica, vol. 8, no. 10, p. 1350, Oct. 2021, doi: 10.1364/OPTICA.437453.

[92] Y. Li et al., “Wide-steering-angle high-resolution optical phased array,” Photon. Res., PRJ, vol. 9, no. 12, pp. 2511–2518, Dec. 2021, doi: 10.1364/PRJ.437846.

[93] J. J. López et al., “Planar-lens Enabled Beam Steering for Chip-scale LIDAR,” in Conference on Lasers and Electro-Optics, San Jose, California: OSA, 2018, p. SM3I.1. doi: 10.1364/CLEO_SI.2018.SM3I.1.

[94] Y. Liu and H. Hu, “Silicon optical phased array with a 180-degree field of view for 2D optical beam steering,” Optica, vol. 9, no. 8, p. 903, Aug. 2022, doi: 10.1364/OPTICA.458642.

[95] L. Cheng, S. Mao, Z. Li, Y. Han, and H. Fu, “Grating Couplers on Silicon Photonics: Design Principles, Emerging Trends and Practical Issues,” Micromachines, vol. 11, no. 7, p. 666, Jul. 2020, doi: 10.3390/mi11070666.

[96] A. Hosseini et al., “Unequally Spaced Waveguide Arrays for Silicon Nanomembrane-Based Efficient Large Angle Optical Beam Steering,” IEEE J. Select. Topics Quantum Electron., vol. 15, no. 5, pp. 1439–1446, 2009, doi: 10.1109/JSTQE.2009.2021956.

[97] A. Hosseini et al., “On the fabrication of three-dimensional silicon-on-insulator based optical phased array for agile and large angle laser beam steering systems,” Journal of Vacuum Science & Technology B, Nanotechnology and Microelectronics: Materials, Processing, Measurement, and Phenomena, vol. 28, no. 6, p. C6O1-C6O7, Nov. 2010, doi: 10.1116/1.3511508.

[98] D. Wu, Y. Yi, and Y. Zhang, “High efficiency end-fire 3-D optical phased array based on multi-layers **Si3N4**/**SiO2** platform,” Applied Optics, vol. 59, no. 8, pp. 2489–2497, 2020.

[99] D. Wu, B. Yu, V. Kakdarvishi, and Y. Yi, “Photonic integrated circuit with multiple waveguide layers for broadband high-efficient on-chip 3-D optical phased arrays in light detection and ranging applications,” 2022.

[100] D. Wu, K. Owen, B. Yu, and Y. Yi, “Fabrication of a self-aligned multi-waveguide-layer passive Si3N4/SiO2 photonic integrated circuit for a 3-D optical phased array device,” Opt. Mater. Express, vol. 14, no. 1, p. 13, Jan. 2024, doi: 10.1364/OME.507523.

[101] S.-M. Kim, T.-H. Park, C.-S. Im, S.-S. Lee, T. Kim, and M.-C. Oh, “Temporal response of polymer waveguide beam scanner with thermo-optic phase-modulator array,” Opt. Express, vol. 28, no. 3, p. 3768, Feb. 2020, doi: 10.1364/OE.383514.

[102] S.-M. Kim, E.-S. Lee, K.-W. Chun, J. Jin, and M.-C. Oh, “Compact solid-state optical phased array beam scanners based on polymeric photonic integrated circuits,” Sci Rep, vol. 11, no. 1, p. 10576, May 2021, doi: 10.1038/s41598-021-90120-x.

[103] E.-S. Lee, J. Jin, K.-W. Chun, S.-S. Lee, and M.-C. Oh, “High-performance optical phased array for LiDARs demonstrated by monolithic integration of polymer and SiN waveguides,” Opt. Express, vol. 31, no. 17, p. 28112, Aug. 2023, doi: 10.1364/OE.499868.

[104] C. Wang et al., “Efficient Line Beam Scanning Based on a Hybrid Optical Phased Array Rendering Flexible Field-of-Views,” IEEE Photonics J., vol. 15, no. 2, pp. 1–9, Apr. 2023, doi: 10.1109/JPHOT.2023.3245623.

[105] R. J. Mailloux, *Phased array antenna handbook*, 2nd ed. in Artech House antennas and propagation library. Boston: Artech House, 2005.

[106] A. Cala’ Lesina, D. Goodwill, E. Bernier, L. Ramunno, and P. Berini, “On the performance of optical phased array technology for beam steering: effect of pixel limitations,” Opt. Express, vol. 28, no. 21, p. 31637, Oct. 2020, doi: 10.1364/OE.402894.

[107] https://optics.ansys.com/hc/en-us/articles/360034396734-FDE-solver-analysis-Mode-List-and-Deck

[108] C. A. Balanis, *Antenna Theory: Analysis and Design.* 3rd ed., Hoboken, NJ, USA: Wiley, 2005.

[109] Yariv and P. Yeh, *Photonics: Optical Electronics in Modern Communications*, Sixth Edition, Sixth Edition. in The Oxford Series in Electrical and Computer Engineering. Oxford, New York: Oxford University Press, 2006.

[110] https://optics.ansys.com/hc/en-us/articles/360042304694-Evanescent-waveguide-couplers

[111] Nicolas Le Thomas, Romuald Houdré, Maria V. Kotlyar, David O'Brien, and Thomas F. Krauss, "Exploring light propagating in photonic crystals with Fourier optics," J. Opt. Soc. Am. B 24, 2964-2971 (2007)

[112] P. Stepanov, A. Delga, N. Gregersen, E. Peinke, M. Munsch, J. Teissier, J. Mørk, M. Richard, J. Bleuse, J. M. G´erard, and J. Claudon, "Highly directive and Gaussian far-field emission from "giant" photonic trumpets," Applied Physics Letters 107, 141106 (2015).

[113] J. Nakamura, Ed., *Image sensors and signal processing for digital still cameras*. Boca Raton, FL: Taylor & Francis/CRC Press, 2006.

[114] J. C. Mullikin, L. J. van Vliet, H. Netten, F. R. Boddeke, G. van der Feltz, and I. T. Young, "Methods for CCD camera characterization," in *Image Acquisition and Scientific Imaging Systems*, SPIE, May 1994, pp. 73–84. doi: 10.1117/12

[115] Y. Yang *et al.*, "Phase coherence length in silicon photonic platform," *Opt. Express*, vol. 23, no. 13, p. 16890, Jun. 2015, doi: 10.1364/OE.23.016890.

[116] J. Kennedy' and R. Eberhart, "Particle Swarm Optimization".

[117] J. Robinson and Y. Rahmat-Samii, "Particle swarm optimization in electromagnetics," *IEEE Trans. Antennas Propagat.*, vol. 52, no. 2, pp. 397–407, Feb. 2004, doi: 10.1109/TAP.2004.823969.

[118] X. He, T. Dong, J. He, and Y. Xu, "Design of an Optical Phased Array with Low Side-lobe Level and Wide-angle Steering Range Based on Particle Swarm Optimization," in *Asia Communications and Photonics Conference/International Conference on Information Photonics and Optical Communications 2020 (ACP/IPOC)*, Beijing: Optica Publishing Group, 2020, p. M4A.138. doi: 10.1364/ACPC.2020.M4A.138.

[119] J. Skaar and K. M. Risvik, "Genetic algorithm for the inverse problem in synthesis of fiber gratings," presented at the European Workshop on Optical Fibre Sensors, B. Culshaw and J. D. C. Jones, Eds., Peebles, Scotland, United Kingdom, Jun. 1998, pp. 273–277. doi: 10.1117/12.309689.

[120] M. G. Bray, D. H. Werner, D. W. Boeringer, and D. W. Machuga, "Optimization of thinned aperiodic linear phased arrays using genetic algorithms to reduce grating lobes during scanning," *IEEE Trans. Antennas Propagat.*, vol. 50, no. 12, pp. 1732–1742, Dec. 2002, doi: 10.1109/TAP.2002.807947.C. T. Phare, M. C. Shin, S. A. Miller, B. Stern, and M. Lipson, "Silicon Optical Phased Array with High-Efficiency Beam Formation over 180 Degree Field of View," p. 12, Feb. 2018.

[121] Q. Liu *et al.*, "Silicon Optical Phased Array Side Lobe Suppression Based on an Improved Genetic Algorithm," in *Asia Communications and Photonics Conference/International Conference on Information Photonics and Optical Communications 2020 (ACP/IPOC)*, Beijing: Optica Publishing Group, 2020, p. T2D.3. doi: 10.1364/ACPC.2020.T2D.3.

[122] S. Guerber *et al.*, "Development, calibration and characterization of silicon photonics based optical phased arrays," in *Smart Photonic and Optoelectronic Integrated Circuits XXIII*, S. He and L. Vivien, Eds., Online Only, United States: SPIE, Mar. 2021, p. 4. doi: 10.1117/12.2582679.

[123] M. A. Vorontsov, G. W. Carhart, and J. C. Ricklin, "Adaptive phase-distortion correction based on parallel gradient-descent optimization," *Opt. Lett.*, vol. 22, no. 12, p. 907, Jun. 1997, doi: 10.1364/OL.22.000907.

[124] M. A. Vorontsov, "Decoupled stochastic parallel gradient descent optimization for adaptive optics: integrated approach for wave-front sensor information fusion," *J. Opt. Soc. Am. A*, vol. 19, no. 2, p. 356, Feb. 2002, doi: 10.1364/JOSAA.19.000356.

[125] Z. Wang *et al.*, "Improved SPGD Algorithm for Optical Phased Array Phase Calibration," *Applied Sciences*, vol. 12, no. 15, p. 7879, Aug. 2022, doi: 10.3390/app12157879.

[126] Z. Wang *et al.*, "Calibration of 16 × 16 SOI optical phased arrays via improved SPGD algorithm," *Optics & Laser Technology*, vol. 157, p. 108743, Jan. 2023, doi: 10.1016/j.optlastec.2022.108743.

[127] J.-Y. Kim *et al.*, "Deep neural network-based phase calibration in integrated optical phased arrays," *Sci Rep*, vol. 13, no. 1, p. 19929, Nov. 2023, doi: 10.1038/s41598-023-47004-z.

[128] L. Leng *et al.*, "Phase calibration for integrated optical phased arrays using artificial neural network with resolved phase ambiguity," *Photon. Res.*, vol. 10, no. 2, p. 347, Feb. 2022, doi: 10.1364/PRJ.435766.

[129] J. Sved, S. Song, Y. Chen, L. Zhou, R. Minasian, and X. Yi, "Machine learning assisted two-dimensional beam-steering for integrated optical phased arrays," *Optics Communications*, vol. 540, p. 129517, Aug. 2023, doi: 10.1016/j.optcom.2023.129517.

[130] S. Guerber, D. Fowler, J. Faugier-Tovar, K. A. Carim, B. Delplanque, and B. Szelag, "Wafer-level calibration of large-scale integrated optical phased arrays," *Opt. Express*, vol. 30, no. 20, p. 35246, Sep. 2022, doi: 10.1364/OE.464540.

[131] T. Komljenovic and P. Pintus, "On-chip calibration and control of optical phased arrays," *Opt. Express*, vol. 26, no. 3, p. 3199, Feb. 2018, doi: 10.1364/OE.26.003199.

[132] J. Shim *et al.*, "On-chip monitoring of far-field patterns using a planar diffractor in a silicon-based optical phased array," *Opt. Lett.*, vol. 45, no. 21, p. 6058, Nov. 2020, doi: 10.1364/OL.399263.

[133] S. Chung, M. Nakai, S. Idres, Y. Ni, and H. Hashemi, "19.1 Optical Phased-Array FMCW LiDAR with On-Chip Calibration," in *2021 IEEE International Solid- State Circuits Conference (ISSCC)*, San Francisco, CA, USA: IEEE, Feb. 2021, pp. 286–288. doi: 10.1109/ISSCC42613.2021.9366004.

[134] J. O. Kjellman *et al.*, "Densely Integrated Phase Interrogators for Low-Complexity On-Chip Calibration of Optical Phased Arrays," *J. Lightwave Technol.*, vol. 40, no. 16, pp. 5660–5667, Aug. 2022, doi: 10.1109/JLT.2022.3179437.

[135] L. Bodis, "Quantification of Spectral Similarity: Towards Automatic Spectra Verification".

Conclusions and outlook

Summary of accomplishments

This thesis work focused on two main challenges in remote optical sensors: optical frequency shifting for heterodyne interferometers, and optical beam steering. These challenges lie in achieving the required functionalities in a compact form, leveraging photonic integration, since current implementations rely on bulk optical components and, in the case of beam steering, on mechanical parts. This work leverages two photonic integration platforms: the 'TriPleX' silicon nitride platform of LioniX for the implementation of optical frequency shifters (OFSs) and the 'PolyBoard' polymer-based platform of Fraunhofer Heinrich Hertz Institute for optical phased arrays (OPAs).

In the TriPleX platform, a thin-film PZT layer was deposited on top of the SiN waveguide structure to implement phase modulators based on stress-optic index modulation. These devices offer modulation bandwidths in the MHz range, significantly exceeding those of thermo-optic phase shifters in SiN, which are typically limited to a few kilohertz. In this work, a novel electrode configuration was implemented, in which both driving electrodes are positioned on top of the PZT layer to reduce capacitance and enhance the modulator bandwidth. Two optical frequency shifter (OFS) configurations were designed, fabricated, and experimentally characterized: a serrodyne frequency shifter (SFS) and a single-sideband frequency shifter (SSB-FS). Both configurations were analyzed theoretically (1.3.1), and their performance was simulated to capture key trade-offs in conversion efficiency (CE) and sideband suppression ratio (SBSR) in the electrical domain. Frequency shifts of 100 kHz and 2.5 MHz were demonstrated using the SFS and SSB-FS, respectively. The measured CE and SBSR showed excellent agreement with theoretical predictions, validating the developed models (1.3.3). The frequency shift achieved with the SFS is limited to the kHz range due to the bandwidth-demanding nature of the ramp driving signal, the fall time of which is critical for maintaining high SBSR performance. The driving circuit, which was a custom design based on discrete components, is, in principle, capable of supporting modulation frequencies up to 20 MHz, assuming adequate thermal management and appropriate design of the PIC-hosting PCB (1.3.3.3). Under these conditions, frequency shifts of up to 800 kHz and 20 MHz would be feasible with the SFS and SSB-FS, respectively.

This work extended beyond device characterization to demonstrate system-level functionality using the developed components, targeting a heterodyne Laser Doppler Vibrometer (LDV) operating at 1550 nm. A proof-of-concept LDV was first implemented based on the SSB-OFS device. For signal detection, a dual-polarization coherent receiver was designed, fabricated, and characterized on the PolyBoard platform. The receiver incorporated thin-film polarization-handling elements embedded in etched slots and edge-coupled InP-based photodetectors. Furthermore, the system employed a commercial low-linewidth ECL source from LioniX, a probe head from Polytec for beam focusing and light collection, as well as the demodulation software by Polytec, all of which constituted valuable contributions to this effort. All the different PICs and components of the system were connected via fiber. Vibration measurements up to 15 kHz were demonstrated using the SSB-FS, achieving a displacement resolution of 10 pm. Although the system is, in principle, capable of detecting vibration frequencies up to 1 MHz, the experiments were restricted to the acoustic range due to the vibrating source used, which was a loudspeaker. As a further step toward achieving high compactness, a novel hybrid-integration approach was employed to combine the TriPleX and PolyBoard platforms into a single die. Leveraging the fabrication flexibility of polymer-based platforms, a PolyBoard circuit was embedded within an etched window on a TriPleX substrate, forming a powerful 3D hybrid PIC that integrates a PZT-based SFS in the TriPleX section with a dual-polarization coherent detection circuit in the PolyBoard section. Experimental characterization of the hybrid PIC demonstrated a 100 kHz frequency shift using the SFS, with performance comparable to that of the individual PICs. Despite the observed excess coupling losses between the two platforms of approximately 15 dB, attributed to mask misalignment during fabrication, simulations suggest that an order-of-magnitude reduction can be achieved by enhancing fabrication accuracy. This work serves as a proof of concept, demonstrating that hybrid integration of polymer with other material platforms such as SiN is feasible within a wafer-scale process, paving the way for photonic systems of greater complexity and enhanced functionality.

The second part of the work focused on the development of OPAs for optical beam steering in the PolyBoard platform, around 1550 nm wavelength. By exploiting the spin-coating manufacturing versatility of polymers, which enables the fabrication of multiple stacked waveguiding layers, an approach for realizing two-dimensional rectangular apertures at the edge of PolyBoard PICs was introduced. While the concept of rectangular

edge-emitting (end-fire) OPAs based on multiple stacked waveguiding layers has been proposed previously, this work constitutes the first experimental realization that supports active phase control of the OPA channels and thus enabling dynamic beam steering. Uniform single-layer and dual-layer OPAs with four channels per layer were fabricated and characterized experimentally as proof-of-concept. Active phase tuning was performed to achieve 2D beam steering over a field of view of 12º×8º, with a corresponding beamwidth of 3.3º×5.9º. Subsequently, a four-layer passive OPA comprising eight channels per layer was designed and fabricated. A separate PolyBoard PIC incorporating thermo-optic phase shifters was developed to provide phase control for the 32 channels of the 4 × 8 passive OPA. Although the assembly of the two PICs was not completed and experimental validation was therefore not available, the successful fabrication of a four-layer PolyBoard PIC represents a significant milestone, demonstrating the present capabilities of multi-layer PolyBoard technology. Furthermore, leveraging the inherently high thermo-optic coefficient and low thermal conductivity of polymers, thermo-optic phase shifters with phase-shift efficiency as low as 1.3 mW/π were realized within this work, further supporting the scalability of the proposed technology.

A complete workflow for modeling, design, fabrication, and characterization of PolyBoard-based optical phased arrays (OPAs) was established in this work. A dedicated simulation platform was first developed to calculate the far-field radiation pattern of the elementary emitter using the field equivalence principle, providing higher accuracy than conventional simulation methods, as confirmed by measurements on test structures. In addition, a comprehensive simulation toolset was implemented to extract key performance indicators of OPAs. This toolset was further enhanced with optimization algorithms to facilitate the design of aperiodic arrays. Linear arrays consisting of 16 unequally spaced emitters were designed, fabricated, and experimentally validated. Independent phase control across all 16 channels enabled one-dimensional beam steering while effectively suppressing grating lobes, achieving more than 8 dB suppression within the 12° FOV. To characterize the fabricated PICs, a dedicated measurement setup was developed. Specifically, an imaging system was implemented to capture the far-field emission patterns of the OPAs, while global optimization algorithms were employed to perform phase calibration and generate the desired beam-steering profiles.

Table 10 summarizes the research objectives defined at the outset of this work and the corresponding scientific results that fulfilled them.

#	Objectives	Accomplishments
1.1	Employ stress-optic index modulation technology on TriPleX (SiN platform) to realize optical frequency shifting	• Design, fabrication and testing of two OFS PICs using PZT-based stress-optic modulators on TriPleX. • Demonstration of serrodyne frequency shift (SFS) of 100 kHz, -1 dB CE, 22.1 dB SBSR. • Demonstration of single-sideband frequency shift (SSB-FS) of 2.5 MHz, -14.7 dB CE, 39 dB SBSR.
1.2	Demonstrate a miniaturized PIC-based Laser Doppler Vibrometer (LDV)	• Demonstration of heterodyne LDV measurements with 10 pm resolution (up to 1 MHz), using a TiPleX-based OFS and a dual-pol coherent receiver in PolyBoard. • Fabrication, assembly and testing of a hybrid PIC combining PolyBoard and TriPleX PICs into a single die.
2.1	Develop an advanced simulation platform for PolyBoard OPAs	• Development of a MATLAB tool to compute the far-field of the elementary emitter using the field equivalence principle; E/H fields imported from RSoft simulations. • Development of a MATLAB tool to calculate 1D/2D OPA far-fields using the array factor (AF) and emitter pattern. • Experimental validation of the simulation platform via testing 1×4 and 2×4 uniform OPAs.
2.2	Demonstrate 2D optical beam-steering using multi-layer PolyBoard OPAs	• Design, fabrication, and testing of 1×4 and 2×4 uniform OPAs in PolyBoard, with lateral element pitch 6, 8, and 10 μm, and vertical pitch 7.2 μm. • Demonstration of 2D beam-steering within a 12º×8º FOV, and beamwidth 3.3º×5.9º (6 μm lateral pitch). • Fabrication of a 4×8 uniform passive OPA and a 1×32 phase control PIC. Beam-steering results were not available due to lack of PIC assembly/packaging.
2.3	Develop an OPA far/near-field characterization setup	• Development of a Fourier imaging setup with a high NA MO to map the OPA far-field on a CCD camera; near/far-field selection by removing a single lens. • Implementation of a PIC characterization setup with a six-axis optical alignment stage, electrical probes for heater control, and task-automation features (measure/alignment selection PCB, OPA PIC control). • Development of a GUI for image processing and data visualization.
2.4	Develop a platform for non-uniform OPA design	• Development of a MATLAB optimization platform using a custom genetic algorithm. • Design, fabrication, and testing of 1×16 sparse aperiodic OPAs.
2.5	Develop OPA calibration techniques	• Design of calibration methods using batch and stochastic parallel gradient descent algorithms. • Performed calibration of 1×4 and 2×4 uniform OPAs, and 1×16 non-uniform OPAs, considering heater self-heating and efficiency variations.

Table 10: Key accomplishments of this work.

Future work

The integrated heterodyne interferometer demonstrated in this work can be further enhanced through improvements in fabrication and packaging processes. Regarding stress-optic index modulation using PZT thin films in the TriPleX SiN platform, issues related to yield, uniformity, and aging-induced performance degradation could be mitigated by optimizing both the fabrication process and the material properties. Additional process refinement is also required for the hybrid integration of TriPleX with PolyBoard, particularly in forming polymer waveguides on top of the TriPleX platform. Improved mask alignment and process control would help achieve coupling efficiencies closer to the simulated values. Although not explored in this work, integrating the laser source with the rest of the photonic circuit is an important direction for future development. As LioniX has already commercialized integrated low-linewidth external cavity lasers (ECLs) in TriPleX, such as the one used in this work, its incorporation would be a logical next step toward a fully integrated system.

The primary focus of the work on PolyBoard OPAs was the proof-of-concept demonstration of two-dimensional beam steering based on the multi-layer PolyBoard platform, along with the development of optimization techniques to improve the radiation characteristics of the proposed structures, such as through aperiodic aperture design. Moving forward, several steps can be taken to advance this technology toward practical beam-steering and scanning systems, including component-level optimization, improved aperture design, and advances in assembly and packaging. A key challenge in PolyBoard is expanding the FOV of the elementary waveguide emitter. Modest adjustments to the refractive index contrast in the PolyBoard platform are expected to improve mode confinement and consequently enhance beam divergence in free space, without significantly affecting waveguiding losses. Additional component-level improvements include optimizing the vertical multimode interference (MMI) couplers used for interlayer

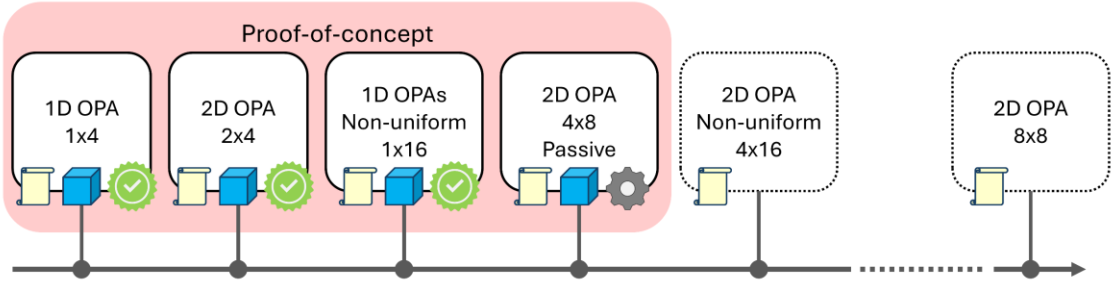

Figure 1: Target polymer-based OPA PICs.

light transfer to further reduce insertion losses. A logical next step is the assembly and characterization of the 4×8 OPA presented in Section 2.6, accompanied by the development of a robust assembly and packaging methodology for multi-layer photonic circuits. Subsequent efforts could focus on scaling the approach to larger arrays, such as eight-layer chips enabling 8×8 or 8×16 OPA configurations. The concept of non-uniform element spacing to improve radiation performance, shown in section 2.4, can also be directly applied to the 2D multi-layer OPA architecture. Designing a 2D aperiodic array, such as a 4×16 configuration, would represent a natural extension of this concept. Future studies should explore the theoretical boundaries of 2D aperiodic array performance and quantify their dependence on process-induced variations, such as emitter alignment tolerances and imbalances in the MMI couplers. Furthermore, exploring more sophisticated phase-control schemes for the OPA channels, such as those discussed in Section 2.1.3.2., would be valuable for improving overall system performance. From a system design perspective, an interesting direction would be to employ the stress-optic modulators presented in Section 1.3.2 for phase control of the OPA channels, combining the TriPleX platform with the polymer-based 3D PIC through hybrid integration, as outlined in Section 1.6.1. A complementary architecture is also worth exploring, in which PolyBoard is utilized for the phase-control section, taking advantage of its low-power thermo-optic devices, while TriPleX is used to implement grating-based OPAs. Finally, system-level demonstrations, such as free-space optical communication links or LiDAR experiments, represent essential next steps toward validating the proposed technology in practical applications. These demonstrations could include bidirectional operation, where the OPAs are employed not only for beam transmission but also for light collection, thereby showcasing their full potential in integrated optical systems.

Figure 2: Packaged 2×4 OPA prototype.

List of publications

[1] A. Raptakis *et al.*, “Integrated heterodyne laser Doppler vibrometer based on stress-optic frequency shift in silicon nitride,” *PhotoniX*, vol. 4, no. 1, p. 30, Sep. 2023, doi: 10.1186/s43074-023-00105-4.

[2] A. Raptakis *et al.*, “Fully integrated Laser Doppler Vibrometer (LDV) based on hybrid 3D integration of silicon nitride and polymer photonic circuits with operation in the kHz regime,” in *Integrated Optics: Devices, Materials, and Technologies XXVII*, S. M.

[3] A. Raptakis *et al.*, “2D Optical Phased Arrays for Laser Beam Steering Based On 3D Polymer Photonic Integrated Circuits,” *J. Lightwave Technol.*, vol. 39, no. 20, pp. 6509–6523, Oct. 2021, doi: 10.1109/JLT.2021.3099009.

[4] A. Raptakis et al., “Sparse Aperiodic Optical Phased Arrays on Polymer Integration Platform,” IEEE Photon. Technol. Lett., vol. 36, no. 7, pp. 469–472, Apr. 2024, doi: 10.1109/LPT.2024.3367973.

Appendix

OPA characterization setup: co-ordinate system of

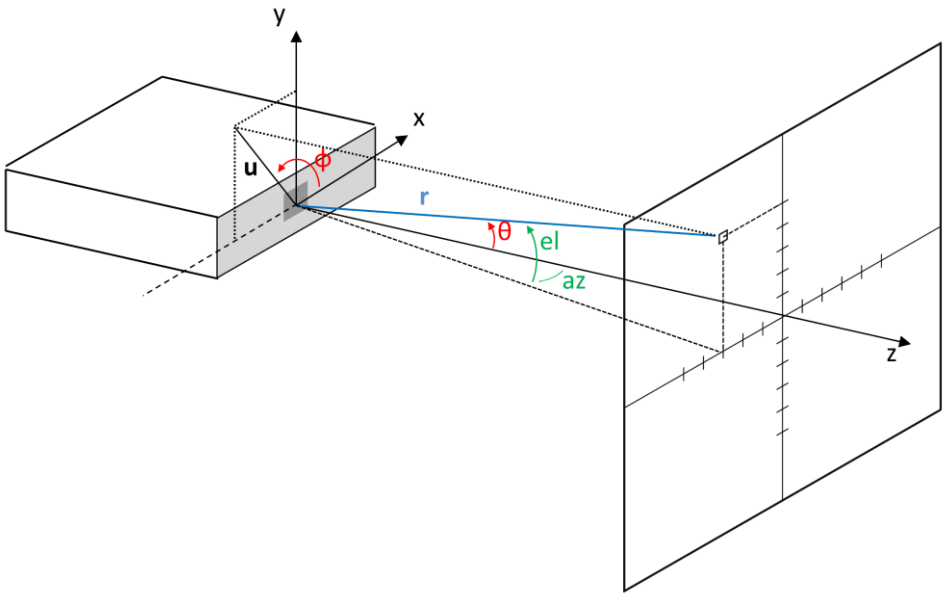

Figure 1: Co-ordinate system

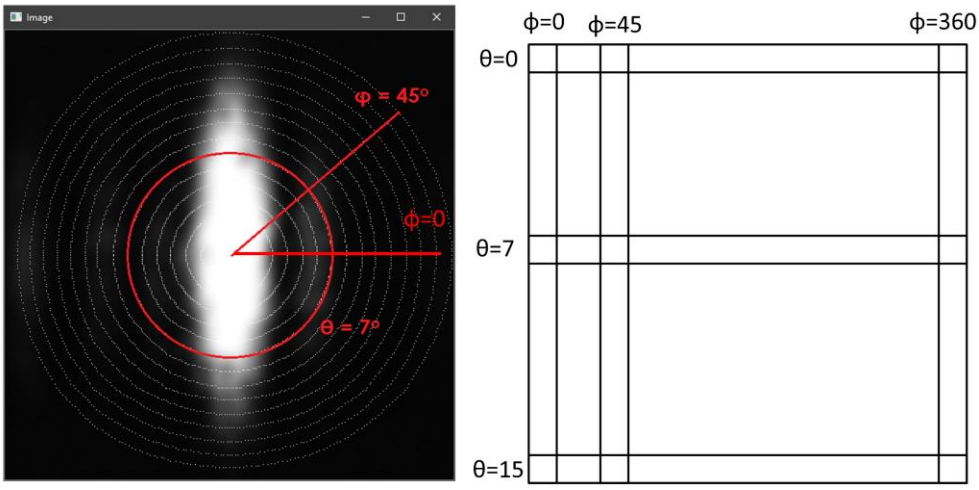

Figure 2: Data arrangement for digital processing

GUI for OPA testing setup

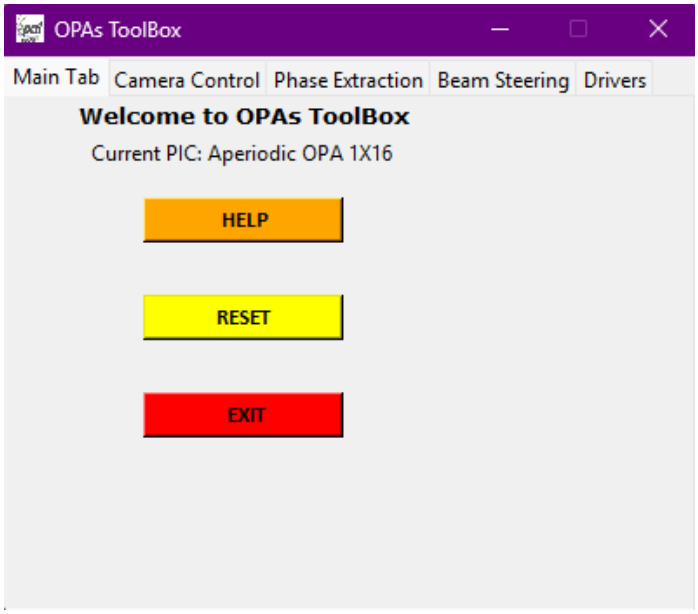

Figure 3: Welcome tab.

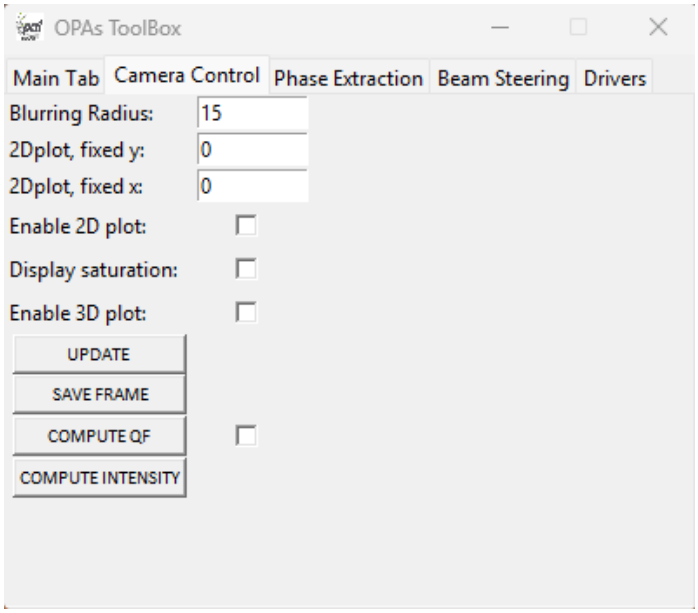

Figure 4: Monitor tab

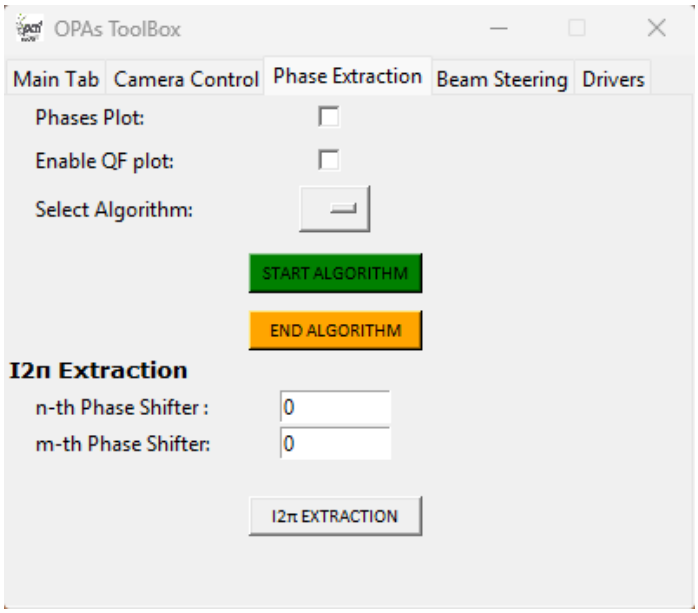

Figure 5: Phase calibration tab

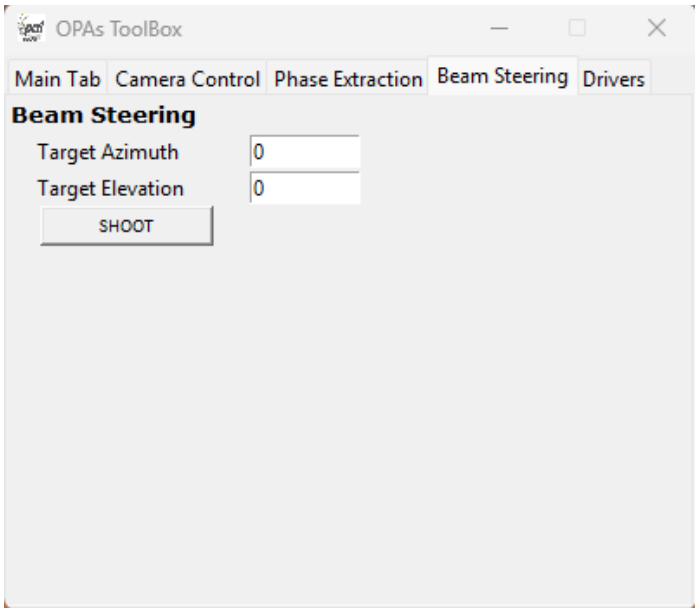

Figure 6: Beam-steering tab

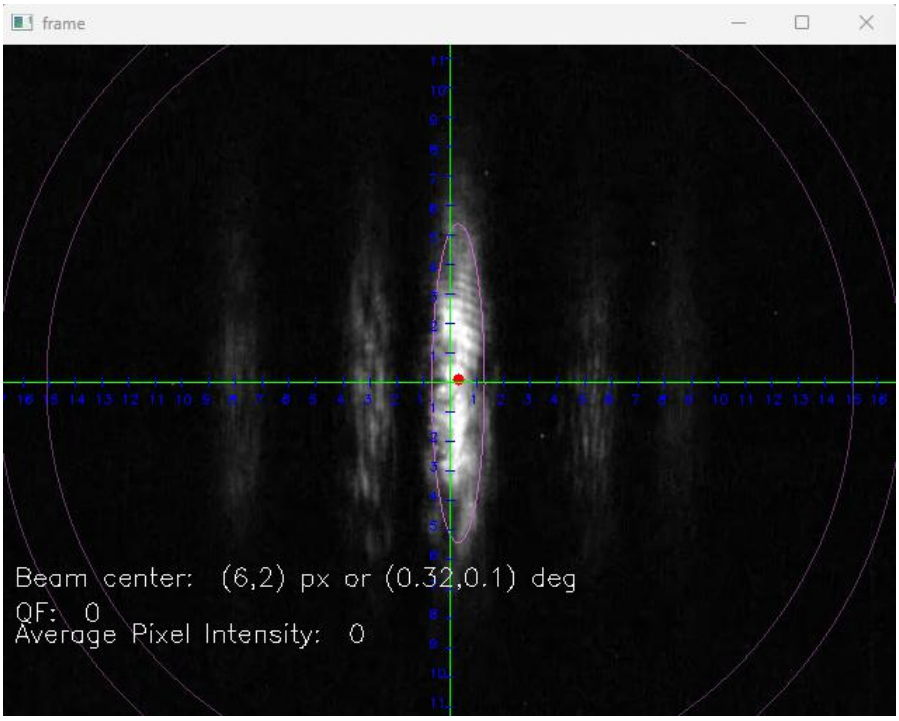

Figure 7: Example frame

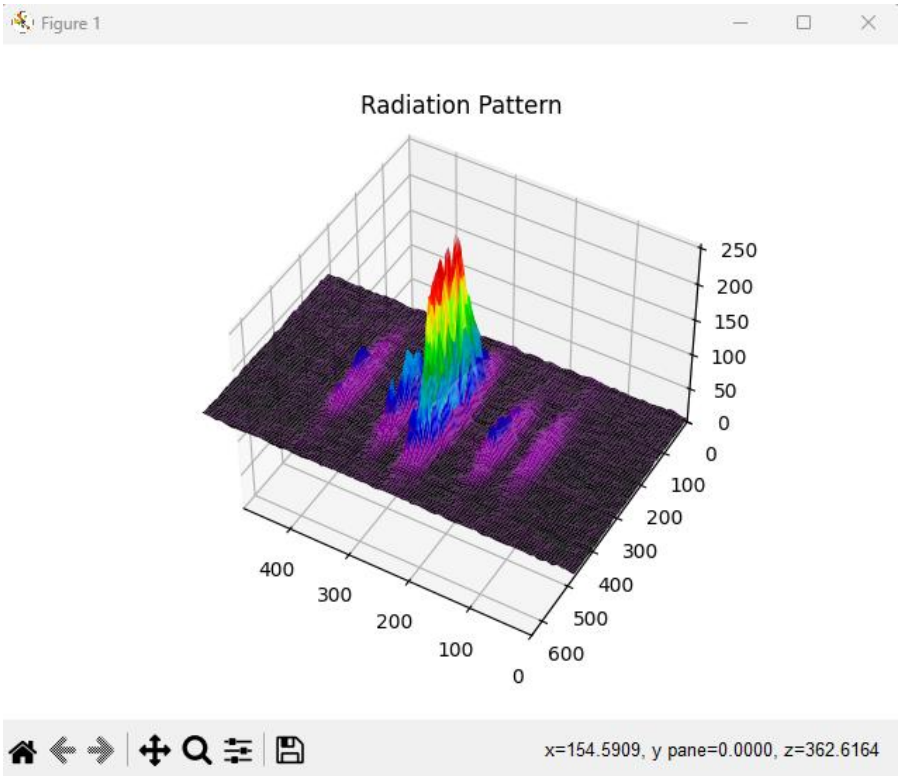

Figure 8: Example frame visualization in a 3D plot

Non-uniform OPAs: Post-processing of experimental data

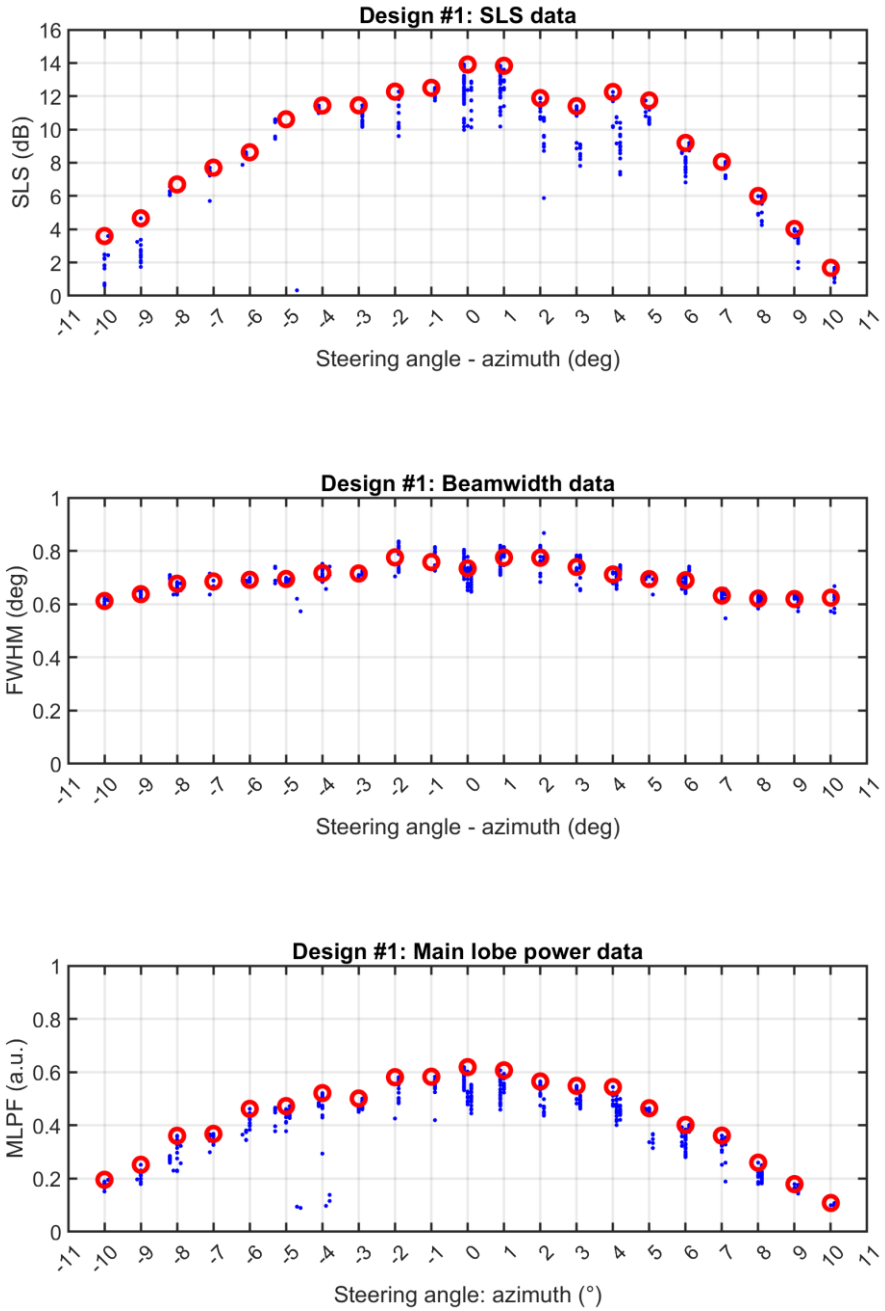

Figure 9: Experimental data from the aperiodic 16-channel linear OPA, design #1 in Table 6. The measurements selected for the figures presented in section 2.4.2 are highlighted in red.

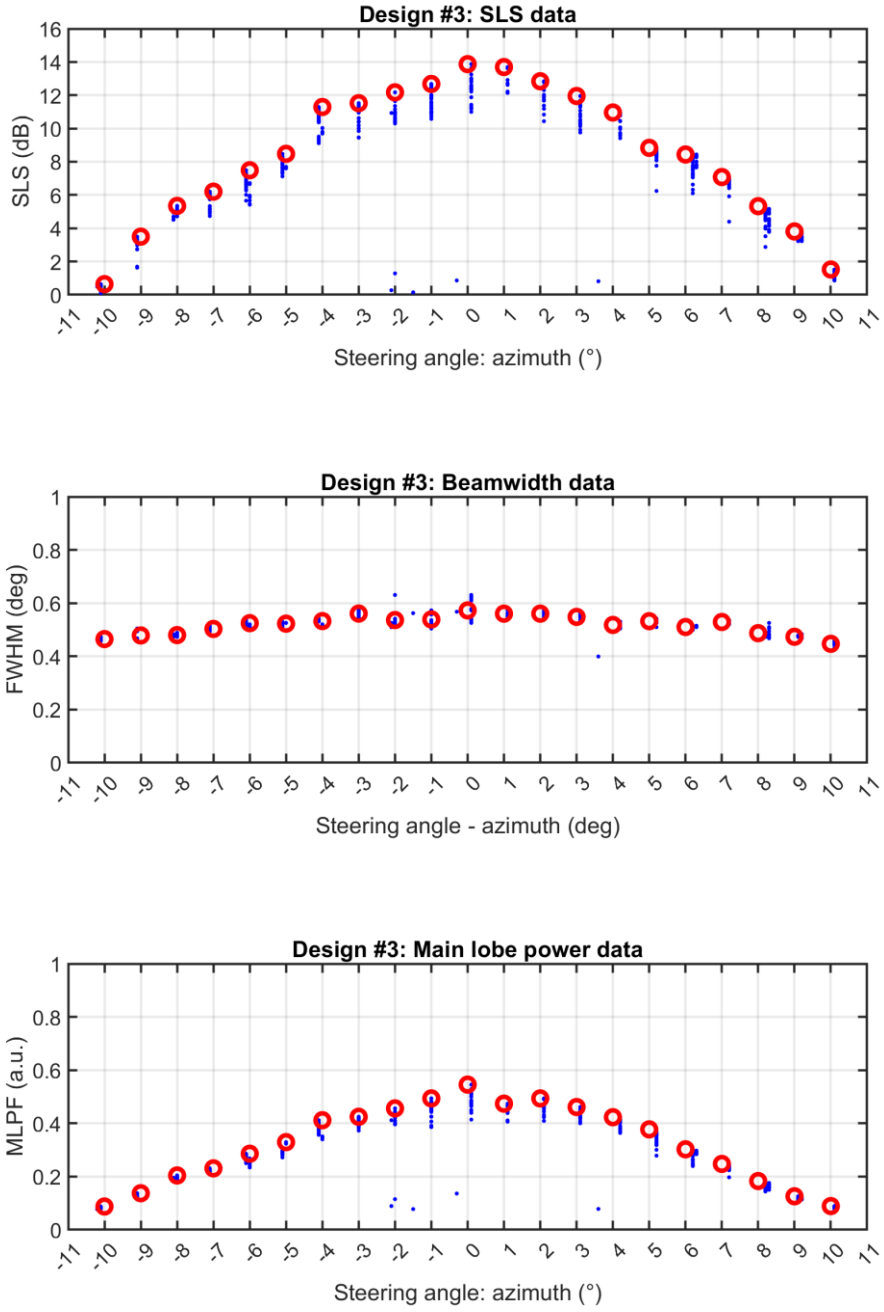

Figure 10: Experimental data from the aperiodic 16-channel linear OPA, design #3 in Table 6. The measurements selected for the figures presented in section 2.4.2 are highlighted in red.

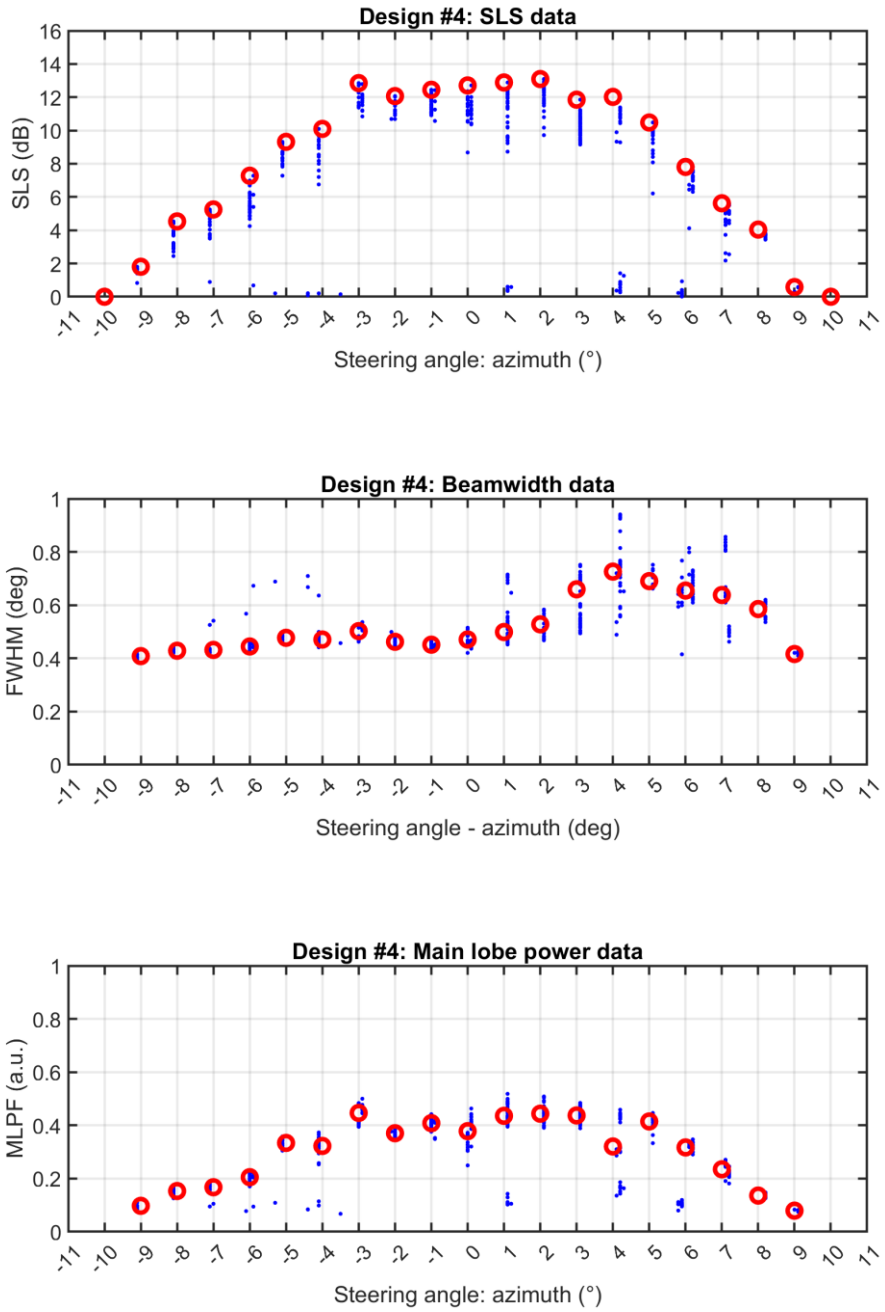

Figure 11: Experimental data from the aperiodic 16-channel linear OPA, design #4 in Table 6. The measurements selected for the figures presented in section 2.4.2 are highlighted in red.

List of figures

List of tables